Chemostratigraphy of the lowermost iron-manganese cycle of the Hotazel Formation, and implications for its primary depositional environment

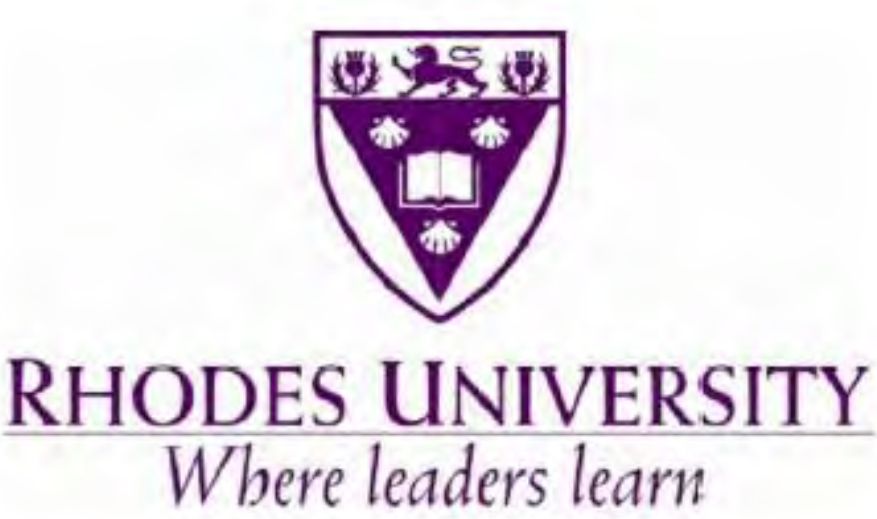

A thesis submitted to the Faculty of Science, Rhodes University, South Africa, in fulfillment of the requirements for the degree of Master of Science in Geology

Author: Ntseka Masoabi

Supervisor: Prof. Harilaos Tsikos

Declaration

All work in this thesis is the original work of the author, except where specific acknowledgement is made to the work of others.

Signed: 

.....

Acknowledgements

The support of the DSI-NRF Centre of Excellence (CoE) for Integrated Mineral and Energy Resource Analysis (DSI-NRF CIMERA) towards this research is hereby acknowledged. Opinions expressed and conclusions arrived at, are those of the author(s) and are not necessarily to be attributed to the CoE.
I sinclerely also like to express my deepest gratitude to ASSMANG for assisting in funding my studies and, ultimately, supporting me to attain the experience of gaining higher level education from a prestigious institution such as Rhodes University. I want to give thanks to Prof. Harilaos Tsikos for granting me the privilege of undertaking a monumental project that so transformed many aspects of who I am not only as a post-graduate pupil, but as a human being in general. How I so wish I could accurately articulate the impact your input and efforts in making me understand what natural science is really all about, through your willingness and enthusiasm in making me tackle my project diligently and with absolute determination. It is largely through your passion and sincere approach to science-based matters that I got to really enjoy every single second of all the seemingly unending discussions and 'hardships' that form an integral part of being a Master of Science student. You, sir, undoubtedly embody a quote I once encountered by an unknown author that says, " the great and curious truth about the human experience is that selflessness is the best thing you can do for yourself." A huge thank you to the Rhodes University, Geology department staff members, namely Andile Pikoli, Thulani Royi, Vuyo Nkayi, Ashleigh Goddard and Andrea King for their brilliant administrative assistance during my journey.

I also want to express my sincere gratitude to Dr. Xolane Mhlanga. You, sir, truly are and will remain my hero. Thank you so very much for your assistance with the technical side of my project. Your journey through academia, your ability to stand up for yourself and, most importantly, your sheer determination really inspired me to give my absolute best in whatever venture I so choose to undertake. Lastly, thank you for all the laughs and the good time we had at 76 Bathurst street. A great deal of my fondest memories are from that time.

To my beautiful and dearest sister, 'Malira Masoabi, there are literally no words to define and express your immense and selfless efforts towards ensuring that I am taken good care of. You are, by far, the most strongest and bravest person I have ever met. Without you I wouldn't be who I am. Thank you. And Khauhelo Majara, I really do not know how our friendship grew and became what it is today. Throughout my journey as a Master of Science student, you played so many roles ranging from a friend, mentor, advisor and, above all, family. Your approach to life really has, to a considerable degree, inspired me to commit to excellence and intelligent planning in everything I do. I honestly look up to you like an older sister. I also want to express my sincere gratitude to Mr. Julian Jacobs (JJ). Sir, I really

am standing on your shoulders... Thank you so very much for being there for me and playing a role of a father figure during my stay at Makhanda. Your proactive approach to life has taught me so many things about what this life can offer, if only we are humble and always willing to try things out. Above all, thank you for teaching me about the principles of *Ubuntu.* And Refiloe Namane, where do I begin, and what do I say? The last six months of compiling this dissertation was, arguably, the best period I could have ever asked for, as a student. Working with you at my 'home office' has truly showed me how powerful the human mind is. I also learned that the pursuit to what is reffered to as 'success' can be attained through simplicity, and that empathy can be our greatest strength. I wish you all the best in life my beloved friend.

A big thank you to the PRIMOR team – namely Donald Motilaodi, Mawande Ntantiso, Mamello Thokoa, Jarryd Labuschagne, Kenneth Chukwuma, Emma Ikwen, Stephen Dorbor and Esau Harawa. You guys are simply and truly the best. Each individual's liking for education and living life to the fullest really did leave an imprint in my life. I truly wish all of you the best in life.

Finally, I want to express my sincere gratitude to my beloved friends – Katlego Mphahlele, Tiego Thotse, Rethabile Taole, Chuma KaSigadla, Bafokeng Sekaleli, Teboho Ts'ehloane, Bokang Khabo, Yamkela Ciko and Thato Mofammere. I really do not have the proper words to express the amount of love and admiration I have for each and every one of you.

This is only the beginning of a monumental journey one is to tread on. Afterall, when one door closes the other opens.

Out of the night that covers me,
Black as the Pit from pole to Pole,
I thank whatever gods may be
For my unconquerable soul.

In the fell clutch of circumstance
I have not winced nor cried aloud.
Under the bludgeonings of chance
My head is bloody, but unbowed.

Beyond this place of wrath and tears
Looms but the horror of the shade.
And yet the menace of the years
Finds, and shall find, me unafraid.

It matters not how strait the gate,
How charged with punishment the scroll,
I am the master of my fate.
I am the captain of my soul

William Ernest Henley

Abstract

The giant Kalahari Manganese Field (KMF), located in the Northern Cape Province, South Africa, comprises approximately half of the world's manganese resources, estimated at about eight billion tons at grades ranging from 20-48 wt%. The KMF is linked to a period in geological time when the Earth's atmospheric and oceanic conditions underwent a major transition from oxygen-deficient to oxygen-enriched conditions – an event famously referred to as the Great Oxidation Event (GOE) that occurred around 2.4 Ga. The KMF deposits are hosted in Banded Iron Formation (BIF) of the Paleoproterozoic Hotazel Formation in the uppermost Transvaal Supergroup. The sedimentary Mn ores are interbedded with Hotazel BIF in the form of three alternating depositional cycles of BIF, transitional hematite lutite and laminated, carbonate-rich manganese ore. The lowermost and thickest of the three cycles is the most economically significant and has been mined for several decades on a large scale from the southernmost KMF.

In this study, two drill cores from the southern KMF were inspected, logged and sampled at a high resolution of approximately half-meter interval per sample. The selected cores, namely G774, capturing the lower portion of the Hotazel Formation from the Mamatwan locality, and MP-56, capturing the corresponding portion from the Middleplaats locality, are geographically proximal to each other, with a horizontal distance of roughly 3 km separating the two of them. The G774 drill core is characterized by a conspicuously thick manganese layer covering a thickness of 50 m, with the overlying BIF reaching a total thickness of 11 m. The MP-56 drill core, on the other hand, has a relatively thinner corresponding manganese layer of 30 m in thickness, while the overlying BIF layer exhibits a thickness of 24 m. The extent of sampling up-section was constrained by an apparently coeval black shale layer which represents the chosen upper stratigraphic marker for the lower part of the Hotazel section in the broader area that is under investigation in this thesis. That way, a high resolution chemostratigraphic approach was employed to elucidate the potential factors contributing to the relative sedimentary lateral thickness variations seen across the southernmost KMF. High-resolution geochemical data were used to explore relationships and signals that might constrain relative precipitation rates for iron and manganese against detrital species, fluctuating redox conditions in the original environment of deposition, and chemostratigraphic correlation. All geochemical data (i.e., major oxides, minor and trace elements and carbonate carbon isotopes) were obtained respectively through employing X-ray Fluorescence (XRF), Laser Ablation Inductively Coupled Mass Spectrometry (ICP-MS), and Gas-source mass spectrometry.

Comparative considerations made between the bulk geochemistry of the two sequences (i.e., Mamatwan and Middleplaats sections) reveal that periods of high-Mn deposition in the Hotazel Formation appear to be very Ca-carbonate rich (as indicated by high CaO, LOI and Sr concentrations). This, in turn, suggests that the Mn abundance is in the Hotazel ores is controlled mainly by the silicate phase braunite and is diluted by the deposition of Ca-carbonate through time. Bulk-rock concentration results for trace elements of the High Field Strength Element (HFSE) group (namely Zr, Hf, Y, Nb and Sc) were utilized to constrain the rates of either clastic and/or volcanic detrital inputs, as they traditionally represent refractory mineral particles of a common detrital/volcanic origin. The two chemosedimentary sequences preserve these elements in very low and thus quantitatively negligible concentrations – suggesting that the Hotazel depositional environment received very low and insignificant influx of a terrigeneous detrital component. A selection of these elements was therefore used to deduce, with caution, the relative as opposed to absolute precipitation rate of the major chemical constituents (i.e., Fe + Si vs Mn + carbonate), assuming a constant detrital flux through time. It was found that the relative abundances of Zr, Y and Nb is roughly 1.5 – 2 times as high in the BIF lithofacies relative to the Mn ones at both localities. This led to the inference that the Mn-enriched portion of the sediment must have been deposited at approximately twice the rate that the Fe-rich (BIF) portion was originally deposited.

In terms of redox-sensitive elements, the elements Co and Mo seem to reveal the most valuable insights into the redox environment of primary chemical deposition. Cobalt displays a unique pattern in that its highest concentration is attained at the hematite lutite transitions (similarly with the REE in this regard), while very low and seemingly invariant concentration is exhibited within the core of the main orebodies. The same pattern seems to be reproduced to a degree by the corresponding bulk MgO component, whereby MgO abundance maxima are associated with the basal hematite lutite and the hematitic flanks of the Mn-ore zone, while the core of the Mn-rich layer attains relatively low and essentially invariant MgO concentrations. This implicates a close and direct association of Co with the hematite fraction of the rocks and a concurrent enrichment in Mn-rich carbonate (dolomite). On the other hand, Mo seems to have a direct and clear association with peak MnO_2 content of the rocks, which in turn presents a high possibility of Mo having adsorbed onto primary Mn-oxyhydroxides in the water column, thus providing evidence that Mn-oxide must have acted as an important Mo sink, at least locally.

Finally, the carbonate-carbon isotope results provide a useful tool that brings the two stratigraphic sections “together“, in conjunction with other correlatable chemostratigraphic parameters (e.g. Co, Mg). The results demonstrate that bulk carbon fluxes and isotopic signals in the sediments must reflect primary processes of deposition, and that correlation across two apparently disparate lithostratigraphic sections can be effected. The key finding is that, at times, manganese deposition in one part of a

stratified basin was evidently accompanied by simultaneous BIF deposition at another, thus painting a very complex picture of massive primary chemical precipitation of Fe and Mn at the dawn of the GOE.

Table of Contents

List of Figures

List of tables

1. Introduction

1.1 General background

Iron formations, defined as stratigraphic units of sedimentary rock characterized by distinctive layering, bedding or laminae that contain at least 15% iron, and in which iron-rich mineral bands are interlayered with quartz, chert or carbonate-rich ones, are economically significant sedimentary rocks known to have been deposited more than three billion years ago (Bekker et al., 2010; Konhauser et al., 2017). During that time, the Earth system went through critical changes that, consequently, affected the style of iron deposition through time. Such changes in the Earth system incorporated the merging and breaking up of supercontinents operating in tandem (Nance et al., 1988; Hoffman, 1992). Mantle perturbations and super-plumes that influenced fusion and breakup of these supercontinents are thought to have been prime factors for large-scale alterations in the Earth's environment through geologic history. These included aspects such as the evolution of the biosphere, volcanism and oceanic composition, sea-level changes, weathering and sedimentation, and climate variations from greenhouse to icehouse conditions (Hutson and Logan, 2004; Holland, 2005; Bekker et al., 2010; Konhauser et al., 2017). The intercontinental steel industry owes its sustenance to iron ores, namely hematite and martite-rich concentrations of commercial value, that are derived from iron formations through processes of secondary (epigenetic) enrichment (Beukes and Gutzmer, 2008). On a global scale, these iron-ore deposits rank high among the largest ore deposits available to humanity (Beukes and Gutzmer, 2008; Bekker et al., 2010).

The distribution of iron formations is widely spread across the Precambrian geological record, ranging in age from the early Archaean (Isua, 3.8 Ga) to the Neoproterozoic Rapitan iron formations as late as 0.6 Ga (Figure 1; Bekker et al., 2010). At approximately 2.5 Ga, however, their overall volume seems to have reached a maximum (e.g., as exemplified in the Hamersley Basin iron formations of Western Australia and the Transvaal Supergroup iron formations of South Africa) while at approximately 1.8 Ga they became absent from the geological record, only to re-appear between in the Neoproterozoic between 0.8 and 0.6 Ga (Klein, 2005). Nonetheless, these unique sedimentary rocks, also referred to as Banded Iron Formations (and henceforth BIFs) owing to their distinct banded nature, may have had their size and extent misconstrued for certain time periods in Earth history, particularly with reference to the Archean. Generally, Archaean BIFs have experienced tectonic dismembering and deformation, and are thus normally discontinuous and poorly preserved – hence the underestimation of their true size and extent (Klein, 2005).

1.2 Classification and major BIFs globally

Precambrian iron formations are strictly divided into three major categories, largely based on their depositional setting. The first category of iron formations, known as Algoma-type BIFs, are known to be older than ~ 3.0 Ga and are largely present in Archaean volcano-sedimentary successions of greenstone belts that range in age from Eoarchean to the earliest Paleoproterozoic (Goodwin, 1973; James, 1983; Bekker et al., 2010; Konhauser et al., 2017). Their largest peak deposition is associated with a major plume event at approximately 2.75 to 2.70 Ga, and their presence is considered to mirror intra-basinal surges of magmatic and hydrothermal activity during the deposition of volcano-sedimentary greenstone successions (Hutson and Logan, 2004; Bekker et al., 2010; Konhauser et al., 2017). This class of iron formations is normally preserved in direct association with volcanic rocks and, in some cases, clastic sedimentary facies (greywacke). They are believed to have formed by exhalative hydrothermal processes in close proximity to volcanic centres. In view of their size and extent, they are relatively much thinner and less voluminous overall, rarely extending for more than 10 km along strike.

By contrast, Superior-type BIFs are considered to have been deposited in near-shore continental-shelf settings owing to their common inter-layering with carbonates, quartz arenites and black shale (Gross, 1980). These BIFs formed in continental shelves during episodes of high sea-level operating on a global scale and coupled with surges of intensified magmatic and hydrothermal activity. In terms of their size and aerial extent, they are relatively large both stratigraphically and laterally, with some major rock successions of the world hosting estimated mass of BIF in the range of 10^{14} Mt at 15 wt% iron content on average (James, 1983; Isley, 1995; Bekker et al., 2010; Konhauser et al., 2017).

Finally, the third type is the Rapitan-type BIFs as exemplified by the homonymous locality in Canada, with important other examples in many other parts of the world, such as the Urucum BIF in Brazil. These BIFs appear in Neoproterozoic sedimentary successions with a distinct stratigraphic setting linked directly to glaciogenic lithologies such as diamictite. Their origin is thus interpreted to be the result of transient marine anoxia and ferruginous deposition in direct association with peak glacial conditions of a snowball Earth environmental system (Klein and Beukes 1993; Klein and Ladeira, 2004).

It should be noted at this point that the above classes of iron-formations are generally mineralogically very similar, characterised by banded assemblages containing variable proportions of Fe oxides, silicates and carbonates along with much chert. In Archean stratigraphic units in particular, a precise distinction between Algoma-type and Superior-type BIF is thus difficult to decipher, especially because the rocks in that time frame were affected by intense deformation and shearing that lead to tectonic dismemberment of often genetically unrelated packages (Bekker et al., 2010; Konhauser et al., 2017).

As mentioned earlier, the reconstruction of the depositional basin and general geologic setting for the greatest majority of Archean BIFs is almost nearly impossible as these sequences have been subjected to tectonic deformation and metamorphism resulting in very scant preservation (Klein, 2005). Arguably the largest BIFs known are represented by a handful of successions around the world (e.g., Brazil, South Africa, India and Australia) which belong to the Superior type. These are present in well-preserved supercrustal sequences of a Neoarchaean to Paleoproterozoic (2.6 – 2.2 Ga) age that have been only slightly deformed and are essentially unmetamorphosed (Trendall, 2002; Bekker et al., 2010; Konhauser et al., 2017). These include the BIFs in Minas Gerais, Brazil, the early Proterozoic Asbestos Hills sequence of South Africa (Kuruman and Griquatown Iron Formations), the Hamersley BIFs of Western Australia (e.g. Brockman Iron Formation), and the Mulaingiri Formation of India (Klein and Beukes, 1989; Klein and Ladeira, 2002). Several slightly younger Superior-type BIFs (1.9 – 1.8 Ga) from the homonymous Lake Superior region (USA) and the Labrador Trough (Canada), are, by comparison, smaller in volume and have also experienced variable degrees of regional or contact metamorphism. These include the Negaunee Iron Formation, northern Michigan, the Mesabi Range, northern Minnesota, the Sokoman Iron Formation in the Labrador Trough, and the Gunflint Iron Formation in Ontario, Canada (Klein, 1966; French, 1968; Floran and Papike, 1975; Klein and Fink, 1976; Haase, 1982; Bekker et al., 2010).

1.3 Manganese deposits from deep time to present

The global geological record for the earliest part of Earth history, especially the first billion years or so, is practically devoid of any major economic manganese deposits, particularly those of a sedimentary origin. This scarcity of manganese-rich ore-deposit formation during that time is regarded as a strong indication of deficiency in free molecular oxygen in the atmosphere and hydrosphere. The late Archean marks the appearance of the first manganese deposits on record, which is reportedly correlated with the growth of oxygen oases in an otherwise reducing hydrosphere and atmosphere (Roy, 1997). Marine sedimentary manganese deposits in the Paleoproterozoic reach an evident peak through the development of the Kalahari Manganese Field (KMF), the main topic of this thesis. This is a period in geological time when the Earth's atmosphere and oceans evidently transitioned from oxygen deficient to oxygen enriched conditions, marking an event famously and widely referred to as the Great Oxidation Event (GOE) that occurred at around 2.4 – 2.3 Ga (Figure 2; Holland, 2006; Lyons et al., 2014).

Further on across geological time, the distribution of manganese deposits seems to become slightly more variable and diverse (as shown in Table 1). While the Paleoproterozoic is characterized by a single yet giant sedimentary manganese deposit (KMF), the Neoproterozoic era preserves smaller manganese deposits restricted to glaciogenic sequences in association with Rapitan-type BIF. Eventually, the

Phanerozoic eon is characterized by significant variation in size and age in the distribution of manganese deposits, especially for the Paleozoic and Mesozoic eras (Roy, 2006). As for the present ocean, this is known to contain substantial resources of manganese in the form of the vast occurrences of manganese nodules littered across the global oceanic abyssal plains (Roy, 2006).

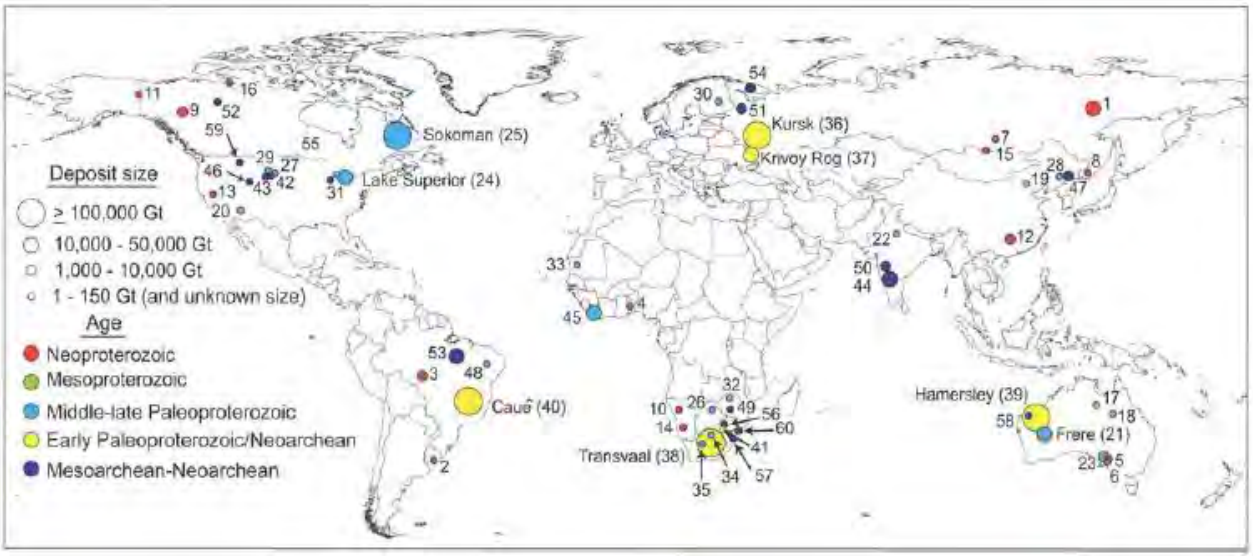

#	Formation/Group/Deposit	Location	Age (Ma)
1	*Maly Khinghan Formation*	Russia	560
2	Yerbel Formation	Uruguay	560
3	*Jacadigo Group (Urucum district)*	Brazil	600
4	*Bisokpabe Group*	Togo	600
5	Chestnut Hill Formation	USA	600
6	*Holowilena Ironstone*	Australia	650
7	*Braemar Iron Formation*	Australia	650
8	*Vil'va and Koyva Formations*	Russia	650
9	Bakeevo (Tolparovo) Formation	Russia	650
10	*Dzhefymtau Suite*	Kyrgyzstan	650
11	UK Formation	Russia	700
12	Yamata Formation	Russia	700
13	Lake Khanka Formation	Russia	700
14	*Rapitan Formation*	Canada	715
15	*Chuos Formation*	Namibia	715
16	*Tindir Group*	USA	715
17	*Fulu Formation*	China	741
18	*Medvezhevo Formation*	Russia	700-750
19	*Kingston Peak Formation*	USA	700-750
20	*Numees Formation*	Namibia	700-750
21	*Mugur Formation*	Mongolia	767
22	Nizhne-Angara Formation	Russia	800
23	Aok Formation (Shaler Supergr.)	Canada	840
24	Xiamaling Formation	China	1368
25	Roper Group	Australia	1490
26	South Nicholson Group	Australia	1500
27	Shoshong Formation	Botswana	1600
28	Chuanlinggou Iron Formation	China	1650-1600
29	Pike's Peak Iron Formation	USA	1728
30	Frere Formation	Australia	1890
31	Alwar Group (North Delhi fold belt)	India	1850-2000
32	Lake Superior region	USA+CAN	
-	Gunflint Iron Formation	Canada	1878-1850
-	Negaunee Iron Formation	USA	1874-1850
-	Biwabik Iron Formation	USA	1880-1850
-	Ironwood Iron Formation	USA	1880-1850
-	Riverton Iron Formation	USA	1880-1850
33	Sokoman Iron Formation	Canada	1877
34	Rochford Formation	USA	1884
35	Liaohe Group	China	1950-2050

#	Formation/Group/Deposit	Location	Age (Ma)
36	Estes Formation	USA	2020-2100
37	Pääkkö Iron Formation	Finland	2080
38	Glen Township Formation	USA	2100
39	Lomagundi Group	Zimbabwe	2100-2200
40	Caldeirão belt	Brazil	>2078 - <2687
41	Ijil Group	Mauritania	2200
42	Nimba Itabirite	Liberia	>2100 - <2615
43	Hotazel Iron Formation	South Africa	>2200 - <2426
44	Timeball Hill Formation	South Africa	2320
45	Kursk Supergroup	Russia	2450
46	Krivoy Rog Supergroup	Ukraine	2450
47	Transvaal Province	South Africa	
-	Griquatown Iron Formation	South Africa	2431
-	Kuruman Iron Formation	South Africa	2465
-	Penge Iron Formation	South Africa	2480
48	Hamersley Basin	Australia	
-	Boolgeeda Iron Formation	Australia	2445
-	Weeli Wolli Formation	Australia	2449
-	Brockman IF (Joffre Mbr)	Australia	2461
-	Brockman IF (Dales Gorge Mbr)	Australia	2461-2495
-	Mt. Sylvia Formation	Australia	2505
-	Marra Mamba Iron Formation	Australia	2597
49	Caué Formation	Brazil	2450
50	Indian Creek Metamorphic Suite	USA	2470
51	Ruker Series	Antarctica	2450-2480
52	Benchmark Iron Formation	USA	2480-2560
53	Hutchison Group (Middleback)	Australia	2500
54	Nemo Iron Formation	USA	2560-2890
55	Chitradurga Group	India	2614
56	Beardmore-Geraldton assemblage	Canada	2700
57	Anshan Iron Formation	China	2700
58	Manjeri Iron Formation	Zimbabwe	2700-2830
59	Bababudan Group	India	2720
60	Central Slave Cover Group	Canada	2730-2920
61	Carajás Formation	Brazil	2740-2750
62	West Rand Group	South Africa	2960
63	Pongola Supergroup	South Africa	2960
64	Jack Hills belt	Australia	>3080
65	Moodies Group	South Africa	3230

Figure 1: Major sediment-hosted iron formations of the world, including BIF, GIF, and Rapitan-type iron formations from the Mesoarchean to Neoproterozoic (Bekker et al., 2010).

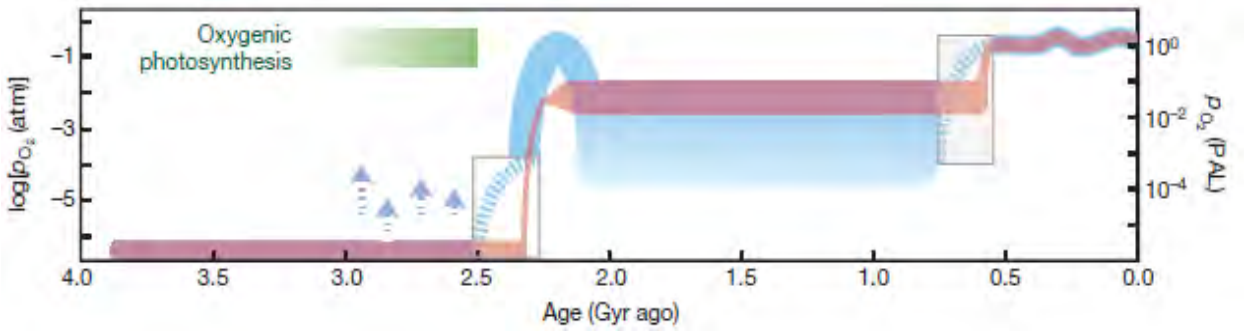

Figure 2: Evolution of Earth's atmospheric content through time. Note the timing of the GOE around 2.4 Ga (Lyons et. al., 2014).

1.3.1 Source and transport of manganese

The actual source of manganese in the formation of ancient sedimentary deposits remains, to this day, complex and elusive. Prevailing notions point towards hydrothermal and terrestrial weathering mechanisms as likely primary sources for manganese in the eventual depositional environments. It has been well established that in modern oceanic settings, for example, manganese dispersal from mid-ocean ridge hydrothermal fields occurs through buoyant plumes caught by ocean currents (Klinkhammer and Hudson, 1986; Roy, 1997). Hence, the hydrothermally sourced manganese component is transported across considerable distances from the initial sites of hydrothermal supply.

By contrast, dissolution and redistribution of manganese from terrestrial sources takes place through surface weathering mechanisms, particularly in humid, tropical climates (Roy, 1997). In the early Phanerozoic, for instance, decomposing vegetation is thought to have produced organic acids capable of leaching manganese at varying rates, under climate conditions promoting low-pH development in soils (Nicholson, 1990; Roy, 1997). This leached manganese is then carried by ground and surface waters down-slope to lakes, rivers and ultimately the oceans. Transportation of manganese to the oceanic environment is thought to be most effective as colloids or particulates, as compared to the dissolved, divalent state of Mn(II), as Mn is very stable as a solid oxy-hydroxide in oxic surface environments. The situation would have been markedly different, however, in the early Earth when oxygen contents in the atmosphere were vanishingly low, and therefore mobility of reduced manganese in aqueous solutions would have been much more favoured (Sapozhnikov, 1970; Roy, 1997).

1.3.2 Hydrothermal manganese deposits

This class of manganese deposits is typically stratabound in nature but could also exist as epithermal veins and irregular bodies in a diverse field of host rocks (Nicholson, 1992). Subduction-related stratabound and vein-type hydrothermal manganese deposits, as an illustration, are generally hosted in

sedimentary rocks such as cherts, hemipelagic and volcano-clastic rocks that overlie island-arc type basalts, andesite, dacite and rhyolite (Roy, 1997).

In quite a number of localities, Phanerozoic hydrothermal manganese deposits exhibit distinctive tectonic, mineralogical and chemical signatures that are correlateable to deposits developed hydrothermally in marine domains adjacent to spreading centres, mid-plate seamounts and island-arc settings. Several hydrothermal deposits from active plate margins, for instance (e.g., northern Apennine assemblages, Pindos and Orthris zones and Olympic Peninsula) arise from fossil spreading centres and ancient mid-ocean ridge domains that have been obducted onto continental crust through orogenic processes (Park, 1946; Bonatti et al., 1976; Robertson and Varnavas, 1993; Roy 2019).

1.3.3 Sedimentary manganese deposits

By comparison to hydrothermal deposits, sedimentary manganese deposits are large in terms of size and distribution. They are hosted mainly in two types of sedimentary successions, namely chemical and organic-rich sediments (limestones and black shales respectively) in continental shelf-type settings of the Phanerozoic (Maynard, 2010; Roy, 1997), and in iron-formations. The former type appears to be associated with alternating periods of marine transgression and regression (Frakes and Bolton, 1992), which caused a switch in deep-water depositional conditions from anoxic (reduced manganese preservation in soluble form) to oxic (manganese precipitation as oxide, later modified into carbonates through anaerobic diagenesis). The BIF association is exemplified by the KMF deposit and will naturally be the focus of subsequent sections.

1.4 Manganese associated with iron formations

Only a handful of manganese-rich districts across the world have been identified to have a direct linkage with sedimentary iron formations, and these are associated primarily with the Neoproterozoic Rapitan BIF class (see earlier reference in this chapter). In principle, the close chemical association between manganese and iron implies, to a certain degree, that natural solutions that are rich in iron could have also been a major source of manganese (Schissel and Aro, 1992). As early as 1957, Krauskopf argued that the dissociation of iron from manganese in an oceanic setting can take place under fluctuating Eh conditions: if, as an illustration, deep and oxygen-deficient, iron and manganese-rich waters, upwell onto a continental shelf area, iron facies (i.e., carbonates, oxides, and silicates) would be expected to be the first chemical sediments to precipitate, forming banded iron formation facies. Manganese-rich

facies would, eventually, precipitate as the lingering oceanic solutions would reach the shallower and more oxidising side of the shelf (Schissel and Aro, 1992).

Table 1: Age distribution of selected manganese deposits (Roy, 2006).

	Age	Deposits/sequence	Geological setting
Phanerozoic	Early Oligocene	Nikopol, Ukraine; Chiatura, Georgia	Shallow-shelf sandstone–glauconite–claystone hosted Mn oxide grades basinward to Mn carbonate **(TR). G**
	Cretaceous (Cenomanian–Turonian)	Imini–Tasdremt, Morocco	Mn oxide interbedded with dolomite; inner shelf sequence **(TR). L**
	Cretaceous (Cenomanian–Turonian)	Ulukent–Gökçeovack; S.W. Taurides, Turkey	Mn carbonates and oxide beds in cherty limestone–black shale sequence **(TR). S**
	Cretaceous (Late Albian–Early Cenomanian)	Groote Eylandt, Australia	Pisolitic–oolitic Mn oxide horizon overlying siltstone with Mn carbonate and pyrite **(TR). L**
	Late Jurassic (Kimmeridgian)	Molango, Mexico	Mn carbonate beds overlying black shale **(TR). G**
	Early Jurassic (Early Toarcian)	Úrkút, Hungary	Mn carbonate beds in radiolarian clay–marlstone horizon underlying black shale in OAE sequence. **S**
	Late Devonian (Famennian)	Karadzhal, Central Kazakhstan	Mn oxide and carbonate interbeds in siliceous clayey limestone **(TR). L**
	Middle Ordovician	Taojiang, China	Mn carbonate interbedded with black shale; shallow shelf **(TR). S**
Neoproterozoic	ca. 625 Ma	Santa Cruz Fm., Jacadigo Group, Brazil. (=Boqui Group, Bolivia)	Glaciomarine sequence. Mn oxide beds alternate with BIF and clastic rocks with dropstones **(TR). M**
	ca. 625 Ma	Datangpo Sequence, Liantuo–Nantuo ice age, China	Glaciomarine sequence. Black shale-hosted Mn carbonate beds. No BIF **(TR). S**
	ca. 750–650 Ma	Chuos Fm., Damara sequence, Namibia	Glaciomarine sequence. Mn oxide interbedded with BIF **(TR). M**
	ca. 800 Ma	Penganga Group, India	Shelf sequence. No evidence of glaciation. Interbedded Mn oxide (rare Mn carbonate) and chert enclosed in limestone. No BIF **(TR). S**
Paleoproterozoic	2.0 Ga	Sausar Group, India	Shelf orthoquartzite–carbonate–pelite (metamorphosed). Mn oxide and Mn silicate±carbonate beds hosted in pelite/quartzite/carbonate **(TR). L**
	2.0 Ga	Gangpur Group, India	Shallow-shelf Mn oxide±silicate interbedded with pelites overlying black shale horizon. **S**
	ca. 2.2–2.1 Ga	Franceville Group, Gabon	Cratonic shelf. Mn carbonate interbedded with black shale, dolomite, sandstone **(TR). L**
	ca. 2.3–2.0 Ga	Birimian Supergroup, West Africa	Intracratonic rift-related greenstone belt. Mn carbonate beds in black shale **(TR). M**
	ca. 2.4 Ga	Itabira Group, Minas Supergroup, Brazil	Stable shelf. Mn oxide interbedded with BIF and dolomite **(TR). M**
	ca. 2.4 Ga	Hotazel Formation, Postmasburg Group, Transvaal Supergroup, South Africa	Shallow-shelf. Mn oxide–carbonate ore interbedded with BIF at several levels **(TR). G**
	>2.4	Rooinekke Formation, Koegas	Mn oxide ore interbedded with BIF **(TR). S**
	<2.5 Ga	Subgroup, Ghap Group, Transvaal Supergroup, S. Africa	
Archean	≥2.6 Ga	Chitradurga Group, India	Shallow shelf. Interbedded Mn oxide–chert–phyllite. Close association with stromatolite. **S**
	>2.6 Ga	Sandur Group, India	Shallow shelf. Interbedded Mn oxide–quartzite–greywacke–stromatolitic carbonate. **S**
	>2.6 Ga	Eastern Ghats sequence, India	Shallow shelf. Mn oxide/carbonate–silicate interbanded with leptynite, calc silicates, pelitic granulites. **S**
	2.78–2.72 Ga	Nova Lima Group, Minas Gerais, Brazil	Basin margin. Mn silicate–carbonate rock hosted in black shale overlying volcanics. **S**
	2.9–2.7 Ga	Jequi Complex, Bahia, Brazil	Mn silicate–carbonate rock hosted in carbonaceous marls metamorphosed to granulites. **S**

Relative sizes of deposits: **G**=giant, **L**=large, **M**=medium, **S**=small.
(TR)=transgression related.

Such a conceptual facies model would, in principle, explain alternations of Fe and Mn-rich sedimentary facies in an environment favouring iron formation deposition, as a result of fluctuating Eh conditions with changes in water depth (e.g. transgression-regression cycles; Button et al., 1982; Cannon and

Force, 1983). However, Mn deposits are indeed extremely scarce in association with the voluminous Superior-type iron formations which dominate the BIF record before the GOE (Bekker et al., 2010; Konhauser et al., 2017). It thus may be that the lack of oxygen from the atmosphere and oceans before the GOE, did not allow major sedimentary manganese precipitation to take place in association with iron formation deposition. A notable exception to this rule is the KMF deposits of the Hotazel iron formation, which as already indicated, will be described in a lot more detail in later sections. A brief first description of the KMF is made here along with a couple of occurrences of manganese ores of the world in evident association with Superior- and Algoma-type iron formation before the GOE.

1.4.1 Minas Gerais, Brazil – Mesabi Range, Minessota

Manganese deposits in this region are closely linked with iron formation of the 2.4 Ga Itabira Group, which forms part of the Minas Series Supergroup in Minas Gerais, Brazil (Dorr and Barbosa, 1963; Maxwell, 1972; Morgan et al., 2013; Schissel and Aro, 1992). The Itabira Group is sub-divided into the Caue Itabirite and the Upper Gandarela Formation. The Caue Itabirite is a rock sequence characterized by oxide facies banded iron formation with alternating bands of quartz, hematite, magnetite and martite (Maxwell, 1972). Minor chlorite and talc schists are inter-fingered with the iron formation. Upwards along the sequence, at the top of the iron formation, small manganese-rich beds occur. These manganese ore-beds are manifested as discontinuous lenses interrupted by pinch and swell structures ranging in size from a couple of centimetres to over 7 m thick. These manganese occurences consist of manganite, pyrolusite and psilomelane, and are inter-layered with argillite schist as well as banded iron formation (Schissel and Aro, 1992). The oxide-rich nature of these manganese occurrences suggest that they represent the products of supergene enrichment of parts of the primary stratigraphy with generally low contents in contained manganese. Similar occurrences of sub-economic supergene manganese ores of this type have also been reported from the Sokoman iron formation in the USA (Klein and Fink, 1976).

1.4.2 Noamundi-Singhbhum, Orissa, India

The western Singhbhum region in Orissa state, India, preserves deposits of manganese that are associated with iron formation. Economically, the present manganese production, as compared to historical figures, has depreciated substantially. There remains roughly 200 small open-pit mines in the Keonjhar region, with manganese ore-grades that are generally low by comparison to those for iron (Coffman, 1992; Schissel and Aro, 1992).

The so-called Noamundi Group, belonging to the Iron ore Supergroup, is arguably one of the very few good examples of manganese associated with a volcanosedimentary succession of Archaean age containing Algoma-type iron formation. The Noamundi Group in its entirety, has been folded into a sequence of northeast-plunging anticlines and synclines. This has made the accurate stratigraphic thickness measurements and facies associations nearly impossible, although field evidence broadly maintains a cyclic deposition of banded iron formation, manganese carbonate and dolomite, and manganese oxides interbedded with shales (Schissel and Aro, 1992).

Stratigraphically, the Noamundi Group comprises the Lower Shale Formation, the Banded Hematite Jasper Formation, and the Manganiferous Shale Formation. The Lower Shale Formation comprises shale interbeds and mafic lava flows and tuffs (Banerji, 1977; Schissel and Aro, 1992). Similarly, the Banded Hematite Jasper Formation consists of interlayered shales and volcaniclastic tuffs at its base, followed by hematite jasper (iron formation). The lower portion of the Upper Manganiferous Shale Formation preserves manganese ore-beds occurring stratigraphically above the iron-formation. Mineralogically, the manganese in the ore beds occurs as rhodochrosite with psilomelane and manganite associations upon supergene reworking.

1.4.3 Kalahari Manganese Field, South Africa

The giant Kalahari Manganese Field (KMF), stretching over a roughly oval-shaped geographical area of approximately 40 km from north to south, comprises the world's largest manganese resource, estimated at eight billion tons at ore grades ranging from 20 – 48% Mn (Gutzmer and Beukes, 1995, 1996). The KMF is therefore the major resource of manganese metal in the world, and its giant resource base is foreseen to remain active for many years to come. The deposit occurs within the Hotazel Formation in the uppermost Paleoproterozoic Transvaal Supergroup (Tsikos and Moore, 1997; Tsikos et al., 2003). The stratiform manganese beds are directly and intimately associated with banded iron formation in the form of three alternating depositional cycles of BIF, transitional hematite lutite, and manganese ore (Beukes, 1973; Tsikos and Moore, 1997; Tsikos et al., 2003). The sections that follow provide a comprehensive background of the regional-to-local geological setting of the KMF.

1.5 Regional geologic setting

The southern African Kaapvaal craton, covering an area of approximately 1.2×10^6 km^2, preserves an accumulated sequence of sedimentary (clastic and chemical) and igneous rocks distributed among three

major sub-basins (Figure 3). It is recognized as one of the best-preserved Archean cratons, exhibiting a thorough documentation of Palaeoarchean to Palaeoproterozoic sedimentation, interrupted by a few large-scale surges of magmatic activity (Anhaeusser et al., 2006; Humbert et al., 2017). The craton is also comprised of severely deformed early Archean greenstone belts with tonalitic gneisses intrusions (ca. 3.6 – 3.7 Ga), and several granitic plutons (3.3 – 3.0 Ga).

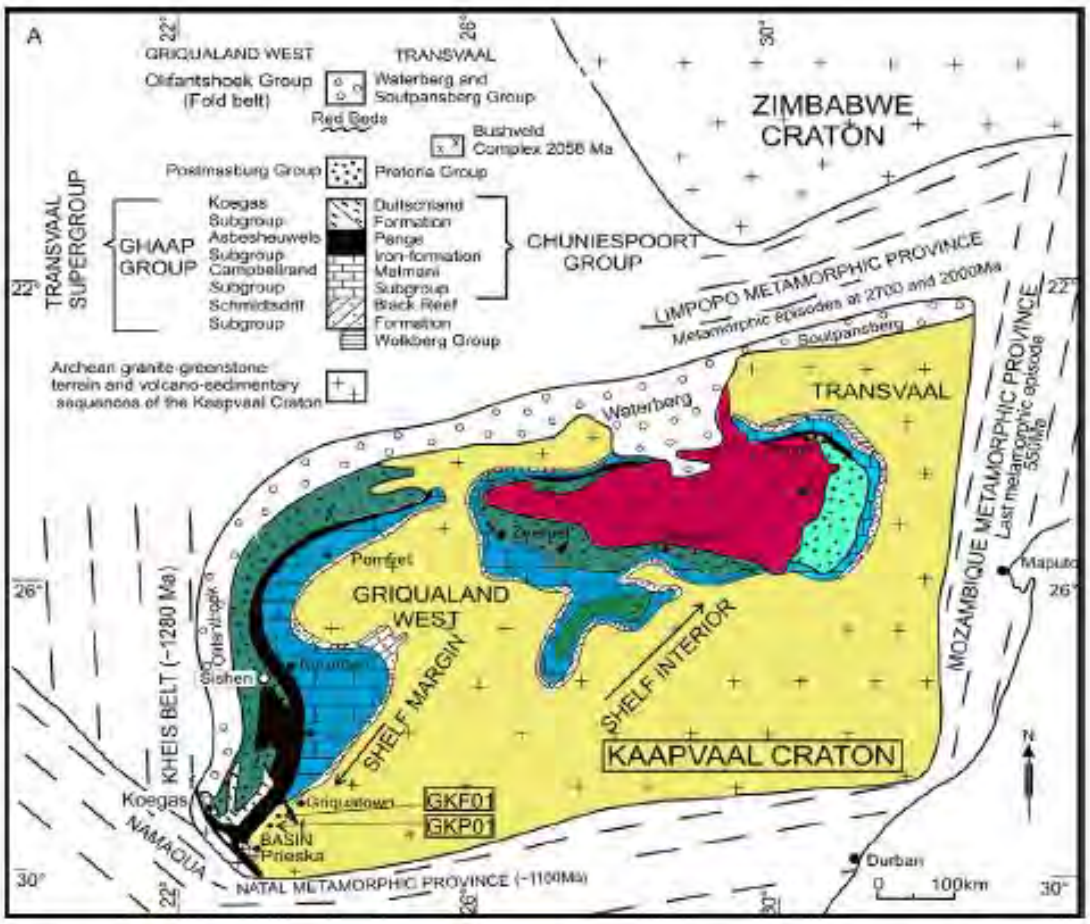

Figure 3: Map of the Kaapval craton displaying the distribution of major rock stratigraphic units of the Transvaal Supergroup in the Griqualand West and Transvaal areas (Knoll and Beukes, 2009).

The Transvaal Supergroup, out of several large rock successions, corresponds to an extended interval of largely uninterrupted sedimentary deposition on the craton during the Palaeoproterozoic (Humbert et al., 2017). The Supergroup was deposited in three basins, namely the Griqualand West Basin situated on the western part of the Kaapvaal craton, and the Kanye and Transvaal basins situated on the north and central part of the craton respectively (Humbert et al., 2017). These basins are identified by lithostratigraphically comparable depositional facies (Eriksson et al., 2006; Humbert et al., 2017). In each basin the sediments rest unconformably on the Neoarchaean Ventersdorp Supergroup (Armstrong et al., 1991; Altermann and Wotherspoon, 1995). Carbonate facies are the most abundant across all three basins forming the basal part of the corresponding Supergroups along with lesser siliciclastic

sediments (Eriksson et al., 1995). Laterally extensive and thick BIF overlies the carbonate lithofacies in all instances. From the three sub-basins, the Griqualand West one concerns the topic of this thesis and will be the main focus below.

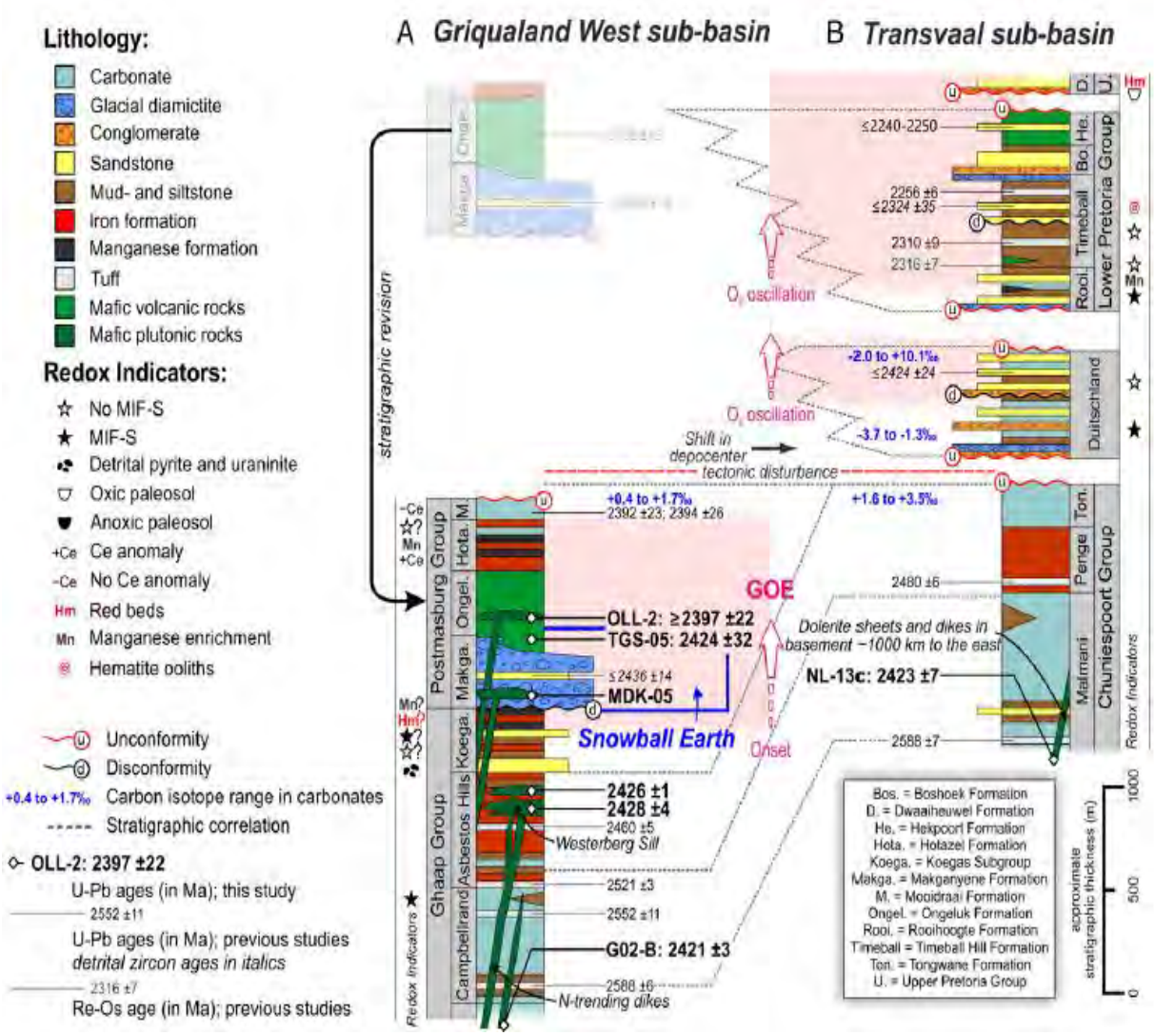

Figure 4: Stratigraphic synthesis of the Transvaal Supergroup as preserved in two main basins: (A) Griqualand West in the southwest and (B) Transvaal in the northeast (Gumsley et. al., 2017).

1.5.1 The Griqualand West Basin

1.5.1.1 Ghaap group

The Transvaal Supergroup in the Griqualand West Basin contains two major stratigraphic sub-divisions of rock sequences, known as the lower Ghaap Group and the upper Postmasburg Group (Figure 4). The stratigraphy and sedimentary facies of the Ghaap Group is further sub-divided into the Schmidtsdrift, Campellrand, Asbestos Hills and Koegas Subgroups (Beukes, 1983; Altermann and Hälbich, 1990; Figures

3 and 4). The basal Schmidtsdrift Subgroup, ranging in thickness from 10 – 250 m, lithostratigraphically comprises shale, quartzite and lesser carbonates (Beukes, 1983). The Campellrand Subgroup, which conformably overlies the Schmidtsdrift Subgroup, is a very thick sequence of predominantly carbonate strata (dolostone and limestone) with lesser BIF and shale, ranging from 1500 – 1700 m in total stratigraphic thickness. Within the Campbellrand Subgroup, there are two major paleofacies domains recognized in the literature, geographically developed on either side of the so-called Griquatown fault (Fig. 5). These are known as the Ghaap Plateau facies and the Prieska facies (Beukes, 1987), further subdivided into several different formations.

The Campbellrand Subgroup, in turn, is overlain by the Asbestos Hill Subgroup, a succession covering a total thickness of 250 – 750 m and 200 – 250 m for the Kuruman and Griquatown Iron Formations, respectively (Fig. 5). The lower Kuruman Iron Formation is lithologically characterized by microbanded facies iron formation, while the Griquatown Iron Formation overlying it comprises clastic-textured, granular iron formation (Beukes and Smits, 1987). The Kuruman Formation is further subdivided into three Members – the basal Kliphuis Member (comprised of alternating chert and ankerite mesobands), the middle, cherty Groenwater Member, and the occasionally riebeckite-rich Riries Member. Likewise, the Griquarown Iron Formation is divided into three members of its own, which comprise from the base upwards the Middlewater Member (characterized by siderite-hematite rich assemblages) the Danielskuil member (typified by siderite-greenalite-rich lutites) and the Pietersberg member, lithologically represented by greenalite-rich lutites and minor siliciclastic interlayers (Beukes, 1983). The Kuruman and Griquatown Iron Formations constitute key source rocks for major hematite iron ore deposits found in the broader region (e.g., Sishen iron ore deposit; Beukes and Gutzmer, 2008).

Finally, the Koegas Subgroup forms the stratigraphic top of the Ghaap Group. It is largely composed of siliciclastic facies and intercalated iron formations, with minor carbonates at its uppermost part. It attains a total thickness between 240 – 600 m and is manifested exclusively in the southern parts of the broader region (Beukes, 1983).

1.5.1.2 Postmasburg group

The Makganyene Formation forms the stratigraphic base of the Postmasburg Group. This body of rock comprises glacial diamictites interlayered with shale, sandstone, and minor BIF, developed as a relatively thin succession of 50 – 150 m (Beukes and Smit, 1987; Moore et al., 2001). The diamictite is described as a generally massive rock containing facetted and striated clasts that that are poorly sorted (Moore et al., 2001). Previously, the stratigraphic contact between the Makganyene Formation and the underlying Koegas Subgroup was interpreted as unconformable with a hiatus lasting as much as 200 Ma.

(Beukes 1980; Moore, et al., 2001). This was based in part on a disputed 2.2 Ga age for the overlying Ongeluk volcanics (see below for details) However, the fact that the Makganyene Formation lies on a single, 50 m thick member of the Asbestos Hills Subgroup extending across a 200 km strike distance between the towns of Hotazel and Griquatown, was deemed indicative of the absence of a major discontinuity between the Ghaap and Postmasburg Groups (Moore et al., 2001). This contention was further supported by radiometric age constraints for detrital zircon grains collected from the Makganyene Formation (Moore et al., 2011). The Makganyene Formation was thus interpreted as a boundary surface during a regression event, being conformably interbanded with Koegas-type sediments in the west and at the same time being transgressive across Asbestos Hills iron formations on the flanks of the Vryburg arch to the east, within the Griqualand West Basin (Moore et al., 2001).

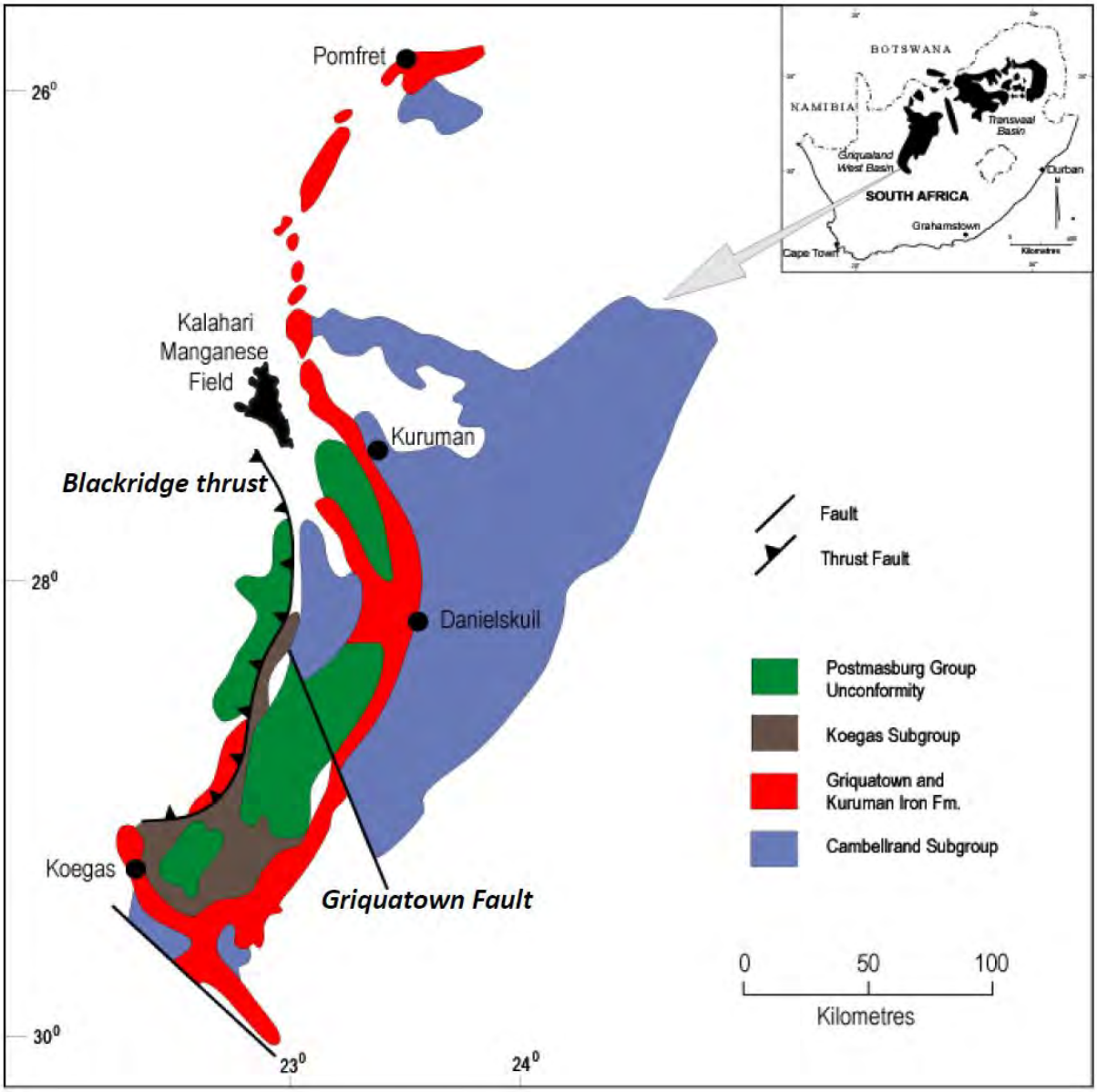

Figure 5: Regional geological map and broad-scale regional stratigraphy of the Transvaal Supergroup in the Griqualand West Basin. The outline of the KMF is also indicated.

The volcanic Ongeluk Formation conformably overlies the Makganyene Formation and forms the base of the so-called Voëlwater Subgroup in the upper Postmasburg Group (Beukes and Smit, 1987; Tsikos and Moore, 1997). The Ongeluk rocks comprise massive basaltic andesite flows with recognized pillows in their upper portions, attaining a total thickness generally between 600 and 900 m. The age of the Ongeluk Formation was contentious for many years, largely because of an earlier published whole-rock 2.2 Ga age (Cornell and Schütte, 1995). However, recent dating of dykes interpreted to have acted as feeders to the Ongeluk volcanic flows have yielded a radiometric age at 2.43 Ga (Gumsley et al, 2017), which is corroborated further by a recently published tuff age from the overlying Hotazel Formation itself at 2.4 Ga (Schier et al., 2020).

The Ongeluk Formation is conformably overlain by a maximum of 200 m thick chemical sedimentary rocks of the Hotazel Formation, recognized by the characteristic cyclic succession between BIF and Mn-rich layers through hematite lutite transitions (Gutzmer and Beukes, 1995; Tsikos and Moore, 1997; Tsikos et al., 2003; Tsikos et al., 2010). The Hotazel Formation is preserved beneath a 40 to 70 m sand-calcrete cover of the Tertiary Kalahari Formation, and outcrops at the Black Rock hillock in the northern KMF, wherein thrusting (Blackridge thrust) apparently duplicated the Hotazel rock sequence (Tsikos and Moore, 1997; Tsikos et al., 2003; Fig. 5,6). In turn, the Hotazel Formation is overlain by the Mooidraai Formation which terminates the Postmasburg Group stratigraphy with a package of limestone (locally dolomitized) and minor cherts (Tsikos et al., 2003; Fairey et al., 2013).

1.6 The Hotazel Formation in the KMF

The Northern Cape Province of South Africa is the locality that is bestowed with the giant Kalahari Manganese Field (KMF) and its world class manganese mineralization (Fig. 5,6). The KMF occupies an area of approximately 400 km^2 located in the southernmost margin of the Kalahari savannah, approximately 60 km north of the city of Kuruman (Tsikos and Moore, 1997; Tsikos et al., 2003; Kuleshov, 2010; Chetty and Gutzmer, 2012). The KMF is globally recognized as an area that hosts at least eight billion tons of commercially viable, massive manganese ores at an ore-grade range between 20 and 48% Mn (Tsikos et al., 2003; Tsikos and Moore, 2005). This is considered to represent as much as 75% of the presently documented manganese resources from all continental deposits (Laznicka, 1992; Beukes et al., 1995; Astrup and Tsikos 1998; Tsikos et al., 2003).

The manganese deposits of the KMF are hosted in the Hotazel Formation of the Voëlwater Subgroup, in the classic and instantly recognisable cyclic sequence of four BIF layers interbedded with three layers of sedimentary manganese - rich material (Tsikos and Moore, 1997; Tsikos et al., 2003, 2010). The Hotazel sedimentary succession overlies and is frequently interfingered with pyroclastic an hyaloclastic volcanic

rocks of the underlying Ongeluk Formation (Kleyenstüber, 1984; Tsikos and Moore, 1997; Gutzmer and Beukes, 1998). At its stratigraphic top, it is overlain conformably with the carbonate strata of the Mooidraai Formation (Bau et al., 1998; Tsikos et al., 2001; Fairey et al., 2013).

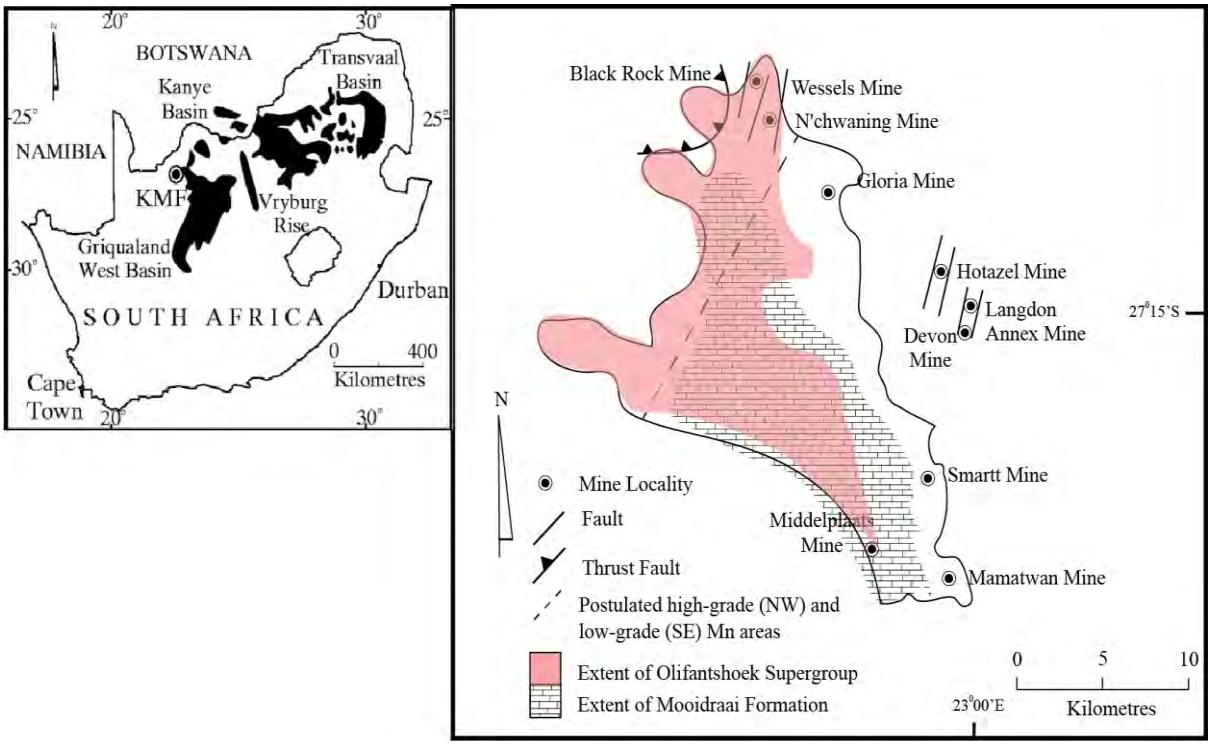

Figure 6: Locality map of the Kalahari Manganese Field showing the distribution of major lithologic formations, important structural features and location of some defunct and operating manganese mines (modified after Tsikos and Moore, 2005).

The Hotazel BIF is a finely laminated rock that fits perfectly the description of a classic microbanded facies BIF. At the base, and immediately above the Ongeluk lavas, the BIF is red in colour as it contains substantial amounts of oxidized iron in the form of hematite. Magnetite is also a key component of the rock here as disseminations and mm- to sub mm-scale microlaminations, along with much fine-grained quartz (chert) and lesser carbonate minerals in the matrix. This red BIF grades upwards into what is called a hematite lutite, namely a very fine-grained rock containing "dusty" hematite, mm-scale carbonate laminae and microscopic oval-shaped carbonate "ovoids" (Kleyenstüber, 1984; Tsikos et al., 2003, 2010). The amount of magnetite from the red BIF in these lutites becomes gradually less and less up section until it is not seen, and the same occurs with the abundance of fine-grained hematite and chert in the matrix. In turn, the rock progressively becomes darker and richer in the mineral brunite, a Mn- silicate with the formula Mn_7SiO_{12} dominated by trivalent Mn(III) in its structure (Kleyenstuber, 1984; Gutzmer and Beukes, 1995). Carbonate laminae and ovoids continue to dominate in the rocks, although their colour seems to become progressively lighter (whiter) as the rock becomes darker (i.e. more Mn-rich). Further upwards, the Mn-rich zone gives way again to hematite lutite, and finally to BIF again.

The above situation essentially repeats itself another two times further up in the stratigraphy, except that the BIF changes above the lowermost and thickest manganese-rich layer (up to 45 m), which also constitutes the most economically important part of the Hotazel sequence (Kleyenstüber, 1984; Tsikos and Moore, 1997; Tsikos et. al., 2003). Mineralogically, the BIF above the lower Mn layer becomes hematite-free, silicate- and magnetite-rich, and progressively also more carbonate-rich compared to silicate content higher in the stratigraphy (Tsikos and Moore, 1997; Tsikos et al., 2003). This sequence of BIF is punctuated with another two Mn layers, a thin one of no more that 5 m in thickness, usually, and the uppermost and second thickest one which can be up to 20 – 25 m in places (Tsikos and Moore, 1997; Tsikos et al, 2003). The transitions from the BIF to the Mn layers and back are characterised by hematite-lutite zones again, of variable thickness from one contact to the other. Mineralogically, the Hotazel BIF is comprised of abundant chert and magnetite throughout, the carbonates ankerite, calcite and siderite in increasing modal amounts stratigraphically upwards, and the iron-rich silicates greenalite, minnesotaite, stilpnomelane and very occasional riebeckite (Tsikos and Moore, 1997).

1.7 Manganese ore types in the KMF and localized metasomatism

Two major types of manganese ore exist within the boundaries of the Kalahari Manganese Field; namely low-grade Mamatwan-type ore and hydrothermally altered, high-grade Wessels-type ore (Kleyenstüber, 1984; Gutzmer and Beukes, 1995, 1996). The former is typified by the very fine-grained braunite-rich material as described in the previous section, with dominant braunite and manganiferous carbonates (kutnahorite, Mn calcite) and lesser, finely intergrown hematite. This ore type is the one mined currently (or previously) at Mamatwan, Middelplaats and Gloria Mn mines (Fig. 6) and is regarded as diagenetic to very low grade metamorphic in origin at best, with the abundance of manganese reaching a highest value of 42 wt%.

In the northernmost KMF, there is a plethora of normal NS faulting that intersects the Hotazel Formation in the area near the Black Rock Mine (Fig. 6). Adjacent to these faults, relatively lower-grade sedimentary-diagenetic Mamatwan-type ore is interpreted to have been upgraded to high-grade "Wessels-type" ore largely by a metasomatic alteration process which was proposed to have occurred at ca. 1.25 Ga (Dixon, 1989; Gutzmer and Beukes, 1995, 1996, 1997). This upgrading is thought to have resulted from a process of leaching of Mg, Ca, CO_2 and SiO_2 from the original Mamatwan-type "protore", leading subsequently to Mn enrichment of mainly residual nature. This is supported by features such as increase in porosity and a decrease in preservation of the initial sedimentary lamination (Beukes et al., 1995; Gutzmer and Beukes, 1997). The enrichment process also seems to have been accompanied by much compaction of the entire Hotazel sequence and especially of the Mn layers, up to two-thirds of their original stratigraphic thickness (Gutzmer and Beukes, 1997; Tsikos et al.,

2003). This is especially well illustrated in the study of Tsikos et al. (2003) where they show how the lowermost Mn layer in the Wessels-N'chwaning area of hydrothermal metasomatism (Fig. 6) has a thickness not greater than 6 – 8 m, whereas the same ore layer in the unmetasomatised Gloria area immediately further to the south has a thickness of 10 – 12 m on average, i.e. much lower than the thicknesses seen in the southernmost part of the KMF (i.e. Mamatwan and Middelplaats mines). That type of ore is in fact what is thought to have been the protore to the high-grade metasomatized ores in the northernmost KMF.

With regard to the high-grade Wessels-type ore, this appears to be coarse crystalline and with a characteristic oxide and silicate-rich mineralogy, dominated by calcic braunite (braunite II), hausmannite and bixbyite (Gutzmer and Beukes, 1995, 1996, 1997). The Wessels-type ore manganese content is reported to be as high as 55 wt% (Gutzmer and Beukes, 1995). Geographically, it is important to emphasize again that this ore type is bound to the northernmost part of the KMF, an area characterized not only by faulting but also thrusting to the immediate west (Gutzmer and Beukes, 1995; Figs. 5,6). These structures have been regarded since earlier times to have played a major role in forming the high-grade ore (Kleyenstuber, 1984), although the relative roles of the thrust and fault structures remain to be investigated further.

1.8 Aims and objectives of the study

The inception of this study grew in large part from the fundamental question regarding the underlying causes and reasons for the relative thickness variations seen in the Hotazel Formation between the BIF and Mn-rich layers. As mentioned in the previous section, in the northernmost KMF one sees very reduced stratigraphic thicknesses between the Hotazel intersections of the metasomatized (Wessels-N'chwaning) and neighbouring unmetasomatised (Gloria) areas (Fig. 6). Tsikos et al (2003) highlighted these thickness variabilities and noted that they probably reflect the overall reduction in thickness of the Hotazel Formation following metasomatic leaching and compaction. However, across the larger part of the KMF, major thickness variability also occurs, as also illustrated in the study of Tsikos et al. (2003). Although there is a general trend to suggest that the Hotazel sequence becomes thinner overall as one moves from south to north, there are also substantial thickness variations in the individual BIF and Mn-rich strata of the Hotazel Formation over short distances. This was highlighted already in an earlier study by Tsikos and Moore (1997), where it was noted that the thickness variations appear antithetic,

i.e. they show that when the Mn layers are getting thicker, the BIF around them is becoming correspondingly thinner, without the total thickness changing very much. Importantly, in these areas

there is no evidence of the kind of metasomatic processes that we see in the northernmost KMF containing the Wessles-type high-grade ores.

The abovementioned features form the basis of the current study. The aim of this thesis is to investigate the reasons that may have caused this relative thickness variation in the Hotazel strata. The first fundamental hypothesis that was initially made by the author in his discussions with his supervisor in designing this project, is that the thickness variation must be related to the primary depositional environment of the Hotazel sediments, as there seems to be no major tectonic process that would have dismembered or duplicated the rocks. Therefore, it is thought that any thickness variation must be related to processes taking place in the primary depositional basin, and they may have to do with factors such as, for example, differences in the precipitation rates for primary Fe and Mn minerals across the original basin. Understanding such causes and controls is crucial not only for the original formation mechanisms of the Hotazel Formation, but also for its economic potential, as thicker Mn layers with higher Mn contents would also be the most favourable ore materials for mining companies interested in exploiting manganese ore in the KMF. This is also illustrated in historical reconstructions of the lateral stratigraphic variability in the Mamatwan and Middelplaats areas, which appear to represent a geographically Mn-rich end-member (SE) against a more Fe-rich end-member in the SW (Figs. 7,8).

The original environment of deposition of Fe and Mn is, of course, also very important in its own right; the KMF deposits are thought to be at the centre of the GOE, which as mentioned earlier was a period in Earth history characterized by an increase in oxygen in the atmosphere and oceans. Such an increase would have influenced greatly the deposition of manganese and iron (Lyons et al., 2014), but how exactly did these metals precipitate in the first place: how did they develop these clear cycles which show that they must have precipitated in a decoupled way? And more crucially, how did the thicknesses vary so much of the individual Fe and Mn strata, and why did they do so antithetically (Tsikos and Moore, 1997; Tsikos et al., 2003)? This antithetic relationship (shown in Figure 9), leads to the hypothesis that if the depositional rate for Fe and Mn was more or less the same across the basin and especially over small distances, would that mean that at certain times in certain parts of the basin where manganese was precipitating forming Mn-rich sediment, in nearby parts of the same basin (by a few kms) Fe may have been precipitating forming what is now BIF? This spectacular possibility and its possible significance, sits at the very heart of the current investigation.

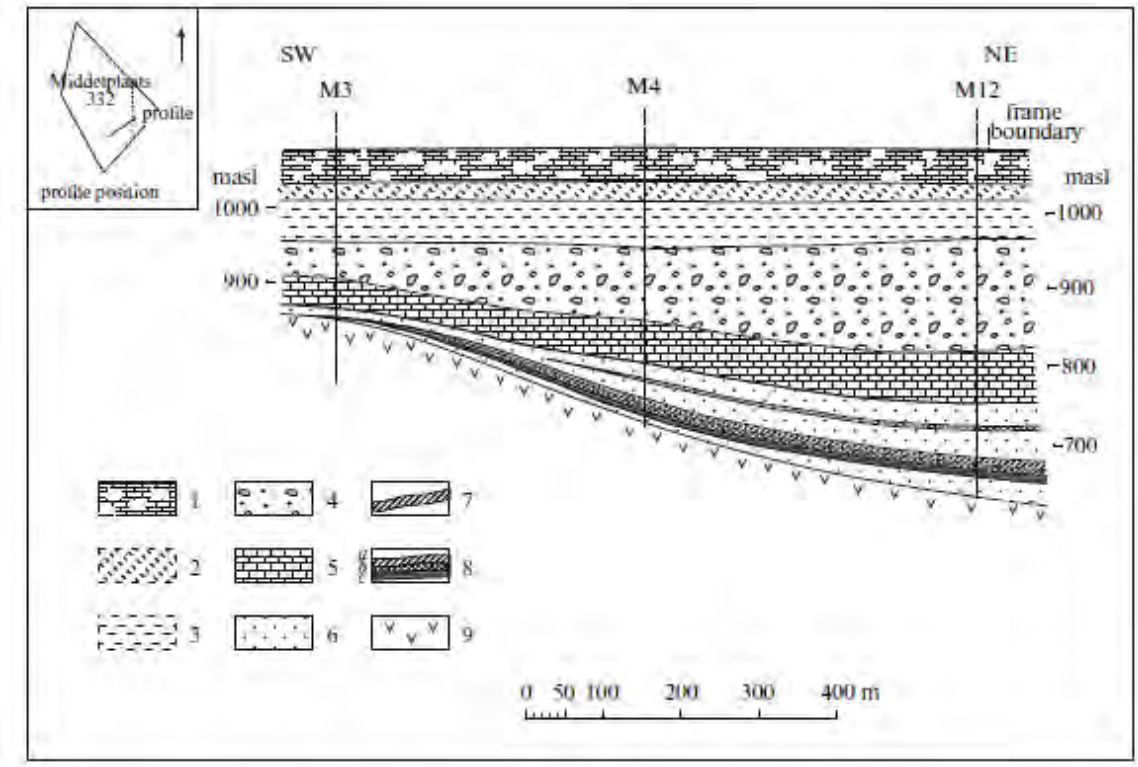

Figure 7: Schematic geological section across the Middelplaats deposit (Kalahari manganese field, South Africa) (Jennings, 1986). (1–3) Kalahari Formation: (1) calcretes; (2) red clay; (3) brown clay; (4) Dwyka Formation (tillites); (5) Mooidraai Formation (dolomites); (6–8) Hotazel Formation: (6) banded ferruginous silicites; (7) middle manganese ore horizon; (8) ores of the lower manganese ore horizon: (a) low_grade, (b) medium_grade, (c) high_grade; (9) Ongeluk Formation (andesitic basalt lavas).

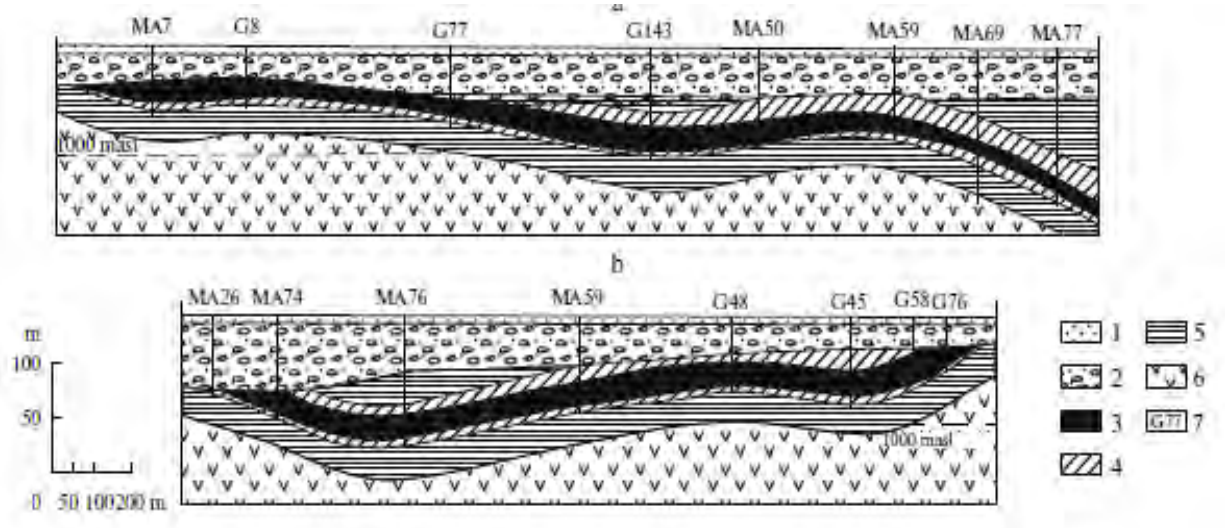

Figure 8: Schematic geological sections across the Mamatwan deposit (Kalahari manganese field, South Africa) (Nel et al., 1986). (a) SE–NW; (b) SW–NE. (1) Kalahari Formation (sand); (2) Kalahari Formation (pebble, sand, and calcretes); (3–5) Hotazel Formation: (3) upper manganese ore sequence; (4) lower manganese ore sequence; (5) banded ferruginous silicites; (6) Ongeluk (andesitic basalt lavas); (7) boreholes.

In order for this project to be carried out, two drillcores had to be selected that record these thickness variations mentioned above in the best possible way, and which are also geographically quite proximal. These drillcores were made available by the company SOUTH32, who have been instrumental for the

facilitation and execution of this project and are sincerely acknowledged. The cores selected were from the Middleplaats and Mamatwan areas in the southern KMF, where marked thickness relationships are seen (Fig. 9). The two drill cores, namely G774 (capturing the section from the Mamatwan area) and MP-56 (capturing the section from the Middleplaats area) were obtained roughly 3 km apart from each other. Drill core G774 attains a conspicuously thick layer of manganese as high as 49 m, with the overlying BIF being no more than 11 m thick. The corresponding manganese layer in drill core MP-56 has a roughly 24 m thickness, while the overlying BIF layer displays a thickness of about 25 m (Figure 9). It should be noted that the thickness of the two BIF sections was constrained by a dark shale layer which serves as a stratigraphic marker for the bottom part of the Hotazel section in the broader area, a few meters below the middle manganese layer.

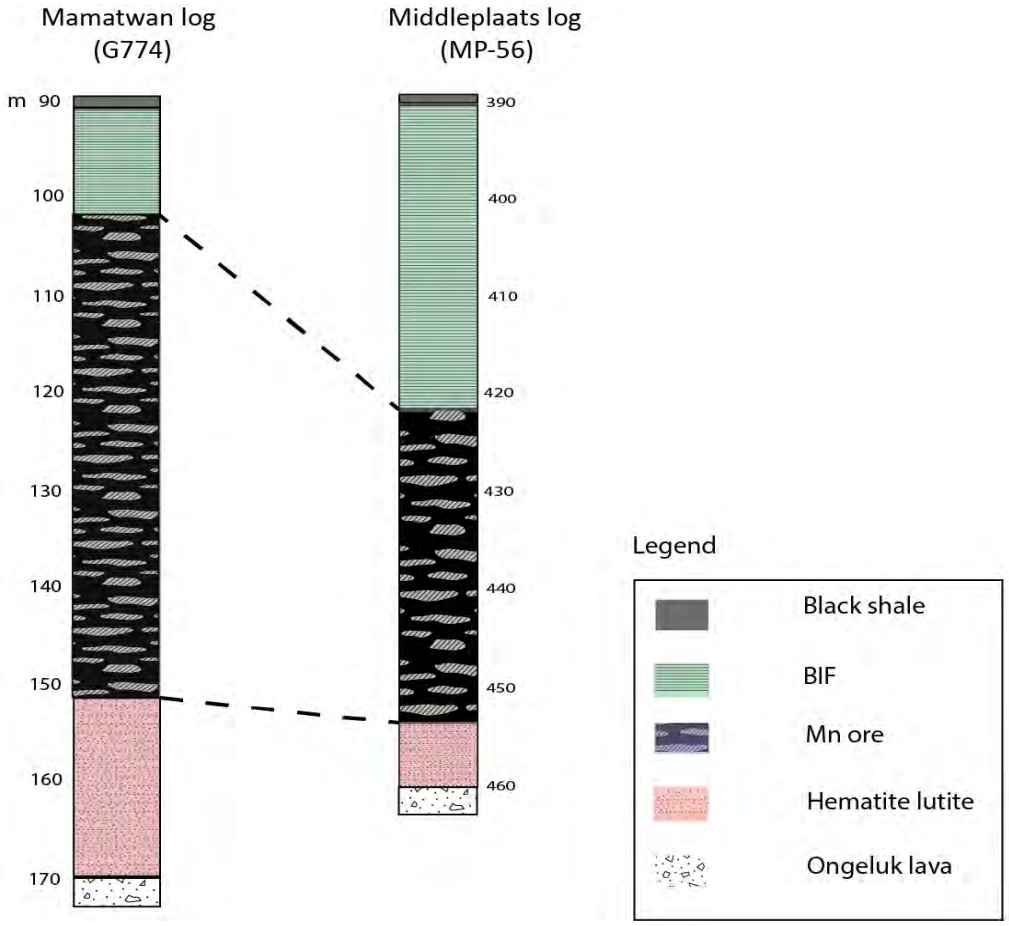

Figure 9: Schematic stratigraphic logs capturing the lower part of the Hotazel Formation from the mine areas of Mamatwan (G774) and Middleplaats (MP-56), and selected for high-resolution study.

In light of the above considerations, an unprecedentedly high-resolution chemostratigraphic approach was chosen in order to elucidate the potential factors contributing to lateral thickness variations seen in the southernmost KMF. The chosen approach borrows principles from chemostratigraphy (see brief review below), and specifically the establishment of basinal correlation through comparing geochemical variations of geochemical proxies such as carbon isotopes and major-trace chemical components.

In summarizing, this study will utilize high-resolution geochemical data in a stratigraphic context, to shed light on the following overarching objectives:

1) Any geochemical relationships that will illuminate relative precipitation rates for iron and manganese in the primary depositional basin of the Hotazel Formation;
2) Any geochemical signals that illuminate the redox environment of the same environment, with emphasis on vertical and possible lateral gradients in redox conditions; and,
3) Any geochemical parameters that serve best for chemostratigraphic correlation and therefore reconstructions of the primary depositional environment of the Hotazel Formation on a scale applicable to at least the part represented by the southernmost KMF area.

1.9 Chemostratigraphy as a research tool

Chemostratigraphy, also referred to as chemical stratigraphy, is defined as the study of variations in the chemical content of sediments (Halverson et al., 2010). It is a sub-discipline that began to grow considerably in the late 1970s, through various notable contributions (e.g. Berger et al., 1978; Weissert et al., 1979; Scholle and Arthur, 1980; Weissert et al., 1979; Duplessy et al., 1981, to name a few). The significance of stable carbon isotope geochemistry for stratigraphic purposes and paleoceanographic reconstructions, has been acknowledged since those times (Weissert et al., 2008). Earlier reports (as early as the 1950s) have also been mentioned, with researchers utilizing carbon isotopes to explore ancient, as well as modern, environments, ecosystems and climate (Gröcke, 2020). In particular, Emiliani (1955) was among the very first researchers to utilize the principles of investigating stratigraphic variations in isotopes and their utility for correlation. He showed, for example, the way oxygen isotopes in planktonic foraminifera in drill cores from the Caribbean varied across time and their paleoclimatic (paleotemperature) significance in recording several glacial-interglacial cylces. A decade later, the term 'isotope stratigraphy' appears to have been formally coined by Gonfianti (1965; from Gröcke, 2020).

Chemostratigraphic applications on the ancient rock record range widely, and modern techniques are continually being established. These include paleoenvironment reconstruction, establishing the tectonic setting of sedimentary basins, and indirect dating and development of correlations on a regional – global scale (Halverson et al., 2010). When used in concert with bio-and magnetostratigraphy, it becomes a very powerful stratigraphic weapon. Generally, chemical signals exploited in chemostratigraphy could be utilized as provenance indicators and are also proxies for the chemistry of the marine environment or environmental conditions at the time of deposition of sediments. Fluctuations in seawater chemistry, especially in several isotope compositions, make proxy data very

useful in correlations at regional to global scale (Halverson et al., 2010). Furthermore, proxies that exhibit a larger degree of variation and are not susceptible to being altered by diagenetic and/or secondary processes, are intrinsically effective.

The Precambrian era is certainly fertile ground for chemostatigraphy due to limited abundance of fossils (Knoll and Walter, 1992), but applications are rather minimal for very old chemical sedimentary sections (Paleoproterozoic or earlier), probably due to relatively poor preservation. By contrast, the Neoproterozoic Earth history is particularly recognized as a period of time wherein chemostratigraphy finds substantial application, especially in light of the remarkable biospheric and geochemical changes and outliers associated with Rodinia break-up, assembly of Gondwana, snowball glaciations, ocean oxygenation and appearance of fauna, amongst others (Halverson et al., 2010). This study therefore constitutes a very rare (if not unique) example of Paleoproterozoic chemical sedimentary sequences being the subject of high-resolution chemostratigraphy, and to the knowledge of the author, the very first targeting Fe- and Mn-rich chemical sedimentary rocks.

1.9.1 Sample collection, preparation, and analytical techniques

The logging and sampling of vertical drillcores G774 and MP-56 was carried out at the premises of the *South32 Ltd* core yard in Hotazel, Northern Cape Province, South Africa. The drilling of these cores was undertaken by *South32 Ltd* as part of their mining operations, exploration and grade control. *South32 Ltd* is a mining company enlisted on the Australian Securities Exchange (ASX), London Stock Exchange (LSE) and the Johannesburg Stock Exchange (JSE). It is involved in mining and production of coal and other base metals.

Altogether, 288 manganese-rich and BIF samples were collected from drill cores G774 (Mamatwan) and MP-56 (Middleplaats) (Figure 10 and 11). These represent, on average, a sample per 0.5 m of drillcore section. The intersected strata in this area have a very gentle dip at no more than 5-10^{o}, and therefore to all intents and purposes are considered to be essentially horizontal. The samples represented half cores for the BIF sections, and quarter cores for the Mn-rich intersections, as the other halves of the latter were previously analysed by the company for their routine grade distribution and control.

Starting with drillcore G774, sampling commenced from the basal 15 m dark reddish-brown BIF directly overlying the Ongeluk lavas, gradually and rather imperceptively grading into the transitional hematite lutite. The dark brown to black manganese-ore unit with white to very light brown ellipsoidal carbonate ovoids then followed, also in an extremely gradational fashion. The thickness of the Mn ore layer is extremely difficult to define with certainty, as its contact with the adjacent hematite lutite transitions is

extremely gradational. The zone which had previously been sub-sampled by the company has a thickness of about 49 m. Further upwards, the overlying BIF is encountered through a relatively thin and sharp hematite lutite transition and is dominated by a light greenish-grey microbanded appearance, becoming progressively less greenish upwards. The very thin black shale marker layer denoting the end of the sampling, was encountered approximately 11 m from the hematite-lutite-BIF contact below (Figure 9).

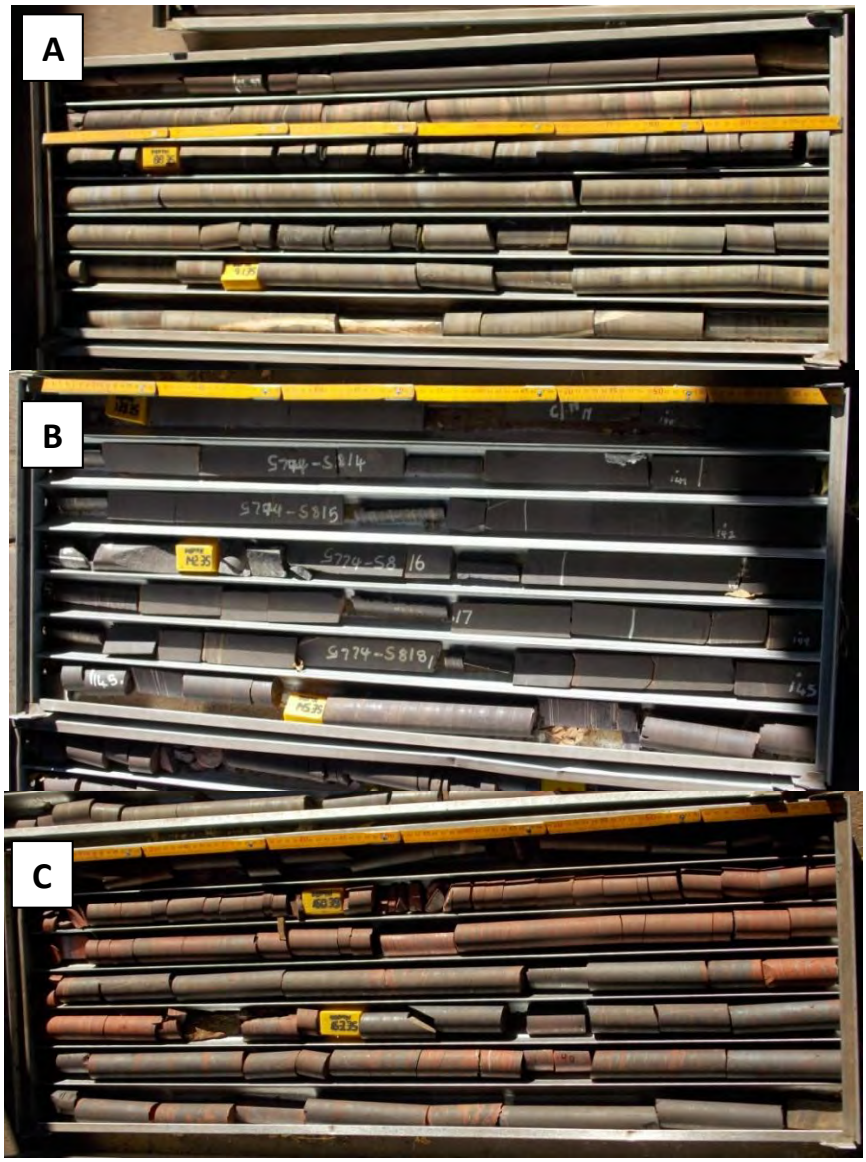

Figure 10: Photographs displaying (A) BIF, (B) Mn-ore and (C) Hematite lutite lithologies from G774 drill-core.

Precisely the same sampling approach was employed for the MP-56 (Middleplaats) drill core, starting with the basal reddish microbanded BIF overlying the Ongeluk lavas, and grading upwards into the manganiferous hematite lutite. The thickness of the basal BIF here appears to be substantially smaller than the Mamatwan drillcore intersection (less than 10 m), a possible effect of basin paleotopography. The dark brown to black manganese ore layer with its characteristic carbonate ooids then follows

upwards, with a thickness approximately half of that seen in the Mamatwan drilcore further afield. Finally, an upward light greenish-grey to grey microband BIF similar to that seen in the Mamatwan drillcore G774 was seen, again through a relatively sharp hematite lutite transition. The dark shale marker was encountered approximately 24 m from the latter contact (Figure 9).

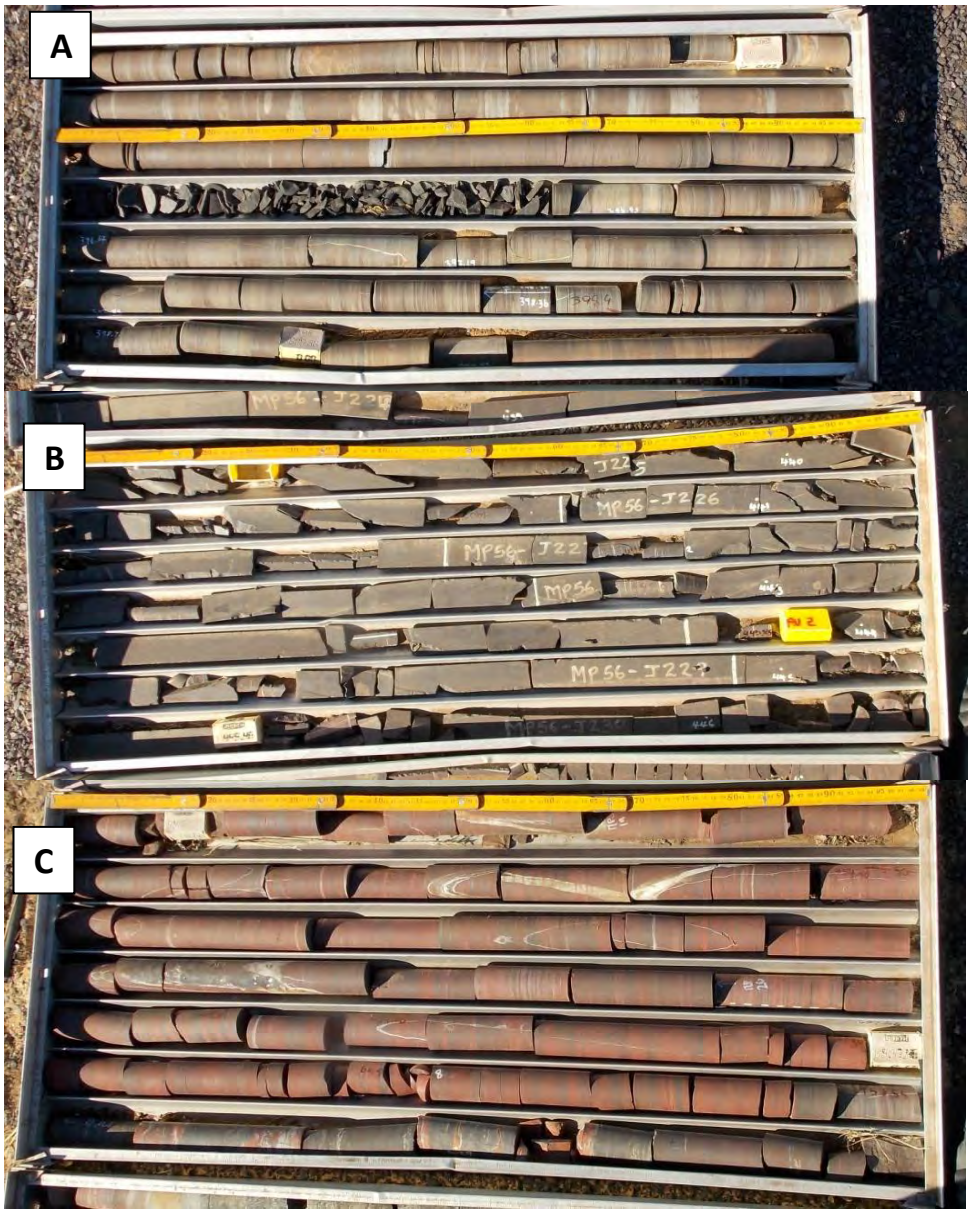

Figure 11: Photographs displaying (A) BIF, (B) Mn-ore and (C) Hematite lutite lithologies from MP-56 drill-core.

The samples were all labeled according to their drillcore name and depth of intersection below surface, as recorded in the original cores. Resident geologists from SOUTH32 indicated minimal to no core-loss during drilling of both cores, ensuring continuous intersections for sampling. The entire set of samples collected during the field work were then split into two sets: the BIF samples from the two cores above the two Mn layers (total of 53+24=77 samples), were shipped unprocessed to Utrecht University in the Netherlands, for the execution of a similar but shorter MSc study by Mr Sten Jacobs on the said BIF

intersections, under the supervision of Prof P.R.D. Mason. That study was concluded in 2020, and the thesis produced is duly acknowledged and referenced in this thesis. The remaining sample set (211 samples) which corresponded to the rest of the bottom Hotazel stratigraphy from both intersections (lowermost red BIF-hematite lutite-Mn ore layer) was processed as part of this study. However, because the analytical approach used for both studies was identical and the timing of completion of the Utrecht MSc study (Jacobs, 2020) facilitated the integration of its results with those from this study well before it was due to be concluded, a more holistic presentation and treatment of all the results was possible by the author.

1.9.2 Bulk geochemical analysis

All samples were firstly subsampled and then crushed into fine powder using a swing mill at the Rhodes University Geology Department. Particular care was taken at that stage in order to process the most pristine and clean materials without any secondary veining (usually calcitic) or surfaces indicating supergene exposure and oxidation. The samples were also crushed sequentially based on their stratigraphic position, in order to minimize as much as possible cross-contamination of material from disparate samples (i.e. hematite BIF crushed before or after a very Mn-rich sample).

A fraction of the produced sets of powders were then sent for major and trace element analyses at the Central Analytical Facilitues (CAF) of Stellenbosch University in the Western Cape Province of South Africa. Major elements were analyzed on fused glass beads using XRF spectrometer fitted with a Rhodium tube and the following analytical crystals: LIF200, LIF220, PE002, GE111 and PX1. Trace elements (including REE) were determined on the same fused beads via LA-ICP-MS, using a Resolution M-50-LR Excimer laser ablation system connected to an Agilent 7700 ICP-MS. The instrument is also fitted with a gas-flow proportional counter and a scintillation detector. The gas flow proportional counter uses a 90% Ar to 10% methane gas mixture. Mounted and polished NIST standards and certified reference materials are used for quantification, using standard bracketing. Data was processed using either Iolite or Glitter software. Detection limits for the elements quoted, depending on the matrix (combination of elements present), are typically 0.5 ppm.

A second fraction of the same sample powders above was processed for their bulk carbonate-carbon isotope composition at Scottish Universities Environmental Research Centre (SUERC), Glasgow, Scotland, on an Analytical Precision AP2003 mass spectrometer equipped with a separate acid injector system. CO_2 was released by reaction with 105% H_3PO_4 overnight under a helium atmosphere at 50°C. Bulk analyses at that temperature and length of reaction were undertaken on the basis that there is

very little to no siderite in the samples, while data for the remaining individual carbonate minerals in these rocks (calcite, dolomite-ankerite, kutnahorite) have been shown to be very similar (Tsikos et al., 2003), and therefore modal mineralogical variations in carbonate minerals are expected to have little effect on the bulk data. The carbon isotope ratios are reported relative to Vienna PeeDee Belemnite (VPDB) using the conventional delta (δ) notation. Mean analytical reproducibility based on replicates of the internal laboratory standard MAB-2 (Carrara Marble) was around ±0.2%. MAB-2 is extracted from the same Carrara Marble quarry as the IAEA-CO-1 international standard. It is calibrated against IAEA-CO-1 and NBS-19 and has the same C and O isotope values as IAEA-CO-1 (–2.5% and 2.4% VPDB, respectively).

2. Bulk-rock chemical stratigraphy

2.1 General

A substantial body of published research work has revealed the geochemical characteristics of the iron formation and the lower-grade manganese ore belonging to the Hotazel Formation in the southern KMF. Work by Tsikos and Moore (1997) and Tsikos et al (2003) report bulk-rock geochemical results for the Hotazel banded iron-formation that show the classic dominance of SiO_2, Fe_2O_3, CaO and MgO, at abundances ranging crudely from 28 – 43 wt%, 32 – 51 wt%, 3 – 16 wt% and around 2 wt%, respectively. The remaining major and minor element chemical species, namely MnO_2, Al_2O_3, Na_2O and K_2O, are reported to occur in negligible concentrations, not exceeding the value of 1 wt% (Tsikos and Moore, 1997; Tsikos et al., 2003). With regard to minor and trace elements that are commonly characterized as terrigenous detrital species and thus as indicators of continental input sources, namely Zr, Ti, Nb, Sc, and Rb, are present in concentrations barely exceeding the value of 10 ppm. Similarly, transition metals such as Cu, Zn, Ni, Co and V, which are often interpreted as deriving from direct volcanogenic hydrothermal input into chemical precipitates, also occur at very low concentrations on the order of a few ppm to a few 10s ppm (Tsikos and Moore, 1997; Tsikos et al., 2003; Thibon et al., 2019).

By contrast with the Hotazel iron formation, the low-grade, Mamatwan-type manganese ore layers in the southern KMF have a bulk chemical composition dominated by manganese, at concentrations generally ranging from as low 10 wt% to as high as 40 wt% (Tsikos et al., 2003). The corresponding total Fe oxide contcentrations are generally below the value of 10 wt%, but these increase markedly (while the ones for total manganese drop substantially) as one moves away from the center of the manganese layer towards the transitional hematitic margins. Unlike the Hotazel iron formation, the bulk SiO_2 concentration in the manganese layers is also very low at a few wt%, but that is also known to increase with increasing iron content towards the margins of the ore-layers. In contrast, carbonate contents in the manganese layers are high, at an average CaO abundance of around 15 wt%, which ties closely with similar levels of Loss on ignition (LOI) which corresponds to the CO_2 content of the rocks. Finally, the trace element abundances of the manganese ore layers are comparable with those recorded in the adjacent iron formations (Tsikos and Moore, 1997; Tsikos et al., 2003).

Finally, published bulk carbonate $\delta^{13}C$ data for the Hotazel iron formation and manganese ore layers, have values generally ranging between -5 and -13 ‰ (PDB). Although the carbonate mineralogy of the Hotazel iron formation and manganese strata involves mixtures of calcite and ankerite or kutnahorite respectively, the isotopic results as reported by Tsikos et al. (2003) show similar ranges, with the calcite

being usually of a slightly higher $\delta^{13}C$ value from coexisting ankerite (in BIF) or kutnahorite (in the Mn layers) (Tsikos et al., 2003).

2.2 Presentation approach

As also indicated in the introduction, this dissertation will report for the first time ever, high-resolution bulk-rock geochemical data for the lowermost portion of the Hotazel Formation. A comparable account of high-resolution bulk-rock chemostratigraphic results for two sections from Middleplaats and Mamatwan mines is presented, incorporating major and minor oxide chemical components (i.e., Mn, Fe, Si, Ca, Mg), trace elements (i.e., Cr, Ni, V,Cu, Zn, Mo, Co, Sr, Ba, Sc, U, Zr, Nb, Ba, Sr and REE) as well as bulk carbonate carbon isotopes. Minor element oxides (TiO_2, K_2O, P_2O_5, Al_2O_3 and Na_2O) record negligible and invariant concentrations across stratigraphy and have therefore been omitted from further consideration. The abundance profiles of major elements are reported in mineralogically-constrained sub-divisions comprising those known to dominate the oxide (Si, Mn and Fe) and carbonate (Ca, Mg and LOI) fractions of the rocks. The profiles for trace elements have been subdivided following mainly basic geochemical conventions, such as High Field Trace Elements (HFSE) representing mainly detrital species, transition metals as tracers of hydrothermal input (e.g. Cu, Ni, Zn) and possible redox processes during deposition (e.g. Mo, Co) and alkali-earth metals as possible proxies of the carbonate rock fraction and its origins (Sr, Ba). In some cases, however, transition metals that appear to behave as HFSE (detrital) species, have been grouped together for convenience. The raw data of all geochemical components shown in the plots that follow, can be found in the Appendix section of the dissertation.

For the purpose of simplicity and convenience, the lithostratigraphy of the lowermost portion of the Hotazel Formation in this dissertation is subdivided into three units, namely a basal hematite lutite section, the lowermost manganese ore layer, and the classic BIF that overlies the manganese layer. In other words, there was no attempt in this study to examine and log very subtle lithostratigraphic variabilities of the Hotazel rocks, in order to match them to possible geochemical signatures following the production of the analytical data. Instead, the approach employed focuses on identifying possible chemostratigraphic signals that otherwise cannot be seen and therefore predicted with any certainty through standard visual examination of the rocks with the naked eye. For the same reasons as indicated above, the subdivision between the three stratigraphic subunits was fairly easy in the case of the Mn layer-BIF contact, which is lithologically sharp. By contrast, the contact between the basal hematite lutite and the Mn layer is extremely gradual and thus more subjective; in this case, the convention

followed is that the contact be placed at the last hemnatite lutite sample before a sharp increase in Mn content and drop Fe content is recorded, and this was then used for all other datasets plotted.

2.3 Major element oxide chemostratigraphy

The basal hematite lutite zone at the Mamatwan stratigraphic section attains an overall thickness of approximately 15.0 m (Figures 12A and 13A). It exhibits bulk average Fe_2O_3 and SiO_2 concentrations of 45.8±10.0 wt% and 24.2±9.26 wt%, respectively. The CaO and MgO concentrations are at 2.38±1.97 wt% and 4.20±4.00 wt% respectively, while MnO_2 and LOI concentrations range between 12.6±8.49 wt% and 10.9±4.00 wt%. Characteristic here is a sharp positive spike in MgO values which is mimicked by high MnO_2 and LOI ones at the same level. At the Middleplaats stratigraphic section, the hematite lutite section is shorter than the one at Mamatwan, at ~5.35 m (Figure 12B and 13B). The bulk geochemical composition of this section exhibits comparatively higher bulk average Fe_2O_3 and similar SiO_2 concentrations of 57.7±6.69 and 26.2±7.82 wt% respectively, slightly higher CaO and lower MgO concentrations (with no apparent spike for MgO) of respectively 3.90±2.20 and 1.83±0.62 wt%, and lower average MnO_2 and LOI concentrations at 4.17±1.12 wt% and 6.23±2.45 wt%.

The transition to the overlying Mn-ore zone at the Mamatwan section, which records a total thickness of ~49.8 m, is marked by a gradual decline in the bulk Fe_2O_3 and SiO_2 concentrations, a gradual rise in MnO_2 concentrations and a sharp spike in MgO concentrations (Figure 12A and 13A). This thickest Mn-ore zone exhibits bulk average MnO_2 concentration of 38.0±13.7 wt%, and average Fe_2O_3 and SiO_2 concentrations at 13.6±12.2 wt% and 6.82±5.10 wt%, respectively. The MnO_2 profile shows three maximum intervals, in the form of one upper and one lower bell-shaped positive excursions, separated by a sharper spike of high Mn in between them. Corresponding average CaO and MgO concentrations are at 17.0±7.14 wt% and 4.08±1.86 wt%, respectively, while average LOI is at 20.5±4.64 wt%. The CaO and LOI profiles also exhibit characteristic maxima and minima in the form of three successive bell-shaped excursions and one at the very top of the Mn section terminating against the overlying BIF.

At the Middleplaats section, the transition to the overlying Mn-ore layer, which here attains a much lower thickness of ~31.2 m, is marked by a gradual decline in bulk Fe_2O_3 and SiO_2, and a similar sharp spike in MgO concentration as in the Mamatwan section (Figure 12B and 13B). The bulk geochemical composition of this Mn-ore zone has lower bulk average MnO_2 than at Mamatwan, at 34.3±15.3 wt%. Average Fe_2O_3 and SiO_2 concentration averages are comparatively higher at 16.9±12.4 wt% and 9.28±10.6 wt%, while average CaO, MgO and LOI concentrations are comparable to those at Mamatwan, at 15.5±8.16 wt%, 4.24±2.82 wt% and 19.7±5.48 wt%. The MnO_2 profile in the Middelplaats sections shows a relatively simple bell-shaped increase containing small-scale spikes and troughs, while

the MgO profile shows another spike at the top contact with the overlying BIF, that is not recorded at Mamatwan. The CaO and LOI profiles however are a bit more “noisy” and show a more asymmetric increase in concentration stratigraphically upwards towards the contact with the BIF above.

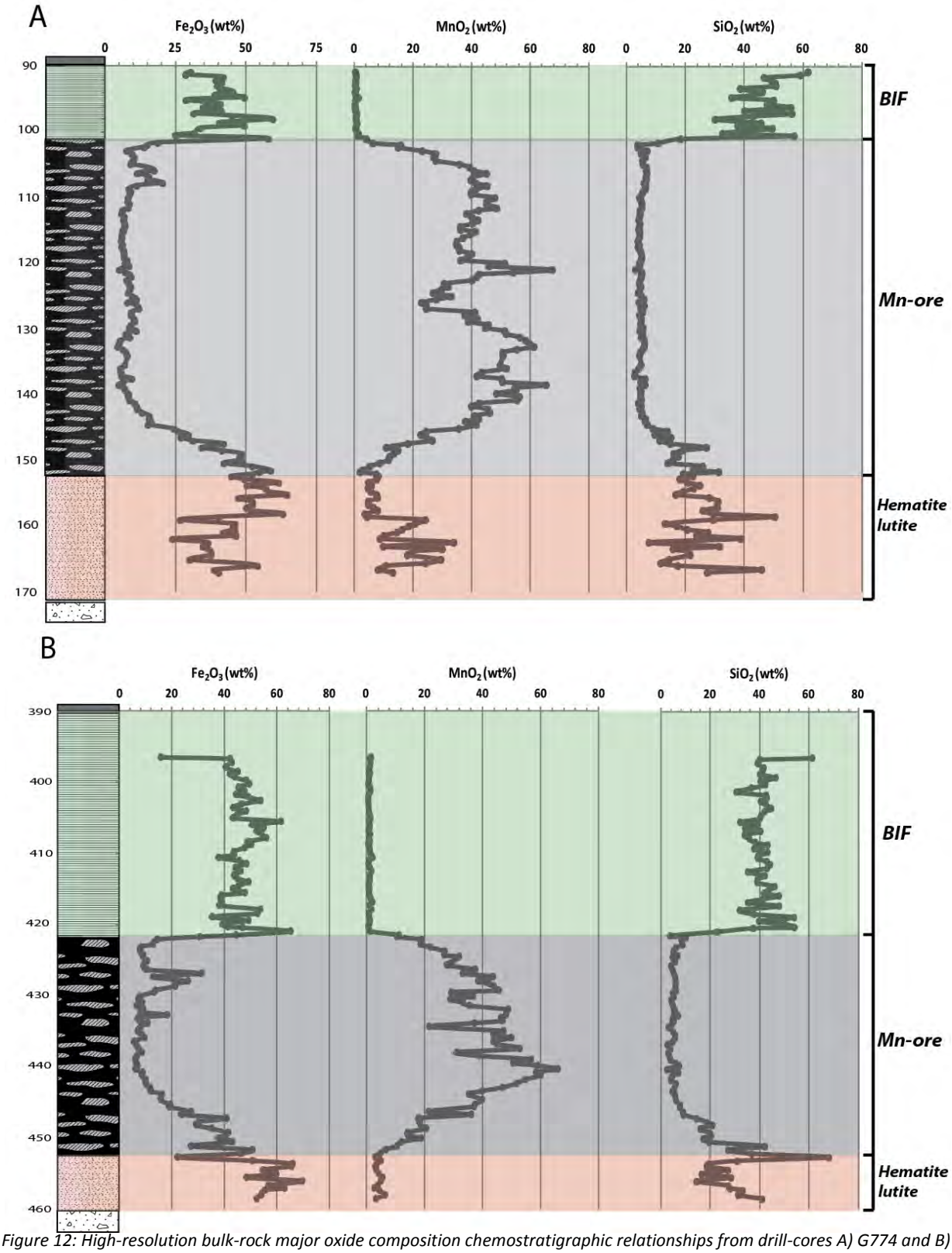

Figure 12: High-resolution bulk-rock major oxide composition chemostratigraphic relationships from drill-cores A) G774 and B) MP-56.

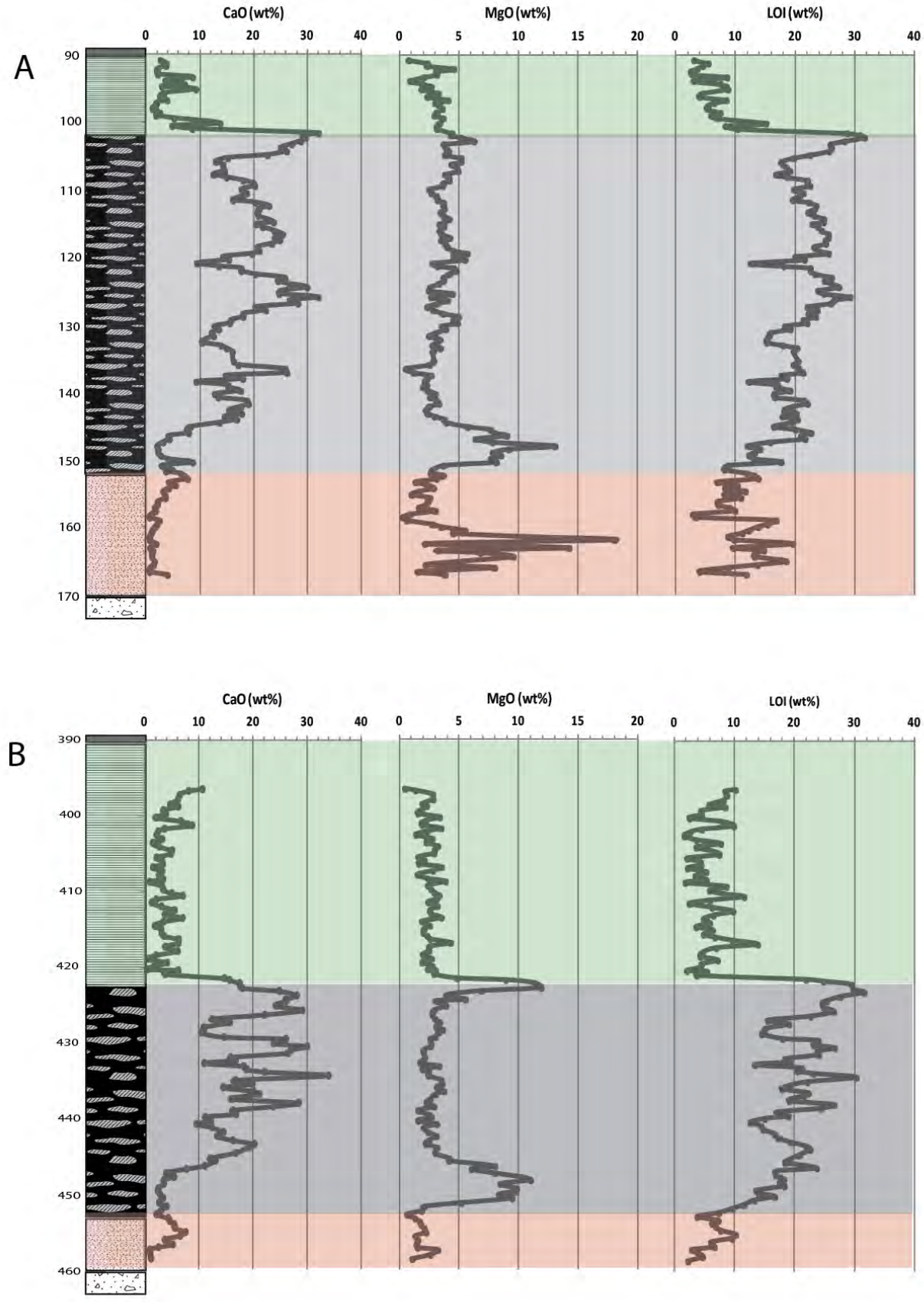

Figure 13: High-resolution bulk-rock major oxide composition chemostratigraphic relationships from drill-cores A) G774 and B) MP-56.

The transition to the overlying BIF zone at Mamatwan section, which attains a stratigraphic thickness of ~10.8 m, is marked by an expected sharp increase in Fe_2O_3 and SiO_2 concentrations, and a sharp decrease in CaO and MnO_2 concentrations (Figure 12A and 13A). All profiles show essentially invariant concentration profiles. The bulk-rock average Fe_2O_3 and SiO_2 concentrations within this interval are typical of global BIF at 38.9±9.66 wt% and 43.9±12.2 wt% respectively. By contrast, the concentrations of MnO_2 are very low and those for CaO are much lower than in the underlying Mn layer, with values at 1.00±1.36 wt% and 5.41±6.42 wt% respectively. Corresponding LOI runs at 7.22±5.40 wt%, while the bulk MgO concentrations follow closely those for the underlying Mn, at an average of 2.89±0.94 wt%.

In the Middleplaats section, similar trends are observed with the Mamatwan BIF section but the BIF layer here is thicker, at ~25.5 m. The Fe_2O_3 and SiO_2 profiles show sharp increases compared to the underlying Mn layer, while corresponding sharp decline is seen in concentration values for CaO and MnO_2 (Figure 12B and 13B). MgO contents are again closely comnparable as those in the underlying Mn layer. The average bulk Fe_2O_3 and SiO_2 concentrations stand at 45.6±7.16 wt% and 40.8±6.11 wt% respectively, CaO and MgO concentrations are at 3.82±2.16 wt% and 2.51±0.70 wt%, MnO_2 concentration is at 1.00±0.36 wt% and LOI concentration is at 5.90±2.67 wt%.

2.4 Trace element relationships

2.4.1 Transition metals

It must be noted upfront, that the Co abundances (i.e., at depth intervals 90.81 – 101.64 m and 396.45 – 420.92 m; from G774 and MP-56 cores, respectively) as determined at Utrecht University for the purpose of the parallel MSc thesis of Mr S. Jacobs on the Hotazel BIF (Jacobs, 2020) were compromised during the sample preparation process through comtamination by the crusher used. For that reason, the resultant data appeared approximately 15-20 ppm higher than the expected concentrations. This was verified by comparison of the Jacobs data with those of Thibon et al (2019), who also sampled the same BIF section at Middelplaats for their study, but also the data of Tsikos and Moore (2003) from other Hotazel BIF intersections. As the Thibon et al (2019) study only made use of a few samples across the BIF section, it was decided that our samples taken at the same stratigraphic height with the samples of Thibon et al (2019) be used to produce a crude correction factor to be applied across the entire BIF section for both selected drillcores (i.e. Middelplaats and Mamatwan). The correction factor for Cobalt finally applied across our entire BIF dataset (see section A7 of Appendix, for the calculations) was essentially the average of the difference in the measured concentrations between the two corresponding sample subsets.

Apart from the above issue with the BIF Co data, the majority of the transition metals analyzed in this study (Cr, Ni, V, Zn, Cu, Mo and Co) display moderate to low variability across the chemostratigraphy of the lower part of the Hotazel Formation, in most cases with occasional spikes in concentration likely indicate localised “nugget effects” (Figures 14 and 15). Most of these elements, as expected (Tsikos et al., 2003) occur at concentrations in the order of a few tens of ppm, while Mo occurs at very low concentrations of a few ppm and Pb is mostly below detection (thus it was not included in the current chemostratigraphic considerations). In a comparative sense across the three lithofacies (Hematite lutite, Mn layer and BIF), the elements Ni and Cr show a clear sharp increase from the lower stratigraphic sections into the overlying BIF, the Cu, V and Zn values show no clear increase or decrease, while the Co and Mo concentration values show a relative decrease across the same transition. Arguably the most insightful profiles in terms of stratigraphic variability in concentration is displayed in the Co and Mo profiles, therefore these will be interrogated further in a later chapter.

In the Mamatwan stratigraphic profile, Co (Figure 16A) and Zn (Figure 15A) appear to display the highest bulk average concentration values among all three lithofacies. The hematite lutite layer specifically exhibits average Co and Zn concentrations of very high variance, of 30.9±26.9 ppm and 27.5±14.6 ppm, respectively. The high Co values appear to occur with the spike in MgO and MnO_2 mentioned in the previous section. In the Mn-ore layer, bulk average Co and Zn concentrations recorded are similarly high, at 31.6±9.98 ppm and 24.3±21.4 ppm, respectively (Figure 16A and 15A). In the BIF layer, Cr (Figure 14A) appears to display the highest average concentration at 35.2±8.4 ppm, followed by Zn (e.g., Figure 15A) at an average concentration value of 26.2±5.02 ppm. As mentioned earlier, Mo exhibits the lowest concentration among all the transition metals in all three lithofacies, with the BIF layer showing the lowest bulk average Mo concentration at 0.62±0.51 ppm. The Mn-ore layer and hematite lutite layer exhibit relatively higher values at average Mo concentrations of 3.38±1.01 ppm and 2.39±0.55 ppm, respectively (Figure 16A).

In the Middleplaats section, the transition metals with the highest concentrations in the hematite lutite layer are those of Cr and V, with average concentrations respectively of 30.2±6.97 ppm and 18.3±2.30 ppm (Figure 14B). In the Mn-ore layer above Zn and Co are the most abundant, just like with the Mamatwan section, with bulk average Zn and Co concentrations at 44.9±34.6 ppm and 30.2±11.3 ppm, respectively (Figure 15B and 16B). Cr and Zn appear to be the most abundant metal elements in the BIF layer at bulk average concentrations at 29.1±4.58 ppm and 25.2±7.99 ppm respectively (Figure 14B and 15B). Again, Mo shows the lowest concentration values among the entire set of transition metals analyzed, with the BIF layer exhibiting the lowest bulk average Mo concentration of 0.34±0.22 ppm. Average Mo concentration values appear to be the highest in the Mn-ore layer at average Mo

concentration of 2.25±0.67 ppm, with slightly lower values in the hematite lutite layer to a bulk average Mo concentration of 2.12±0.38 ppm (Figure 16B).

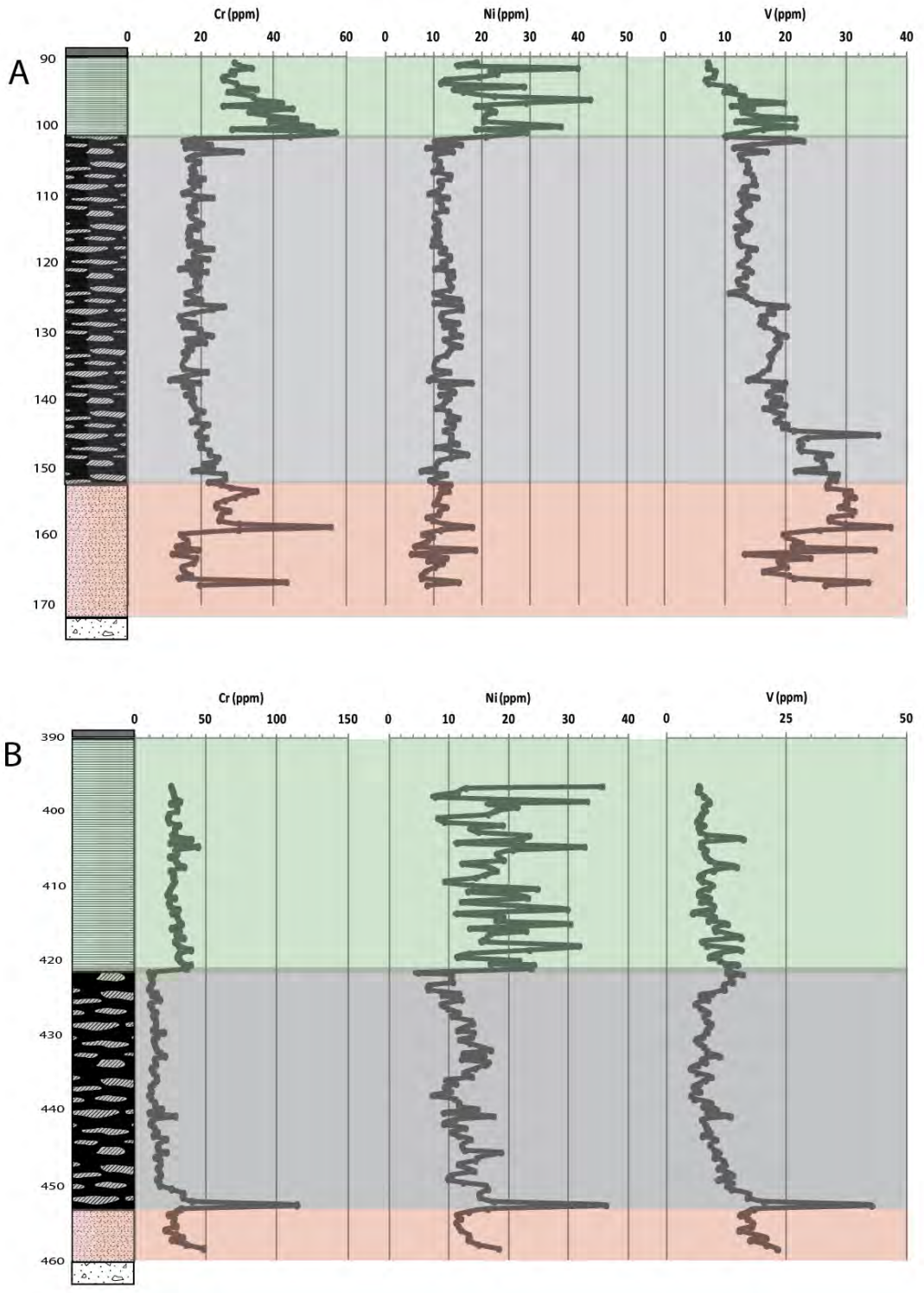

Figure 14: High-resolution bulk-rock transition metal (Cr, Ni, V) chemostratigraphic relationships from drill cores A) G774 and B) MP-56.

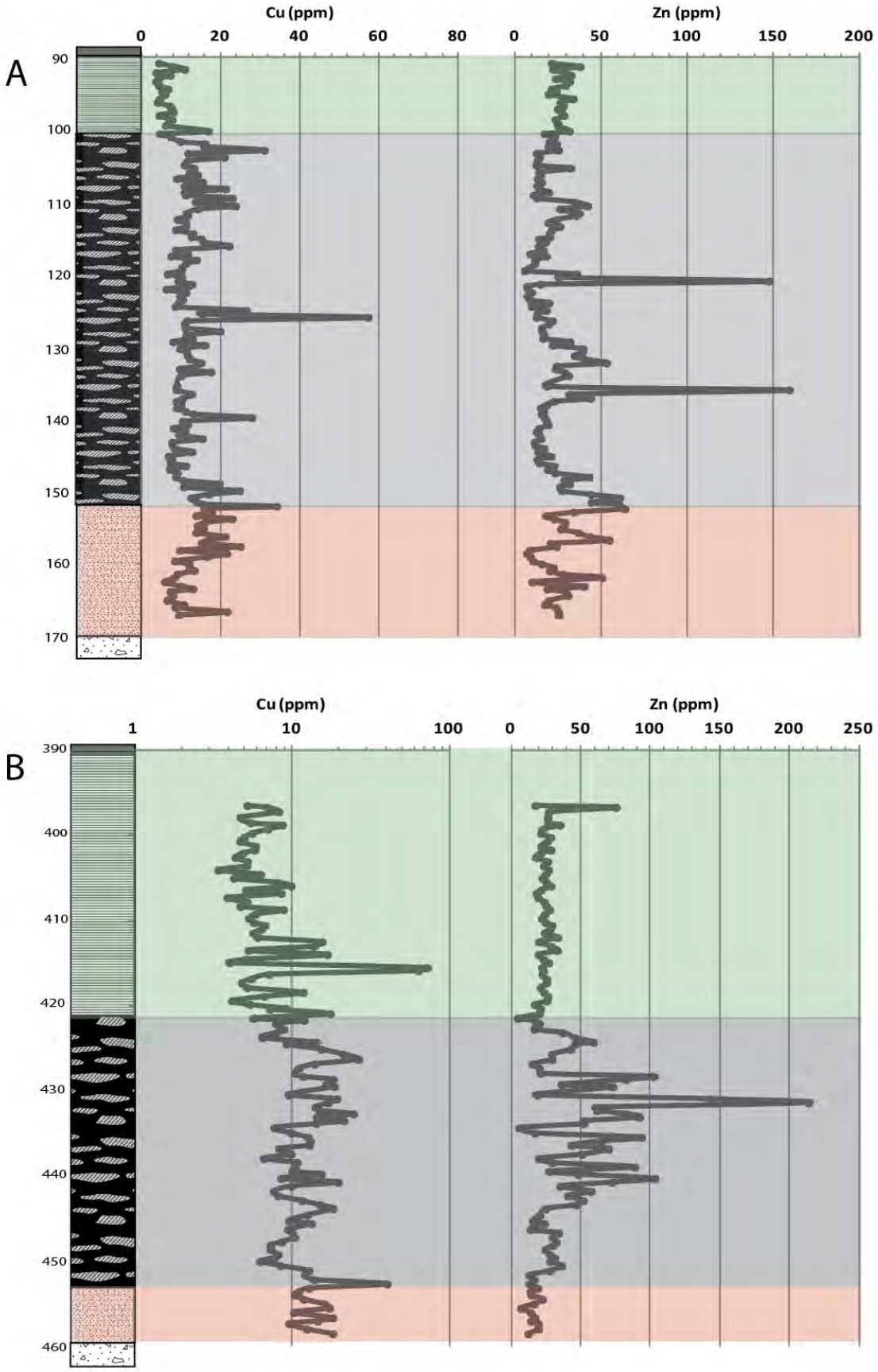

Figure 15: High-resolution bulk-rock transition metal (Cu and Zn) chemostratigraphic relationships from drill cores A) G774 and B) MP-56.

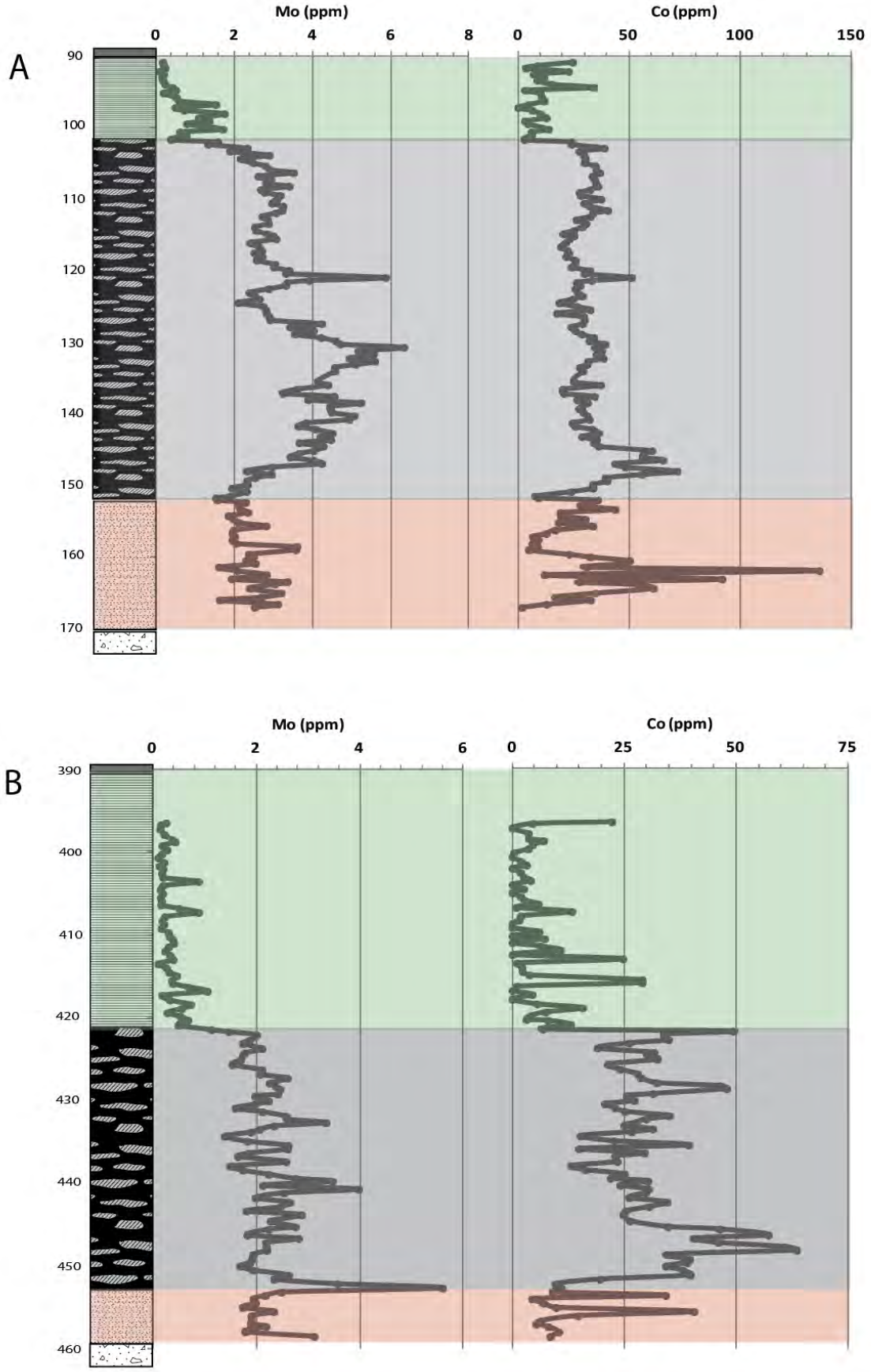

Figure 16: High-resolution bulk-rock transition metal (Mo and Co) chemostratigraphic relationships from drill cores A) G774 and B) MP-56.

2.4.2 "Detrital" elements (mainly HFSE)

With regards to the detrital elements, which are classically represented by the High Field Strength Element (HFSE) group (as represented by the elements Zr, Nb, Y, Sc and U), low and largely invariant concentration values are recorded across most of the Mamatwan section lithostratigraphy. The only marked concentration change appears to occur at the contact with the overlying BIF, where all elements appear to spike in concentration. The only element among them that appears to show some degree of stratigraphic variability is Y, and this will be discussed in a later chapter in the context also of the REE, with which Y shows strong geochemical similarity.

The average concentration values for Y across the Mamatwan stratigraphy are of 7.13±1.94 ppm for the hematite lutite, 5.48±2.24 ppm for the Mn layer and 10.4±3.03 ppm for the BIF above (Figure 17A). Bulk average Zr concentration values are relatively high in BIF, of 8.21±4.96 ppm, and low throughout the Mn-ore layer and hematite lutite layer, of 5.53±5.38 ppm and 5.94±3.57 ppm, respectively. Bulk average Sc concentration is low (1.34±0.32 ppm) for hematite lutite layer, 0.98±0.30 ppm for the Mn layer and 3.44±1.47 ppm for the BIF layer. Average Nb concentration is very low throughout: 0.35±0.12 ppm for the hematite lutite layer, 0.33±0.10 ppm for Mn-ore and 0.67±0.38 ppm for BIF layer. Finally, average U concentration is the lowest and most invariant of all the HFSE, with the hematite lutite layer recording average concentration of 0.08±0.03 ppm, 0.11±0.04 ppm for the Mn layer, and 0.59±1.06 ppm for the BIF (Figure 17A).

In the Middleplaats stratigraphic profile, the HFSE display similar behaviour with that seen in the Mamatwan section, namely low absolute concentration values and very low variability in their stratigraphic behaviour. The BIF section is certainly the one with the highest abundances in almost all elements, although it must be noted that at least three of the profiles shown appear to record a progressive small decline in concentration from the base of the section upwards into the Mn layer, a signature not clearly seen at Mamatwan.

Bulk average concentrations are comparable to the Mamatwan section. The Zr is low at 6.09±0.97 ppm for the hematite lutite, 4.17±1.46 ppm for the Mn layer and 5.5±2.21 ppm for the BIF layer. The Y concentrations are the highest among all related elements, particularly in the BIF layer, at bulk average concentration of 12.9±5.08 ppm, but much lower in the Mn layer to an average concentration of 5.09±1.59 ppm, and slightly higher in the hematite lutite at an average concentration value of 8.22±1.75 ppm (Figure 17B). Bulk average concentration for Sc is low at 1.91±0.46 ppm in the hematite lutite, comparably low in the Mn layer at 1.09±0.35 ppm, and slightly higher in the BIF at 2.6±0.75 ppm. With regard to bulk average Nb concentrations, they are very low throughout the Middelplaats stratigraphy, very similar between the hematite lutite and BIF layer at average Nb concentrations of 0.50±0.10 ppm

and 0.48±0.18 ppm, respectively, and lowest in the Mn layer at 0.33±0.13 ppm. Finally, Uranium content appears to be extremely low throughout the Middelplaats section, at average values of 0.10±0.03 ppm for the hematite lutite, 0.09±0.03 ppm for the Mn layer, and 0.23±0.39 ppm for the BIF layer (Figure 17B).

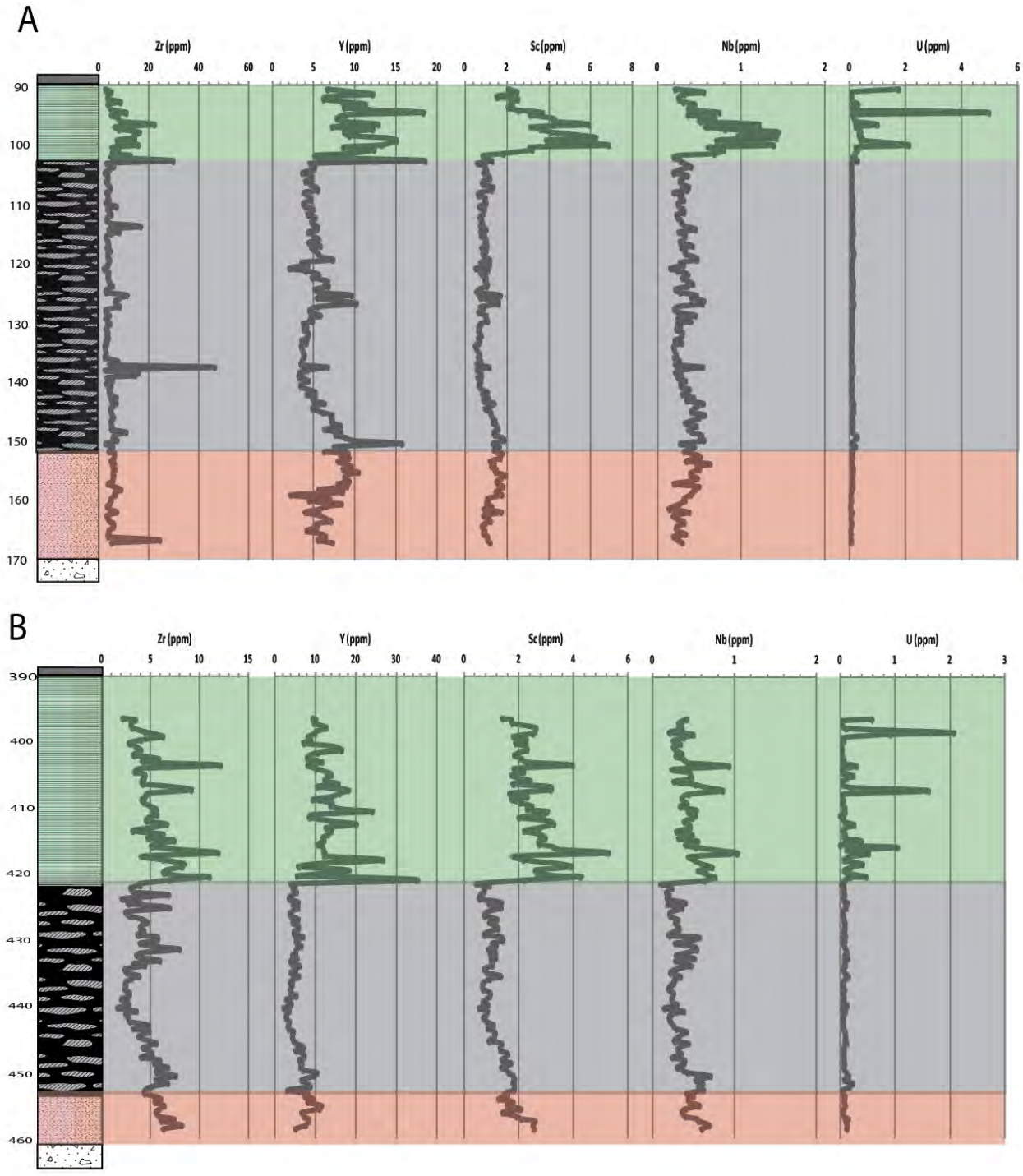

Figure 17: High-resolution bulk-rock HFSE (Zr, Y, Sc, Nb, U) chemostratigraphic relationships from drill cores A) G774 and B) MP-56.

2.4.3 Alkali-earth metals

The alkali and alkali-earth metals (namely Rb, Sr, Ba, and Cs) in both stratigraphic sections display considerably diverse behaviour across the sampled stratigraphy, both quantitatively and in terms of variability. The alkali metals Rb and Cs, however, are present in very low concentrations which are mostly below the limit of detection, and therefore they have been omitted from further consideration. By contrast, the alkali earths Ba and Sr show considerable concentration levels, particularly the former which shows its highest content in the hematite lutite layer at very high variance, namely 395.74±1298.18 ppm. It is expected that both these elements are associated with the carbonate mineral fraction of the rocks. Very high spikes in Ba abundance in fact seem to coincide with the high Mg-Mn spike in the lower hematite lutite reported in an earlier section. Thereafter, Ba concentration declines to an average value of 245±562.73 ppm in the Mn-ore layer and, finally, to its lowest concentration in the BIF at 19.2±19.1 ppm. The Sr concentrations appear to be highest and considerably variable within the Mn-ore layer, at a high-variance bulk average value of 188.19±143.54 ppm. While the BIF layer also registers relatively high Sr concentrations at high variance, at a bulk average of 91.04±140.47 ppm, the hematite lutite zone records the lowest average Sr concentration at 11.91±6.69 ppm (Figure 18).

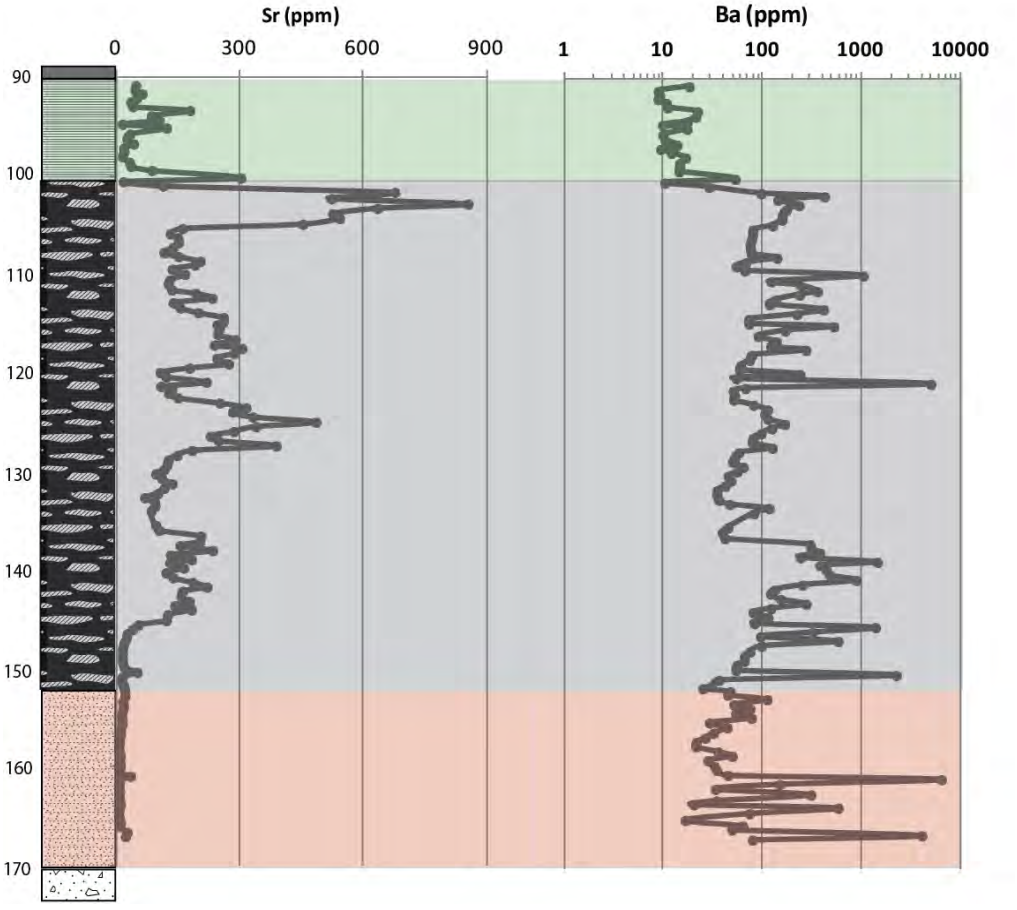

Figure 18: High-resolution bulk-rock chemostratigraphic variations in alkali and alkali earth elemental (Sr and Ba) abundance from drill core G774.

In the Middleplaats section, the situation with both alkali earths is rather comparable to what is seen in the Mamatwan section. The concentrations for Ba are again high and highly variable, with maximum abundances recorded in the Mn layer, at a bulk average Ba concentration of 244.58±878.91 ppm. Again, the variance for ba appears to be very high, but it appears to show only one major spiky peak of values in the lower half of the stratigraphy of the Mn layer, whereas in the Mamatwan section previously it appears to show a stratigraphically lower and a higher peak with a similarly spiky manifestation. By contrast, lower average Ba concentration values are recorded in both the hematite lutite and the BIF layer at 20.7±11.7 ppm and 10.76±15.6 ppm, respectively. In a somewhat similar manner with the Ba, the Sr values are also highest but similarly variable within the Mn layer, at bulk average Sr concentration of 76.39±61.6 ppm. The notable feature of the Sr profile is that it is quite similar in both sections (Mamatwan and Middelplaats), with a generally noisy but progressively rising abundance in Sr towards the top of the Mn layer with a spike right before the contact with the overlying BIF. Finally, the hematite lutite layer has the lowest average Sr concentration at 9.6±2.83 ppm, while the BIF layer records a relatively higher average content than the hematite lutite, at 29.2±20.5 ppm (Figure 19).

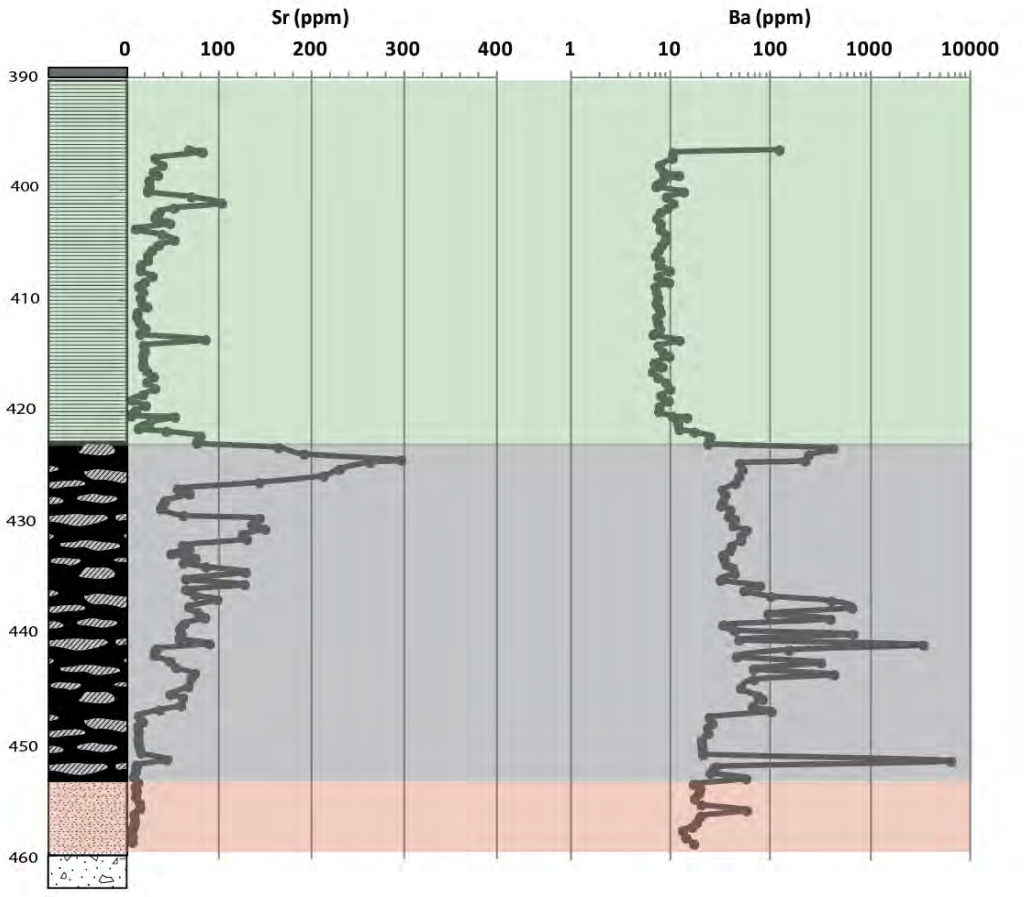

Figure 19: High-resolution bulk-rock chemostratigraphic variations in alkali and alkali earth elemental (Sr and Ba) abundance from drill core MP-56.

2.5 Rare earth elements

2.5.1 General

Lanthanides, as represented by the rare earth elements (REEs), have been identified as the most frequently utilized geochemical proxies to gain insights into the chemical nature of ancient seawater (Bekker et al., 2010; Schier et al., 2020). The distribution of rare earth elements in marine chemical sediments have reliably constrained the prime element sources to the marine domain, and provided oceanic and atmospheric redox levels during marine chemical sediment deposition (Bau, 1993; Alexander et al., 2009; Alibert and McCulloch; 1993; Bau and Dulski, 1996).

Pure BIFs (i.e., devoid of major detrital contamination and post-depositional alteration events) and sedimentary-type carbonates have been known to be exceptional archives of primary REE pattern during burial and exhumation, as little fractionation takes place during incorporation of REE from seawater into marine chemical sediments (Bekker et al., 2010, Alexander et al., 2008, Bau and Alexander, 2009; Kamber et al., 2004). Nonetheless, REE patterns in marine chemical sediments (e.g., iron formations) that have experienced certain levels of metamorphism (e.g., at amphibolite facies and above) or have been affected by high fluid/rock alteration during metamorphism, should be investigated with caution, particularly in deciphering primary depositional redox states (Bau, 1993; Slack et al., 2009; Bekker et al., 2010).

Central to the discourse around the distinctively trivalent REE distribution in marine chemical sediments is the subject around provenance and redox conditions accountable for the deposition of marine chemical sediments (e.g., BIFs and stromatolitic carbonates; Bekker et al., 2010). Amongst a dozen or so of the REEs, there are two elements regarded to be redox-sensitive in the Earth's natural environment, and known to be uniquely decoupled from other REEs under particular physic-chemical settings (Bau and Müller, 1993; Zhang and Nozaki, 1996, 1998).

Europium (Eu) enrichments, or rather, a positive Eu anomaly in chemical sediments is an indication that hydrothermal fluids influenced a parcel of ancient seawater from which the sediments precipitated (Derry and Jacobsen, 1990; Bekker et al., 2010). In such instances, Eu^{3+} got reduced to Eu^{2+} (i.e., under hot (>250°C) and acidic conditions) during sea-floor high-temperature hydrothermal alternation, hence a positive Eu anomaly in the resultant body of high-temperature hydrothermal fluids (Allen and Seyfried, 2005; Bau and Dulski, 1999).

In oxic marine environments, cerium (Ce) is present as Ce^{4+}, from the oxidation of Ce^{3+}; a phenomenon known to reduce Ce solubility substantially in oceanic settings, leading to its preferential removal onto Mn-Fe oxyhydroxides, organic matter and clays (Byrne and Sholkovits, 1996; Bekker et al., 2010).

Negative Ce anomalies in shale-normalized REE signatures of water bodies and, in turn, chemical sediments precipitating from such bodies of water are produced (Bau et al., 1998; Viehmann et al., 2016). Comparably, anoxic-suboxic water masses are negative Ce anomaly- deficient because of mechanisms such as reductive dissolution of sinking manganiferous particles (German et al., 1991; Byrne and Sholkovits, 1996). Additionally, light REE depletion is common in oxic water masses owing to the preferential removal of light *versus* heavy REEs onto Mn-Fe oxyhydroxides and other particle surfaces (German et al., 1991; Byrne and Sholkovits, 1996).

The grouping and treatment of REE as a collective set of geochemical data is based on their proven geochemical similarities. For that reason, classic evaluation and interpretations of REE data is applied through standard normalisation spidergrams. The use of individual REE in chemostratigraphy is thus not a common application, and when REE are considered in chemostratigraphic studies, they are treated either through the analytical sum of all of them together (ΣREE), or by focusing on specific numerical parameters of REE behaviour, such as the level of Ce or Eu anomalies or the degree of slope of the REE spidergrams. In this section, REE results will be shown as collections of spidergrams for all samples from each stratigraphic unit, and they will be evaluated in the next chapter more holistically.

2.5.2 Results

Post-Archean Average Shale (PAAS)-normalized REE patterns for the entire sample set of the Mamatwan and Middleplaats stratigraphic sections are shown in the spidergrams of Figures 20 and 21 respectively, accompanied by seawater compositions from Zhang and Nozaki (1996), for comparison purposes. Both sections show striking similarities in REE behaviour, and therefore they are discussed here together. With regard to absolute abundance of REE, it is evident that the normalized REE concentrations in all three lithofacies is conspicuously lower than PAAS, suggesting that all analyzed samples are depleted with respect to PAAS in both localities. In the context of the Hotazel strata themselves, the BIF subsections are the ones with the relatively higher contents in REE, by comparison to the hematite lutite and Mn layers.

A striking feature is the characteristic positive slope recorded in practically all samples, suggesting the classic seawater-like relative depletion of LREE (La-Sm) as compared to HREE (Eu-Lu, plus Y) (Oonk et al., 2018; Schier et al., 2020). The three lithofacies also share common attributes regarding their apparent negative Ce anomalies in practically all samples, which is nevertheless obscured in terms of its true magnitude by the common positive La anomaly recorded in BIF (Schier et al., 2020). Finally, although the population of data plotted in our spidergrams is arguably very high and does not allow clear observation of specific anomalies, the Hotazel dataset also records inconsistent Eu behaviour with

positive and negative anomalies alike. This is a feature that has also been reported before from a much smaller sample population of the Hotazel Formation (Tsikos and Moore, 1997).

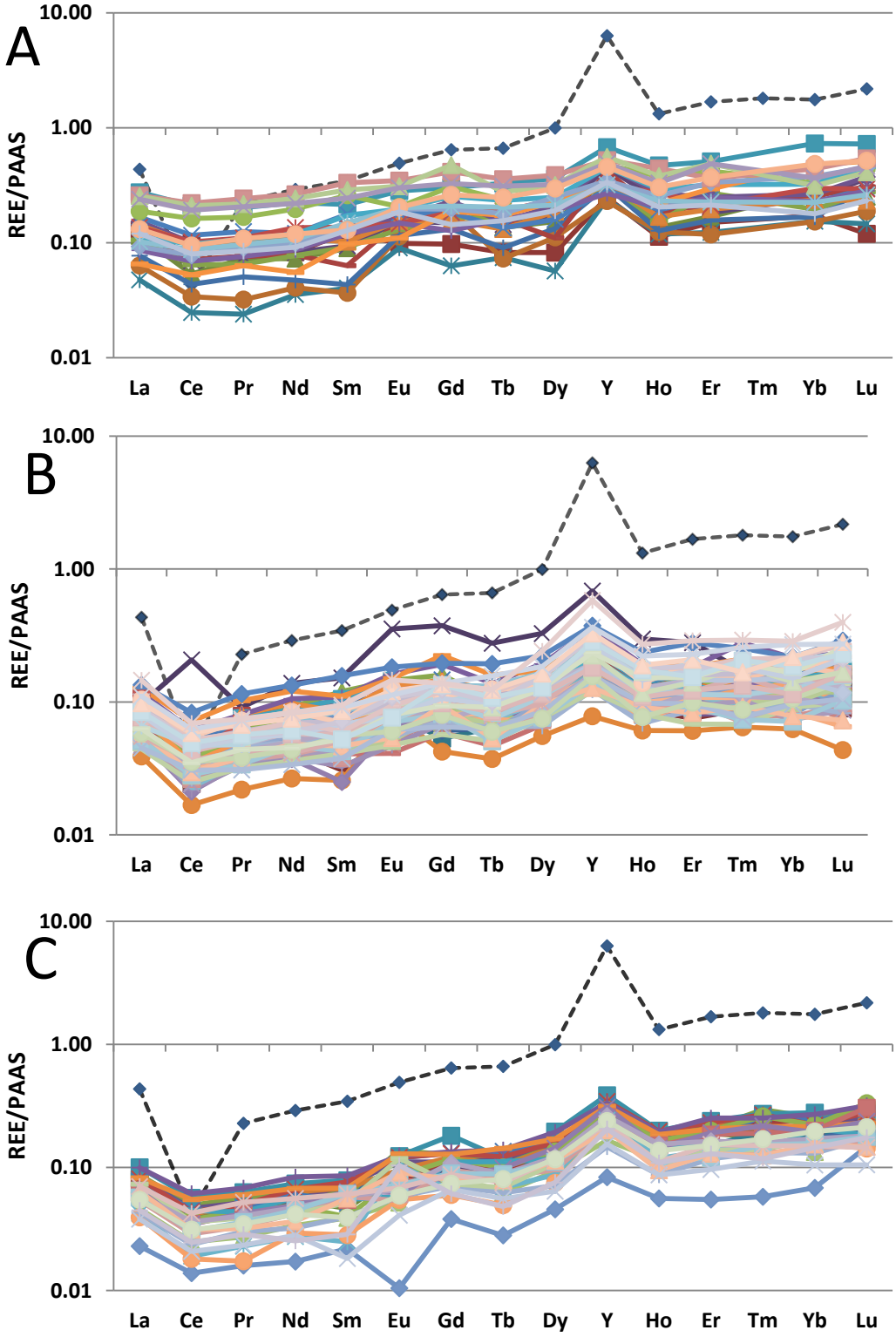

Figure 20: Bulk-rock REE/PAAS patterns from A) BIF, B) Manganese ore and C) Hematite lutite from drill core G774. (Dashed lines represent seawater compositions, from Zhang and Nozaki (1996)).

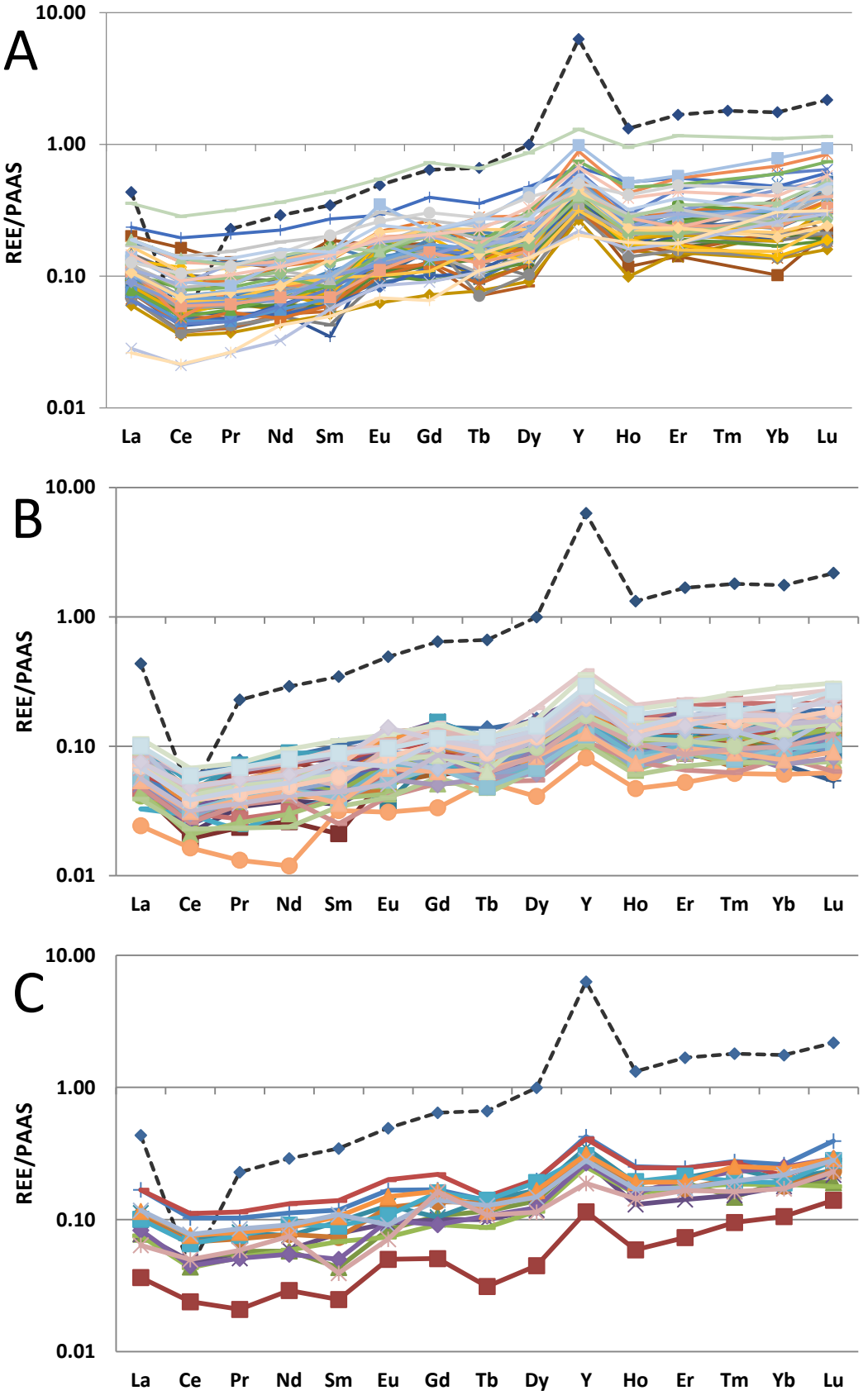

Figure 21: Bulk-rock REE/PAAS patterns from A) BIF, B) Manganese ore and C) Hematite lutite from drill core MP-56. (Dashed lines represent seawater compositions, from Zhang and Nozaki (1996)).

2.6 Carbonate carbon isotopes

As indicated in the introduction, the carbonate carbon isotope data produced for the purposes of this study were from bulk rock analyses of the entire carbonate fraction of the samples. Such bulk-rock analyses can be meaningless when they represent mixtures of carbonate minberals of diverse origins and therefore much different isotopic signatures. The choice of this bulk carbonate-carbon isotope approach is hinged on the similarities in the $\delta^{13}C$ data that have already been reported for individual carbonate minerals in the Hotazel Formation (Tsikos et al., 2003). This of course does not guarantee that the individual carbonate minerals in the Hotazel strata share the exact same origin, but this does not have to affect their value as a record of chemostratigraphy. It must be noted that, although there are numerous suggestions in the literature (as discussed and summarized in the paper by Siahi et al., 2020), that the low-$\delta^{13}C$ carbonate minerals in BIF are diagenetic in origin and therefore cannot record seawater signals, these views have been recently put into question (Siahi et al., 2020).

Bearing in mind the above, the stratigraphic sections for $\delta^{13}C$ in the examined sections of Mamatwan and Middelplaats, show interesting trends. Firstly, the isotopic dataset for both sections shows a very small degree of small-scale variability which results in a very smooth stratigraphic pattern across both stratigraphic profiles. In the Mamatwan section, $\delta^{13}C$ values range from as high as -6.3 ‰ to a minimum value of -21.2 ‰, with the hematite lutite zone exhibiting the most depleted isotopic values on average, at -17.0±2.38 ‰. The range of measured $\delta^{13}C$ values at Middelplaats is directly comparable with that from Mamatwan, from -6.24 ‰ to -20.7 ‰.

Stratigraphically, the transitions upwards from the hematite lutite sections to the Mn layers are characterised by a steady rise in the $\delta^{13}C$ values but which are manifested in slightly different ways in the two sections. In the Mamatwan section (Figure 22A), this net upward rise in $\delta^{13}C$ is punctuated by intervals of plateaus, small rises and drops in $\delta^{13}C$ values, which result in a somewhat complex stratigraphic pattern. By contrast, the thinner Mn layer in Middelplaats (Figure 22B) records a much smoother and steadier rising pattern of $\delta^{13}C$ values, with only two small-scale negative spikes at the base and near the top of the Mn section. In terms of absolute $\delta^{13}C$ values, however, both sections are almost identical in their data ranges which are within 1-2 per mil around the value of -10 ‰.

Further upwards in the BIF layer, isotopic values sharply decline to among the lowest $\delta^{13}C$ values recorded, as low as -21.2 ‰ in the Middelplaats section. However, the two BIF sections show significant differences: the Middelplaats section records a sustained interval of very low $\delta^{13}C$ values at around the value of -18.0 ‰ on average (Figure 22B), which only begin to rise slightly in the uppermost few meters of section. In the Mamatwan BIF section, however (Figure 22A), the interval of similarly low $\delta^{13}C$ is very thin, and is followed upwards by a characteristic positive excursion to $\delta^{13}C$ values as high as -10 ‰.

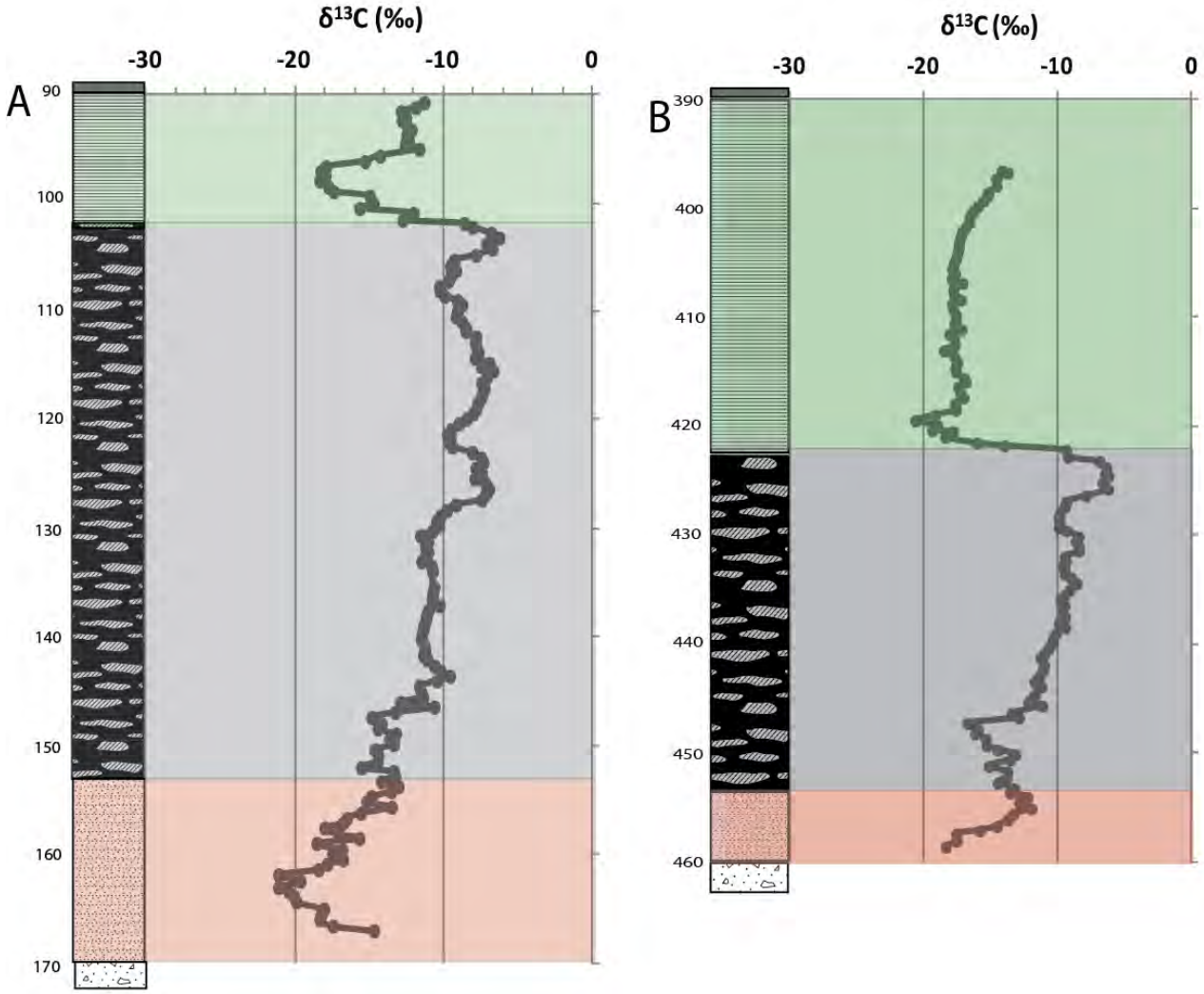

Figure 22: High-resolution chemostratigraphic variations in $\delta^{13}C$ value of bulk-rock carbonate from drill cores A) G774 and B) MP-56.

2.7 Summary

The lowermost portion of the Hotazel Formation shows interesting and in some cases directly comparable features between the two chemosedimentary sequences (i.e., Mamatwan and Middleplaats sections). The all-encompassing, salient points that could be drawn from both section's bulk-rock major and trace element and $\delta^{13}C$ patterns, and REE relationships in the Hotazel Formation are as follows:

- Periods of high-Mn deposition in the Hotazel Formation as represented by the Mn layers, appear to be very Ca-carbonate rich, as indicated by the high concentration and characteristic peaks of CaO, LOI and Sr in the Mamatwan and Middleplaats sections. This, in turn, also indicates that the Hotazel's Mn abundance is actually diluted by increased deposition of Ca carbonate.

- Maxima in MgO and Co characteristically occur at the flanks of the manganese ore layers in both localities, while an additional spike of high Mg and Mn is also enriched in Co in the lower part of the basal hematite lutite section at Mamatwan. It should be noted though that in the same section at Mamatwan, the upper flank of the Mn layer in contact with the BIF, is lacking the MgO-Co spike.
- The transition into the overlying BIF unit of both sections is marked by a rapid change in many chemical parameters, with increases in certain transition metals, and HFSEs and decreases in other chemical species, including $\delta^{13}C$ values.
- Elements of common detrital derivation such as Zr, Nb, but also Al and Ti which were not used in chemostratigraphy, are in very low abundance across the examined two sections. . This is indicative of insignificant input of detrital material during the deposition of the lowermost portion of the Hotazel Formation.
- The REE patterns of the three lithological units in both sections display similar attributes; a positive slope suggesting a relative depletion of LREE (La-Sm) as compared to HREE (Eu-Lu, plus Y), a conspicuous negative Ce anomaly, and variable Eu anomalies. The BIF lithofacies records relatively high abundance of REE, as compared to the Mn-ore and hematite lutite layer.

3. Data exploration

This chapter presents a critical evaluation of the data reported in the previous section. In light of the highly variable geochemical signals across the chemostratigraphic sequences of both cores, concentration relationships between major-oxide element *versus* major-oxide element, major-oxide element *versus* trace element and trace element *versus* trace element will be scrutinized, with the intention of uncovering the controlling factors and effects one chemical component may or may not exert on another. The chemostratigraphic variations between the two profiles will, therefore, be investigated in a more rigorous and systematic manner. For that purpose, where geochemical signals are observed across specific stratigraphic subsections of data, these data will be treated as independent entities and discussed that way. For the same reason, binary diagrams highlighting any statistical significance of the observed stratigraphic signals will be accompanying the profiles discussed, either in part or in whole. For correlation purposes, the following convention will be adopted for the statistical evaluation of plotted data subsets: an r^2-value < 0.60 will be considered to be a moderate to poor correlation; r^2-value ranging from 0.60 – 0.75 will be regarded as fair to good correlation; while an r^2-value > 0.75 will represent a very good to excellent correlation.

In a fundamental sense, inter-elemental relationships portrayed in the current chapter is likely to reveal the way in which element adsorption mechanisms, particularly the incorporation of trace elements into major element oxides, may or may not have been significant during primary deposition of the Hotazel sediments in the ambient seawater of the time. Research studies conducted by several authors since very early times (e.g. Krauskopf, 1956, Hewett et al., 1963; Murray and Brewer, 1977) have pointed out the way oxides of manganese and iron are effective scavengers of ionic species, regardless of surface charge. Considering these and numerous more recent studies (e.g. Mohapatra et al., 2009), one might conclude that the abundances of minor and trace elements in mainly manganese and iron oxide ores may have been primarily controlled by adsorption mechanisms during primary Fe and Mn oxide formation and deposition. Some of the factors accountable for a high adsorption capacity of the classically presumed primary metal oxides (i.e., MnO_2, Fe_2O_3) include their large surface area during precipitation, specific adsorption potential that is independent of charge attributes, and ion exchange via electrostatic attraction (Chao and Theobold, 1976; Mohapatra et al., 2009).

However, it must be noted that diagenesis has the capacity to modify and erase such oxide-related signal preservation in the Hotazel strata, via the reduction of Fe and Mn oxides in the presence of reductants in the primary sediment like organic matter or methane (see Siahi et al., 2020). Such diagenetic processes have been widely used to explain the dominance of reduced Fe and Mn

mineralogy in the Hotazel Formation and in BIF in general (Siahi et al., 2020). Therefore, the signals observed may not represent primary processes of trace element behaviour, but rather incorporation of trace elements in newly formed Fe and Mn minerals in the Hotazel rocks during diagenesis. Another possibility of course is that the behaviour of certain trace and minor elements may be related to primary formation of at least some of the reduced Fe and Mn minerals observed in the rocks, such as the carbonate minerals, as it has been argued recently in the review paper of Siahi et al (2020). Finally, it may also be that some minor and trace elements are related simply to low concentrations of fine mineral particles of detrital or volcanogenic origin (e.g. tuffs), and therefore have very little more to say about their possible partitioning into oxides of Fe and Mn, or into reduced silicate and carbonate minerals containing Fe(II) and Mn(II) (see Oonk et al., 2017). These issues will hopefully be illuminated in the sections which follow.

3.1 Signals in the carbonate fraction

In this section, emphasis will be placed on the elements that are known from previous studies to be associated with the carbonate fraction of the Hotazel rocks, namely Ca and Mg (e.g. Tsikos et al., 2003). This of course does not mean that the elements in question are hosted only in carbonate minerals (Mg is also known to partition in some Fe silicate minerals; Oonk, 2017), but they will be treated as being mainly carbonate-controlled for the purpose of convenient discussion of the results moving forward. The results will be discussed and evaluated showing each time the corresponding profiles first for the Mamatwan stratigraphic section and then for the Middelplaats one.

3.1.1 Manganese versus magnesium

The combined major geochemical species MnO_2 and MgO exhibit insightful chemostratigraphic patterns and signals especially within the Mn-ore zone and adjacent transitions for both stratigraphic sections analysed. Specifically, sharp Mg-maxima appear to develop on the flanks of the high Mn part of the Mn layer, while the latter appears to be characterized by a low and essentially invariant MgO concentration in both stratigraphic sections (Figure 23, 25). The MgO behaviour at the Mamatwan chemostratigraphic profile (Figure 23), however, is not developed quite in the same manner as in the Middleplaats chemostratigraphic profile (Figure 25). Specifically, while in the Middelplaats section there are two clear spikes flanking the high Mn zone above and below, in the Mamatwan section an upper spike is not recorded. It is uncertain why that is, but the assumption that can be made is that it may have been missed due to the sample resolution chosen for this study (one sample per 0.5 m), it may be much more subtle (see Fig. 23) or it may not have developed in the primary sediment pile for unknown reasons.

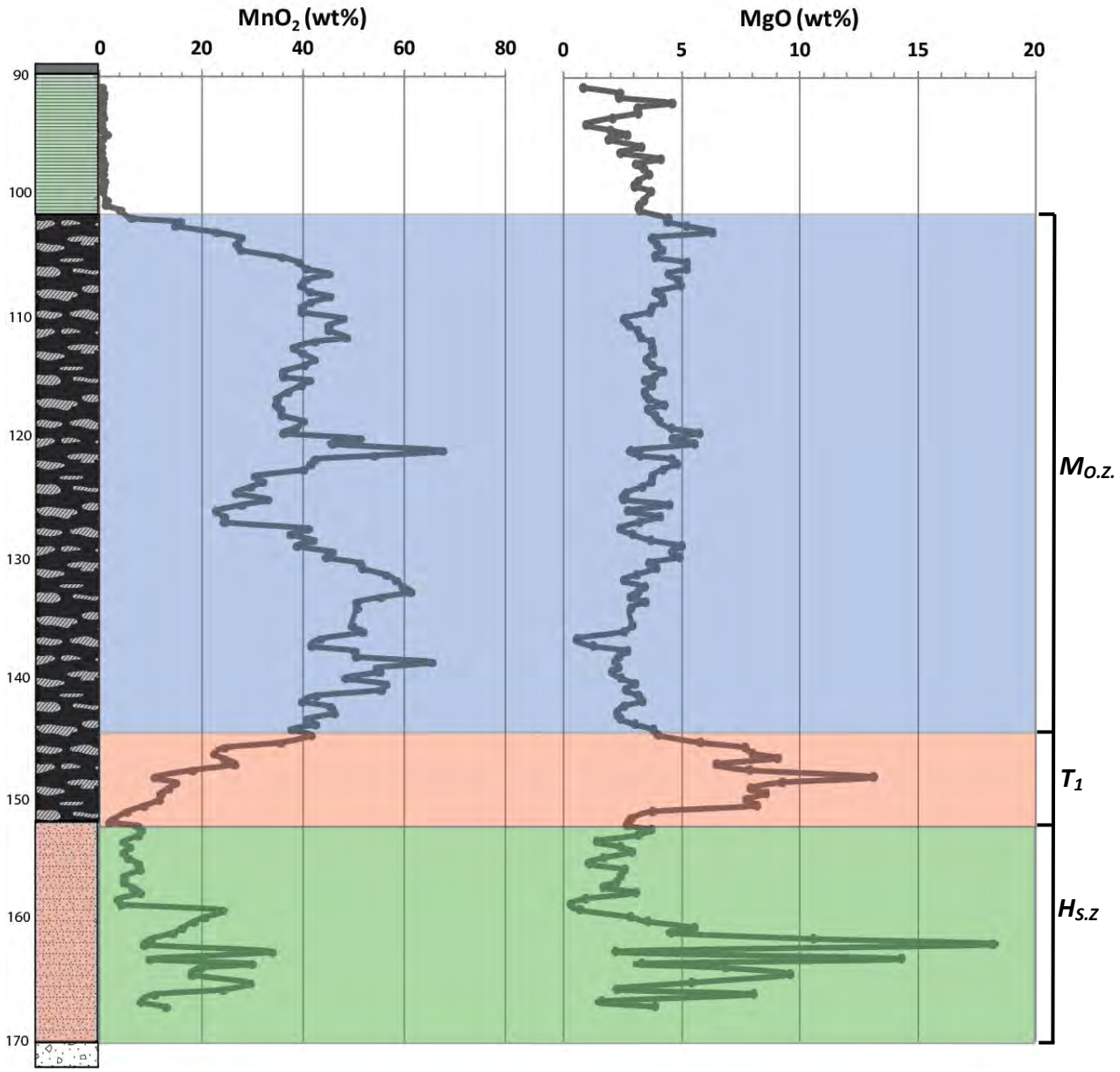

Figure 23: High-resolution chemostratigraphic relationship between MgO and MnO_2 from drill core G774.

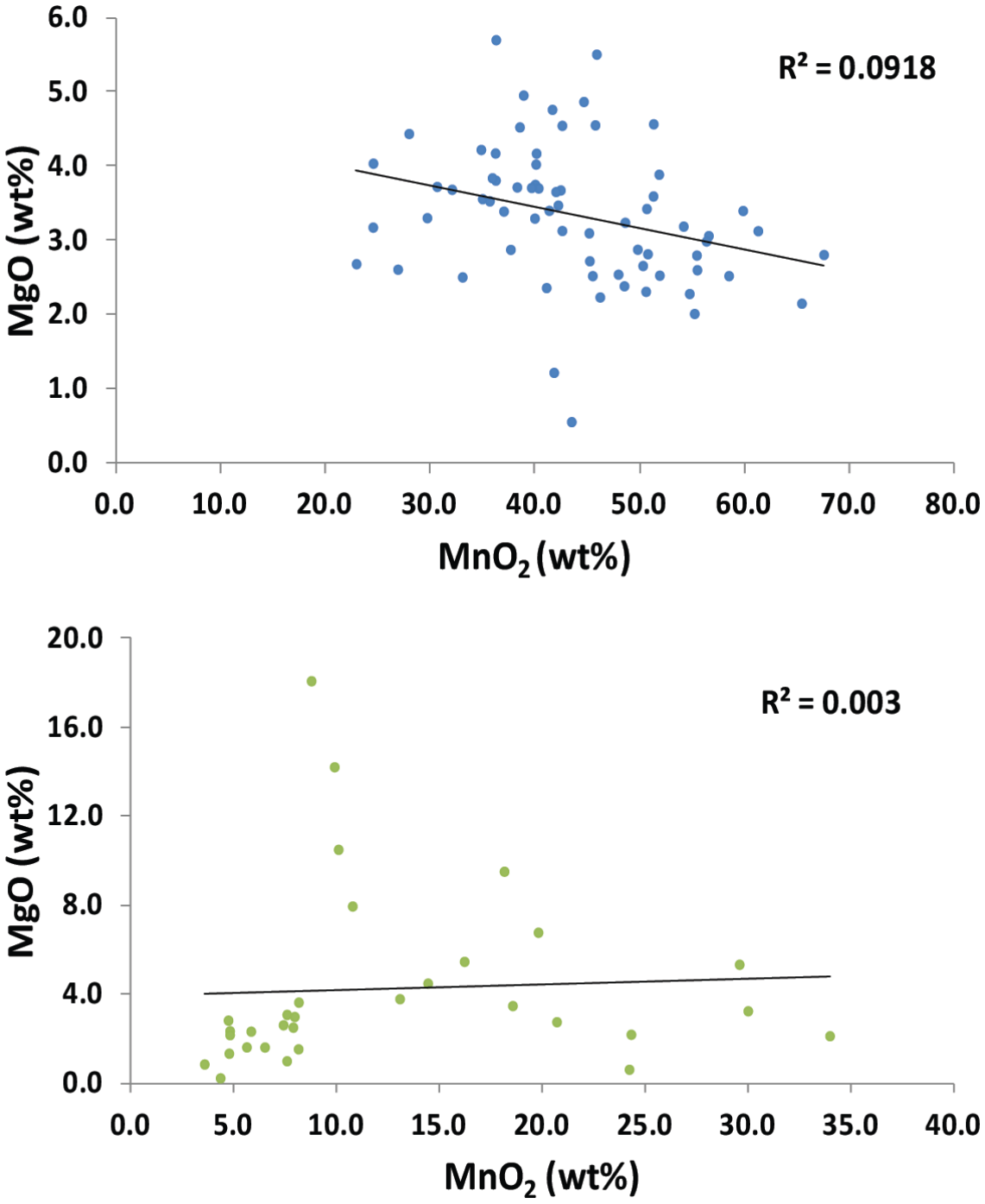

Figure 24: Bulk-rock MgO versus MnO_2 corresponding binary plots for Manganese ore ($M_{O.Z}$) and Hematite lutite ($H_{S.Z.}$) zones from drill core G774. (Manganese ore zone [$M_{O.Z}$] – Blue markers. Hematite lutite zone [$H_{S.Z.}$] – Green markers).

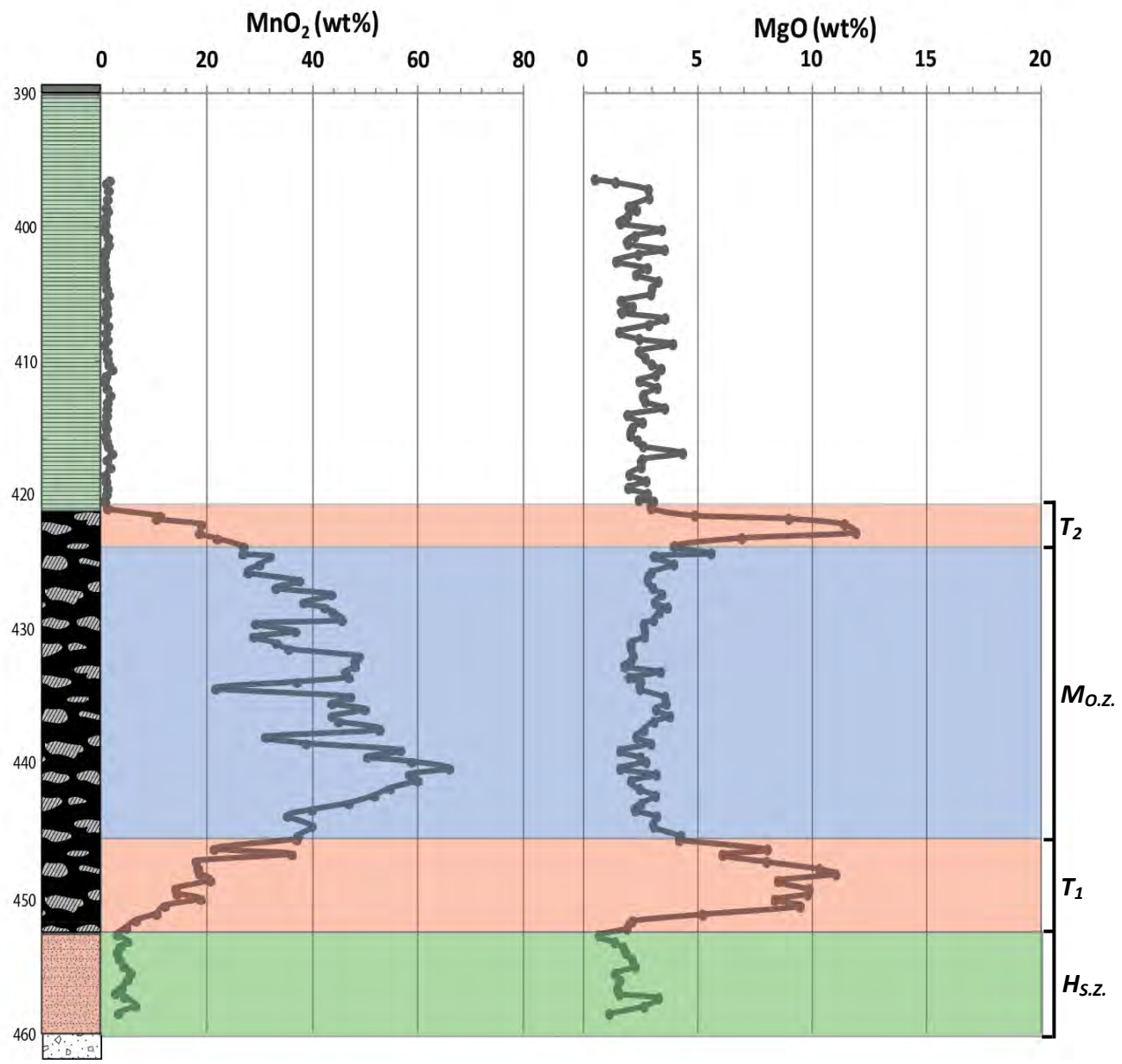

Figure 25: High-resolution chemostratigraphic relationship between MgO and MnO_2 from drill core MP-56.

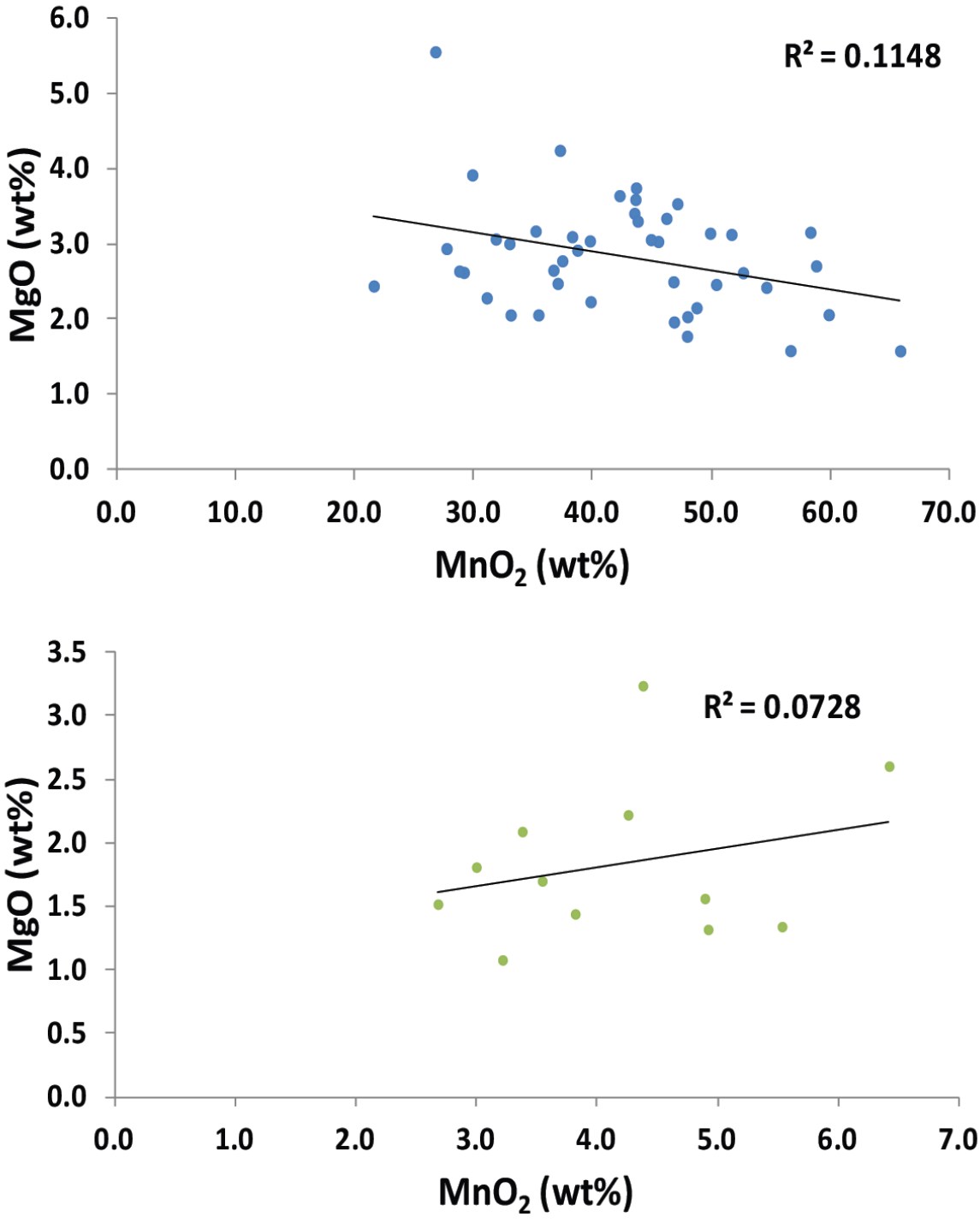

Figure 26 : Bulk-rock MgO versus MnO_2 corresponding binary plots for Manganese ore ($M_{O.Z}$) and Hematite lutite ($H_{S.Z.}$) zones from drill core MP-56. (Manganese ore zone [$M_{O.Z}$] – Blue markers. Hematite lutite zone [$H_{S.Z.}$] – Green markers).

In spite of the above-mentioned difference in the two MgO profiles, it is clear that these striking MgO spikes can be seen as defining two corresponding subzones in the examined sections that envelop the high Mn layer in both instances. It was therefore decided that these subzones must be delineated, and the corresponding datasets treated independently in the upcoming sections, in case when other anomalous element behaviour in these sub-sections appears to occur. These transitional flanking zones of maximum MgO are thus referred to in Figures 23 and 25 as zones T_1 and T_2 (in stratigraphic order) while the main ore-layer is referred to as the "Manganese ore zone" ($M_{O.Z.}$).

There is, however, an issue with the absence of the upper MgO spike from the Mamatwan stratigraphic profile, irrespective of the reason. This complicates the treatment of data in a comparative sense between the two localities. Therefore, in order to keep the treatment of data relatively simple, it was decided to henceforth sub-define only the lower transition (T_1) and the data that correspond to it for both sections, and treat the data for that transition separately and for both profiles when this appears necessary. At the same time, it was decided to treat the remaining data across the two Mn-rich sections for both profiles as one dataset for each, and this convention will be employed henceforth for ease and convenience.

The two stratigraphic profiles for MnO_2 and MgO do not show any evident relationship between the two species where the transitional MgO peaks develop, and therefore binary diagrams connecting these parameters are not shown. The binary profiles for the high Mn zones in Mamatwan and Middleplaats sites exhibit distributions that appear to show extremely weak negative relationships which are nonetheless statistically insignificant (r^2-values of 0.0918 and 0.1148, respectively; Figure 24 and 26). It should be noted here though, that in the hematite lutite basal section of the Mamatwan profile, a very characteristic high MnO_2 – high MgO spike develops in its lower part, which is not recorded in the corresponding stratigraphic section of Middelplaats. The correlation between the two parameters appears to be statistically very poor (r^2-value of 0.003), and therefore it will be considered in the following sections in case other comparable elemental spikes appear at the same stratigraphic level.

The main conclusion that can be drawn from this section which also has a mineralogical bearing, is that the transitions to the high Mn zone of the two stratigraphic sections are characterised by high Mg carbonate material, namely a dolomitic mineral. It is unknown what this mineral may be at this point and whether it is a Mn dolomite (kutnahorite), as the bulk Mn profile represents the sum of Mn from both carbonate minerals and braunite. What can be said at least, is that the spikes in MgO and MnO_2 in the underlying hematite subzone at Mamatwan (Figure 23) most probably represents a Mn-rich dolomitic mineral.

3.1.2 Calcium versus manganese

The stratigraphic comparisons between the bulk CaO and MnO_2 profiles highlight some additional important insights with respect to the carbonate fraction of the rocks. As indicated in the previous section, the Mn layer has been subdivided into the lower T_1 transition zone (pinkish -orange highlight, Fig. 27, 29) and the overlying high Mn zone without further differentiation (bluiesh highlight). The visual relationship between the two species in the high Mn zones for both profiles, appears to be strongly antithetic, with characteristic peaks matching almost perfectly with troughs across the profiles and *vice versa*. These peaks and troughs record major swings in the abundances of CaO against MnO_2 which reach ranges of a magnitude as high as 20 wt% from minimum to maximum values.

From a statistical viewpoint, this antithetic relationship is very well manifested in the binary plot of CaO against MnO_2 for the Mamatwan stratigraphic profile, which shows a rather remarkable antithetic relationship with an r^2 value of almost 0.8 (Fig. 28). In the Middelplaats section, the same profile shows a much less convincing but still apparently negative relationship, with an r^2 value of 0.29 (Figure 30). It is possible, however, that the statistical strength of that relationship is compromised by the fact that the dataset plotted incorporates also the earlier defined upper T_2 sub-section with the characteristic MgO spike that was shown in Figure 25, and therefore probably mixes carbonate material from two mineralogically different subsections. Nevertheless, it looks as though the antithetic relationship in both sections reflects the antithetic abundance of the dominant Mn-rich mineral braunite with Mn poor carbonate, probably calcite, as the corresponding MgO contents are quite low (Figures 23,25). In other words, the fluctuation in calcic carbonate in the Mn rich section results in corresponding fluctuation in the bulk Mn content of the ore zone.

It is interesting here to consider what the results show for the T_1 transition, the data for which are plotted separately in Figures 27 and 29 (and Figures 28 and 30; corresponding binary diagrams). In Figure 28, a moderately positive correlation between CaO and MnO_2 is recorded, with a correlation coefficient of an r^2-value of 0.53. For the Middleplaats stratigraphic section, the same positive CaO *versus* MnO_2 correlation for the corresponding T_1 transition is much less statistically convincing but still shows an r^2 correlation coefficient with a value higher than 0.5 (0.62, Figure 30).

The above information confirms that there must be a clear change in the type of mineralogy in the carbonate fraction of the rocks as one transitions from the hematite lutite section in the basal Hotazel stratigraphy into the zone of maximum Mn deposition. Although that change appears cryptic from the visual inspection of the rocks and the bulk MnO_2 and CaO profiles, it becomes much more obvious from the MgO profiles shown earlier. The significance of these relationships will be discussed later in this chapter and much more in the discussion that follows.

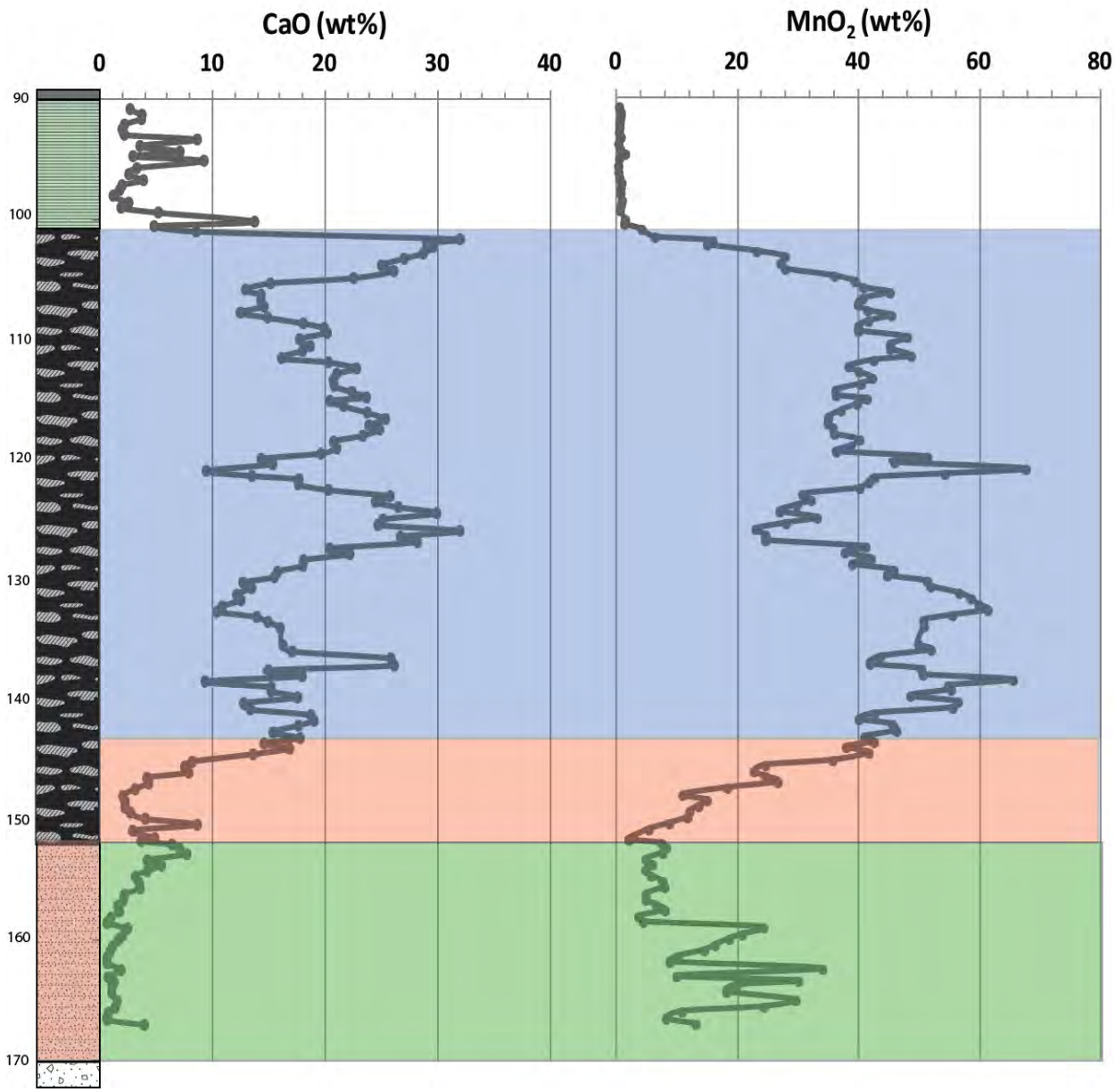

Figure 27: High-resolution chemostratigraphic relationship between CaO and MnO_2 from drill core G774.

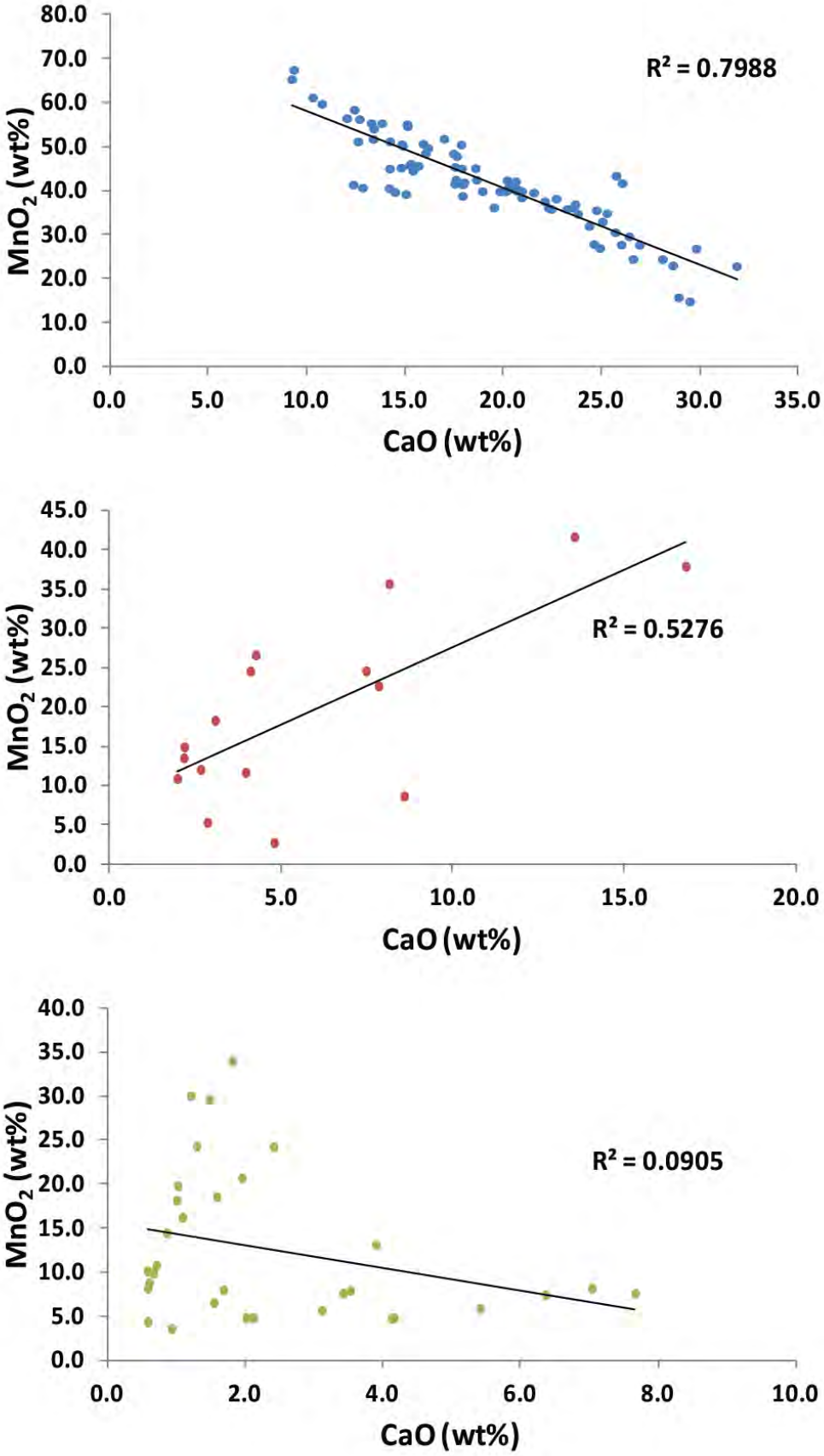

Figure 28: Bulk-rock CaO versus MnO_2 corresponding binary plots for Manganese ore ($M_{O.Z}$), lower transition (T_1) and Hematite lutite ($H_{S.Z.}$) zones from drill core G774. (Manganese ore zone [$M_{O.Z}$] – Blue markers. Lower Transition zone [T_1] – Red markers. Hematite lutite zone [$H_{S.Z.}$] – Green markers).

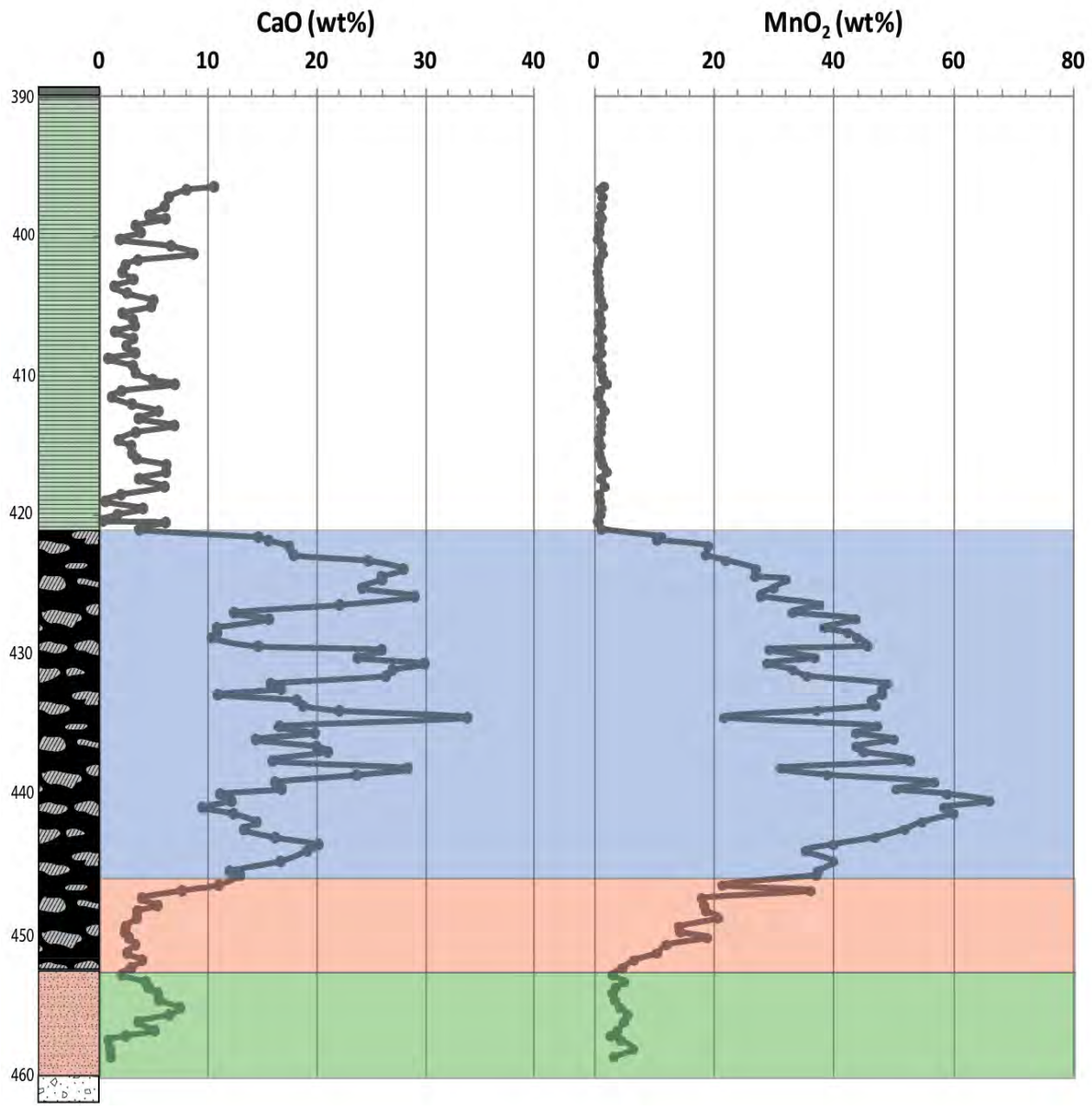

Figure 29: High-resolution chemostratigraphic relationship between CaO and MnO_2 from drill core MP-56.

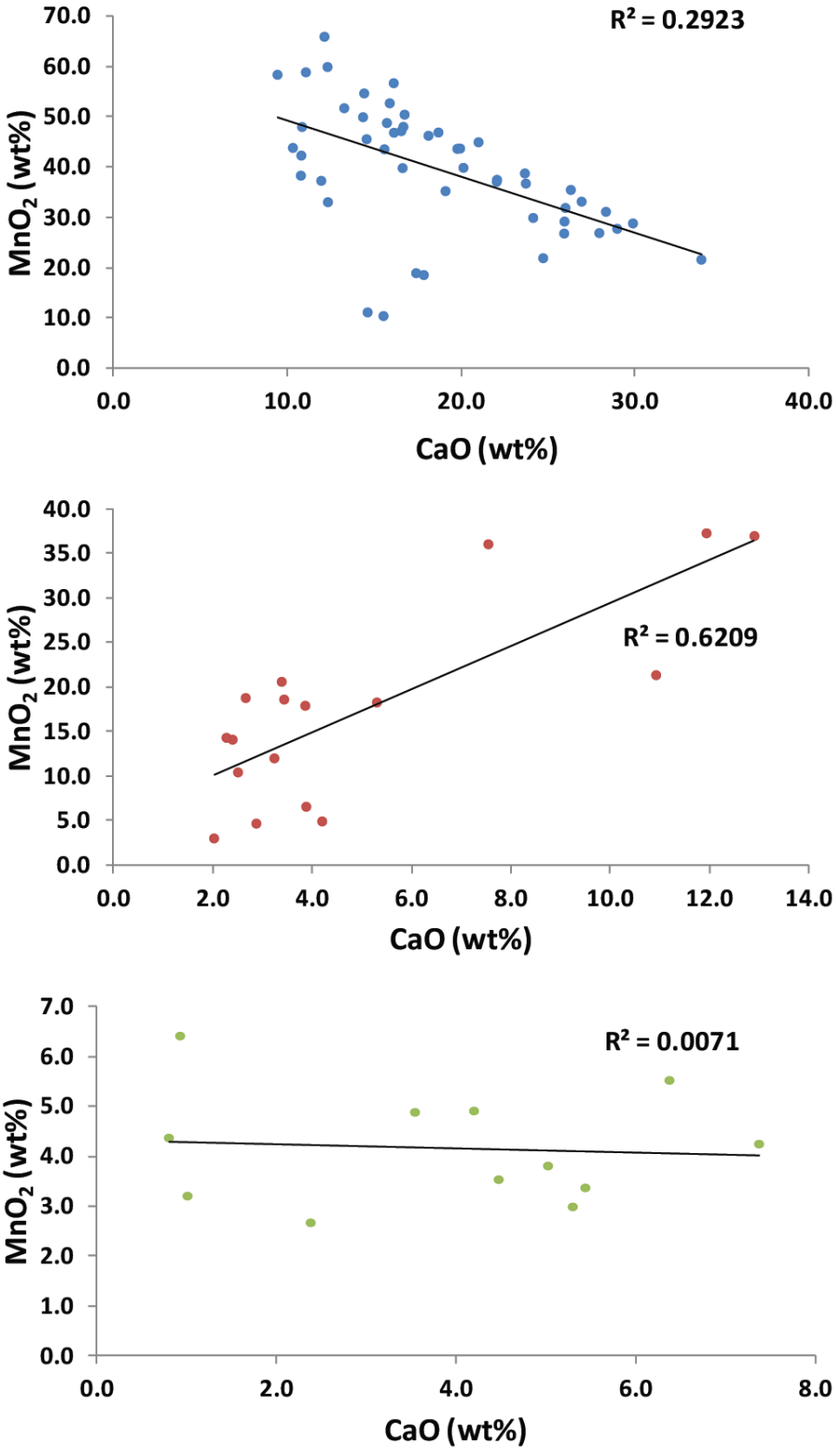

Figure 30: Bulk-rock CaO versus MnO_2 corresponding binary plots for Manganese ore ($M_{O.Z}$), lower transition (T_1) and Hematite lutite ($H_{S.Z.}$) zones from drill core MP-56. (Manganese ore zone [$M_{O.Z}$] – Blue markers. Lower Transition zone [T_1] – Red markers. Hematite lutite zone [$H_{S.Z.}$] – Green markers).

3.1.3 Calcium versus carbon isotopes

One of the components that was analysed in the samples of this study is the bulk carbonate carbon isotopes, as already exemplified in the previous chapter. The $\delta^{13}C$ record is one that speaks directly to the carbonate fraction of the rocks, but of course it is also expected to be dependent on the carbonate mineralogy across the studied stratigraphic profiles and how this mineralogy changes from one facies to another (i.e. hematite lutite, Mn-rich layer, and BIF). As it is known from the literature (Tsikos and Moore, 1997; Tsikos et al., 2003, 2010), one major change in mineralogy concerns the iron carbonate minerals that dominate the BIF (ankerite, calcite, lesser siderite), and the Mn carbonate equivalents in the Mn rich parts of the Hotazel stratigraphy (kutnahorite, Mn calcite, minor rhodochrosite). Nevertheless, one of the common denominators for the carbonate fraction of the Hotazel rocks is the element CaO, which is present in almost every carbonate mineral present. Therefore, the data for bulk carbonate $\delta^{13}C$ were plotted against the bulk CaO value, and the results are shown in Figures 31 and 33.

The first thing that strikes the attention is the smoothness of the carbon isotope profiles and the generally very similar behaviour of the $\delta^{13}C$ values against the examined lithostratigraphies from both localities. In general, the data in both sections seem to increase steadily with small fluctuations of 1-2 per mil, from values as low as -20 per mil in the hematite lutiute at the base, to as high as -8 per mil at the topmost part of the high-Mn layer in both sites. Across the relatively sharp contact with the overlying BIF, the $\delta^{13}C$ data drop sharply again to values as low as -21 per mil in both sections, and thereafter two things happen: the first is in the thin Mamatwan BIF section where the $\delta^{13}C$ data stay at very low values around -18 per mil for a short statigraphic interval of 3-4 meters, and then increase sharply to values up to -12 per mil as the shale boundary is approached. In the thicker Middelplaats BIF section which is relatively thicker, very low $\delta^{13}C$ data persist over more than 10 meters of section and only right in the upper part and before the boundary shale, the values become greadually higher and also reach close to -12 per mil like in the Mamatwan stratigraphic section.

When the CaO profiles are seen next to the isotope ones (Figures 31 and 33) one can see that the CaO records highly fluctuating values across the stratigraphy whereas the $\delta^{13}C$ isotope record is very much smoother. There is also a general similarity that shows a broadly positive correlation between the two parameters, which is confirmed in the binary diagrams of Figures 32 and 34. The relationship in the transitional (T_1) and high Mn ($M_{O.Z.}$) zones of the Mamatwan chemostratigraphic profile are rather weak with correlation coefficients of r^2-values of 0.5759 and 0.5674, while at the Middleplaats site, these positive correlations are even weaker at r^2-values of 0.3521 and 0.3529. The general conclusion that can be drawn from the above is that the more Ca (corresponding to relative calcite) is present in the rocks, the higher the $\delta^{13}C$ value seems to be, and this seems to apply across the entire sections sampled.

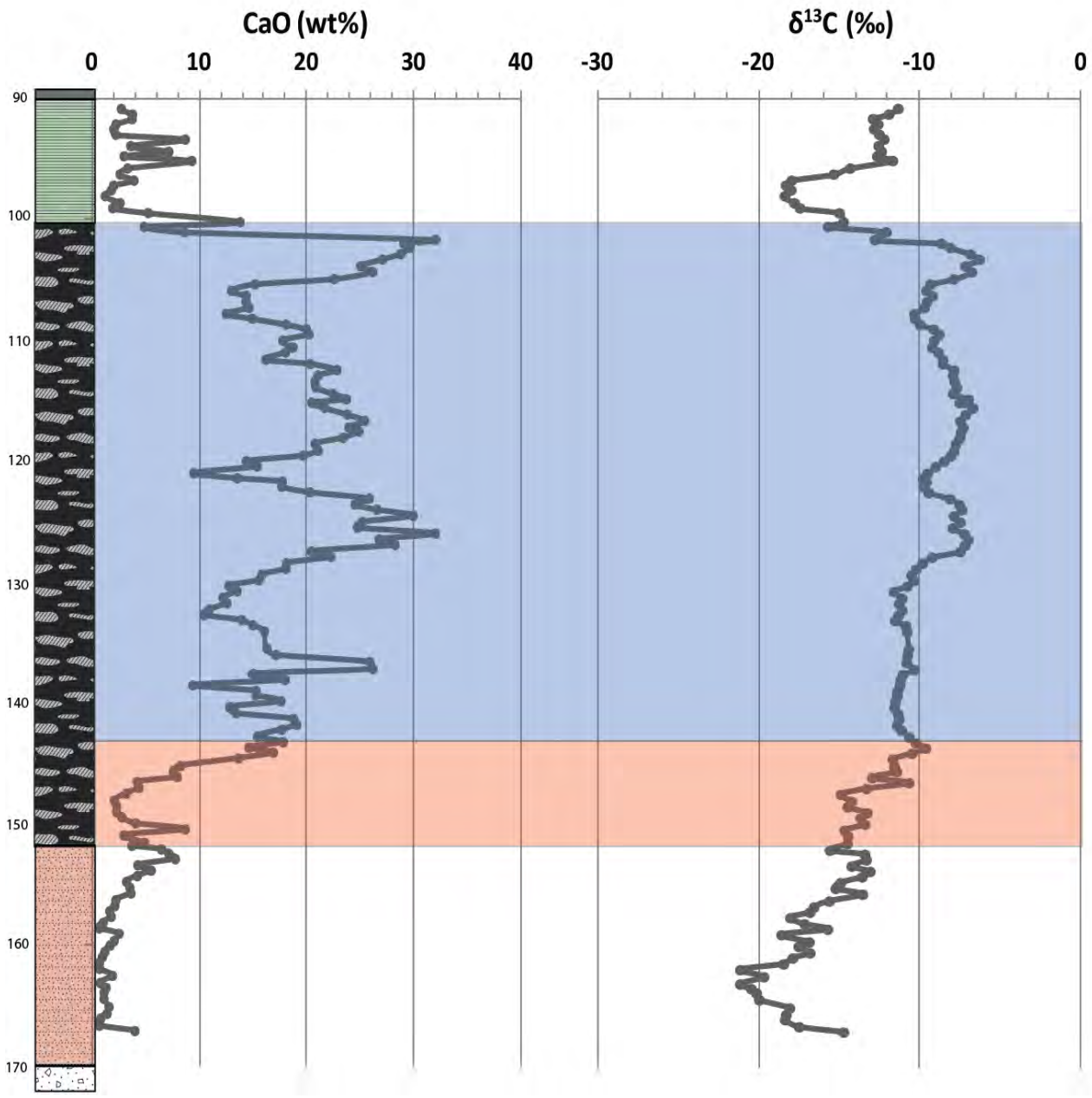

Figure 31: High-resolution chemostratigraphic relationship between CaO and $\delta^{13}C$ drill core G774.

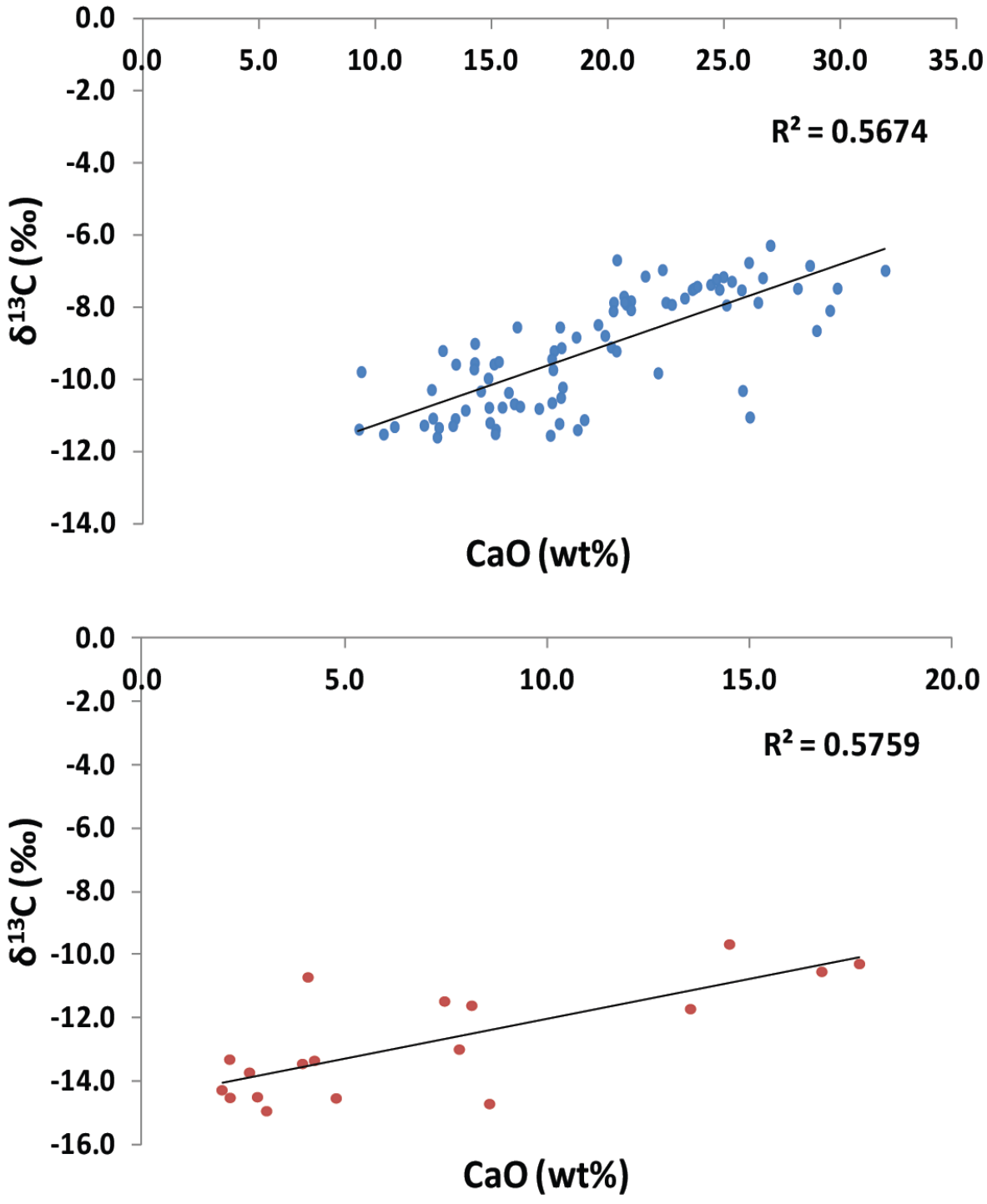

Figure 32: Bulk-rock CaO versus $\delta^{13}C$ corresponding binary plots for Manganese ore ($M_{O.Z}$) and lower transition (T_1) zones from drill core G774. (Manganese ore zone [$M_{O.Z}$] – Blue markers. Lower Transition zone [T_1] – Red markers).

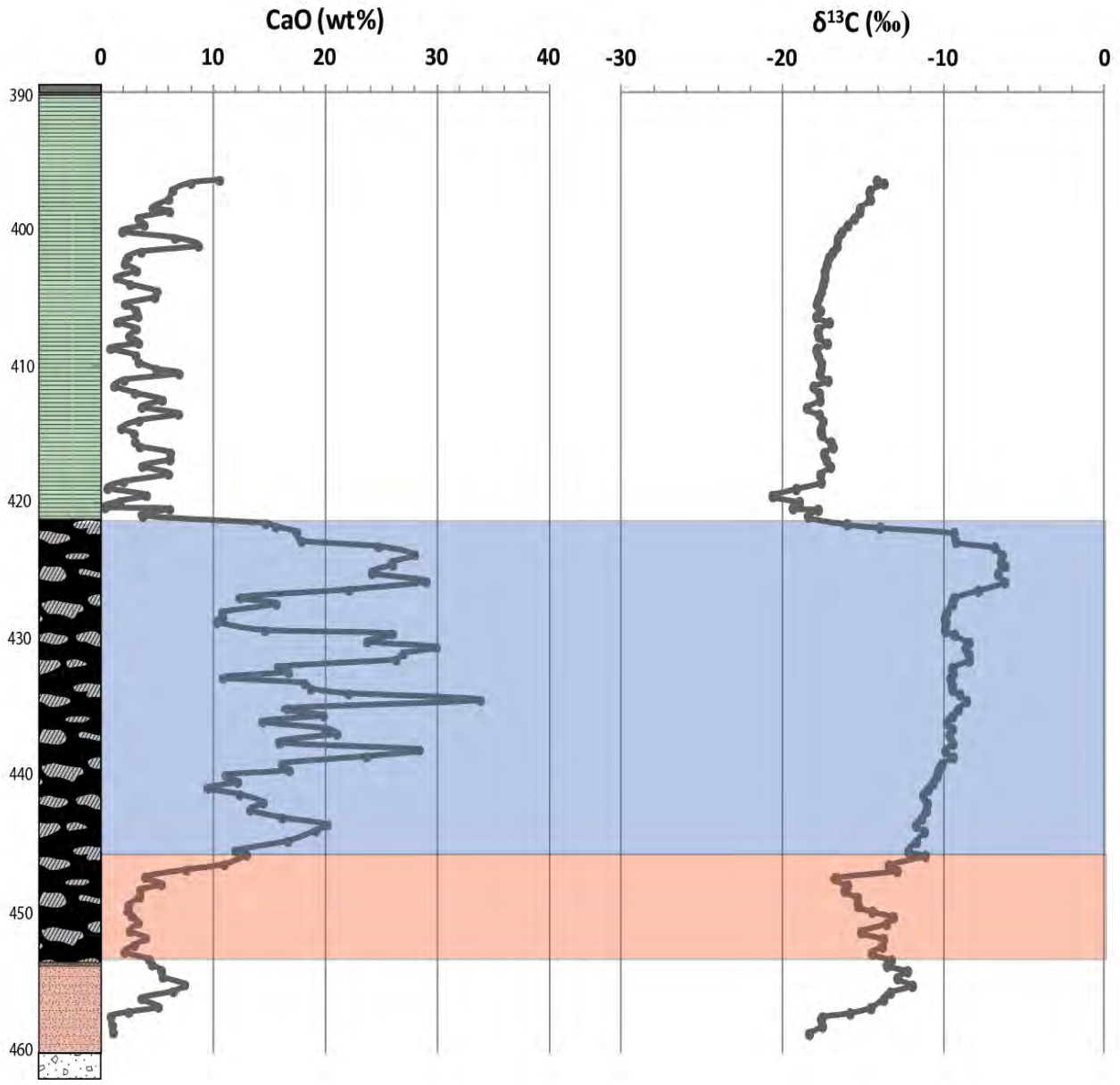

Figure 33: High-resolution chemostratigraphic relationship between CaO and $\delta^{13}C$ from drill core MP-56.

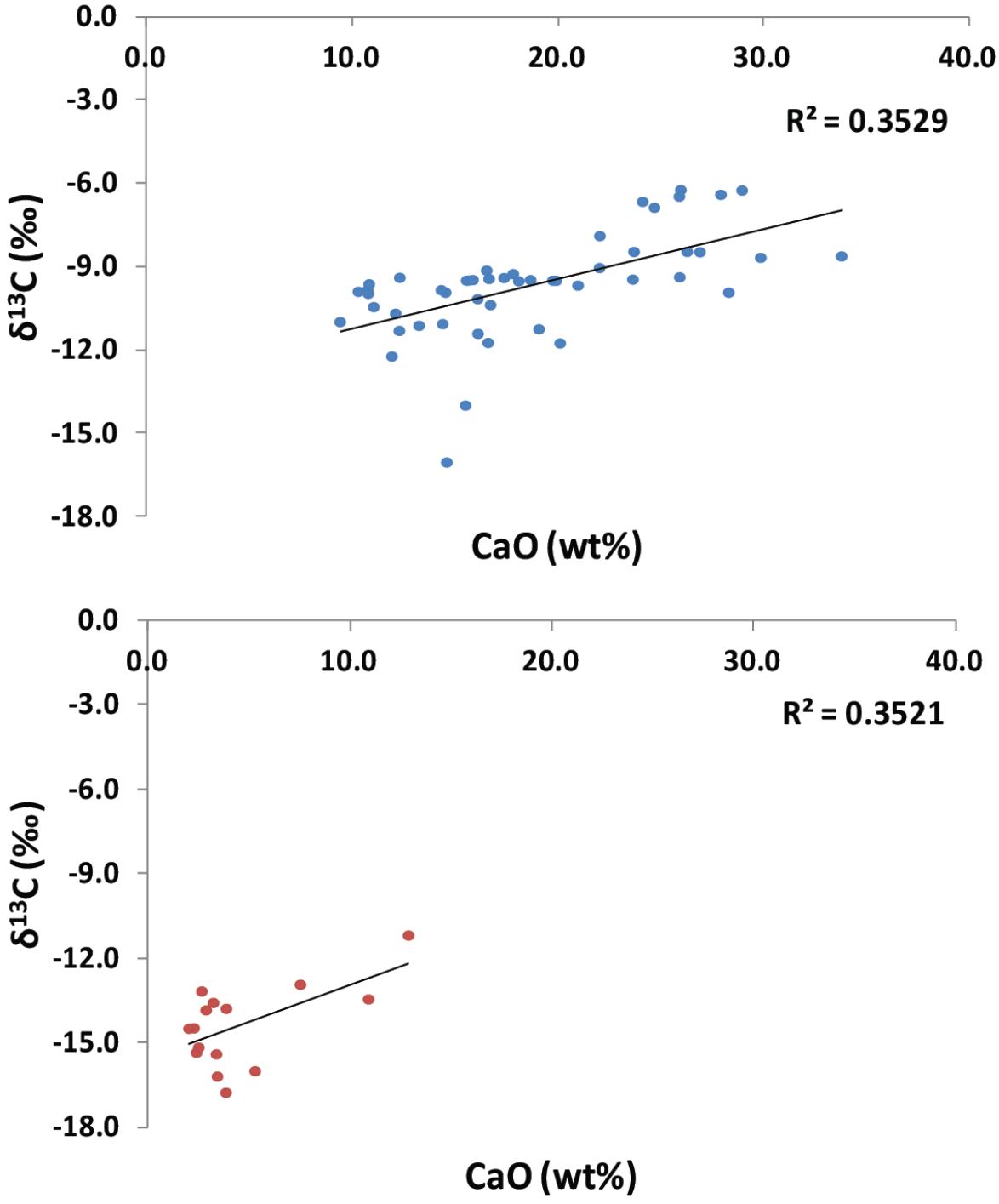

Figure 34: Bulk-rock CaO versus $\delta^{13}C$ corresponding binary plots for Manganese ore ($M_{O.Z}$) and lower transition (T_1) zones from drill core MP-56. (Manganese ore zone [$M_{O.Z}$] – Blue markers. Lower Transition zone [T_1] – Red markers).

3.2 Signals associated with the oxide fraction

3.2.1 Cobalt versus iron

Cobalt and molybdenum are two redox-sensitive metallic elements that were recognised in the previous chapter showing a chemostratigraphic behaviour that may provide insights into the redox controls of metal precipitation in the primary environment of the Hotazel rocks. The two main redox elements in the Hotazel strata are of course the transition metals iron and manganese, which are present in large abundances in the rocks. In contrast to manganese, iron is especially abundant throughout the two stratigraphic intersections chosen for this study, with hematite being the dominant iron mineral in the hematite lutite and less so in the Mn-rich layer, and magnetite in the overlying BIF. The Co behaviour will therefore be assessed below against the bulk iron chemostratigraphy of the two intersections.

The general view of the behaviour of Co in relation to Fe is that it shows the maximum values in the lower hematite-rich part of the stratigraphy. What is even more interesting is that peaks in the abundance of Co in both the Mamatwan and Middelplaats sites (Figures 35 and 37 respectively), appear to be present in the zones where the spikes in MgO also occur, as seen in Figures 23 and 25 shown at the beginning of the present chapter. This is specifically obvious in the Mamatwan stratigraphic section where the cobalt spikes in subzones T_1 and also in the hematite subzone Hsz, with values as high as 100 ppm or more (Figure 35), but also in the T_1 transitional horizon of the Middelplaats stratigraphic section where the cobalt content reaches > 50 ppm (Figure 37). In the main Mn horizon of both localities, the cobalt abundances are relatively lower between 10 and 40 ppm but do not fluctuate much, except for the upper half of the Middelplaats high Mn section where the cobalt appears a bit more spikey and in some places seems to coincide with spikes in total Fe concentration. In the BIF sections, the abundances are even lower on average, below 10 ppm, with very occasional spikes higher than that value.

The lack of any clear statistical relationship (Figures 36, 38) between Co and Fe makes explaning its behaviour difficult, but it looks like it has a relationship with iron mineralogy, rather than manganese content. The fact that the Co is highest in the hematite-rich part of the stratigraphy and lowest in the magnetite and Fe(II)-rich BIF, suggests that the Co must probably have a genetic relationship with primary ferric oxide deposition. If the Co was associated with highest manganese, it would be expected that it peaks in the Mn-rich layer but that is not observed. The Mn rich layer at both sites also contains some hematite, generally not higher than 10 wt% in bulk abundance, but is probably still responsibe for the relatively higher abundances of cobalt in the Mn rich zone than those in the BIF. The main outcome of the above considerations is that Co appears to show a close association with the ferric iron fraction of the rock, which gives interesting insights into the primary redox processes of iron deposition.

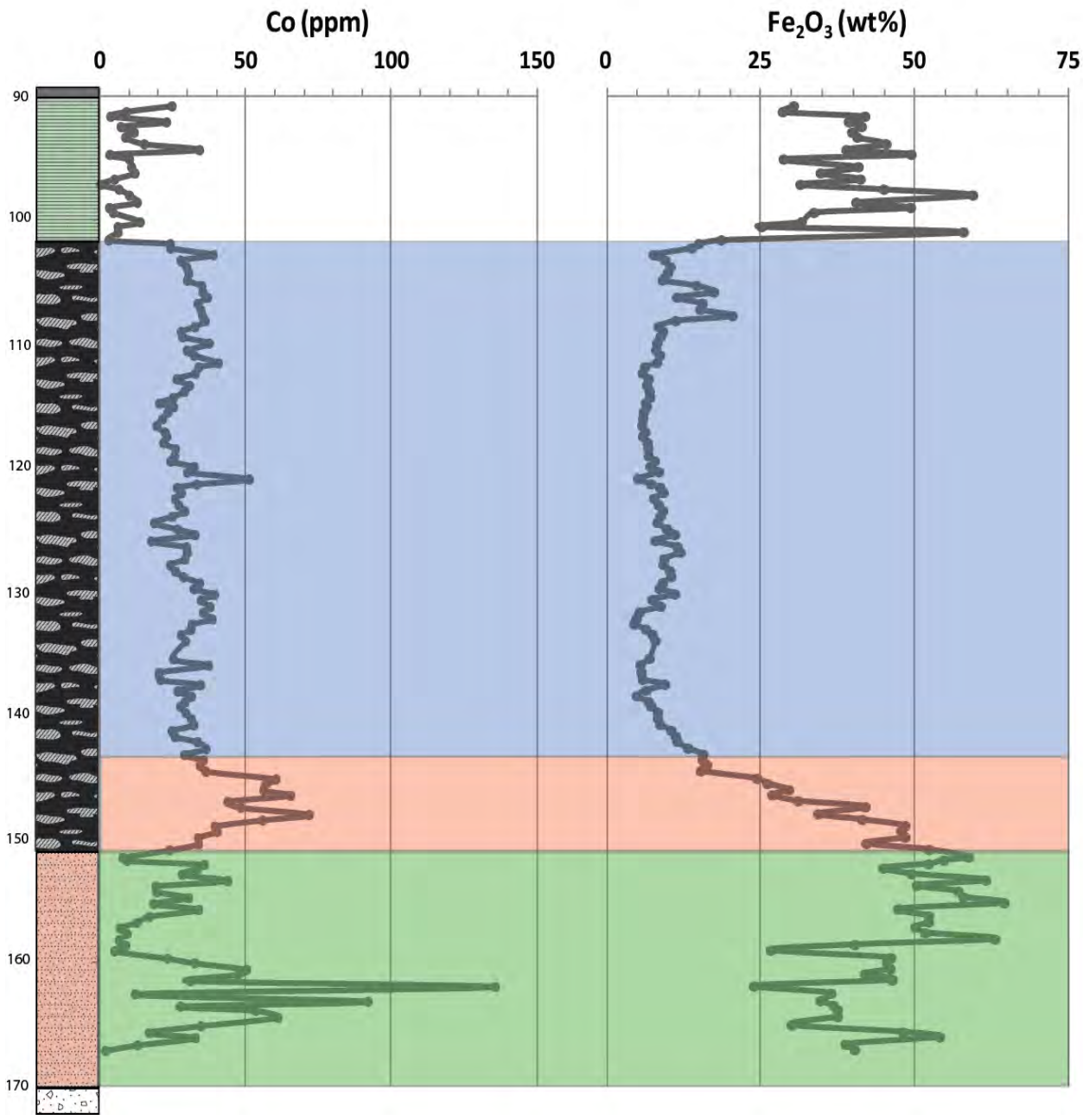

Figure 35: High-resolution chemostratigraphic relationship between Co and Fe_2O_3 from drill core G774.

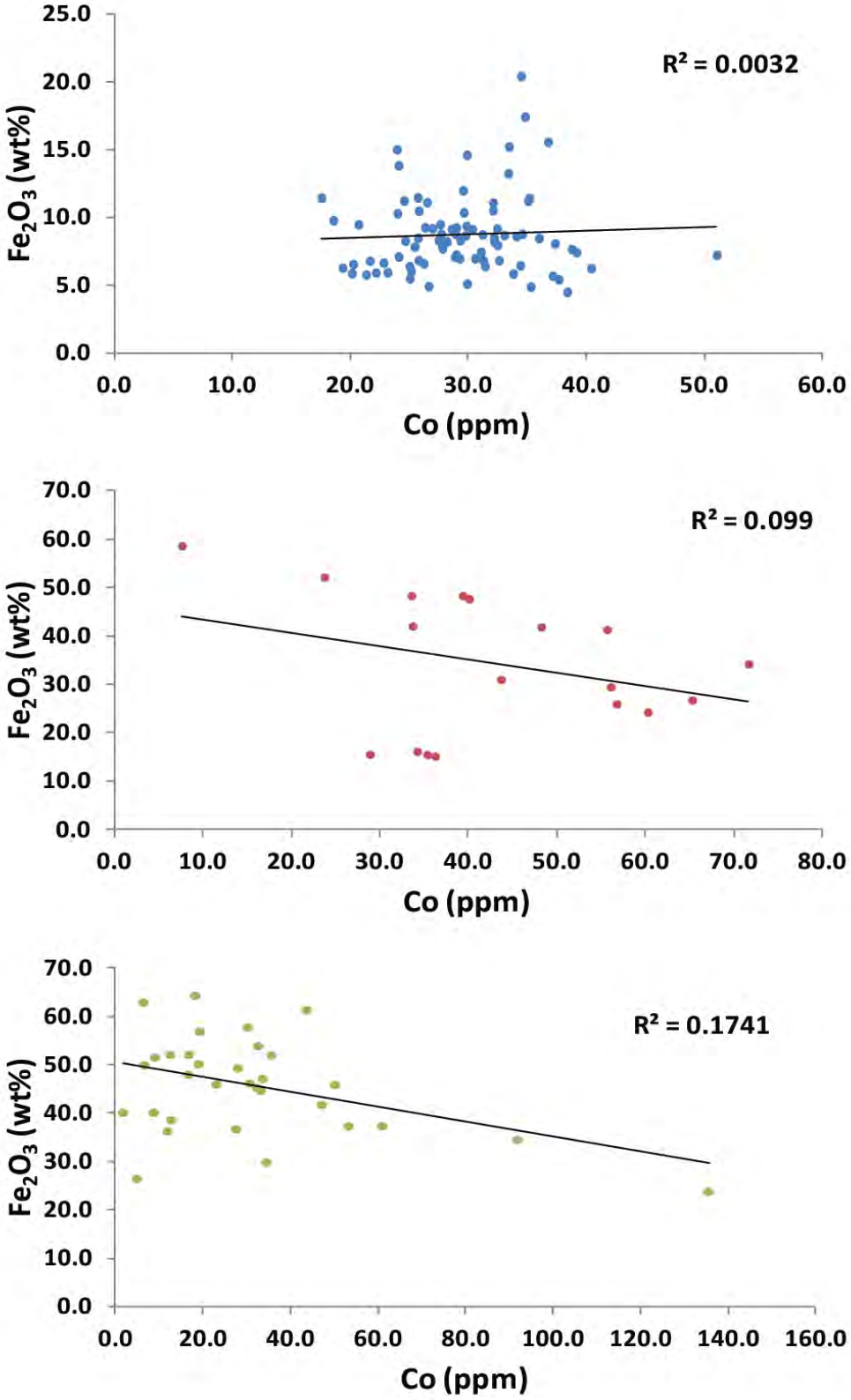

Figure 36: Bulk-rock Co versus Fe_2O_3 corresponding binary plots for Manganese ore ($M_{O.Z}$), lower transition (T_1) and Hematite lutite ($HS_{.Z.}$) zones from drill core G774. (Manganese ore zone [$M_{O.Z}$] – Blue markers. Lower Transition zone [T_1] – Red markers. Hematite lutite zone [$H_{S.Z.}$] – Green markers).

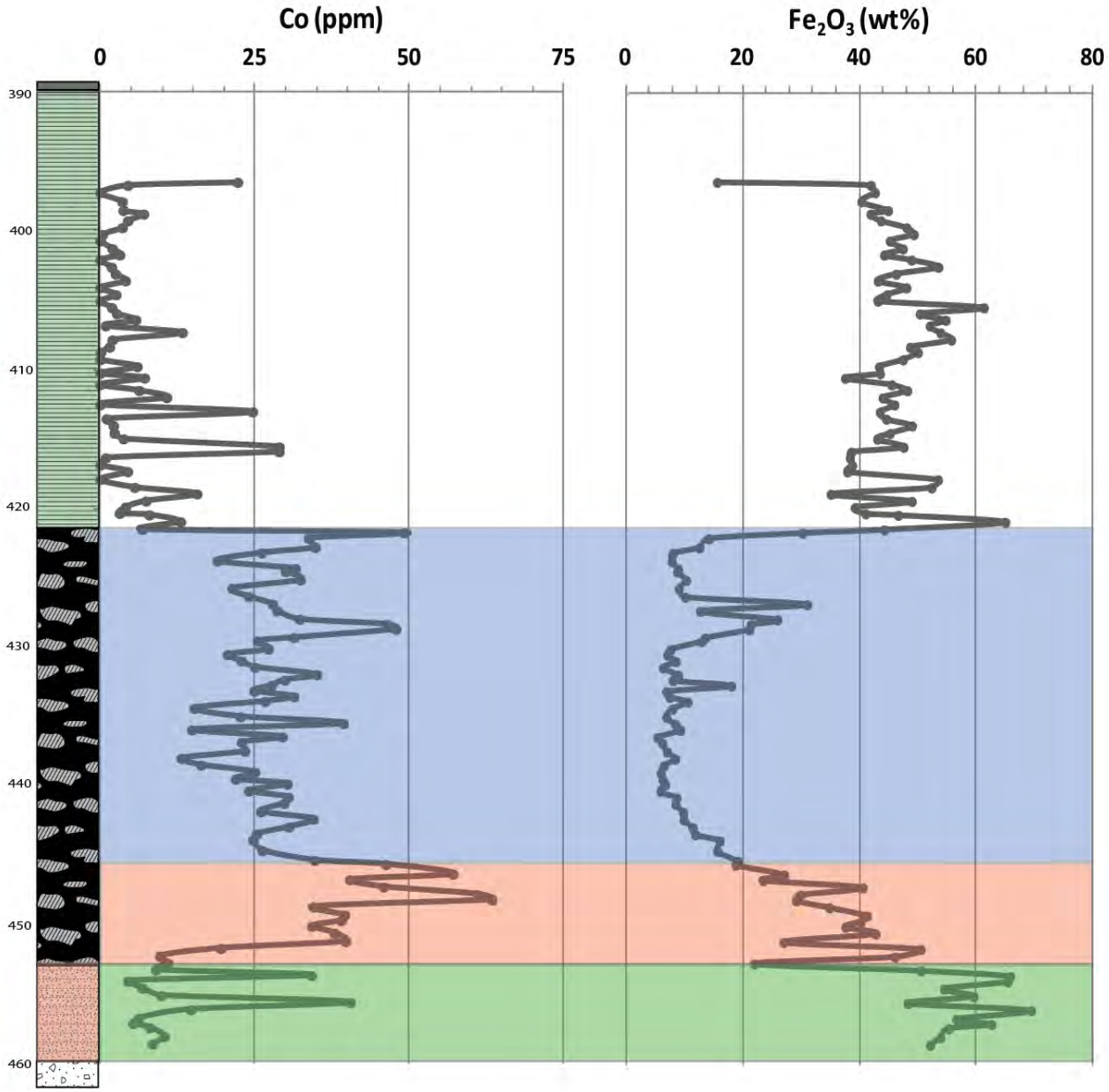

Figure 37: High-resolution chemostratigraphic relationship between Co and Fe_2O_3 from drill core MP-56.

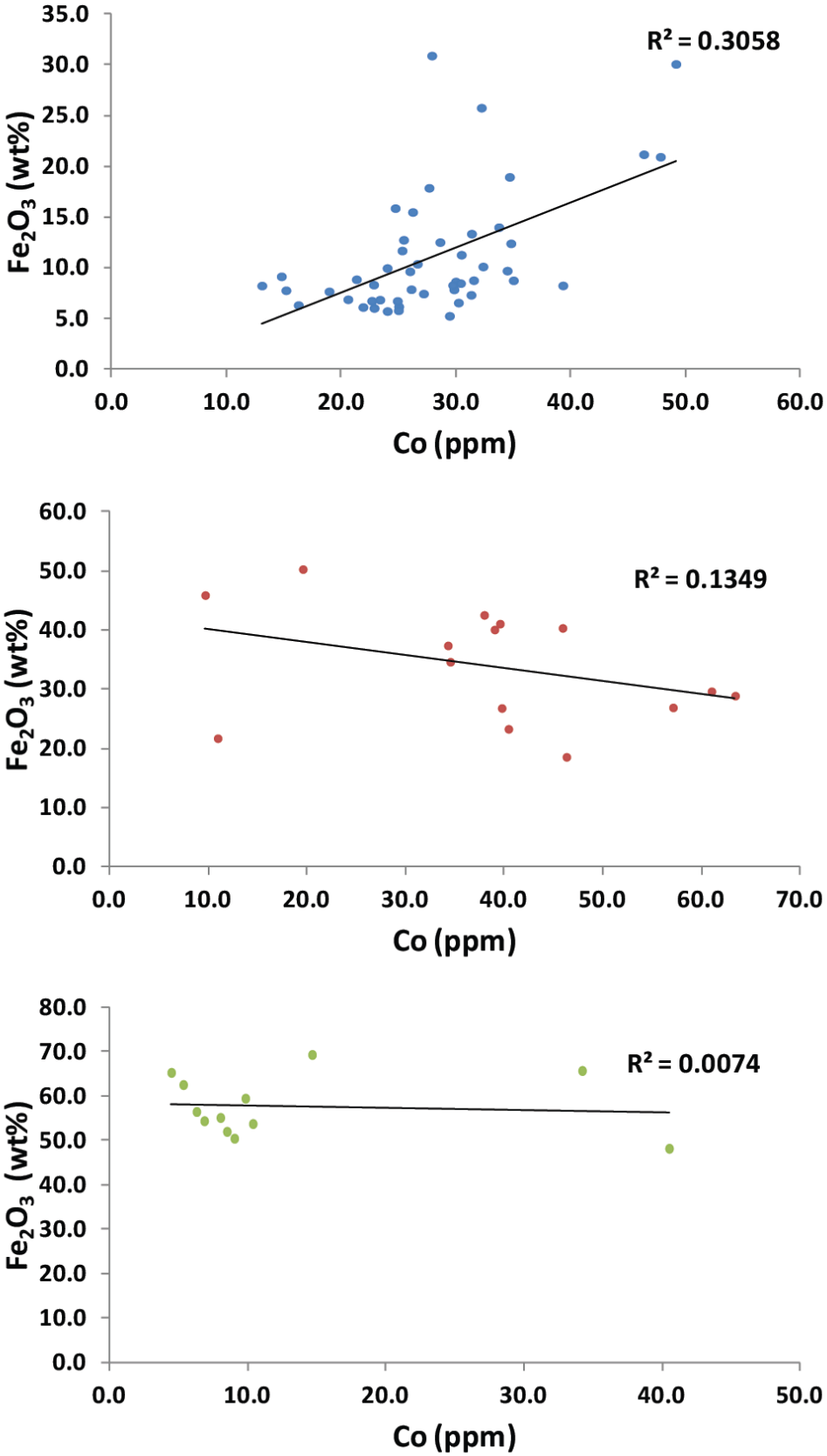

Figure 38: Bulk-rock Co versus Fe_2O_3 corresponding binary plots for Manganese ore ($M_{O.Z}$), lower transition (T_1) and Hematite lutite ($HS_{.Z.}$) zones from drill core MP-56. (Manganese ore zone [$M_{O.Z}$] – Blue markers. Lower Transition zone [T_1] – Red markers. Hematite lutite zone [$H_{S.Z.}$] – Green markers).

3.2.2 Molebdynum versus manganese

The metallic element molybdenum (Mo) has been used extensively in redox considerations of depositional environments in the early Earth, and in some cases is regarded as a key redox proxy for fully oxic conditions associated with manganese oxide precipitation. For example, the theory of oxygen whiffs (Anbar et al, 2007) is based on Mo isotope geochemistry in ancient sediments before the GOE. It becomes clear that the relationship of Mo with possible primary Mn oxide precipitation in the Hotazel Formation, is a feature that needs to be explored in this study as well.

Figures 39 and 41 show profiles of Mo abundance across the Mamatwan and Middelplaats stratigraphic sections respectively, against those of bulk MnO_2. Firstly, the Mo profile for the Mamatwan section records considerable variation across the stratigraphy. The Mo abundances fluctuate between less than 1 ppm and just over 6 ppm, with lowest values seen in the BIF (less than 2 ppm) and relatively higher and invariant in the hematite lutite at the base (between 2 – 4 ppm). In the peak Mn layer, the Mo abundances fluctuate a lot and reach the maximum values of just over 6 ppm at about the centre of the high Mn layer. What is more spectacular, however, is that the relationship between Mo and Mn abundances is positive at an r^2 correlation coefficient of 0.57 for the main Mn zone, and even a strikingly higher one of 0.86 for the T_1 horizon.

The situation appears to be a lot less clear in the Middelplaats section, where the relationship between Mn and Mo is not nearly as good. Molybdenum concentrations in the BIF are even lower in this section than at Mamatwan, never getting higher than the value of 1 ppm. In the rest of the section, the Mo abundances are generally lower than in the Mamatwan stratigraphy, with values ranging between 2 and 4 ppm across the hematite lutite and the high Mn section, where the highest value of 4 ppm is seen to correspond with the point of maximum Mn abundance. The only part of the stratigraphy where a small positive anomaly in Mo abundance is seen is in the T_1 sub-section, where there is a short Mo spike of 6 ppm. These signals result in binary diagrams between Mo and Mn for the high Mn zone and the T_1 transition (Figure 42) that are not as convincingly positive as those in the Mamatwan section (Figure 40).

The aforementioned relationships make the interpretation of the Mo behaviour rather tricky. Although its positive relationship with maximum Mn content and possibly primary Mn oxide deposition is quite clear, in the Middelplaats section this is not so. It may be that the behaviour of Mo is not uniform throughout the primary depositional environment but was more prominent in areas where the deposition of Mn was richest and thickest (like that recorded at the Mamatwan site). This would further suggest that perhaps that Mo was not well mixed across the whole basin but was instead sequestered rapidly near its source, which may have been sites of hydrothermal venting where Mn accumulation was highest. These issues will be revisited in the Discussion section that follows this chapter.

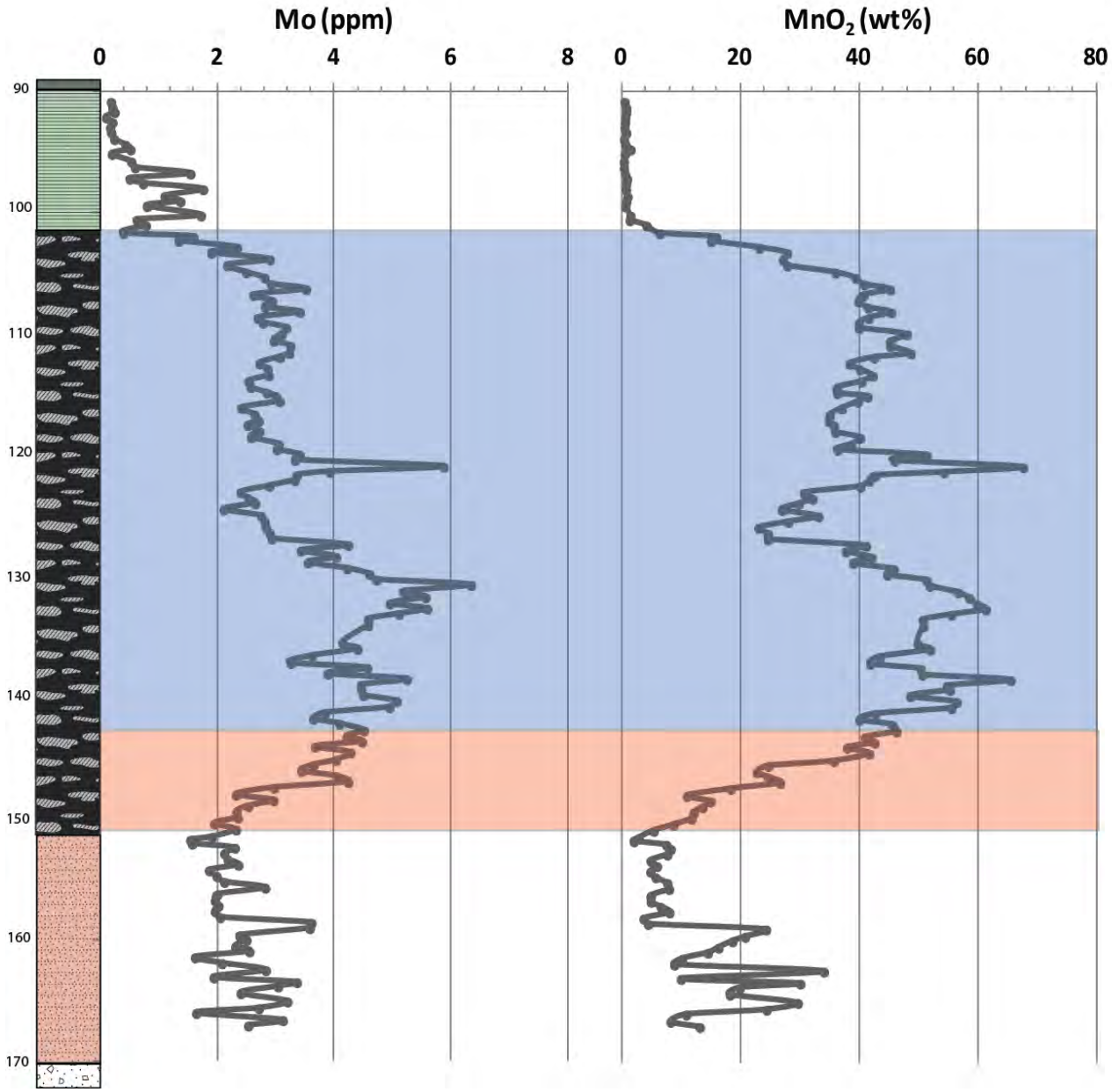

Figure 39: High-resolution chemostratigraphic relationship between Mo and MnO_2 from drill core G774.

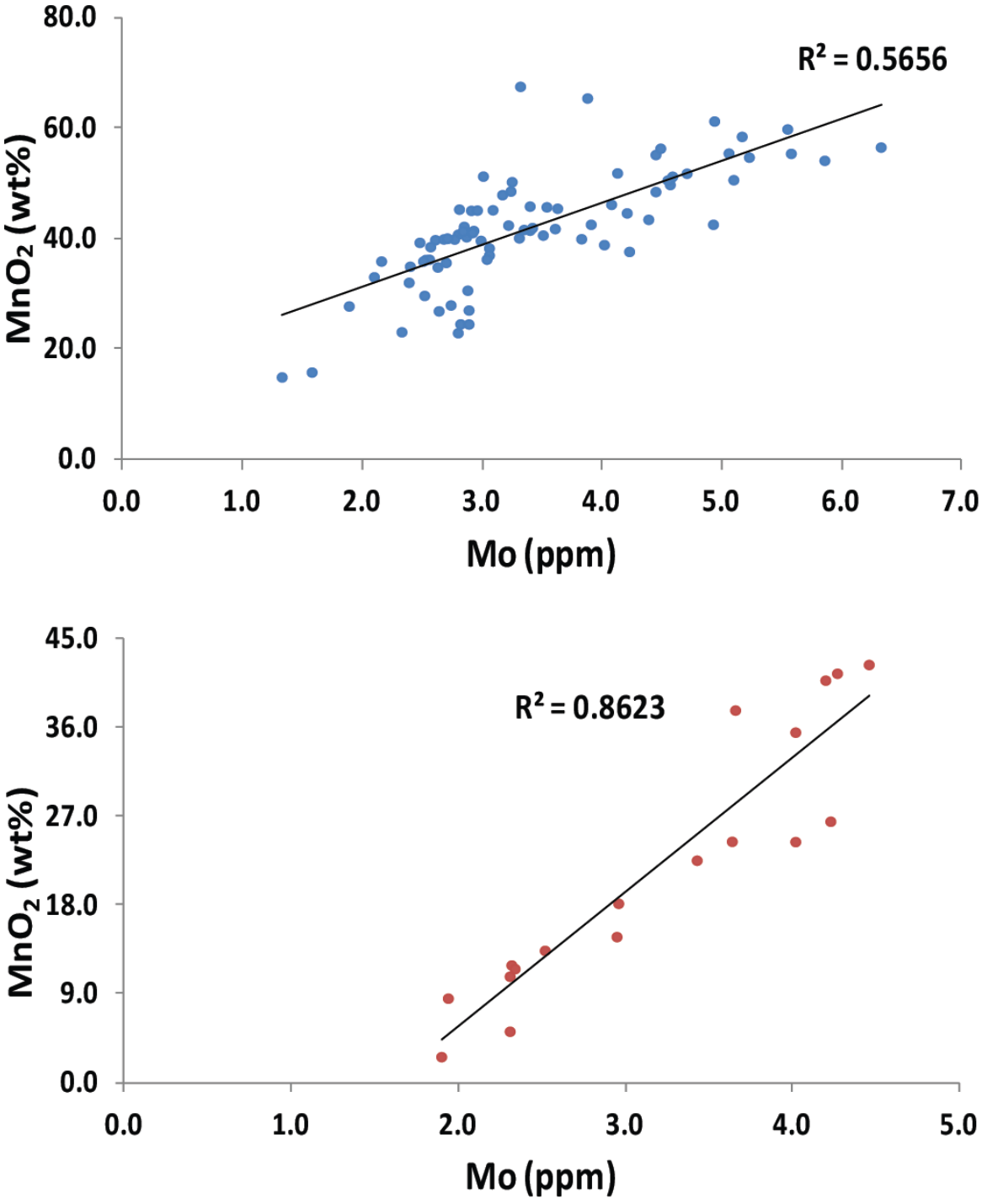

Figure 40: Bulk-rock Mo versus MnO_2 corresponding binary plots for Manganese ore ($M_{O.Z}$) and lower transition (T_1) zones from drill core G774. (Manganese ore zone [$M_{O.Z}$] – Blue markers. Lower Transition zone [T_1] – Red markers).

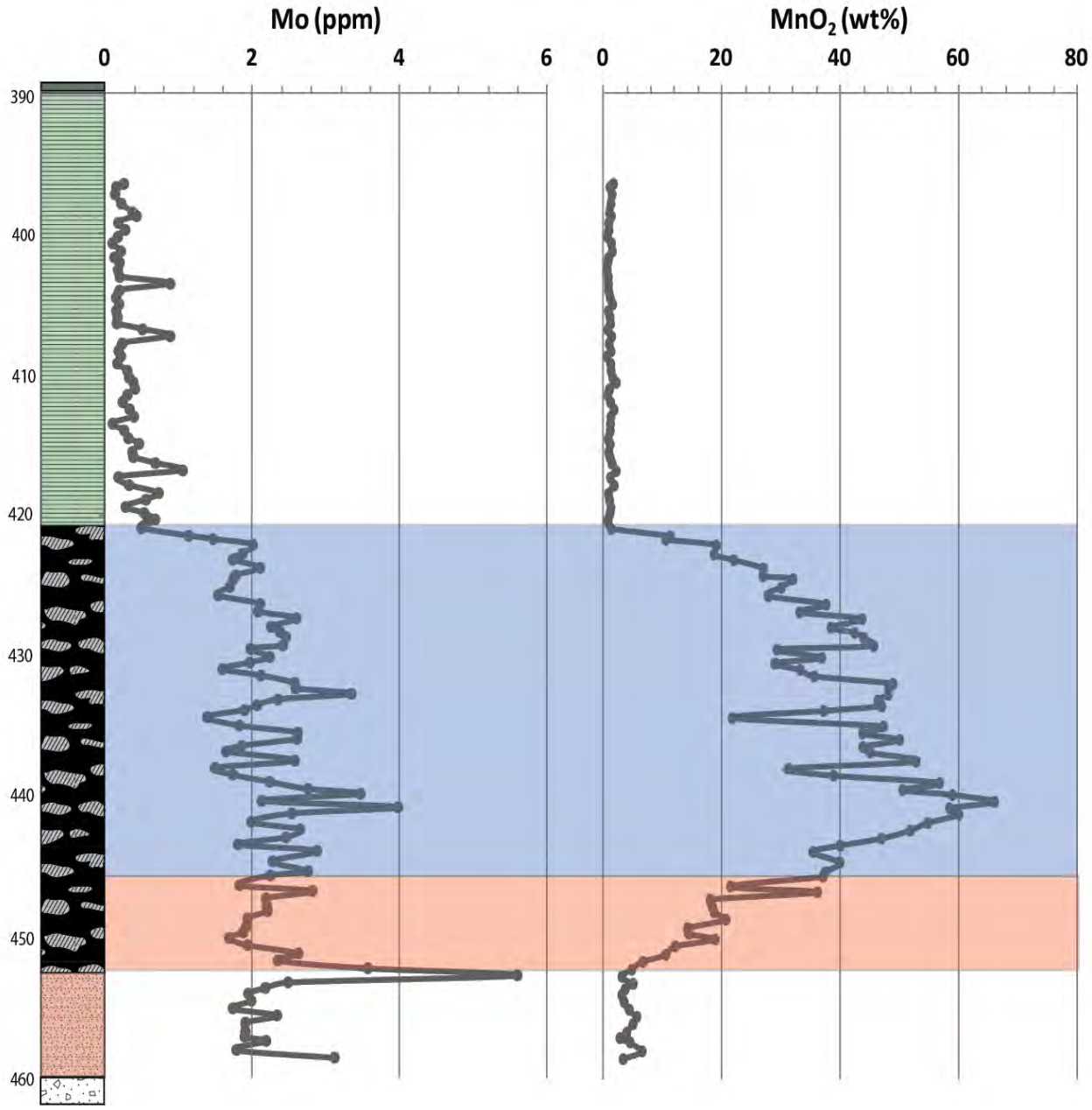

Figure 41: High-resolution chemostratigraphic relationship between Mo and MnO_2, with corresponding binary plots of bulk-rock Mo versus MnO_2 from drill core MP-56.

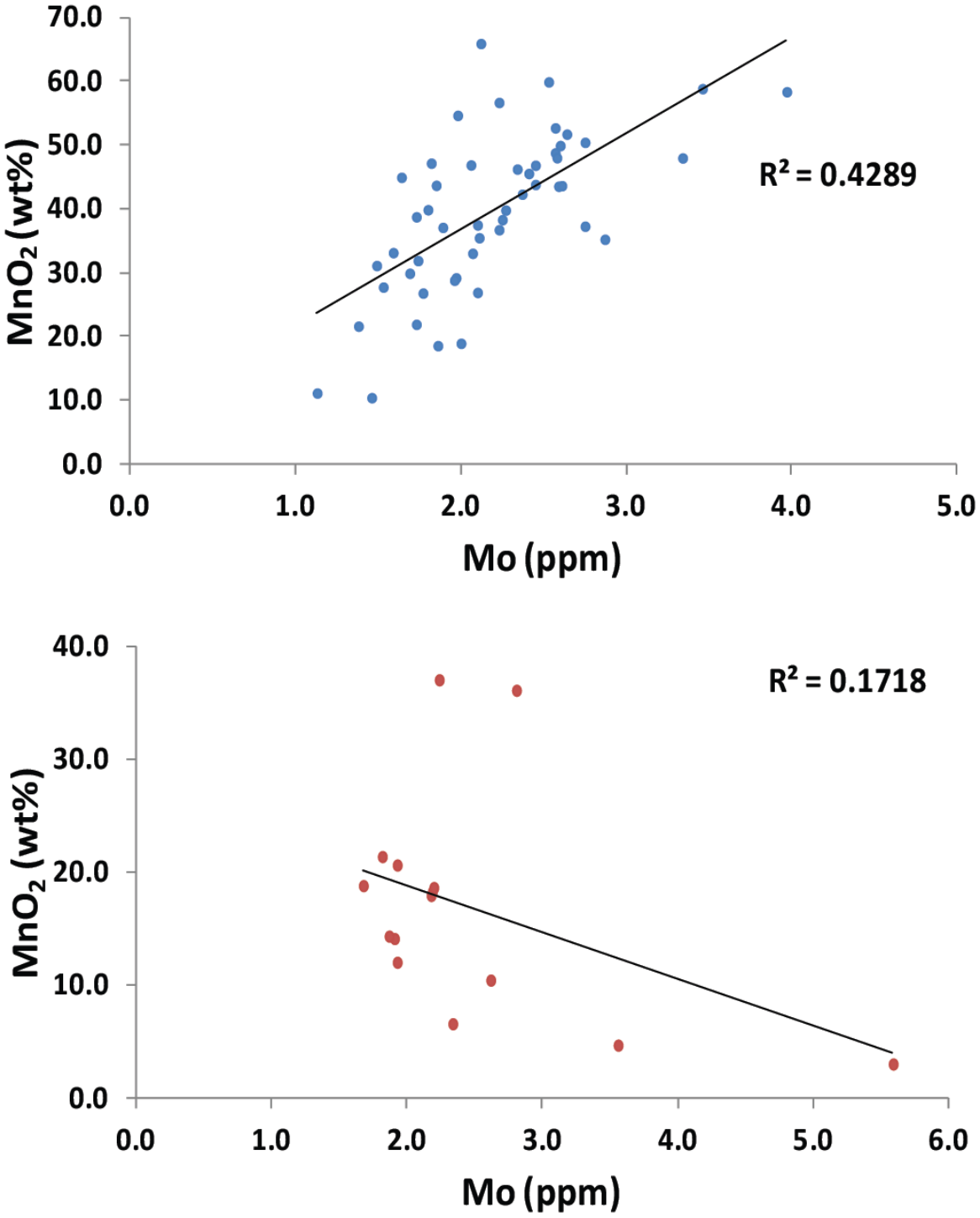

Figure 42: Bulk-rock Mo versus MnO_2 corresponding binary plots for Manganese ore ($M_{O.Z}$) and lower transition (T_1) zones from drill core MP-56. (Manganese ore zone [$M_{O.Z}$] – Blue markers. Lower Transition zone [T_1] – Red markers).

3.3 ΣREE versus iron

In the previous chapter, the REE results for all samples analysed for the two sections (Mamatwan and Middelplaats) were plotted as classic spidergrams normalised against average shale (PAAS). The spidergrams showed a generally very similar behaviour for the REE, which suggests that they all probably share a similar origin. The main difference observed was that the BIF samples appeared to contain relatively larger abundances for REE, relative to the abundances in the statigraphically lower lithologies (Mn layer and hematite lutite). Otherwise, the great majority of samples showed very similar positive-sloping patterns, consistent La positive anomalies and/or Ce negative anomalies, and variable Eu behaviour. On this basis, the REE have been summed (ΣREE) and have been plotted (in total ppm) stratigraphically against the total iron oxide content, in order to assess their behaviour in a holistic way (Figures 43 and 44).

Both chemostratigraphic profiles can be subdivided into two sub-sections, namely the BIF and the underlying hematite lutite and Mn-rich layer together. The BIF sections show very spikey behaviour in the ΣREE, with values generally in the 1-2 ppm range but with occasional spikes that reach as high as 5-6 ppm. In the rest of the stratigraphy at both sites, the ΣREE profiles look much smoother and with similar pattern of change across the stratigraphy, beginning with the relatively highest values at the base of the stratigraphy (2-3 ppm) and then gradually dropping to the lowest levels (1-2 ppm) in the high-Mn layer at both localities. The additional feature in the chemostratigraphy of the ΣREE is that from a visual point of view, the values appear to track to a great extent how the bulk Fe oxide values are changing. However, when this relationship is assessed in the form of binary diagrams for the basal hematite lutite, high-Mn layer and BIF, the statistical correlation is very poor in all cases (r^2-values of 0.2546, 0.2346 and 0.1029 at Mamatwan and 0.0716, 0.2592 and 0.002 at Middleplaats). Therefore, it cannot be said that the two chemical species statistically correlate in any convincing way.

The main conclusion that can be drawn is that there appears to be a control of total Fe on the REE, but this seems to be different between the hematite-rich and hematite-free (BIF) part of the stratigraphy. This difference may have to do in part with the very different iron speciation of the rocks, as the BIF contains the highest Fe(II) content and no hematite, while the rest of the sequence is dominated by Fe(III) in hematite. It is known that the REE are predominantly trivalent elements, and therefore this may explain why the relationship of REE chemostratigraphy is so like the Fe one in the hematite profile. The spikey variability in the BIF may then be due to the variability in the ratio of Fe(II) to Fe(III) in the rocks, which is dependent on the relative abundance of magnetite as the Fe(III) carrier against the other Fe minerals (carbonates and silicates) in which Fe is mainly Fe(II) and thus makes them poor REE hosts.

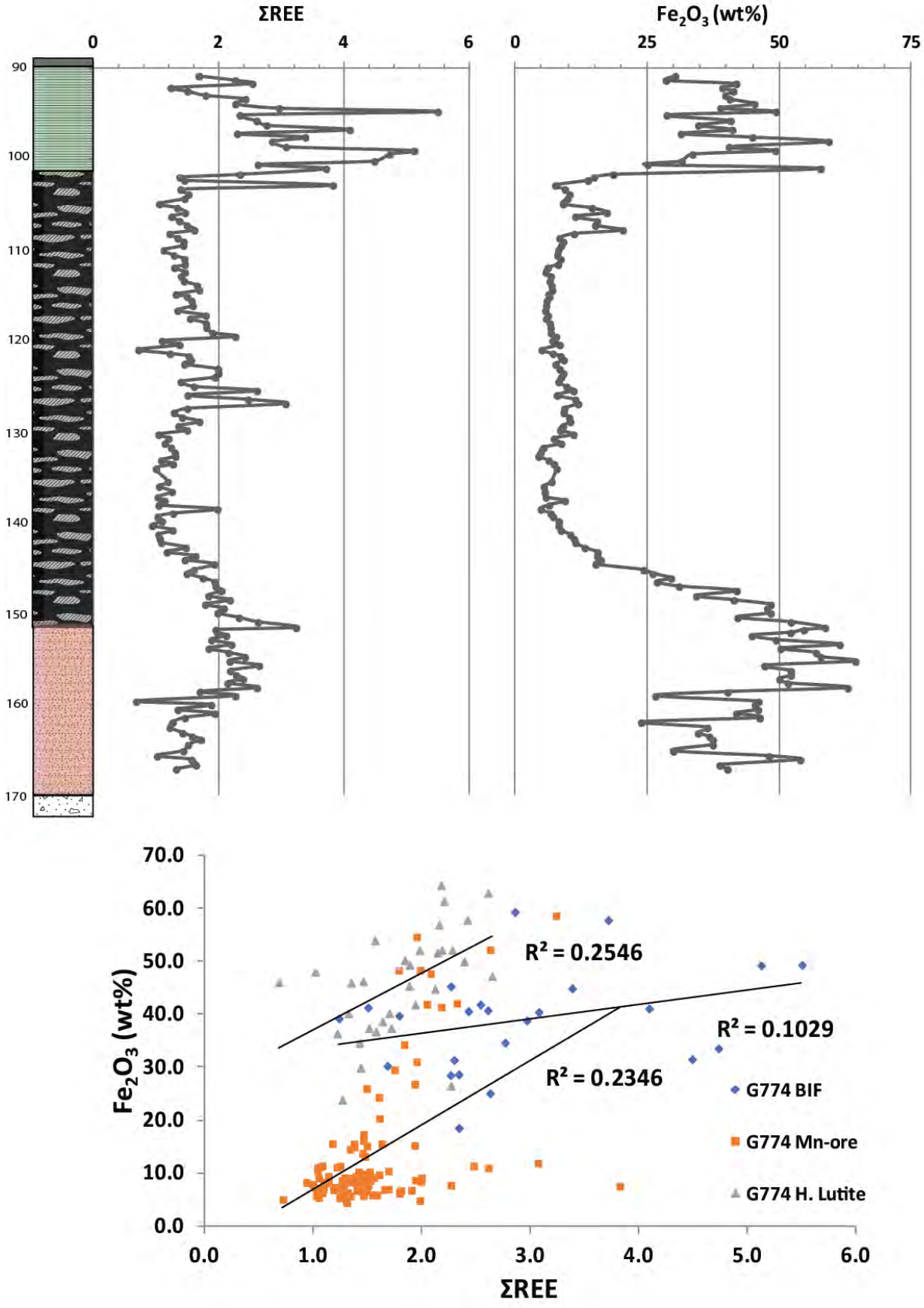

Figure 43: High-resolution chemostratigraphic relationship between ΣREE (as ppm) versus Fe_2O_3, with corresponding binary plots of bulk-rock ΣREE versus Fe_2O_3 from drill core G774.

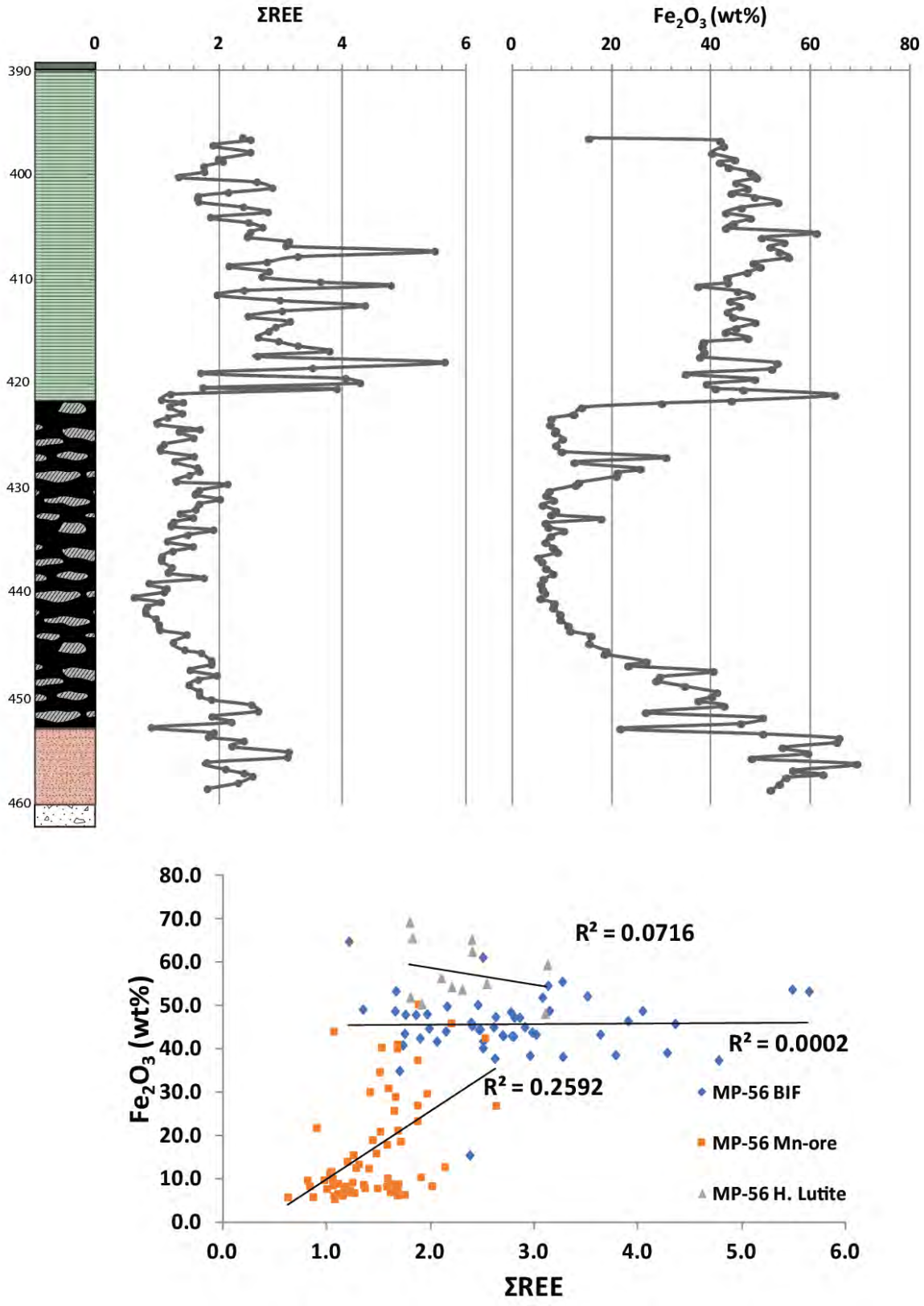

Figure 44: High-resolution chemostratigraphic relationship between ΣREE (as ppm) versus Fe_2O_3, with corresponding binary plots of bulk-rock ΣREE versus Fe_2O_3 from drill core MP-56.

3.4 Geochemical associations of "detrital character"

The element zirconium (Zr) is a High-Field Strength Element (HFSE) which is almost synonymous with detrital contributions in sedimentary rocks (Oonk et al., 2017). It has therefore been used extensively in the literature as an index of detrital contributions in chemical and biochemical sedimentary rocks (e.g. carbonates, BIFs), and is expected to show a similar geochemical behaviour with other HFSE and associated elements of a usual detrital origin, such as Ti, Nb, Ta, Hf, Sc, but also REE+Y in many instances. Based on the chemostratigraphic patterns presented in the previous chapter, the elements that will be assessed below as possible indicators of detrital contribution to the Hotazel Formation are Nb, V, Sc and the ΣREE, with Zr used as the reference element to plot against (Figures 45,46). Simply speaking, positive and broadly linear relationships of each of those elements with Zr, would mean that they probably belong to the "detrital" group, along with Zr.

The results of the assessment of the detrital elements illustrates some interesting results, which are dependent on the sub-section of the stratigraphy considered. The best correlations between Zr and the chosen elements are recorded in the BIF sections. In the Mamatwan stratigraphic section specifically (Figure 45), the r^2-values between Zr and V, Nb and Sc are moderate to fair at 0.6302, 0.7664 and 0.7363, respectively. In the Middelplaats stratigraphic section (Figure 46), the corresponding r^2-values for the BIF are even stronger, standing at 0.8032, 0.7839 and 0.6922 respectively for Zr versus V, Nb and Sc. The relationship between Zr and the REE shows little to no significant statistical correlation in both sections.

The situation becomes more complicated when it comes to the other two subsections of the studied stratigraphy, namely the high-Mn layer and the hematite lutite. Unlike the BIF sections at the two localities, there is hardly any meaningful correlation between Zr and any of the chosen elements or element groups, and this applies especially to the Mamatwan profile (Fig. 45). In the Middelplaats profile, the corresponding relationships appear to be a bit better in terms of the very similar slope of the correlation coefficients, but the r^2 values are still very low (Figure 46).

It is difficult at this point to come up with an explanation that will explain convincingly the afore-mentioned relationships. It is possible that the BIF is the best and most consistent record of the detrital fraction in the form of the Zr, V, Nb and Sc abundances, but this does not seem to apply in the same way in the hematite and Mn-rich lithofacies. It is possible that some of these elements are also affected by local factors such as proximity to hydrothermal venting, as it was argued for the Mo behaviour earlier in this chapter. The REE, on the other hand, do not appear to be of a detrital origin but perhaps only partially so during primary deposition of the BIF parts of the Hotazel stratigraphy.

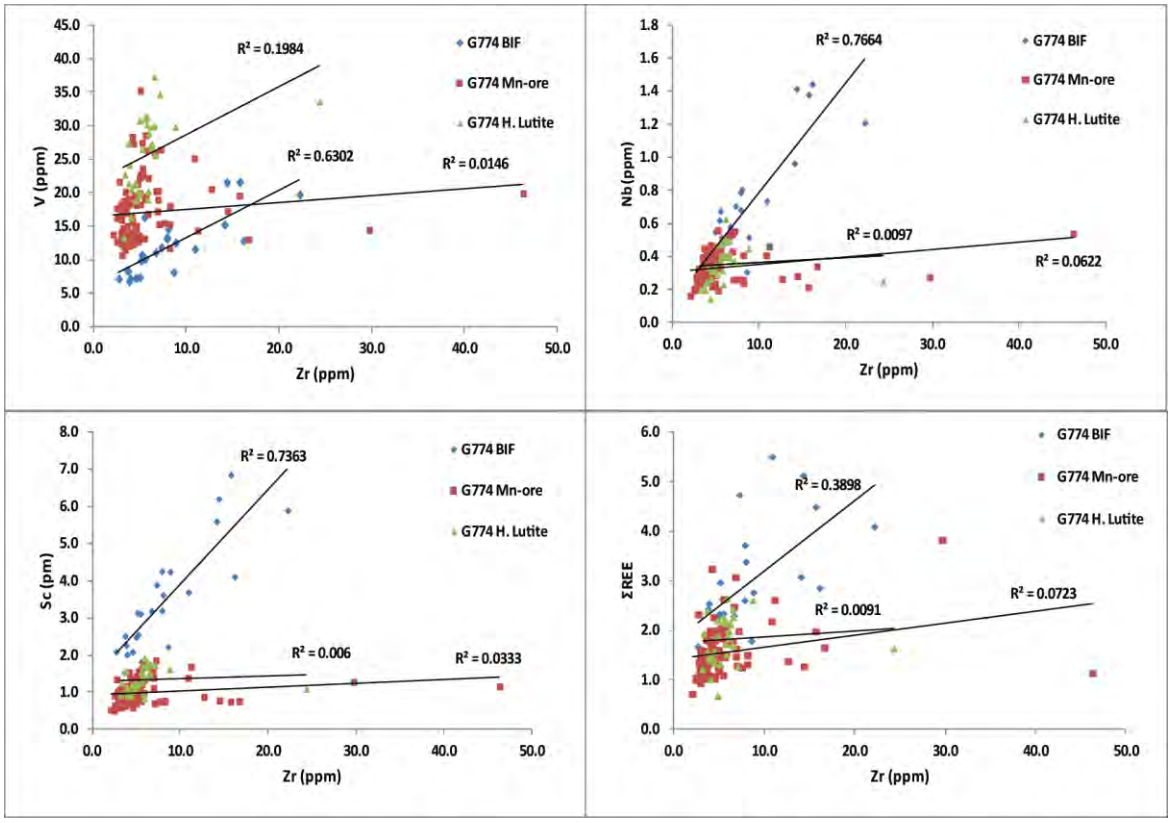

Figure 45: Bulk-rock trace metals (V, Nb, Sc and ΣREE) versus Zr for BIF, Mn ore and hematite lutite, from drill core G774.

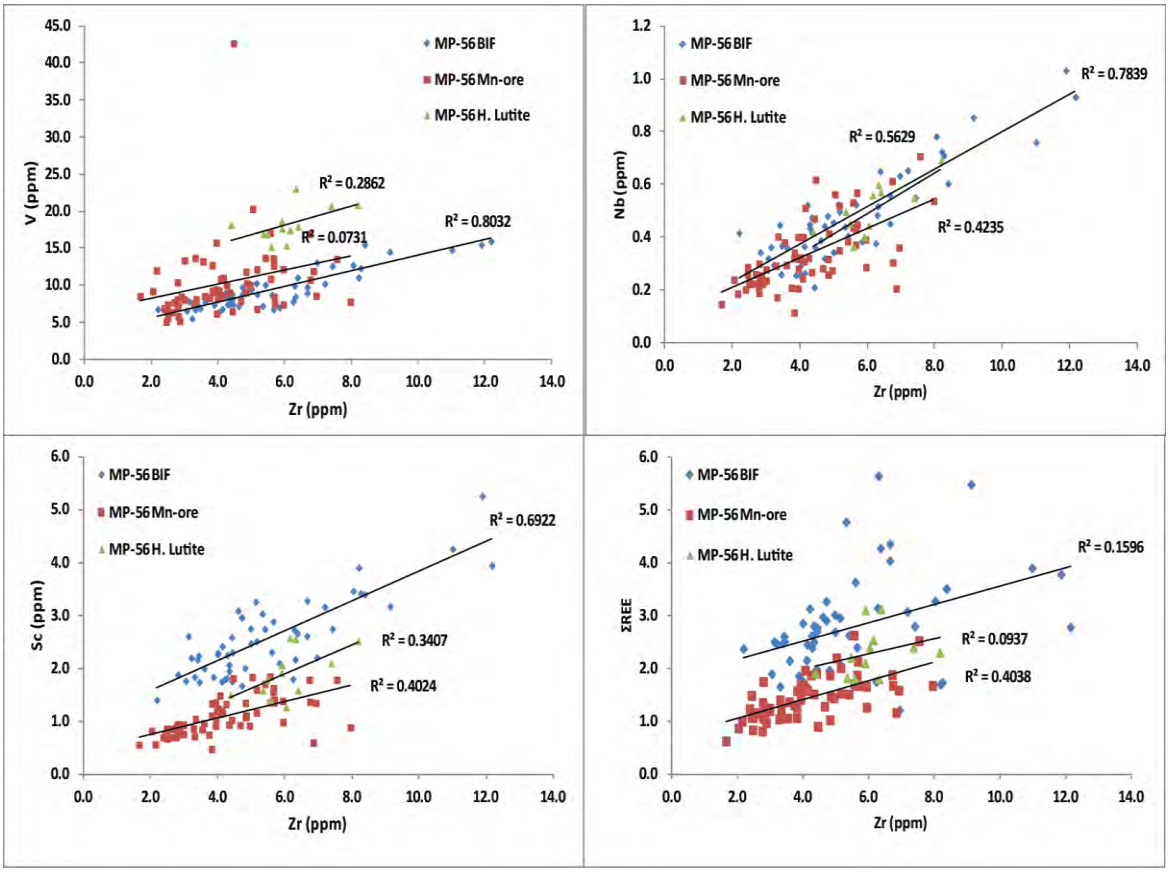

Figure 46: Bulk-rock trace elements (V, Nb, Sc and ΣREE) versus Zr for BIF, Mn ore and hematite lutite, from drill core MP-56.

3.5 Summary

The results of the evaluation of chemostratigraphic signals presented in this chapter can be summarised in the following bullet points:

- The Mn ore layer in both stratigraphies can be distinguished into a central zone characterised by low-Mg carbonate, and transition zones at its flanks that are Mg-rich. High Mg+Mn carbonate zones may also be seen in the basal hematite lutite sections.
- In both stratigraphic sections, the dominant carbonate species in the high Mn-layer appears to be calcite with evidently low Mn content. For that reason, bulk CaO concentrations in this layer show excellent antithetic relationship with bulk Mn content as the latter is exemplified chiefly by the abundance of the mineral braunite.
- The redox-sensitive element Co appears to have an association with the bulk hematite fraction of the rock and shows characteristic maxima in those parts of the section that also show the high MgO spikes. By contrast, the Co concentration in the BIF sections is the lowest. The sum of REE also appears to show a direct association with the bulk Fe fraction of the rocks, with maximum and more erratic values in the BIF where the Fe(II) content is also at a maximum.
- The redox-sensitive element Mo appears to show an excellent correlation with bulk Mn (braunite) content. However, that relationship may be more convincing in one section (Mamatwan) relative to another (Middelplaats), suggesting possible local controls in Mo behaviour in the paleobasin of deposition.
- The carbonate-carbon isotope record for both stratigraphic sections is remarkably smooth and shows a good relationship with fluctuating Ca contents in the rocks, whereby the higher the Ca content (calcite fraction) the higher the $\delta^{13}C$ value.
- The distribution and correlation of elements such as V, Nb and Sc with Zr, suggests that they have a common detrital origin. This is, however, more convincing in the BIF parts of the stratigraphy and less so in the rest of the studied sections, for reasons that may again have to do with local factors in the paleobasin during Mn and Fe(III) deposition.

4. Discussion

4.1 Introduction

In this chapter, the geochemical results and chemostratigraphic signatures that were presented and evaluated in the previous two chapters, will be discussed and interpreted. The structure that will be followed, will deal with the following aspects:

- Constraints on sedimentation rates from the behaviour of the siliciclastic sedimentary fraction of the rocks as this was recognised in the earlier chapters;
- Constraints on the redox behaviour of selected geochemical proxies, and the implications that these elements have in reconstructing the primary redox environment of the Hotazel depositional basin.
- Constraints of the styles and controls of sedimentary patterns on a lateral scale, as these can be gleaned from stratigraphic correlation across the two selected sections from Middelplaats and Mamatwan; and finally,
- Compilation of the findings in a conceptual genetic model for the deposition of the Hotazel strata, following first a review of classic genetic models for BIF and Mn available in the literature.

4.2 Sedimentation rate considerations

As mentioned earlier, the detrital chemical species are classically represented by Al_2O_3, TiO_2 and the trace elements that belong to the HFSE group (High Field Strength Elements, i.e., Zr, Hf, Y, Sc, Nb, U and Th). Such elements have long been used for the determination of either clastic or volcanic detrital inputs, as they are typically presumed to be bound almost exclusively to mineral particles of a common detrital/volcanic origin (Bau and Alexander, 2009). The Hotazel BIF, Mn-rich layer and transitional Hematite lutite lithofacies, preserve the contents of the aforementioned elements in very low and essentially negligible concentrations (see also Chapter 2). This is a feature which is very much consistent with the work of Tsikos and Moore (1997) and Tsikos et al. (2003), with specific respect to the Hotazel Formation. This, therefore, suggests that the Hotazel depositional environment must have received a quantitatively very low and insignificant input of a terrigenous detrital component during largely chemical deposition of the remaining sediment volume (Bau and Alexander, 2009; Sylvestre et al., 2017).

Nevertheless, the abundances of HFSE and particularly of the established proxies of detrital deposition as encapsulated in the elements Zr, Nb and Y, can still be utilised to provide some constraints on the relative, as opposed to absolute, precipitation rates of the major chemical species in the form of the abundant Fe and Mn in the Hotazel strata. The thinking behind such consideration is relatively simple: if the influx of these chemical species was the same throughout the deposition of the three detrital proxies, then one could estimate the relative rates of chemical deposition of Fe versus Mn-rich sediment from the relative difference in the average abundances of the detrital proxies across the two sub-facies. In other words, the lower the relative abundance of the "detritals", the higher the relative rate of the chemical sediment that contains them.

Figure 47 below exhibits the results of such considerations: for both studied stratigraphic sections, it shows the comparative abundance in the concentrations of the three selected HFSEs (Zr, Y and Nb) in the BIF zone, relative to those in the Mn-rich zone. The latter, for convenience, binds together the Mn rich layer and underlying hematite lutite, as they both look as though they behave similarly with each-other. In terms of the average values in the data populations shown, in the Mamatwan BIF section (Figure 47A) bulk average concentration values are 8.2±5 ppm for Zr, 10.4±3 ppm for Y and 0.7±0.4 ppm for Nb, while for the Mn-rich interval, the corresponding values are 5.5±5.4 ppm for Zr, 5.5±2.2 ppm for Y, and 0.3±0.1 ppm for Nb. In an analogous consideration, the Middelplaats BIF section (Figure 47B) bulk average concentration values are at 5.5±2.2 ppm for Zr, 12.9±5 ppm for Y, and 0.5±0.1 ppm for Nb, while the Mn-rich interval has corresponding bulk average concentrations at 4.2±1.5 ppm for Zr, 5.1±1.6 ppm for Y, and 0.3±0.1 ppm for Nb.

The above results must be interpreted with a fair degree of caution, because they have high deviations and are dependent on several assumptions in order to yield very robust results. Firstly, they depend on the corresponding Fe and Mn facies from each locality to have identical precipitation rates, which assumes that these facies would be identical mineralogically and geochemically across the basin, which is certainly not the case. It also assumes that the detrital proxies chosen had a steady influx rate to the basin, are only detrital in origin (which may also not be the case) and have the same geographical source. It is also not certain how the sinking rates of each one of these three elements may have been affected by the relative rates of formation and absorption capacities from one part of the basin to another, of the chief primary mineral phases that formed chemically in the basin (mainly Fe- and/or Mn oxides). The behaviour of the REE for example, showed that they behave very similarly with hematite Fe in the Mn-rich layers, and perhaps the Y behaved very similarly during high Mn deposition too.

In spite of all of the aforementioned uncertainties, it is clear that the relative abundance of the three HFSE proxies is approximately 1.5 to 2 times as high in the BIF part of the stratigraphy relative to the Mn

part, and this seems to apply in both localities studied. One can therefore cautiously argue that the Mn-enriched fraction of the sediment must have been deposited at approximately 1.5 to twice the rate that the BIF sediment was originally deposited.

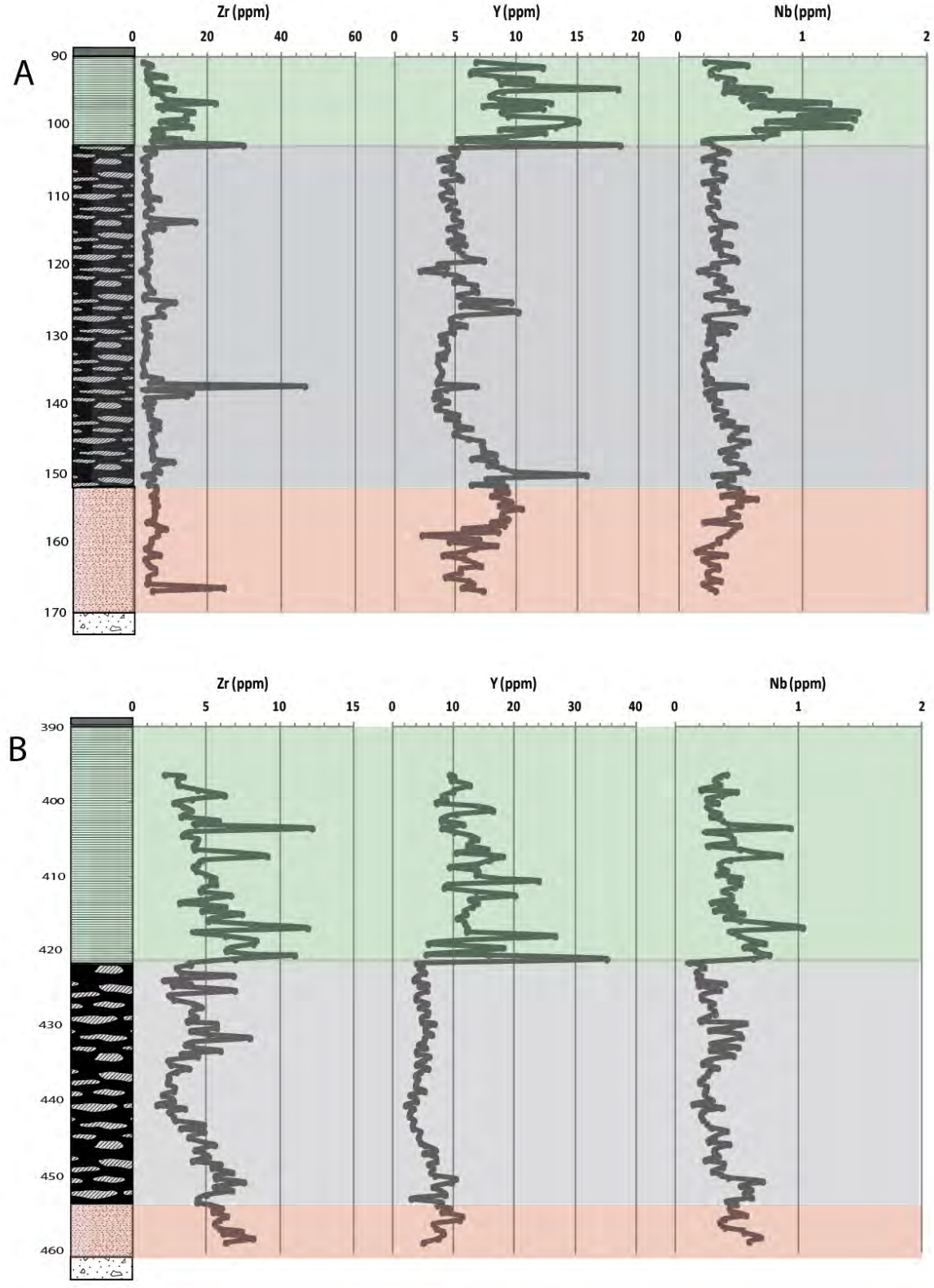

Figure 47: High-resolution bulk-rock HFSE (Zr, Y and Nb) chemostratigraphic relationships from drill cores A) G774 and B) MP-56.

The aforementioned considerations have profound implications for lateral stratigraphic correlation. They suggest that for every meter of BIF sediment deposited in the primary basin, an equivalent of 1.5 to 2 m of Mn-rich sediment was being deposited. It also suggests that the antithetic thickness relationships seen between Mamatwan and Middelplaats must indeed have required, at least for some time, simultaneous deposition of Mn at the one locality while at the other, BIF was being deposited at the same time. The significance of these obesrvations will also be visited again a bit later when the chemostratigraphic correlations and paleoenvironment of deposition will also be discussed.

4.3 Redox considerations

Chemostratigraphic patterns and variations in the concentrations of trace metallic elements preserved in ancient chemical sediments have long been known to aid as geochemical proxies for significant changes in atmospheric and oceanic redox conditions across geological time (Anbar, 2008; Konhauser et al., 2009; Swanner et al., 2014). The abundance of the redox-sensitive elements Co and Mo, to name a few, are examples of such elements with valuable attributes of providing important insights into paleoenvironments of primary chemical deposition (Bau and Moller, 1993; Elderfield, 1988; Piepgras and Jacobsen, 1992).

The behaviour of Co across the hematite lutite and Mn-rich chemosedimentary units of the Hotazel stratigraphic sections studied here (as seen in Chapter 2; Figure 16) display a very characteristic pattern; namely, highest Co concentration attained at the hematite transition zones, and a rather low and almost invariant concentration within the core of the main ore-body. The aforementioned pattern is also mimicked, to an extent, by the MgO component of the same samples, whereby its concentrations are very low within the BIF interval while they peak locally in the basal hematite lutite zone at Mamatwan, as well as in the hematitic flanks of the Mn-ore zone. The core of the Mn-rich layer, by contrast, attains relatively low and invariant MgO concentrations (Figure 48).

In the absence of detailed mineralogical study, it could be cautiously argued that Co has an association with a sedimentary subfacies rich in Mn-rich dolomite, particularly within the flanks of the Mn-rich zones. This association could be further taken to indicate an association of Co with high Mn. The correlation coefficients between Co and MgO at Mamatwan and Middelplaats (r^2-values 0.5627 and 0.5994 respecyively) are not the strongest (Figure 49 and 51), suggesting that the Co is probably not hosted in the dolomite. It may, however, be associated locally with the hematite that is abundant in the same dolomitic subfacies.

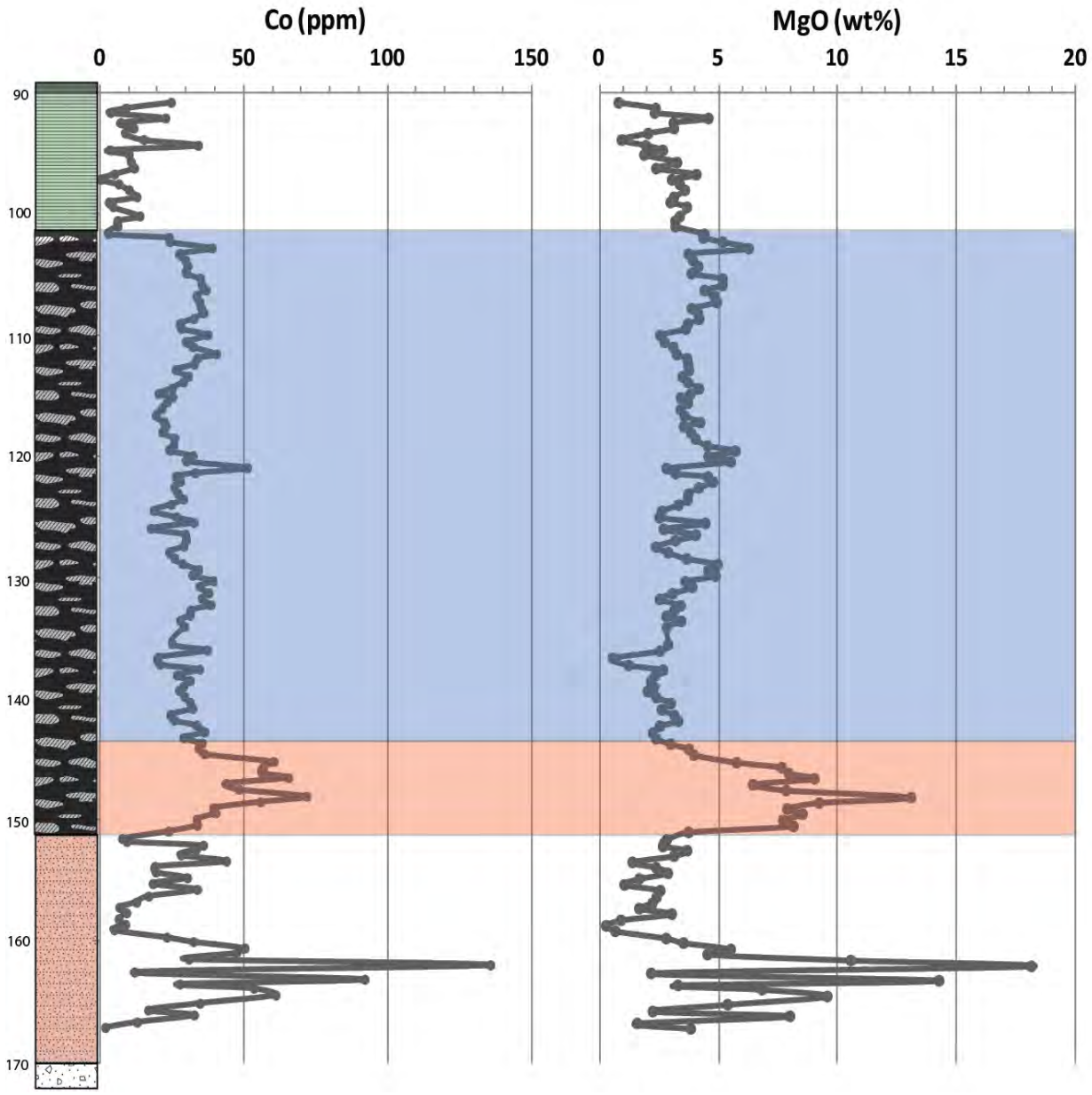

Figure 48: High-resolution chemostratigraphic relationship between Co and MgO from drill core G774.

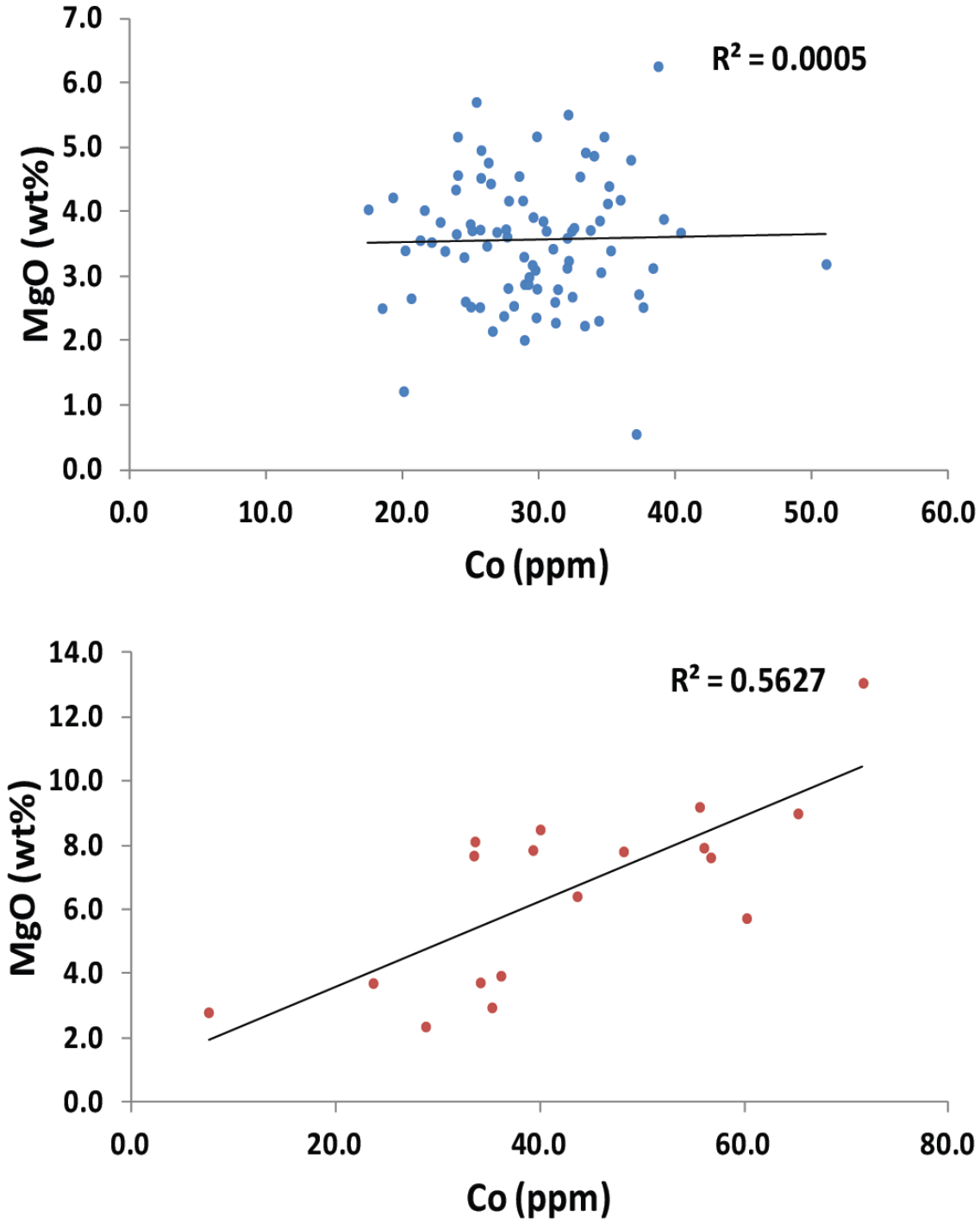

Figure 49: Bulk-rock Co versus MgO corresponding binary plots for Manganese ore ($M_{O.Z}$) and lower transition (T_1) zones from drill core G774.

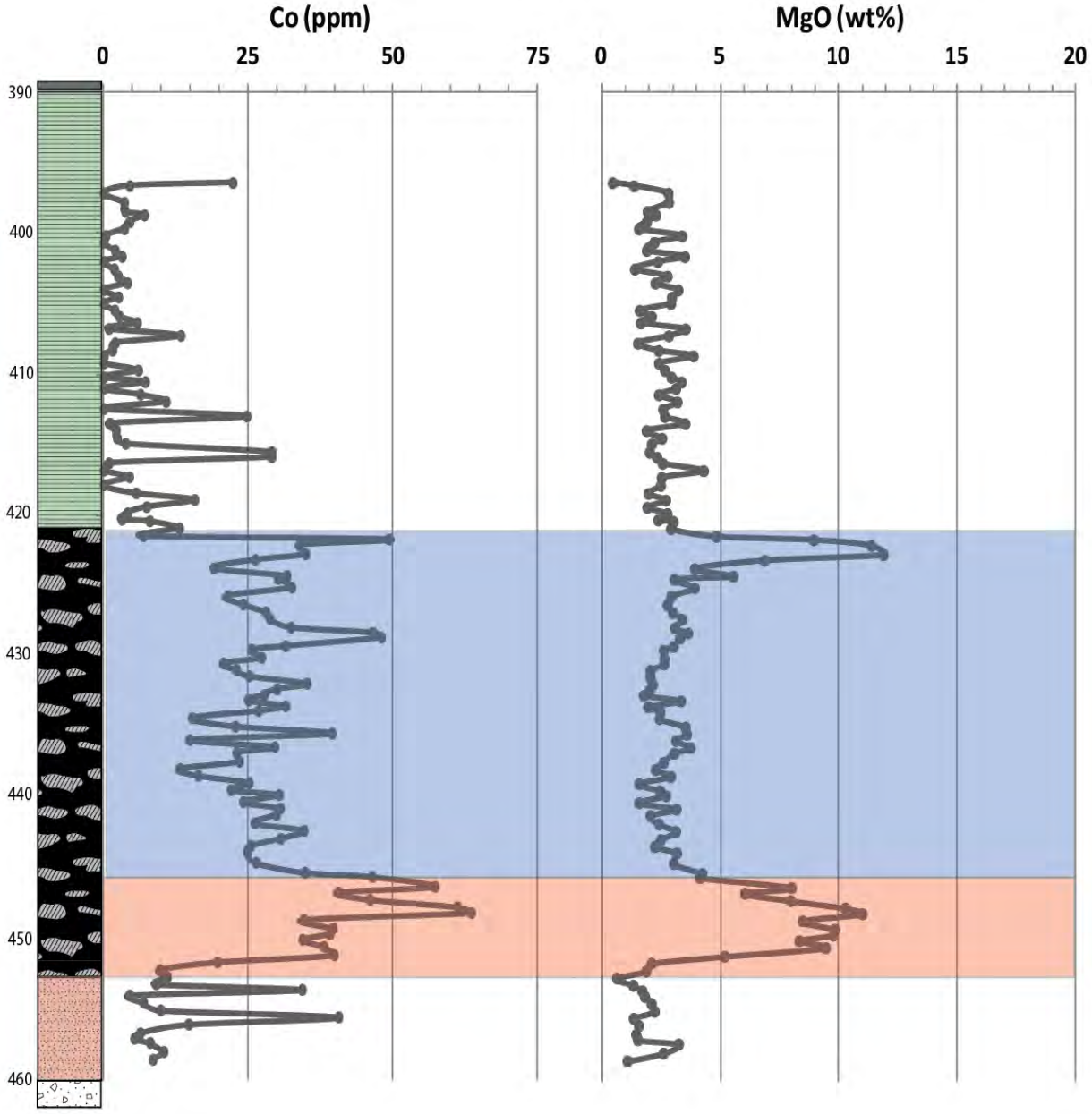

Figure 50: High-resolution chemostratigraphic relationship between Co and MgO from drill core MP-56.

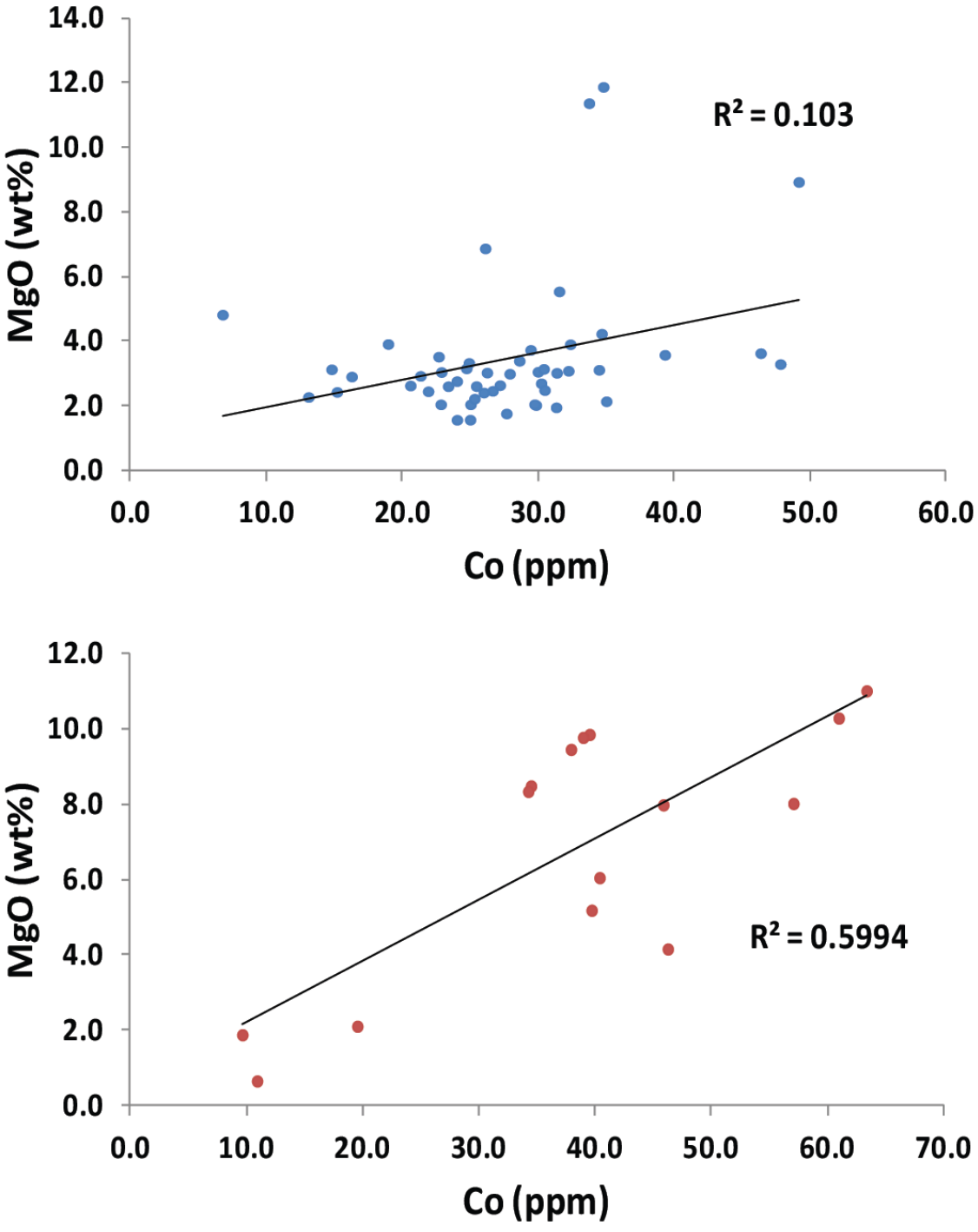

Figure 51: Bulk-rock Co versus MgO corresponding binary plots for Manganese ore ($M_{O.Z}$) and lower transition (T_1) zones from drill core MP-56.

It has been reported in previous studies as far back as from the 70s (e.g., Murray and Dillard, 1979), that Co can be efficiently scavenged by Mn-oxide minerals, as it is also observed extensively in Mn nodules of the modern ocean (Maynard, 2010). Additionally, Jeffery et al., (1978) have also observed through correlation analyses, high degrees of correlation between Co and Mn-oxide in soils and sediments, with correlation coefficients r^2 as high as 0.95. It is highly uncertain, however, whether the Co in the Hotazel rocks can be truly associated with the Mn fraction of the rock. If that was to be the case, then one would expect the high Mn zones to be the ones with the highest Co content, and that is definitely not the case. The other issue of course is that if Mn oxide was reduced during diagenesis and formed Mn-rich carbonates as in the case of the Mn dolomites above, it is not all that certain that Co would be able to be accommodated in the carbonate structure because of a different valence to Mn.

It becomes apparent, therefore, that Fe-oxyhydroxides, particularly ferric iron species, were an important carrier of Co in the Hotazel paleobasin. This controlling effect by ferric-iron species on cobalt has been highlighted by several authors, through effective scavenging of Co under oxic conditions through Co(II) and Co(III) adsorption on Fe(III) oxyhydroxides (Music et al. 1979; Koschinsky and Hein, 2003; Takahashi et al., 2007; Hrishceva and Scott, 2007; Swanner et al., 2014). It is therefore suggested here that the Co is associated with the hematite fraction of the rocks, but perhaps its partitioning was also affected somehow during periods when Mn-rich dolomite formation was favoured simultaneously.

The other key redox trace metal species in the Hotazel strata is Mo. Its abundance appears to be controlled, to a great degree, by the MnO_2 content of the rocks (as already seen in Chapter 3, Figure 40 and 42). The implication behind this concentration relationship between Mo and MnO_2 can be taken to point towards the likely absorption of Mo to Mn-oxyhdroxides in the water column, thus providing evidence that the abundance of Mn-oxide must have acted as a significant Mo sink. This is also fully compatible with experimental investigations of Barling and Anbar (2003), wherein it was found that the adsorption of Mo to Mn-oxyhydroxides is an important attribute in the fractionation of Mo isotopes in oceanic settings. This relationship is not necessarily compatible with other studies, however, (e.g. Planavsky et al. 2014), and particularly speciation studies on BIF, which have shown that Mo and Mn abundances are not necessarily related in terms of their speciation behaviour (Oonk et al., 2017). Rocks such as BIF however are not Mn rich, and the Hotazel BIF is likewise not a great host of Mo as shown earlier. By contrast, the Mn-rich intervals of the Hotazel seem to be better carriers of this metal.

It is therefore more likely that the Mo behaved differently from Co and was associated more with the Mn-rich fraction of the Hotazel sediments and not with Fe(III). This is important for possible use of the isotopes of Mo as a redox proxy for the Hotazel in future studies. It remains curious, however, why the correlation between Mo and MnO_2 appears so strong at Mamatwan, but not so much at Middelplaats.

4.4 Chemostratigraphic considerations

The aforementioned discussion on redox elements brings forward another important use of the chemostratigraphic data as produced in this thesis, which is that of lateral correlation. The interpreted relationship between Co, hematite and Mg-Mn dolomite that was discussed in the previous section, suggests that any excursions in chemical components such as the above, in the form of positive or negative spikes, may be laterally correlatable and reflective of redox processes operating in the primary basin simultaneously. The diagrams of Figures 52 and 53 below display an attempt of lateral correlation on the basis of two of the above associated components, namely MgO and Co.

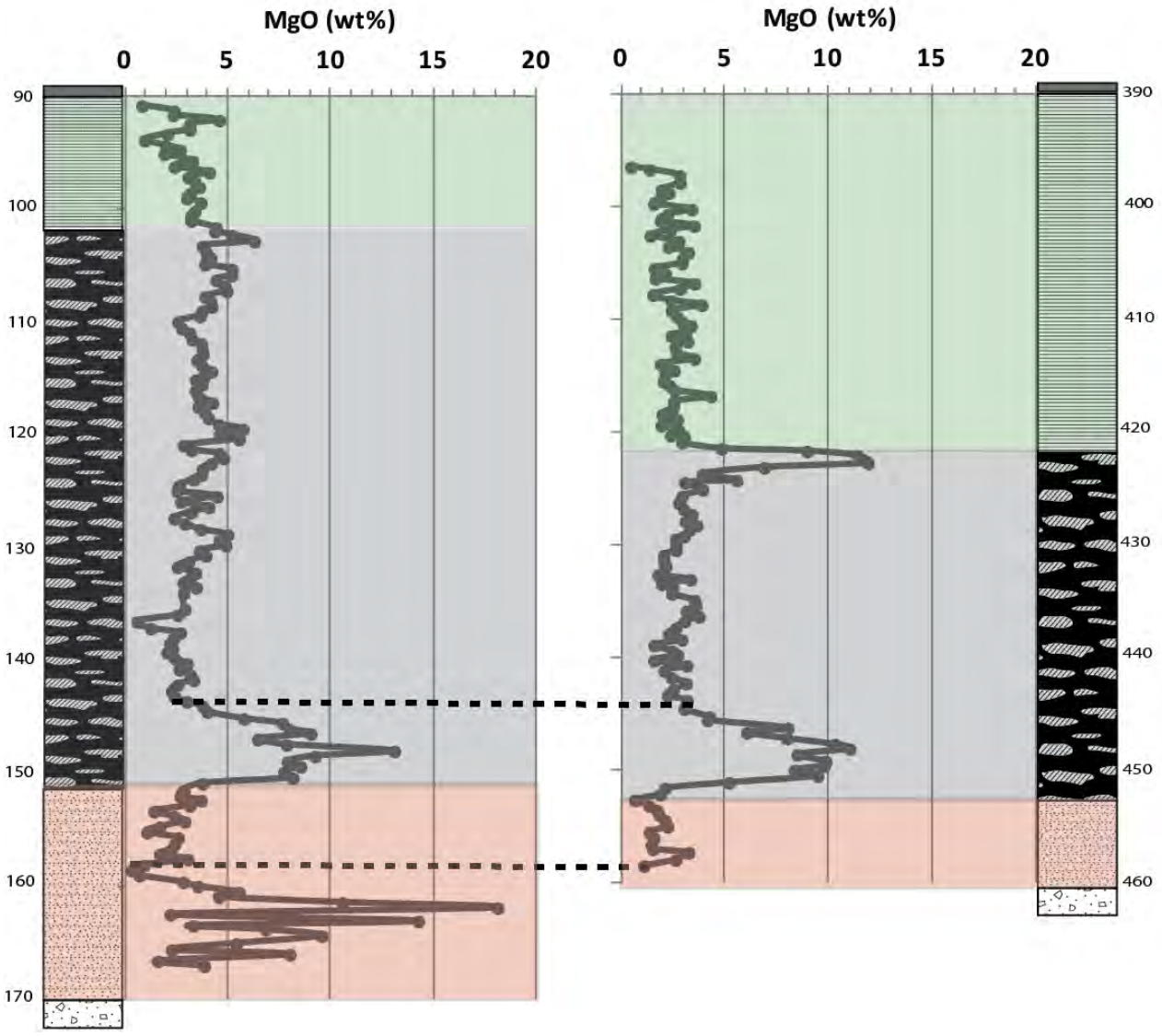

Figure 52: High-resolution MgO chemostratigraphic correlation between Mamatwan (i.e., drill core G774) and Middleplaats (i.e., drill core MP-56) sequences.

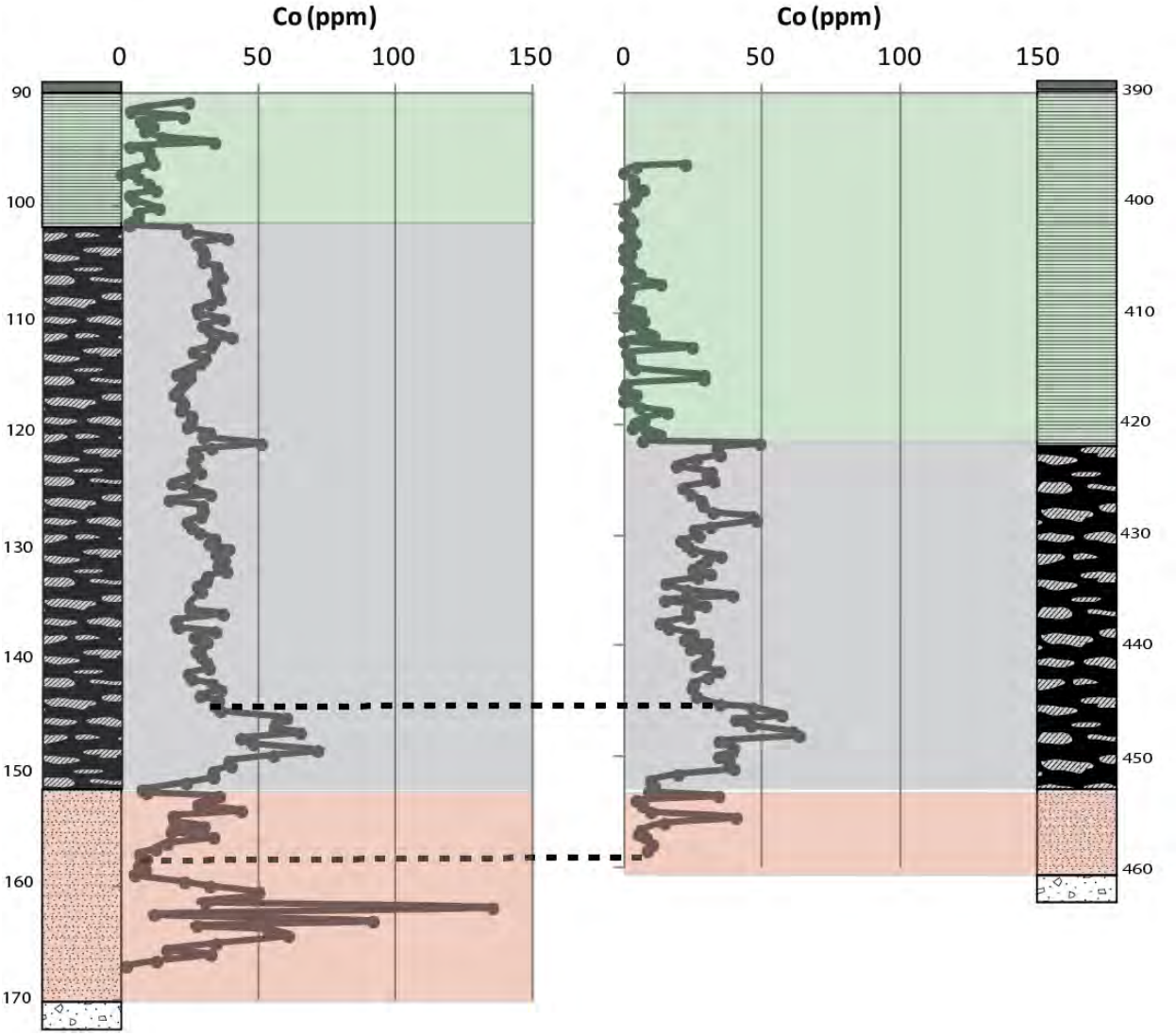

Figure 53: High-resolution Co chemostratigraphic correlation between Mamatwan (i.e., drill core G774) and Middleplaats (i.e., drill core MP-56) sequences.

The spikes in MgO and Co that are illustrated in the above diagrams, have been correlated using dotted lines to indicate the similarity in the way they develop, but also because some of them appear to occur at the same stratigraphic level, which is at the bottom flank of the Mn-rich layer. At the same time, there is a MgO spike at the top flank of the Mn-rich layer at Middelplaats but at Mamatwa it is not seen at the corresponding stratigraphic level. In an opposite way, the hematite lutite zone at Mamatwan records a huge spike in Co and MgO at its base, but a similar spike is not recorded at Middelplaats.

There can be several reasons why the above features happen the way described above. As it was also mentioned in the previous chapters, a MgO spike at the top of the Mn-rich layer at Mamatwan may not be seen because it may develop between two samples and is therefore very thin and was missed by the

sampling resolution. The spike at the base of the Mamatwan hematite lutite may be there because that section developed only at Mamatwan and not at Middelplaats where the hematite lutite is a lot thinner (Figures 52). Whatever is the explanation, the important point that needs to be made in this section, is that the geochemical spikes that occur in the Hotazel strata and which appear to be related to primary redox processes, are not necessarily recorded in every case in the basin and are also not necessarily simultaneous in their occurrence. This relates to what was mentioned earlier in this chapter in light of the detrital HFSE elements, namely that there must have been deposition of different facies of sediment happening in the basin simultaneously. This feature will be investigatred a bit further in the next section using another important chemostratigraphic tool, which is the carbonate carbon isotope data ($\delta^{13}C$).

4.4.1 Carbonate carbon isotope chemostratigraphy

Chemostratigraphy, as reviewed by Halverson et al. (2010), is the study of variations in the chemical compositions of sediments. The identified chemical signatures in such studies are usually proxies for the chemical nature of seawater, or environmental conditions shortly after the deposition of sediments (Halverson et al., 2010). Carbon isotope ratios, as typically represented by the $\delta^{13}C$ notation, are by far the most utilized proxies in exploring the paleo-environment, notably the ancient carbon cycle (e.g. Cerling, 1992; Brand, 2004; Canfield et al., 2020; Gröcke, 2020). Carbon isotope chemostratigraphy has been by far most instrumental – as will be seen in this section of this thesis – in correlating chemical signals on basinal to even global scales. In light of the highly heterogeneous Hotazel strata in terms of geochemistry and sedimentary facies, the $\delta^{13}C$ record of the Hotazel rocks is probably the only one in this thesis that can be used across the entire stratigraphy as a common denominator of correlation.

Figure 54 below illustrates the high-resolution carbonate carbon isotope compositions across the two studied stratigraphic sections at Mamatwan and Middelplaats. As also mentioned in the earlier chapters, these records vary considerably across the Hotazel sequence; relatively lighter $\delta^{13}C$ values are seen across the hematite lutite and BIF units, ranging respectively from -21.2 to -13.1 ‰ and from -18.4 to -11.4 ‰ at Mamatwan, and from -18.4 to -12.0 ‰ and -20.7 to -13.7 ‰ at Middleplaats. Generally heavier $\delta^{13}C$ values appear in the Mn-mineralized zone, ranging from -14.9 to -6.3 ‰ at Mamatwan and -16.8 to -6.2 ‰ at Middleplaats sequence.

It should be noted that the aforementioned isotopic values are consistent with carbonate isotopic data obtained and reported from Tsikos et al. (2003) for the Hotazel Formation, wherein BIF carbonate $\delta^{13}C$ ranges from -18 ‰ to -4 ‰, while the Mn-rich units attain $\delta^{13}C$ values ranging from -12 ‰ to -8 ‰. Additionally, the latter values seem to be comparable with the reports from Phanerozoic sedimentary

Mn deposits at Molango, Mexico, wherein $\delta^{13}C$ data for Mn carbonates (rhodochrosite) highlight very negative isotopic values ranging from -12.9 ‰ to -5.5 ‰ (Okita et al., 1988).

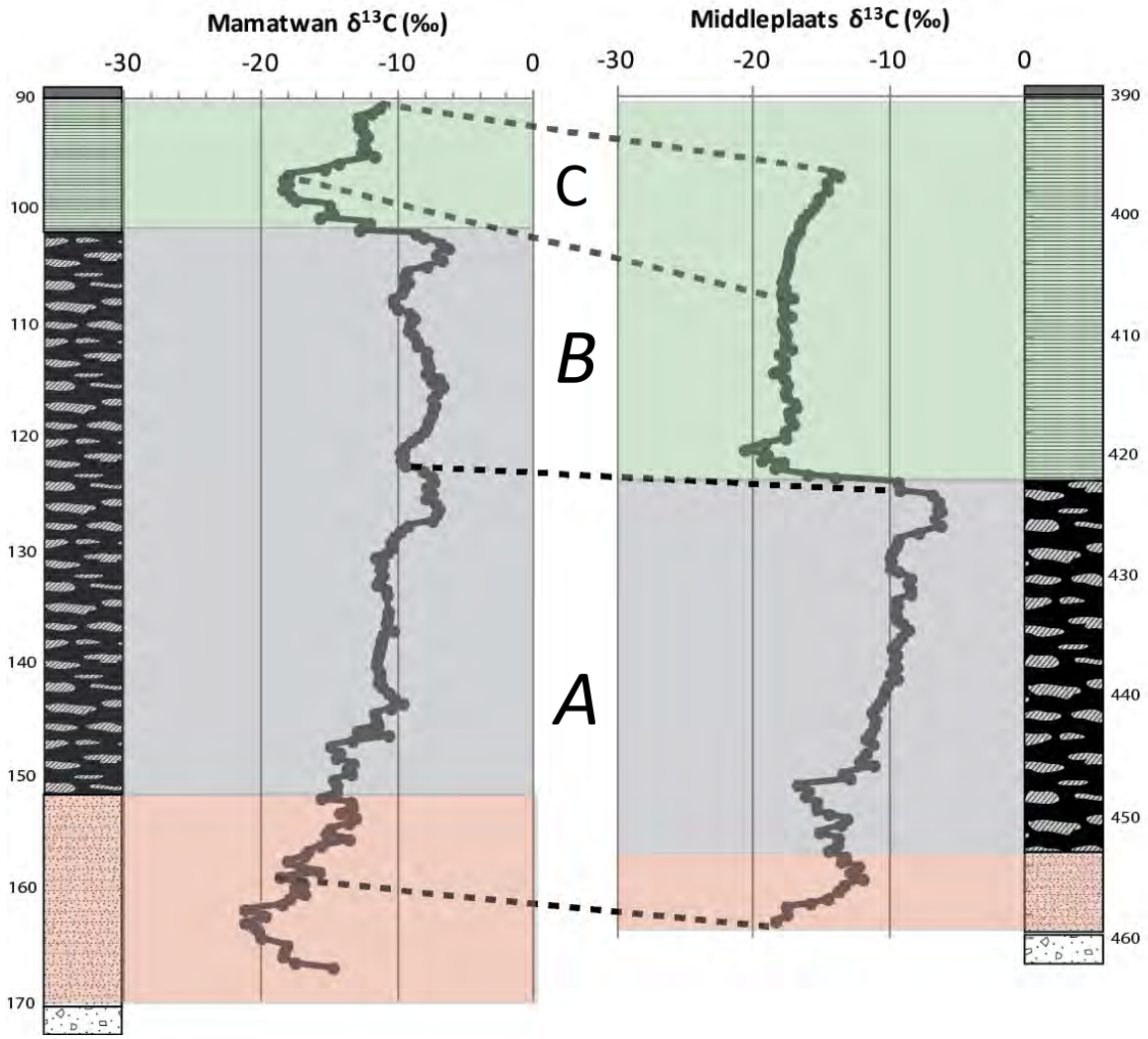

Figure 54: High-resolution $\delta^{13}C$ chemostratigraphic correlation between Mamatwan (i.e., drill core G774) and Middleplaats (i.e., drill core MP-56) sequences.

The negative $\delta^{13}C$ values measured in the Hotazel Fe- and Mn-rich lithofacies (i.e. hematite lutite, Mn-rich layer and BIF) are interpreted to reflect an input of organically derived carbon into primary carbonate formation of a marine $\delta^{13}C$ signature of about 0 ‰. It is expected that the $\delta^{13}C$ of the organic carbon would have ranged somewhere between the values of -20 ‰ to -30 ‰ (e.g., Hudson, 1977; Berger and Vincent, 1986; Tsikos et al., 2003, 2010). The values of the analysed samples and their stratigraphic variation would therefore reflect variable mixtures of the marine and organic carbon sources. This is a classic interpretation that has been proposed previously both for BIF (e.g., Tsikos and Moore 2003, Siahi et al., 2020) and for sedimentary Mn deposits associated with carbonate rocks and

interbedded black shales (Lovely and Phillips, 1988; Okita et al., 1988; Polgâri et al., 1991). Although the light carbonate minerals in the aforementioned BIF and Mn deposits are widely thought to suggest diagenetic processes of organic C incorporation into marine carbonate minerals (Siahi et al., 2020), the assumption that is made here is that these signals record overall primary processes of variable marine and organic carbon inputs.

The general stratigraphic pattern of the high-resolution carbon isotopic record of the Mamatwan chemostratigraphic profile reveals comparable features to that of the Middleplaats one. At the very base of the Mamatwan profile in the hematite lutite, there is a group of values that represent the hematite subzone recognised in Chapter 3 with its high MgO and Co spike. These values track a small declining trend in $\delta^{13}C$ which is not seen at Middelplaats (Figure 54). Above that, however, one can see a generally similar pattern in both sections, which seem to agree both in terms of the general behaviour of the data points and the absolute values in $\delta^{13}C$ (Figure 54, part A). Specifically, the values increase from as low as -18.6 to a highest value of -9.3 ‰ over the interval between 162 and 122 m in the Mamatwan profile, and this agrees reasonably well with the shape and $\delta^{13}C$ range of the corresponding Middleplaats section interval between 422 and 459 m, with $\delta^{13}C$ values from -18.4 to -8.2 ‰ (Figure 54).

Above part A, there is another section where the lithostratigraphies and the isotope signatures of the strata cannot be any more different (Figure 54, part B). In the Mamatwan stratigraphic section, the Mn-rich layer continues for approximately another 20 m with a broad plateau of $\delta^{13}C$ values which sit at around the value of -10 ‰, but with a small positive excursion of 1-1.5 ‰ in the middle part. Above that, there is a brief section of BIF of 3-4 m thickness with very low $\delta^{13}C$ values around -18 ‰, which compare very well with those of the lower section of Middelplaats BIF (Figure 54). In the latter section, once the Mn-rich layer terminates, the section of the -18 ‰ $\delta^{13}C$ BIF that follows is about 15 m thick. In other words, part B is represented almost entirely by a BIF section at Middelplaats with a plateau of very low isotopic values, while in Mamatwan evidently there must have been Mn-rich deposition going on with much higher $\delta^{13}C$, before a very low- $\delta^{13}C$ BIF precipitated over only a few m in thickness.

Finally, the top part of the stratigraphic profile (part C) is defined by a common feature that is recorded by both BIF sections, which is a progressive increase in the $\delta^{13}C$ values within that upper part. However, there is a major difference in the Mamatwan section which exhibits a rather sharp incline in $\delta^{13}C$ values from -18 ‰ to -11.4 ‰, characteristic of the stratigraphic depth interval between 96.7 m and 90.8 m. This brief interval is nonetheless cautiously correlated with the uppermost Middleplaats BIF section which also exhibits an incline towards higher $\delta^{13}C$ values (i.e., from -17.9 to -13.7 ‰), but in a much more gradual manner over the depth interval between 409.2 m and 396.5 m (Figure 54).

4.5 Genetic modelling

4.5.1 Review of Iron-formation depositional models

Several studies have highlighted a contention in biological and abiological BIF depositional models that has endured over many years. The contention largely revolves around the specific manner at which primary iron was deposited, as well as the source of iron and the environment in which iron deposition occured (i.e. restricted basins versus open ocean environment; e.g. Beukes, 1983; Konhauser et al., 2005; Bekker et. al., 2010; Konhauser et al., 2017). Iron sourced from deep-sea hydrothermal processes has been, by and large, the most widely accepted viewpoint, as the Eu abundance in BIF records indicates a strong association of high temperature hydrothermal fluids with seawater as the most likely realm in which these iron-rich chemical sediments precipitated (Klinkhammer et. al., 1983; Derry and Jacobsen 1990). Some earlier studies, however, have also pointed to a continental source, under the premise that continents were more mafic in composition than present and Fe(II) was more easily weathered under an oxygen-deprived atmosphere (Condie, 1993 and James, 1954). Despite the exact mechanisms involving iron formation deposition during the Precambrian, the most supported models, by far, include oxidation of iron (II) by cyanobacterial O_2, metabolic iron oxidation by anoxygenic bacteria, and ultraviolet photooxidation of iron (II) (Bekker et. al., 2010; Figure 55).

The first mechanism involves prokaryotic single-celled microorganisms (early cyanobacteria) that would have produced oxygen photosynthetically, which then oxidizes dissolved iron (II) and produces ferric oxyhydroxide which ultimately precipitates onto the sea floor as the main primary solid precursor mineral of Fe. The second mechanism, namely anaerobic iron oxidation, involves the formation of ferric ions by the intervention of iron (II) oxidizing bacteria, either through chemolithoautotrophic iron oxidation or by photoferrotrophic processes (Konhauser et. al., 2002, 2017). It is thought that under anaerobic conditions where there is an abundance of iron (II), light and CO_2, microbial Fe(II) oxidizers could significantly influence the marine iron cycle and, therefore, increase the rate of ferric iron precipitation.

Ecophysiological laboratory experiments combined with modelling have also demonstrated that iron (II) oxidizing bacteria have the potential to yield primary ferric iron deposited as BIF precursor sediment (Bekker et. al., 2010). UV photooxidation of iron (II), on the other hand, involves oxidation of ferrous iron in solution by high ultraviolet photons, ranging from 300 to 450 nm, that would have interacted with the Earth's system before the rise of atmospheric oxygen and before the development of the ozone layer (Bekker et. al., 2010).

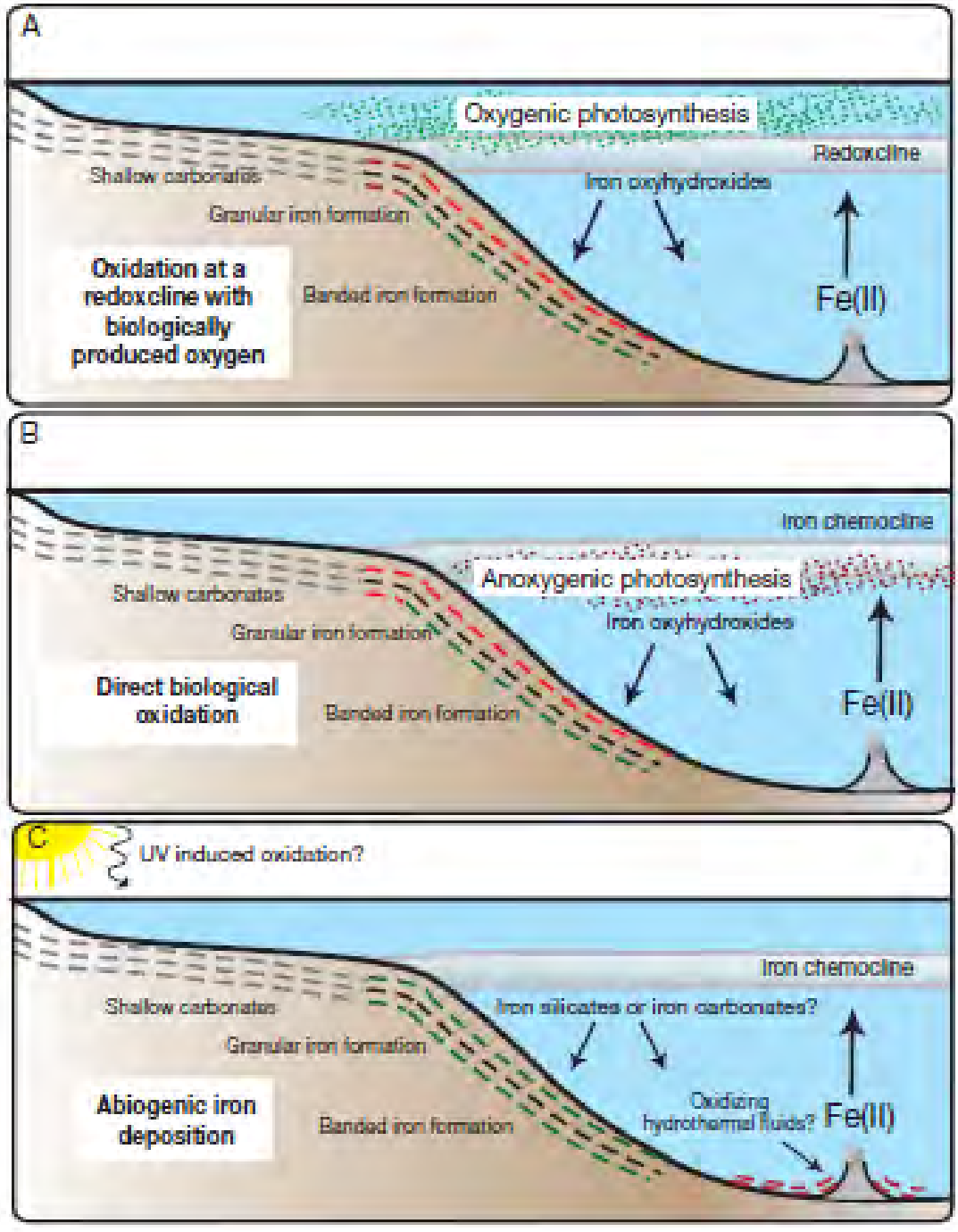

Figure 55: Simplified depositional models of the Archean and Paleoproterozoic iron formations, showing oxygen oases in shallow water environments (A), generated by oxygenic photosynthesis, responsible for ferrous iron oxidation. Anoxygenic photosynthesis (B) responsible for iron oxidation, and (C) photochemical oxidation of iron (Bekker et. al., 2010).

The subsequent production of iron oxyhydroxides, which precipitate in deep water setting, in an open marine environment, would lead to the development of a stratified water column, specifically a dynamic chemocline – which would develop between anoxic, iron-rich deep waters and euxinic shallow waters.

The dynamic chemocline would continue to be present until the hydrothermal iron and atmospheric and/or terrestrial sulphur inputs recedes, leading to a fully anoxic, unstratified ocean (Bekker et. al., 2010).

4.5.2 Review of manganese-rich depositional models

The deposition of manganese has covered much of geological history apart from the Archean when Mn deposition is sporadic at best. A peak in manganese deposition is observed in the Proterozoic and the Paleozoic and steadily increasing in the Phanerozoic to the present day (Roy, 1992). The earliest occurrence of marine sedimentary manganese deposits in the Paleoproterozoic is of paramount significance in Earth history, as it is directly linked to a period in time when the Earth's atmosphere and oceans changed from oxygen deficient to oxygen enriched conditions; an event famously referred to as the Great Oxidation Event (GOE) that occurred around 2.4 Ga (Chapter 1, Figure 2; Holland, 2002; Lyons et. al., 2014; Gumsley et. al., 2017). The Kalahari Manganese Field arguably represents the key candidate for that important period in geological time.

Earliest models for sedimentary manganese deposition implicate changes in sea-level and development of stratified basins playing major roles in the depositional proicess (Roy, 1992; Figure 56). In ancient water bodies, sea-level change would have been closely associated with the development of anoxic-oxic stratification. In instances where the sea-level would be high, the redox interface would get closer to the surface, while the anoxic part of the water body would have expanded to the sea floor. Subsequently, manganese precipitation above the redox interface would occur as the body of water transgressed the cratonic shelf. Essentially, manganese would advect towards the redox interface, inducing oxidation reactions in the parcel of water where conditions are more oxidizing, subsequently leading to precipitation upon crossing the redox-interface (Roy, 1992). Clearly, interplays of ocean chemistry, climate and sea level (tectonics) would have significantly influenced the formation of sedimentary manganese-rich sediments (Frakes and Bolton, 1992).

In terms of sources of manganese, just like with BIF and Fe, submarine volcanic activities and silicate weathering are thought to have been the key provenances. The deposits of manganese ultimately forming are thought to have accumulated as high-valence oxides of manganese following oxidation of soluble divalent manganese ions (Johnson et. al., 2016). Subsequently, reduction of the manganese(IV)-dominated oxyhydroxides to either Mn (III) or Mn (II) phases would have taken place during diagenetic processes involving reductants such as coprecipitated organic matter (Johnson et. al., 2016). In such instances, diagenetic manganese (II) phases would have precipitated as isotopically light manganese-bearing carbonates while manganese (III) phases would form mainly manganese-bearing oxides such as

braunite ($(Mn^{2+}Mn^{3+}{}_6\ SiO_{12}$; Johnson et. al., 2016). In simple words, there is a major redox cycle of manganese taking place during source to sink processes, involving primary mobility of Mn as Mn(II) from the initial source, oxidizing to Mn(IV) during precipitation, and converting back to reduced Mn(III) and Mn(II) upon diagenesis.

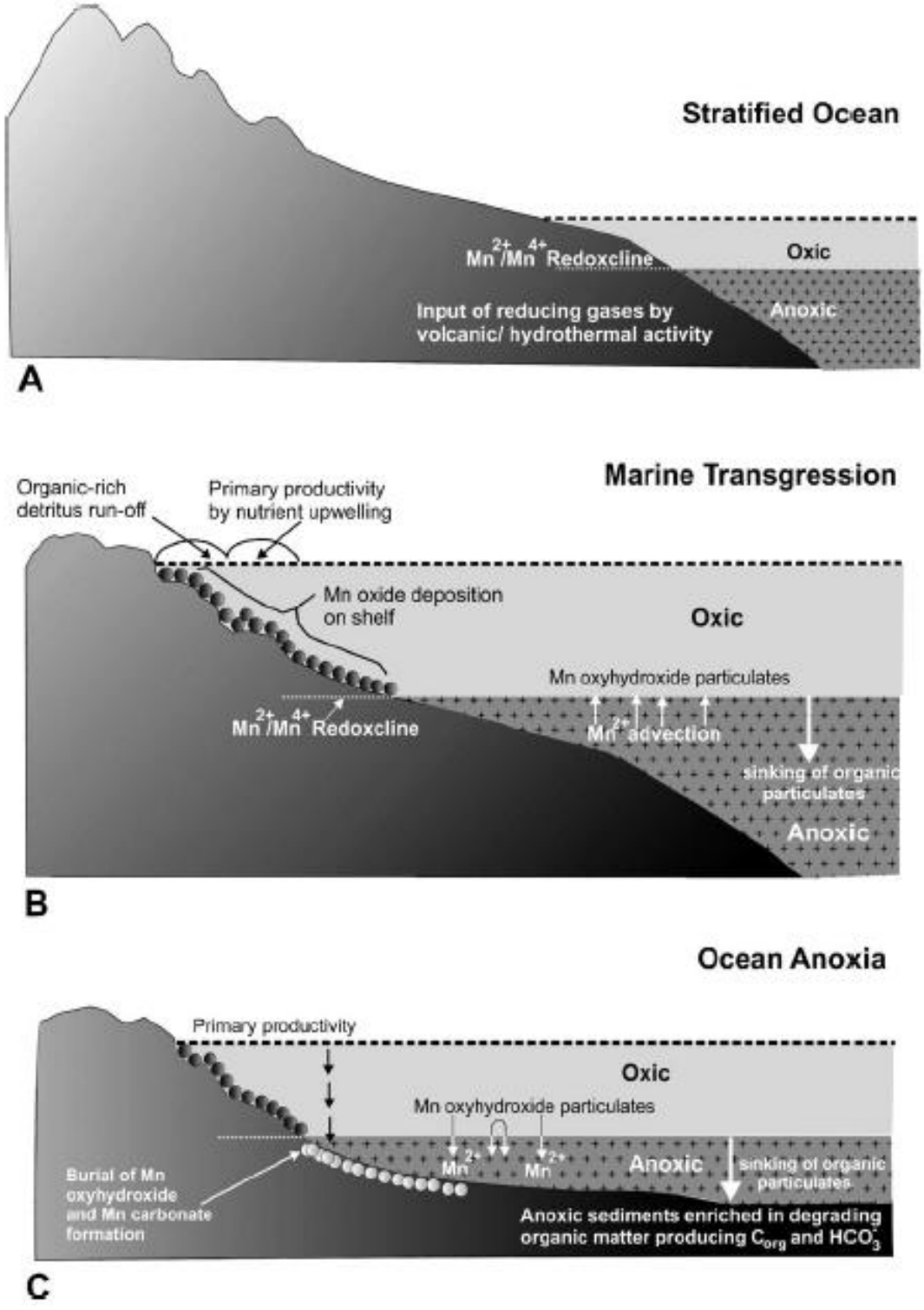

Figure 56: Schematic Manganese depositional models related to sea-level changes (Roy, 2006).

4.5.3 Present constraints on Hotazel depositional models

In this section, a conceptual model for the deposition of the Hotazel Formation with emphasis on the results from the lowermost portion as preserved by the Mamatwan and Middleplaats stratigraphic columns, is envisioned (Figure 57). The model incorporates geochemical findings that were presented, synthesized and discussed in previous sections of this thesis, as well as from previous research on BIF and Mn-rich lithofacies.

The early Proterozoic oceanic environment, as described by Cloud (1973), was assumed to be predominately anoxic with only upper portions oxygenated largely by photosynthetic bacteria. If deep, anoxic iron-silica-manganese-rich waters advected towards a continental shelf and/or basin margin through an upwelling process from deeper parts of a stratified sea, iron oxides with silica would precipitate first and accumulate to form banded iron-formation units. Manganese oxides, as per the same model, would ultimately precipitate as the remaining solutions reached the more oxidized parts of the shelf (Schissel and Aro, 1992).

One can therefore easily infer from the previous model that formation of discrete iron and manganese-rich assemblages with excellent separation as seen in the Hotazel Formation, would require changes in sea-level possibly in the form of transgression-regression events, against a stratified water column constituting the interface between oxidizing and reducing conditions. That interface in reality would have rather been in the form of a chemical gradient, with its lower, anoxic waters being the effective reservoir enriched in dissolved low valence Fe(II) and Mn(II) chemical species (Figure 57).

The concept of oxygen production for the first time as the result of the GOE, is also considered to be a crucial prerequisite for modelling the Hotazel paleoenvironment (e.g., Klein and Beukes, 1989; Sumner and Grotzinger, 1996; Lyons et al., 2014). It is thought that the emergence of free oxygen via photosynthesis would have been the main pathway for dissolved Fe(II) and Mn(II) oxidation within the shallow oxic portions of the water column. This differs from the classic BIF models earlier in Earth history, where Mn deposits are evidently absent (Tsikos and Moore, 1997).

It is difficult in this study to constrain the exact valence state of the primary Fe and Mn species that formed through processes of oxidation. However, it is clear that the two species did not form together in a mixed fashion but were separated in the Mn-poor BIF and the Mn-rich hematite-braunite intervals. The results of this study show that certain trace elements such as Co and Mo, show an association with the hematite and Mn-rich parts of the section respectively, and not with the BIF sections. Therefore, conditions of Fe and Mn deposition were clearly decoupled in the primary depositional environment, in order for such geochemically different depositional facies to form in alternation.

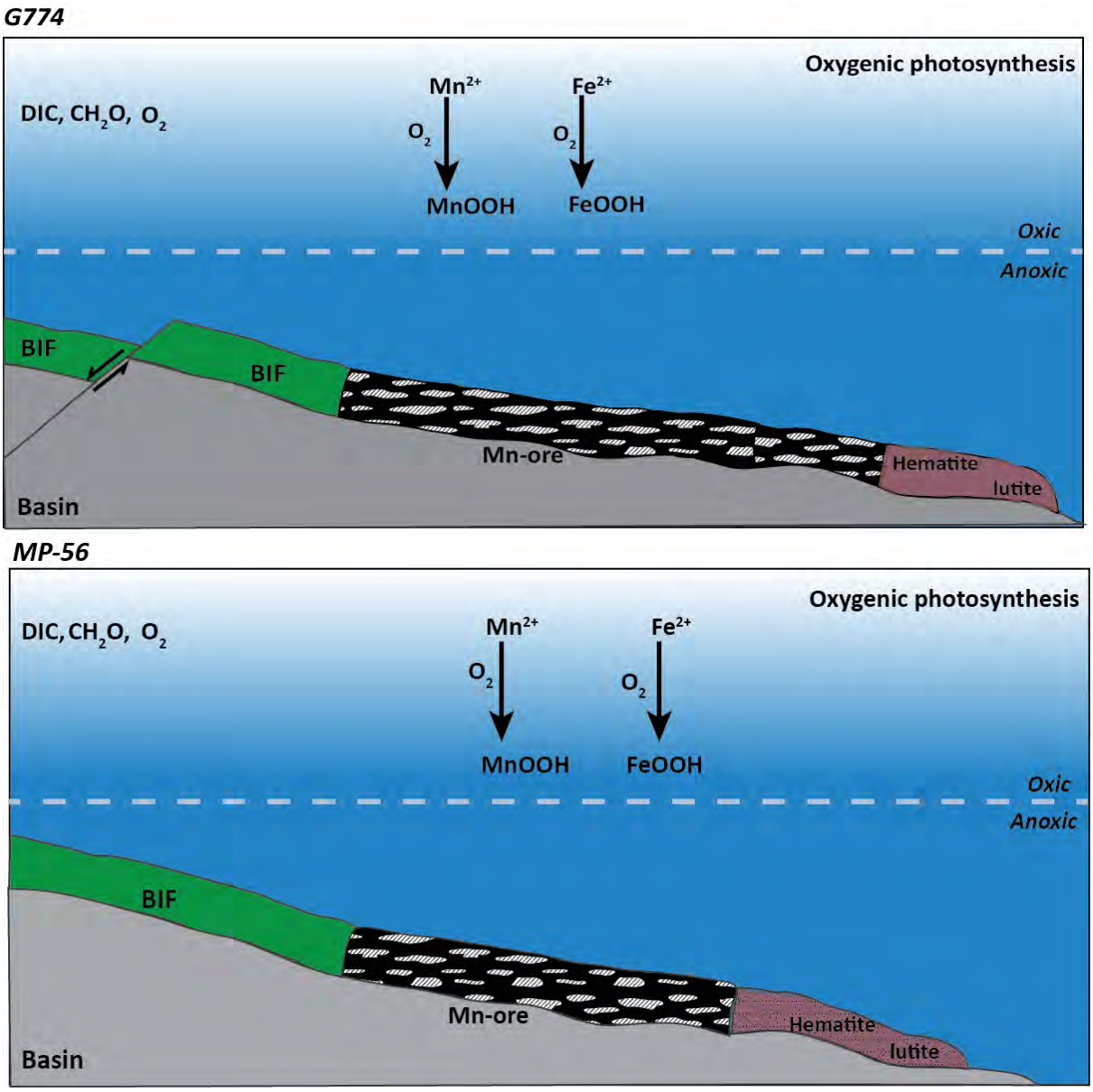

Figure 57: A conceptual model for the deposition of the lowermost portion of Hotazel Formation at Mamatwan depositional site (G774) and Middleplaats depositional site (MP-56).

It is thought that the main process for the alternating Fe and Mn deposition in the Hotazel, must have been the proposed reaction of oxidised Mn(III) with reduced Fe(II), as suggested by Tsikos et al (2010):

$$Mn(III) + Fe(II) = Mn(II) + Fe(III)$$

The above reaction suggests that once Mn(II) was oxidized for the first time during the Hotazel deposition, it would react with reduced iron and oxidize it, and it would itself get reduced again back into solution as Mn(II). This therefore would make the two elements kind of incompatible during redox processes. The only way that Mn deposition as Mn(III) can be envisaged is during periods when the

above reaction is outpaced by high rate of Mn oxidation, which would probably have been in the shallower parts of the paleobasin. In the deeper parts where there would have been much Fe(II) in anoxic waters, reduction of Mn(III) would be the main process taking place.

The thickness variations that are therefore seen in the Hotazel formation laterally, as epitomised in the Middelplaats and Mamatwan localities, may represent different parts of the paleobasin with different depths. In that scenario, what kind of sediment would precipitate at any time would depend on water depth and especially the depth of the chemocline in relation to the depth of the paleobasin floor: if that was relatively shallow, then Mn precipitation and not reduction would be the dominating mechanism, while iron oxidation and manganese reduction would take place in the deeper parts of the basin (Figure 57). Ultimately, transgression-regression cycles against such a complex basin geometry would result in very different sedimentary facies developing almost simultaneously, and this would explain the contrasting stratigraphies and thickness variabilities recorded in the two stratigraphic sections studied in this thesis.

4.6 Conclusions

This project has produced a great deal of results of a mainly geochemical nature (i.e., geochemical relationships and signals in a stratigraphic context and geochemical parameters useful for correlation purposes), from the lowermost portion of the Hotazel Formation, with a view to understanding better its primary depositional environment. It can be concluded that the selected Mamatwan and Middleplaats chemostratigraphic sections are in many ways geochemically comparable but also show differences in other respects, which nevertheless all together lead to at least some profoundly important new findings.

Bulk-rock major element results show that Mn-rich layers of both the Mamatwan and Middleplaats chemostratigraphic sections are consistently very Ca-carbonate rich, as indicated by the elevated concentration values and clearly correlatable spikes between CaO and LOI (representing CO_2). Calcic carbonate prevails also in the BIF, which makes the carbonate carbon fraction and its isotopic character as a potentially very strong correlation tool. In terms of bulk-rock trace elements, elements such as Zr, Nb, Al and Ti in both Mamatwan and Middleplaats chemostratigraphic sections occur at very low and essentially negligible concentrations, suggesting that the influx of a terrigenous detrital component in the Hotazel depositional environment was very low. The results however do suggest that rates of chemical precipitation of Mn-rich facies sediment was higher by a factor of about two compared to that of the BIF, if it is assumed that the precipitation rates and fluxes of the detrital elements remained constant through time and differential compaction effects were minimal.

The carbonate-carbon isotopic results appear to be comparable in the two stratigraphic sections both quantitatively and qualitatively. The chemostratigraphic patters are very smooth and appear to correlate directly across at least certain parts of the two sections. Lighter $\delta^{13}C$ values (sometimes as low as -21 ‰) are seen across the hematite lutite and BIF lithofacies, while relatively heavier $\delta^{13}C$ values characterize the Mn-mineralized sections (from -14.9 to -6.3 ‰ in the Mamatwan Mn-rich zone and from -16.8 to -6.2 ‰ in the Middleplaats Mn-rich zone). These negative $\delta^{13}C$ values are classically interpreted to reflect variable mixtures of isotopically heavy marine and light organic carbon sources, which would have been controlled mainly by processes of primary deposition of carbon in the ancient basin.

The geochemical relationship between Co and Mg in the hematite-lutite transitions appears to be striking and correlatable, suggesting a consistent primary control in Co behaviour by Fe(III) and Mg. With regard to molybdenum (Mo) and manganese oxide (MnO_2), their relationship appears positive but there are dissimilarities in the two chemostratigraphic sections. Specifically, the relationship between these two chemical components appears to be positive across the Mamatwan stratigraphic section, with r^2 values of 0.57 for the main Mn-zone, and a strikingly higher r^2 value of 0.86 for the T_1 horizon. This relationship, however, seems to not be reproduced very faithfully in the Middleplaats section, wherein the correlation coeeficient between Mo and MnO_2 is not nearly as strong (respective r^2 values of 0.4289 and 0.1718). This suggests that the Mo can be tentatively linked to primary Mn oxyhydroxide precipitation as a control, but perhaps this is a feature that did not characterize the paleobasin in its entirety with the same intensity.

Chemostratigraphic correlation between the two stratigraphic sections appears to be possible, with the general stratigraphic signals – as well as absolute values – of high resolution MgO, Co and carbon isotopic records of the two chemostratigraphic profiles revealing features that undoubtedly mimic each other, at least to a certain degree. Arguably, the $\delta^{13}C$ record of the Hotazel rocks showed to be the one that could be used across the entire stratigraphy as a common denominator of correlation. Lateral correlation between the two sections was therefore implemented, and the result showed that at least for a certain period of time, there must have been simultaneous deposition of Fe-rich sediment precursor to BIF in one part (Middleplaats) while in the other, carbonate-rich Mn deposition was ongoing (Mamatwan). This points to the probably very dynamic and transient environment of deposition in which the Hotazel sediments originally precipitated.

Finally, a conceptual model for the deposition of the Hotazel Formation is put forward which borrows principles from other researchers' previous investigations around BIF and Mn-rich sedimentation in the Precambrian, and merges with these the geochemical findings from this very thesis. The key conclusions

that are drawn or are reinforced by the results of this study, is that Fe and Mn deposition in the primary environment of the Hotazel Formation was a very dynamic process, that resulted in the clear decoupling of the two subfacies in the form of the sedimentary cycles observed. Importantly, it was shown that the changes in the paleodepositional environment that led to the switch from Fe-rich to Mn-rich deposition and back, were not simultaneous, but were instead ongoing, dynamic and diachronous. Combination of results from the assumed detrital (minor) and chemical (dominant) fractions combined, indicate that in different yet relatively proximal parts of the basin, BIF deposition was taking place simultaneously with Mn deposition. This is a hugely important result of this study which is hoped that will contribute to future debates about the origin of these remarkable deposits.

To sum up, this study calls for further investigation to be done on clarifying further the mechanism of Fe and Mn separation in such clear-cut sedimentary sub-cycles. To this must be added the mixed messages that redox elements such as Mo and Co have revealed, with the former showing close but not very convincing affinity for primary Mn oxide while the other appears to be enriched in hematitic zones rich in Mg+Mn carbonate. Finally, the utility of carbon isotope ratios on the carbonate fraction of BIF and associated Mn-rich sediments has taken a new meaning as a crucial chemostratigraphic tool of correlation, that should not be ignored in similar future studies. The author firmly believes such follow-up work could open new and perhaps much more effective ways of understanding better the behaviour of a great deal of redox-sensitive elements in the Hotazel depositional environment and in the Precambrian oceanic environment more generally, with Fe and Mn obviously continuing to play the central roles.

5. References

Alexander, B. W., Bau, M., Andersson, P., & Dulski, P. (2008). Continentally-derived solutes in shallow Archean seawater: rare earth element and Nd isotope evidence in iron formation from the 2.9 Ga Pongola Supergroup, South Africa. *Geochimica et Cosmochimica Acta*, *72*(2), 378-394.

Alexander, B. W., Bau, M., & Andersson, P. (2009). Neodymium isotopes in Archean seawater and implications for the marine Nd cycle in Earth's early oceans. *Earth and Planetary Science Letters*, *283*(1-4), 144-155.

Alibert, C., & McCulloch, M. T. (1993). Rare earth element and neodymium isotopic compositions of the banded iron-formations and associated shales from Hamersley, Western Australia. *Geochimica et Cosmochimica Acta*, *57*(1), 187-204.

Alterrmann, W. & Halbich, I. W. (1990). Thrusting, folding and stratigraphy of the Ghaap Group along the Soutwestern margin of the Kaapvaal Craton. *South African journal of geology*, *93*(4), 553-556.

Altermann, W., & Wotherspoon, J. M. (1995). The carbonates of the Transvaal and Griqualand West Sequences of the Kaapvaal craton, with special reference to the Lime Acres limestone deposit. Mineralium Deposita, 30(2), 124-134.

Anbar, A. D. (2008). Elements and evolution. Science, 1481-1483.

Anbar, A.D., Duan, Y., Lyons, T.W., Arnold, G.L., Kendall, B., Creaser, R. A.,... and Bluick, R. (2007). A whiff of oxygen before the great oxidation event?. *Science, 317* (5846), 1903-1906.

Anhaeusser, C. R., Johnson, M. R., & Thomas, R. J. (2006). Ultramafic and mafic intrusions of the Kaapvaal Craton. *The Geology of South Africa. Geological Society of South Africa, Johannesburg/Council for Geoscience, Pretoria*, 95-134.

Armstrong, R. A., Compston, W., Retief, E. A., Williams, I. T., & Welke, H. J. (1991). Zircon ion microprobe studies bearing on the age and evolution of the Witwatersrand triad. Precambrian Research, 53(3-4), 243-266.

Astrup, J., and Tsikos, H. (1998). Manganese, *in* Wilson, M.J., and Anhaeusser, C.R., eds., Mineral resources of southern Africa: Pretoria, South Africa, Council for Geoscience, Handbook 16, p. 450–460.

Banerji, A. K. (1977). On the Precambrian banded iron-formations and the manganese ores or the Singhbhum region, eastern India. *Economic Geology*, *72*(1), 90-98.

Barling, J., & Anbar, A. D. (2004). Molybdenum isotope fractionation during adsorption by manganese oxides. *Earth and Planetary Science Letters*, *217*(3-4), 315-329.

Bau, M. (1993). Effects of syn-and post-depositional processes on the rare-earth element distribution in Precambrian iron-formations. *European Journal of Mineralogy*, *5*(2), 257-267.

Bau, M., & Alexander, B. W. (2009). Distribution of high field strength elements (Y, Zr, REE, Hf, Ta, Th, U) in adjacent magnetite and chert bands and in reference standards FeR-3 and FeR-4 from the Temagami iron-formation, Canada, and the redox level of the Neoarchean ocean. *Precambrian Research*, *174*(3-4), 337-346.

Bau, M., Beukes, N.J., Romer, R.L. (1998). Increase of oxygen in the Earth's atmosphere and hydrosphere between ~2.5 and ~2.4 Ga B.P., in: Goldschmidt Conference Abstracts, Toulouse 1998.

Bau, M., & Dulski, P. (1996). Distribution of yttrium and rare-earth elements in the Penge and Kuruman iron-formations, Transvaal Supergroup, South Africa. *Precambrian Research*, *79*(1-2), 37-55.

Bau, M., & Dulski, P. (1999). Comparing yttrium and rare earths in hydrothermal fluids from the Mid-Atlantic Ridge: implications for Y and REE behaviour during near-vent mixing and for the Y/Ho ratio of Proterozoic seawater. *Chemical Geology*, *155*(1-2), 77-90.

Bau, M., Koschinsky, A., Dulski, P., & Hein, J. R. (1996). Comparison of the partitioning behaviours of yttrium, rare earth elements, and titanium between hydrogenetic marine ferromanganese crusts and seawater. *Geochimica et Cosmochimica Acta*, *60*(10), 1709-1725.

Bau, M., & Möller, P. (1993). Rare earth element systematics of the chemically precipitated component in Early Precambrian iron formations and the evolution of the terrestrial atmosphere-hydrosphere-lithosphere system. *Geochimica et Cosmochimica Acta*, *57*(10), 2239-2249.

Bekker, A., Slack, J. F., Planavsky, N., Krapez, B., Hofmann, A., Konhauser, K. O., & Rouxel, O. J. (2010). Iron formation: the sedimentary product of a complex interplay among mantle, tectonic, oceanic, and biospheric processes. Economic Geology, 105(3), 467-508.

Berger, W. H., Diesterhaass, L., & Killingley, J. S. (1978). Upwelling off northwest africa-holocene decrease as seen in carbon isotopes and sedimentological indicators. *Oceanologica Acta*, *1*(1), 3-7.

Berger, W. H., & Vincent, E. (1986). Deep-sea carbonates: reading the carbon-isotope signal. *Geologische Rundschau*, *75*(1), 249-269.

Beukes, N. J. (1973). Precambrian iron-formations of southern Africa. *Economic Geology*, *68*(7), 960-1004.

Beukes, N. J. (1983). Palaeoenvironmental setting of iron-formations in the depositional basin of the Transvaal Supergroup, South Africa. In *Developments in Precambrian Geology* (Vol. 6, pp. 131-198). Elsevier.

Beukes, N. J. (1987). Facies relations, depositional environments and diagenesis in a major early Proterozoic stromatolitic carbonate platform to basinal sequence, Campbellrand Subgroup, Transvaal Supergroup, Southern Africa. Sedimentary Geology, 54(1-2), 1-46.

Beukes, N. J., & Gutzmer, J. E. N. S. (2008). Origin and paleoenvironmental significance of major iron formations at the Archean-Paleoproterozoic boundary.

Beukes, N. J., Gutzmer, J., & Burger, A. M. (1995). Fault-controlled hydrothermal alteration of Palaeoproterozoic manganese ore in Wessels Mine, Kalahari manganese field. *South African Journal of Geology*, *98*(4), 430-451.

Beukes, NJ & Smit, C. A. (1987). New evidence for thrust faulting in Griqualand West, South Africa: implications for stratigraphy and the age of red beds. *South African Journal of Geology*, *90*(4), 378-394.

Brand, U. (2004). Carbon, oxygen and strontium isotopes in Paleozoic carbonate components: an evaluation of original seawater-chemistry proxies. *Chemical Geology*, *204*(1-2), 23-44.

Bonatti, E., Zerbi, M., Kay, R., & Rydell, H. (1976). Metalliferous deposits from the Apennine ophiolites: Mesozoic equivalents of modern deposits from oceanic spreading centers. *Geological Society of America Bulletin*, *87*(1), 83-94.

Button, A., Brock, T. D., Cook, P. J., Eugster, H. P., Goodwin, A. M., James, H. L., ... & Walter, M. R. (1982). Sedimentary Iron Deposits, Evaporites and Phosphorites State of the Art Report. In *Mineral Deposits and the Evolution of the Biosphere* (pp. 259-273). Springer, Berlin, Heidelberg.

Byrne, R. H., & Sholkovitz, E. R. (1996). Marine chemistry and geochemistry of the lanthanides. *Handbook on the physics and chemistry of rare earths*, *23*, 497-593.

Canfield, D. E., Knoll, A. H., Poulton, S. W., Narbonne, G. M., & Dunning, G. R. (2020). Carbon isotopes in clastic rocks and the Neoproterozoic carbon cycle. *American Journal of Science*, *320*(2), 97-124.

Cannon, W. F., & Force, E. R. (1983). Potential for high-grade shallow-marine manganese deposits in North America. *Unconventional mineral deposits*, 175-189.

Cerling, T. E. (1992). Use of carbon isotopes in paleosols as an indicator of the P (CO_2) of the paleoatmosphere. *Global Biogeochemical Cycles*, *6*(3), 307-314.

Chao, T. T., & Theobald, P. K. (1976). The significance of secondary iron and manganese oxides in geochemical exploration. *Economic Geology*, *71*(8), 1560-1569.

Cloud, P. (1973). Paleoecological significance of the banded iron-formation. *Economic Geology*, *68*(7), 1135-1143.

Coffman, J. S. (1992). *Manganese Availability--market Economy Countries: 1980's Perspective* (Vol. 9327). United States Department of the Interior, Bureau of Mines.

Condie, K. C. (1993). Chemical composition and evolution of the upper continental crust: contrasting results from surface samples and shales. *Chemical geology 104* (1-4), 1-37.

Cornell, D. H., & Schütte, S. S. (1995). A volcanic-exhalative origin for the world's largest (Kalahari) manganese field. *Mineralium Deposita*, *30*(2), 146-151.

Derry, L. A., & Jacobsen, S. B. (1990). The chemical evolution of Precambrian seawater: evidence from REEs in banded iron formations. *Geochimica et Cosmochimica Acta*, *54*(11), 2965-2977.

Dorr, J. V. N., & de Miranda Barbosa, A. L. (1963). *Geology and ore deposits of the Itabira district, Minas Gerais, Brazil* (Vol. 341). US Government Printing Office.

Duplessy, J. C., Bé, A. W. H., & Blanc, P. L. (1981). Oxygen and carbon isotopic composition and biogeographic distribution of planktonic foraminifera in the Indian Ocean. *Palaeogeography, Palaeoclimatology, Palaeoecology*, *33*(1-3), 9-46.

Elderfield, H. (1988). The oceanic chemistry of the rare-earth elements. *Philosophical Transactions of the Royal Society of London. Series A, Mathematical and Physical Sciences*, *325*(1583), 105-126.

Emiliani, C. (1955). Pleistocene temperatures. *The Journal of geology*, *63*(6), 538-578.

Eriksson, P. G., Hattingh, P. J., & Altermann, W. (1995). An overview of the geology of the Transvaal Sequence and Bushveld Complex, South Africa. *Mineralium Deposita*, *30*(2), 98-111.

Eriksson, P. G., Mazumder, R., Catuneanu, O., Bumby, A. J., & Ilondo, B. O. (2006). Precambrian continental freeboard and geological evolution: a time perspective. *Earth-Science Reviews*, *79*(3-4), 165-204.

Fairey, B., Tsikos, H., Corfu, F., & Polteau, S. (2013). U–Pb systematics in carbonates of the Postmasburg Group, Transvaal Supergroup, South Africa: primary versus metasomatic controls. *Precambrian Research*, *231*, 194-205.

Floran, R. J., & Papike, J. J. (1975). Petrology of the low-grade rocks of the Gunflint Iron-Formation, Ontario-Minnesota. *Geological Society of America Bulletin*, *86*(9), 1169-1190.

Frakes, L., & Bolton, B. R. (1992). Effects of ocean chemistry, sea level, and climate on the formation of primary sedimentary manganese ore deposits. Economic Geology, 87(5), 1207-1217.

French, B. M. (1968). Bulletin No. 45. Progressive Contact Metamorphism of the Biwabik Iron-fomation, Mesabi Range, Minnesota.

Goodwin, A. M. (1973). Archean iron-formations and tectonic basins of the Canadian Shield. *Economic Geology*, *68*(7), 915-933.

Gröcke, D. R. (2020). Carbon isotope stratigraphy: Principles and applications. *Carbon Isotope Stratigraphy*, *5*, 1.

Gross, G. A. (1980). A classification of iron formations based on depositional environments. *The Canadian Mineralogist*, *18*(2), 215-222.

Gumsley, A. P., Chamberlain, K. R., Bleeker, W., Söderlund, U., de Kock, M. O., Larsson, E. R., & Bekker, A. (2017). Timing and tempo of the Great Oxidation Event. *Proceedings of the National Academy of Sciences*, *114*(8), 1811-1816.

Gutzmer, J., & Beukes, N. J. (1995). Fault-controlled metasomatic alteration of early Proterozoic sedimentary manganese ores in the Kalahari manganese field, South Africa. *Economic Geology*, *90*(4), 823-844.

Gutzmer, J., & Beukes, N. J. (1996). Karst-hosted fresh-water Paleoproterozoic manganese deposits, Postmasburg, South Africa. *Economic Geology*, *91*(8), 1435-1454.

Gutzmer, J., & Beukes, N. J. (1997). Mineralogy and mineral chemistry of oxide-facies manganese ores of the Postmasburg manganese field, South Africa. *Mineralogical Magazine*, *61*(405), 213-231.

Gutzmer, J., & Beukes, N. J. (1998). The manganese formation of the Neoproterozoic Penganga Group, India; revision of an enigma. *Economic Geology*, *93*(7), 1091-1102.

Haase, C. S. (1982). Metamorphic petrology of the Negaunee Iron Formation, Marquette District, northern Michigan; mineralogy, metamorphic reactions, and phase equilibria. *Economic Geology*, *77*(1), 60-81.

Halverson, G. P., Wade, B. P., Hurtgen, M. T., & Barovich, K. M. (2010). Neoproterozoic chemostratigraphy. *Precambrian Research*, *182*(4), 337-350.

Holland, H. D. (2005). 100th anniversary special paper: sedimentary mineral deposits and the evolution of earth's near-surface environments. *Economic Geology*, *100*(8), 1489-1509.

Holland, H. D. (2006). The oxygenation of the atmosphere and oceans. *Philosophical Transactions of the Royal Society B: Biological Sciences*, *361*(1470), 903-915.

Hudson, J. D. (1977). Stable isotopes and limestone lithification. *Journal of the Geological Society*, *133*(6), 637-660.

Humbert, F., Sonnette, L., De Kock, M. O., Robion, P., Horng, C. S., Cousture, A., & Wabo, H. (2017). Palaeomagnetism of the early Palaeoproterozoic, volcanic Hekpoort Formation (Transvaal Supergroup) of the Kaapvaal craton, South Africa. *Geophysical Journal International*, *209*(2), 842-865.

Isley, A. E. (1995). Hydrothermal plumes and the delivery of iron to banded iron formation. *The Journal of Geology*, *103*(2), 169-185.

James, H. L. (1983). Distribution of banded iron-formation in space and time. In *Developments in Precambrian geology* (Vol. 6, pp. 471-490). Elsevier.

Kamber, B. S., Bolhar, R., & Webb, G. E. (2004). Geochemistry of late Archaean stromatolites from Zimbabwe: evidence for microbial life in restricted epicontinental seas. *Precambrian Research*, *132*(4), 379-399.

Klein, C. (2005). Some Precambrian banded iron-formations (BIFs) from around the world: Their age, geologic setting, mineralogy, metamorphism, geochemistry, and origins. American Mineralogist, 90(10), 1473-1499.

Klein, C. (1966). Mineralogy and petrology of the metamorphosed Wabush Iron Formation, southwestern Labrador. *Journal of Petrology*, *7*(2), 246-305.

Klein, C., & Beukes, N. J. (1989). Geochemistry and sedimentology of a facies transition from limestone to iron-formation deposition in the early Proterozoic Transvaal Supergroup, South Africa. *Economic Geology*, *84*(7), 1733-1774.

Klein, C., & Beukes, N. J. (1993). Sedimentology and geochemistry of the glaciogenic late Proterozoic Rapitan iron-formation in Canada. *Economic Geology*, *88*(3), 542-565.

Klein, C., & Fink, R. P. (1976). Petrology of the Sokoman Iron Formation in the Howells River area, at the western edge of the Labrador Trough. *Economic Geology*, *71*(2), 453-487.

Klein, C., & Ladeira, E. A. (2002). Petrography and geochemistry of the least altered banded iron-formation of the Archean Carajás Formation, northern Brazil. *Economic Geology*, *97*(3), 643-651.

Klein, C., & Ladeira, E. A. (2004). Geochemistry and mineralogy of Neoproterozoic banded iron-formations and some selected, siliceous manganese formations from the Urucum District, Mato Grosso do Sul, Brazil. *Economic Geology*, *99*(6), 1233-1244.

Kleyenstuber, A. S. E. (1984). The mineralogy of the manganese-bearing Hotazel formation, of the Proterozoic Transvaal Sequence in Griqualand West, South Africa. *South African Journal of Geology*, *87*(3), 257-272.

Klinkhammer, G., Elderfield, H., & Hudson, A. (1983). Rare earth elements in seawater near hydrothermal vents. *Nature*, *305*(5931), 185-188.

Klinkhammer, G., & Hudson, A. A. (1986). Dispersal patterns for hydrothermal plumes in the South Pacific using manganese as a tracer. *Earth and planetary science letters*, *79*(3-4), 241-249.

Knoll, A. H., & Walter, M. R. (1992). Latest Proterozoic stratigraphy and Earth history. *Nature*, *356*(6371), 673-678.

Knoll, A. H., & Beukes, N. J. (2009). Introduction: Initial investigations of a Neoarchean shelf margin-basin transition (Transvaal Supergroup, South Africa). *Precambrian Research*, *169*(1-4), 1-14.

Konhauser, K. O., Hamade, T., Raiswell, R., Morris, R. C., Ferris, F. G., Southam, G., & Canfield, D. E. (2002). Could bacteria have formed the Precambrian banded iron formations?. Geology, 30(12), 1079-1082.

Konhauser, K. O., Newman, D. K., & Kappler, A. (2005). The potential significance of microbial Fe (III) reduction during deposition of Precambrian banded iron formations. *Geobiology*, *3*(3), 167-177.

Konhauser, K. O., Pecoits, E., Lalonde, S. V., Papineau, D., Nisbet, E. G., Barley, M. E., ... & Kamber, B. S. (2009). Oceanic nickel depletion and a methanogen famine before the Great Oxidation Event. *Nature*, *458*(7239), 750-753.

Konhauser, K.O., Planavsky, N.J., Hardisty, D.S., Robbins, L. J., Warchola, T.J., Haugaard, R.,... & Johnson, C. M. (2017). Iron formations: A global record of Neoarchaean to Palaeoproterozoic environmental history. *Earth-Science Reviews*, 172, 140-177.

Koschinsky, A., & Hein, J. R. (2003). Uptake of elements from seawater by ferromanganese crusts: solid-phase associations and seawater speciation. *Marine Geology*, *198*(3-4), 331-351.

Krauskopf, K. B. (1956). Factors controlling the concentrations of thirteen rare metals in sea-water. *Geochimica et cosmochimica acta*, *9*(1-2), 1-B32.

Krauskopf, K. B. (1957). Separation of manganese from iron in sedimentary processes. *Geochimica et Cosmochimica Acta*, *12*(1-2), 61-84.

Laznicka, P. (1992). Manganese deposits in the global lithogenetic system: Quantitative approach. *Ore Geology Reviews*, *7*(4), 279-356.

Lovley, D. R., & Phillips, E. J. (1988). Novel mode of microbial energy metabolism: organic carbon oxidation coupled to dissimilatory reduction of iron or manganese. *Applied and environmental microbiology*, *54*(6), 1472-1480.

Lyons, T. W., Reinhard, C. T., & Planavsky, N. J. (2014). The rise of oxygen in Earth's early ocean and atmosphere. *Nature*, *506*(7488), 307-315.

Maxwell, C. H. (1972). *Geology and ore deposits of the Alegria district, Minas Gerais, Brazil* (No. 341-J).

Maynard, J. B. (2010). The chemistry of manganese ores through time: a signal of increasing diversity of earth-surface environments. *Economic Geology*, *105*(3), 535-552.

Moore, J. M., Kuhn, B. K., Mark, D. F., & Tsikos, H. (2011). A sugilite-bearing assemblage from the Wolhaarkop breccia, Bruce iron-ore mine, South Africa: Evidence for alkali metasomatism and 40Ar-39Ar dating. *European Journal of Mineralogy*, *23*(4), 661-673.

Moore, J. M., Tsikos, H., & Polteau, S. (2001). Deconstructing the Transvaal Supergroup, South Africa: implications for palaeoproterozoic palaeoclimate models. *Journal of African Earth Sciences*, *33*(3-4), 437-444.

Mohapatra, B. K., Mishra, P. P., & Singh, P. P. (2009). Manganese ore deposits in Koira-Noamundi province of iron ore group, north Orissa, India: in the light of geochemical signature. *Geochemistry*, *69*(4), 377-394.

Morgan, R., Orberger, B., Rosière, C. A., Wirth, R., da Mota Carvalho, C., & Bellver-Baca, M.T. (2013). The origin of coexisting carbonates in banded iron formations: A micro-mineralogical study of the 2.4 Ga Itabira Group, Brazil. *Precambrian Research*, 224, 491-511.

Muehlenbachs, K. (1998). The oxygen isotopic composition of the oceans, sediments and the seafloor. *Chemical Geology*, *145*(3-4), 263-273.

Murray, J. W., & Brewer, P. G. (1977). Mechanisms of removal of manganese, iron and other trace metals from sea water. *Elsevier Oceanography Series*, *15*, 291-325.

Murray, J. W., & Dillard, J. G. (1979). The oxidation of cobalt (II) adsorbed on manganese dioxide. *Geochimica et Cosmochimica Acta*, *43*(5), 781-787.

Musić, S., Gessner, M., & Wolf, R. H. H. (1979). Sorption of small amounts of cobalt (II) on iron (III) oxide. *Microchimica Acta*, *71*(1), 105-112.

Nicholson, K. (1990). Stratiform manganese mineralisation near Inverness, Scotland: A Devonian sublacustrine hot-spring deposit?. *Mineralium Deposita*, *25*(2), 126-131.

Okita, P. M., Maynard, J. B., Spiker, E. C., & Force, E. R. (1988). Isotopic evidence for organic matter oxidation by manganese reduction in the formation of stratiform manganese carbonate ore. *Geochimica et Cosmochimica Acta*, *52*(11), 2679-2685.

Oonk, P. B. H., Mason, P. R. D., Tsikos, H., & Bau, M. (2018). Fraction-specific rare earth elements enable the reconstruction of primary seawater signatures from iron formations. *Geochimica et Cosmochimica Acta*, *238*, 102-122.

Oonk, P. B., Tsikos, H., Mason, P. R., Henkel, S., Staubwasser, M., Fryer, L., ... & Williams, H. M. (2017). Fraction-specific controls on the trace element distribution in iron formations: Implications for trace metal stable isotope proxies. *Chemical Geology*, *474*, 17-32.

Park, C. F. (1946). The spilite and manganese problems of the Olympic Peninsula, Washington. *American Journal of Science*, *244*(5), 305-323.

Piepgras, D. J., & Jacobsen, S. B. (1992). The behavior of rare earth elements in seawater: Precise determination of variations in the North Pacific water column. *Geochimica et Cosmochimica Acta*, *56*(5), 1851-1862.

Planavsky, N. J., Asael, D., Hofmann, A., Reinhard, C. T., Lalonde, S. V., Knudsen, A., ... & Rouxel, O. J. (2014). Evidence for oxygenic photosynthesis half a billion years before the Great Oxidation Event. Nat Geosci 7: 283–286.

Polgari, M., Okita, P. M., & Hein, J. R. (1991). Stable isotope evidence for the origin of the Úrkút manganese ore deposit, Hungary. *Journal of Sedimentary Research*, *61*(3), 384-393.

Robertson, A. H. F., & Varnavas, S. P. (1993). The origin of hydrothermal metalliferous sediments associated with the early Mesozoic Othris and Pindos ophiolites, mainland Greece. *Sedimentary Geology*, *83*(1-2), 87-113.

Roy, S. (1992). Environments and processes of manganese deposition. Economic Geology, 87(5), 1218-1236.

Roy, S. (1997). Genetic diversity of manganese deposition in the terrestrial geological record. *Geological Society, London, Special Publications*, *119*(1), 5-27.

Roy, S. (2006). Sedimentary manganese metallogenesis in response to the evolution of the Earth system. *Earth-Science Reviews*, *77*(4), 273-305.

Sapozhnikov, D. G. (1970). Geological conditions for the formation of manganese deposits of the Soviet Union. *Manganese Deposits of Soviet Union. Israel Program for Scientific Translations, Jerusalem*, 9-33.

Schier, K., Bau, M., Smith, A. J. B., Beukes, N. J., Coetzee, L. L., & Viehmann, S. (2020). Chemical evolution of seawater in the Transvaal Ocean between 2426 Ma (Ongeluk Large Igneous Province) and 2413 Ma ago (Kalahari Manganese Field). *Gondwana Research*, *88*, 373-388.

Schissel, D., & Aro, P. (1992). The major early Proterozoic sedimentary iron and manganese deposits and their tectonic setting. *Economic Geology*, *87*(5), 1367-1374.

Scholle, P. A., & Arthur, M. A. (1980). Carbon isotope fluctuations in Cretaceous pelagic limestones: potential stratigraphic and petroleum exploration tool. *Aapg Bulletin*, *64*(1), 67-87.

Siahi, M., Tsikos, H., Rafuza, S., Oonk, P. B., Mhlanga, X. R., van Niekerk, D., ... & Harris, C. (2020). Insights into the processes and controls on the absolute abundance and distribution of manganese in Precambrian iron formations. *Precambrian Research*, *350*, 105878.

Slack, J. F., Grenne, T., & Bekker, A. (2009). Seafloor-hydrothermal Si-Fe-Mn exhalites in the Pecos greenstone belt, New Mexico, and the redox state of ca. 1720 Ma deep seawater. *Geosphere*, *5*(3), 302-314.

Sumner, D. Y., & Grotzinger, J. P. (1996). Were kinetics of Archean calcium carbonate precipitation related to oxygen concentration?. *Geology*, *24*(2), 119-122.

Swanner, E. D., Planavsky, N. J., Lalonde, S. V., Robbins, L. J., Bekker, A., Rouxel, O. J., ... & Konhauser, K. O. (2014). Cobalt and marine redox evolution. *Earth and Planetary Science Letters*, *390*, 253-263.

Sylvestre, G., Laure, N. T. E., Djibril, K. N. G., Arlette, D. S., Cyriel, M., Timoléon, N., & Paul, N. J. (2017). A mixed seawater and hydrothermal origin of superior-type banded iron formation (BIF)-hosted Kouambo iron deposit, Palaeoproterozoic Nyong series, Southwestern Cameroon: constraints from petrography and geochemistry. *Ore Geology Reviews*, *80*, 860-875

Takahashi, Y., Manceau, A., Geoffroy, N., Marcus, M. A., & Usui, A. (2007). Chemical and structural control of the partitioning of Co, Ce, and Pb in marine ferromanganese oxides. *Geochimica et Cosmochimica Acta*, *71*(4), 984-1008.

Thibon, F., Blichert-Toft, J., Tsikos, H., Foden, J., Albalat, E., & Albarede, F. (2019). Dynamics of oceanic iron prior to the Great Oxygenation Event. *Earth and Planetary Science Letters*, 506, 360-370.

Trendall, A. F. (2002). The significance of iron-formation in the Precambrian stratigraphic record. *Precambrian sedimentary environments: A modern approach to ancient depositional systems*, 33-66.

Tsikos, H., Beukes, N. J., Moore, J. M., & Harris, C. (2003). Deposition, diagenesis, and secondary enrichment of metals in the Paleoproterozoic Hotazel iron formation, Kalahari Manganese Field, South Africa. *Economic Geology*, *98*(7), 1449-1462.

Tsikos, H., Matthews, A., Erel, Y., & Moore, J. M. (2010). Iron isotopes constrain biogeochemical redox cycling of iron and manganese in a Palaeoproterozoic stratified basin. *Earth and Planetary Science Letters*, *298*(1-2), 125-134.

Tsikos, H., & Moore, J. M. (1997). Petrography and geochemistry of the Paleoproterozoic Hotazel Iron-Formation, Kalahari manganese field, South Africa; implications for Precambrian manganese metallogenesis. *Economic Geology*, *92*(1), 87-97.

Tsikos, H., & Moore, J. M. (2005). Sodic metasomatism in the Palaeoproterozoic Hotazel iron-formation, Transvaal Supergroup, South Africa: implications for fluid–rock interaction in the Kalahari manganese field. *Geofluids*, *5*(4), 264-271.

Tsikos, H., Moore, J. M., & Harris, C. (2001). Geochemistry of the Palaeoproterozoic Mooidraai formation: Fe-rich limestone as end member of iron formation deposition, Kalahari manganese field, Transvaal Supergroup, South Africa. *Journal of African Earth Sciences*, *32*(1), 19-27.

Weissert, H., McKenzie, J., & Hochuli, P. (1979). Cyclic anoxic events in the early Cretaceous Tethys Ocean. *Geology*, *7*(3), 147-151.

Weissert, H., Joachimski, M., & Sarnthein, M. (2008). Chemostratigraphy. Newsletters on Stratigraphy, 42(3), 145-179.

Zhang, J., & Nozaki, Y. (1996). Rare earth elements and yttrium in seawater: ICP-MS determinations in the East Caroline, Coral Sea, and South Fiji basins of the western South Pacific Ocean. *Geochimica et Cosmochimica Acta*, *60*(23), 4631-4644.

Zhang, J., & Nozaki, Y. (1998). Behavior of rare earth elements in seawater at the ocean margin: a study along the slopes of the Sagami and Nankai troughs near Japan. *Geochimica et Cosmochimica Acta*, *62*(8), 1307-1317.

6. Appendix

A1. Major element raw data

G774 – BIF

Sample	Depth	Fe_2O_3	MnO_2	TiO_2	CaO	K_2O	P_2O_5	SiO_2	Al_2O_3	MgO	Na_2O	LOI
	(m)	(wt%)										
G7BF-01	90.81	30.32	0.37	0.00	2.62	0.00	0.07	61.59	0.04	0.80	0.00	3.01
G7BF-02	91.28	28.56	0.65	0.00	3.67	0.04	0.11	58.93	0.08	2.36	0.00	5.36
G7BF-03	91.65	41.89	0.62	0.00	3.63	0.04	0.24	46.67	0.03	2.31	0.00	4.47
G7BF-04	92.10	39.26	0.46	0.00	2.12	0.05	0.04	49.06	0.01	4.56	0.00	3.52
G7BF-05	92.48	41.32	0.43	0.00	1.91	0.05	0.05	50.41	0.04	3.11	0.00	2.47
G7BF-06	92.94	39.80	0.37	0.00	2.11	0.05	0.09	50.66	0.04	3.12	0.00	2.70
G7BF-07	93.34	40.64	0.65	0.00	8.58	0.03	0.12	38.58	0.05	2.04	0.00	8.50
G7BF-08	93.88	45.33	0.26	0.00	3.50	0.01	0.14	46.06	0.04	0.92	0.00	2.90
G7BF-09	94.35	38.88	0.54	0.00	7.05	0.01	0.16	42.39	0.13	1.94	0.00	7.46
G7BF-10	94.73	49.38	1.36	0.00	2.88	0.01	0.09	35.67	0.27	2.66	0.00	8.40
G7BF-11	95.11	28.70	0.40	0.00	9.19	0.04	0.06	49.92	0.16	1.87	0.00	8.67
G7BF-12	95.73	40.82	0.25	0.00	3.22	0.07	0.03	47.70	0.26	3.25	0.00	4.42
G7BF-13	96.23	34.71	0.26	0.00	2.51	0.04	0.06	55.76	0.27	2.37	0.00	3.89
G7BF-14	96.73	41.14	0.42	0.03	3.80	0.03	0.05	40.03	0.88	4.07	0.00	8.38
G7BF-15	97.15	31.42	0.78	0.00	1.91	0.05	0.05	56.16	0.23	3.04	0.00	6.33
G7BF-16	97.54	44.95	0.63	0.00	1.69	0.03	0.09	42.86	0.34	3.37	0.00	5.39
G7BF-17	98.02	59.38	0.60	0.00	1.12	0.02	0.01	30.04	0.59	3.58	0.00	5.18
G7BF-18	98.60	40.48	0.85	0.01	2.50	0.03	0.05	45.55	0.46	3.12	0.00	7.35
G7BF-19	99.02	49.30	0.65	0.02	1.82	0.01	0.24	37.74	0.75	2.98	0.00	5.82
G7BF-20	99.42	33.61	0.48	0.00	5.12	0.05	0.15	49.41	0.37	3.66	0.00	6.83
G7BF-21	100.18	31.58	1.35	0.03	13.68	0.03	0.08	32.60	0.96	3.36	0.00	15.03
G7BF-22	100.56	25.13	1.23	0.00	4.75	0.01	0.06	56.87	0.35	3.18	0.00	8.29
G7BF-23	101	57.85	4.07	0.01	8.49	0.00	0.04	18.28	0.39	3.18	0.00	10.31
G7BF-24	101.64	18.58	6.27	0.01	31.92	0.00	0.05	10.73	0.31	4.40	0.00	28.64

G774 – Hematite lutite

Sample	Depth	Fe_2O_3	MnO_2	TiO_2	CaO	K_2O	P_2O_5	SiO_2	Al_2O_3	MgO	Na_2O	LOI
	(m)	(wt%)										
G7-104	151.75	54.66	1.92	0.01	3.60	0.02	0.08	31.27	0.02	2.71	0.03	5.45
G7-105	152.05	52.15	7.39	0.02	6.35	bdl	0.09	19.26	0.11	2.66	0.04	11.76
G7-106	152.39	44.83	8.13	0.02	7.03	bdl	0.08	22.53	0.16	3.67	0.05	13.12
G7-107	152.85	49.42	7.56	0.03	7.66	0.05	0.08	18.03	0.04	3.12	0.05	13.77
G7-108	153.36	61.46	4.75	0.02	4.15	0.01	0.07	20.61	bdl	1.38	0.05	6.87
G7-109	153.80	50.28	5.82	0.02	5.40	0.04	0.08	24.87	0.01	2.37	0.04	10.23
G7-110	154.26	57.00	4.71	0.02	4.12	0.04	0.10	22.70	0.31	2.86	0.04	8.18
G7-111	154.73	57.89	5.60	0.02	3.10	0.03	0.10	19.31	0.14	1.66	0.05	11.60
G7-112	155.21	64.45	7.56	0.01	3.41	bdl	0.08	16.68	0.06	1.04	0.02	8.05
G7-113	155.69	47.26	7.86	0.01	3.52	0.01	0.08	28.07	0.08	2.55	0.03	10.86
G7-114	156.25	52.23	4.79	0.02	2.11	0.02	0.07	31.02	0.04	2.39	0.03	7.05
G7-115	156.74	52.21	4.79	0.01	2.01	0.03	0.08	30.78	0.03	2.21	0.03	7.03
G7-116	157.17	50.05	6.49	0.01	1.54	0.02	0.04	30.89	0.06	1.66	0.04	8.91
G7-117	157.62	51.68	7.93	0.02	1.68	bdl	0.11	25.89	0.10	3.03	0.03	9.85
G7-118	158.13	62.97	3.56	0.02	0.92	bdl	0.07	29.26	0.16	0.89	bdl	2.86
G7-119	158.58	40.25	4.33	0.01	0.58	0.01	0.13	50.34	0.19	0.27	0.02	3.19
G7-120	159.03	26.59	24.19	0.01	2.41	bdl	0.02	29.46	bdl	0.66	0.02	16.75
G7-121	159.63	46.09	20.67	0.02	1.95	bdl	0.08	13.12	0.08	2.79	0.03	15.32
G7-122	160.00	45.41	18.53	0.02	1.58	bdl	0.04	17.15	0.04	3.52	0.03	13.75
G7-123	160.53	46.01	16.18	0.01	1.08	bdl	0.10	20.56	0.04	5.51	0.03	12.20
G7-124	160.95	41.88	14.41	0.02	0.85	bdl	0.06	27.54	bdl	4.53	0.03	11.05
G7-125	161.44	46.32	10.06	0.00	0.58	bdl	0.05	23.78	bdl	10.54	0.03	8.68
G7-126	161.92	23.90	8.75	0.01	0.60	bdl	0.05	38.80	0.02	18.11	0.03	9.73
G7-127	162.50	36.41	33.94	0.02	1.80	bdl	0.07	7.60	0.19	2.16	0.04	19.54
G7-128	163.10	34.66	9.87	0.01	0.66	0.01	0.09	31.55	0.01	14.25	0.02	9.53
G7-129	163.49	36.80	29.96	0.02	1.20	0.01	0.09	15.79	0.13	3.29	0.02	14.67
G7-130	163.84	37.45	19.77	0.01	1.01	0.01	0.05	20.77	0.20	6.81	0.01	13.31
G7-131	164.40	37.45	18.12	0.01	1.00	bdl	0.04	21.55	bdl	9.56	0.02	13.13
G7-132	165.08	29.97	29.54	0.02	1.48	bdl	0.04	14.38	0.15	5.38	0.02	18.43
G7-133	165.64	48.09	24.28	0.02	1.29	0.01	0.10	11.57	0.13	2.23	0.03	13.55
G7-134	166.04	54.00	10.75	0.01	0.70	bdl	0.12	17.33	0.01	7.99	0.06	8.77
G7-135	166.63	38.71	8.12	0.01	0.58	bdl	0.09	45.82	0.15	1.58	0.04	3.94
G7-136	167.07	40.23	13.04	0.02	3.89	bdl	0.15	27.39	0.15	3.83	0.03	11.80

G774 – Manganese ore

Sample	Depth	Fe_2O_3	MnO_2	TiO_2	CaO	K_2O	P_2O_5	SiO_2	Al_2O_3	MgO	Na_2O	LOI
	(m)	(wt%)										
G7-001	101.94	14.98	15.81	0.01	28.96	bdl	0.05	3.81	0.23	4.35	0.01	30.89
G7-002	102.29	13.79	14.92	0.01	29.53	bdl	0.05	3.81	0.25	5.17	0.01	31.56
G7-003	102.83	7.62	23.09	0.01	28.67	bdl	0.03	6.96	0.31	6.26	0.01	28.16
G7-004	103.27	9.45	27.76	0.01	26.97	bdl	0.03	4.95	0.27	3.73	0.01	25.87
G7-005	103.82	10.33	27.03	0.02	24.95	bdl	0.04	6.29	0.40	3.92	0.02	26.03
G7-006	104.30	9.93	27.81	0.02	26.04	bdl	0.04	5.39	0.33	4.14	0.01	25.66
G7-007	104.88	9.09	35.90	0.02	22.48	bdl	0.03	5.53	0.25	3.86	0.02	22.38
G7-008	105.32	14.57	39.28	0.02	15.09	bdl	0.04	6.67	0.31	5.17	0.04	19.70
G7-009	105.85	17.39	40.75	0.02	12.88	bdl	0.03	6.70	0.15	5.17	0.03	17.58
G7-010	106.27	11.40	45.08	0.02	14.25	bdl	0.04	6.87	0.13	4.40	0.02	17.89
G7-011	106.76	15.54	40.60	0.02	14.23	bdl	0.04	6.54	0.18	4.81	0.03	18.51
G7-012	107.25	15.19	39.76	0.02	14.52	bdl	0.05	6.70	0.23	4.92	0.03	19.06
G7-013	107.76	20.39	41.43	0.02	12.40	bdl	0.05	5.89	0.11	3.87	0.02	16.69
G7-014	108.16	11.18	45.30	0.02	14.84	bdl	0.04	6.44	0.23	4.13	0.02	18.69
G7-015	108.64	8.42	41.48	0.02	17.99	bdl	0.04	6.36	0.30	4.19	0.02	22.01
G7-016	109.03	9.14	39.90	0.02	19.86	bdl	0.05	5.55	0.34	3.71	0.02	21.97
G7-017	109.45	8.74	39.88	0.02	20.13	bdl	0.05	5.16	0.33	3.62	0.02	22.42
G7-018	109.97	8.18	47.91	0.02	17.67	bdl	0.03	4.35	0.14	2.54	0.03	19.76
G7-019	110.54	8.03	45.18	0.02	18.62	bdl	0.02	4.99	0.17	2.72	0.02	21.29
G7-020	110.95	8.64	45.12	0.02	17.92	bdl	0.04	5.17	0.33	3.10	0.02	20.70
G7-021	111.55	8.15	48.56	0.02	16.08	bdl	0.05	5.14	0.33	3.24	0.05	19.52
G7-022	111.89	6.22	42.41	0.02	20.23	bdl	0.04	4.56	0.29	3.68	0.03	22.21
G7-023	112.40	5.82	38.26	0.02	22.73	bdl	0.05	4.60	0.37	3.72	0.02	23.47
G7-024	112.85	6.79	39.98	0.02	20.97	bdl	0.05	4.41	0.33	3.75	0.01	23.23
G7-025	113.38	6.56	42.17	0.02	20.67	bdl	0.04	4.11	0.28	3.47	0.05	22.09
G7-026	113.86	6.94	40.30	0.02	20.78	bdl	0.04	4.52	0.38	3.71	0.03	23.11
G7-027	114.36	7.04	36.19	0.03	22.33	bdl	0.04	4.39	0.38	4.18	0.01	24.74
G7-028	114.82	6.36	36.22	0.02	23.61	bdl	0.04	4.07	0.36	3.81	0.03	24.67
G7-029	115.10	6.51	41.31	0.02	20.37	bdl	0.04	4.38	0.29	3.40	0.02	22.81
G7-030	115.53	6.01	39.63	0.02	21.59	bdl	0.04	4.49	0.32	3.71	0.01	23.77
G7-031	116.08	5.90	36.99	0.02	23.69	bdl	0.04	4.32	0.31	3.39	0.02	24.40
G7-032	116.62	5.74	34.95	0.01	25.31	bdl	0.04	3.81	0.28	3.56	0.02	25.50
G7-033	117.15	6.24	34.82	0.02	23.82	bdl	0.04	4.31	0.37	4.22	0.01	25.49
G7-034	117.49	5.88	35.64	0.01	24.78	bdl	0.03	3.88	0.37	3.53	0.04	25.01
G7-035	118.01	6.62	35.89	0.02	23.28	bdl	0.04	4.61	0.40	3.84	0.03	25.08
G7-036	118.50	6.75	40.06	0.02	20.70	bdl	0.04	5.00	0.37	4.03	0.02	23.13
G7-037	119.07	6.80	38.51	0.02	20.97	bdl	0.04	5.15	0.43	4.53	0.02	23.76
G7-038	119.49	7.79	36.25	0.02	19.56	bdl	0.05	4.91	0.43	5.70	bdl	25.53
G7-039	119.94	7.08	51.27	0.02	14.26	bdl	0.03	4.37	0.10	4.57	0.02	19.95
G7-040	120.38	8.45	45.84	0.02	15.29	bdl	0.03	4.50	0.20	5.51	0.02	21.51
G7-041	120.93	5.07	67.52	0.04	9.38	bdl	0.02	2.98	0.18	2.81	0.05	12.49
G7-042	121.35	7.19	54.13	0.02	13.45	bdl	0.04	5.17	0.10	3.19	0.01	17.96
G7-043	121.63	8.65	42.55	0.02	17.63	bdl	0.04	5.01	0.19	4.55	0.02	22.49
G7-044	122.05	9.23	41.61	0.02	17.57	bdl	0.04	5.00	0.23	4.77	0.02	22.51
G7-045	122.52	7.67	40.10	0.02	20.21	bdl	0.04	4.60	0.19	4.17	bdl	23.26
G7-046	123.04	8.45	30.62	0.02	25.73	bdl	0.04	4.33	0.38	3.73	bdl	26.06
G7-047	123.52	9.15	32.05	0.02	24.41	bdl	0.04	4.82	0.22	3.69	bdl	24.88
G7-048	123.95	8.73	29.68	0.02	26.44	bdl	0.04	4.52	0.34	3.31	0.01	26.05
G7-049	124.46	8.23	26.88	0.02	29.85	bdl	0.03	3.92	0.28	2.61	0.01	27.28
G7-050	124.98	9.74	33.04	0.02	25.08	bdl	0.04	5.00	0.12	2.51	0.02	23.79
G7-051	125.44	11.07	27.94	0.02	24.65	bdl	0.04	5.90	0.44	4.44	0.02	24.74

G774 - Manganese ore (Continued)

Sample	Depth	Fe_2O_3	MnO_2	TiO_2	CaO	K_2O	P_2O_5	SiO_2	Al_2O_3	MgO	Na_2O	LOI
	(m)	(wt%)										
G7-052	125.93	7.92	22.92	0.02	31.91	bdl	0.03	4.14	0.28	2.69	0.02	29.14
G7-053	126.41	11.42	24.53	0.03	26.64	bdl	0.04	5.99	0.40	4.04	0.01	26.41
G7-054	126.87	11.95	24.51	0.03	28.14	bdl	0.04	4.83	0.50	3.18	0.01	25.91
G7-055	127.40	9.34	41.06	0.02	20.35	bdl	0.04	5.44	0.12	2.36	0.02	22.00
G7-056	127.86	9.21	37.64	0.02	22.14	bdl	0.03	4.37	0.08	2.88	0.02	23.65
G7-057	128.37	10.26	41.96	0.02	18.04	bdl	0.04	4.96	0.09	3.66	0.01	22.18
G7-058	128.84	10.45	38.87	0.03	17.96	bdl	0.04	4.93	0.20	4.96	0.02	23.37
G7-059	129.33	9.10	45.71	0.02	15.71	bdl	0.03	4.76	0.12	4.56	0.02	21.31
G7-060	129.79	8.58	44.62	0.02	15.44	bdl	0.04	5.58	0.19	4.87	0.02	21.93
G7-061	130.25	11.05	51.25	0.02	12.64	bdl	0.03	4.45	0.06	3.60	0.02	18.23
G7-062	130.70	7.38	51.79	0.02	13.42	bdl	0.02	5.55	0.11	3.89	0.02	19.11
G7-063	131.24	8.74	56.53	0.02	12.08	bdl	0.03	4.95	0.04	3.06	0.03	15.81
G7-064	131.70	5.38	58.46	0.02	12.46	bdl	0.03	6.02	0.05	2.52	0.01	15.57
G7-065	132.23	4.85	59.81	0.03	10.81	bdl	0.04	6.07	0.18	3.40	bdl	15.16
G7-066	132.66	4.45	61.24	0.02	10.34	bdl	0.03	6.01	0.18	3.13	0.03	15.19
G7-067	133.09	6.37	55.39	0.02	13.86	bdl	0.03	5.38	0.09	2.80	bdl	17.84
G7-068	133.51	7.41	50.62	0.02	14.87	bdl	0.04	4.67	0.07	3.43	bdl	20.25
G7-069	134.02	7.89	50.72	0.02	15.96	bdl	0.03	4.39	0.02	2.82	0.02	19.69
G7-070	135.45	6.93	49.75	0.02	16.20	bdl	0.03	4.90	bdl	2.88	0.02	20.45
G7-071	135.97	5.46	51.85	0.02	17.02	bdl	0.03	4.14	bdl	2.53	0.02	19.67
G7-072	136.55	5.64	43.45	0.02	25.78	bdl	0.03	2.86	0.17	0.56	0.01	20.54
G7-073	137.14	5.83	41.78	0.02	26.09	bdl	0.03	2.71	0.15	1.22	0.03	21.26
G7-074	137.54	9.44	50.26	0.02	14.91	bdl	0.05	6.26	0.31	2.66	0.02	17.62
G7-075	138.03	6.42	50.54	0.02	17.89	bdl	0.03	4.80	0.12	2.31	0.02	18.56
G7-076	138.47	4.88	65.41	0.02	9.28	bdl	0.04	6.26	0.12	2.15	0.02	12.12
G7-077	138.94	6.78	54.70	0.02	15.16	bdl	0.03	4.56	0.11	2.28	0.04	16.98
G7-078	139.29	7.21	55.18	0.02	15.14	bdl	0.03	4.89	0.17	2.01	0.01	16.76
G7-079	139.80	8.29	48.48	0.02	17.51	bdl	0.03	4.77	0.18	2.39	bdl	19.08
G7-080	140.28	8.27	56.32	0.02	12.72	bdl	0.03	4.80	0.09	2.99	0.02	16.46
G7-081	140.79	8.70	55.44	0.02	13.32	bdl	0.03	5.01	0.09	2.60	0.01	16.54
G7-082	141.26	10.47	42.55	0.02	18.68	bdl	0.04	4.01	0.13	3.13	0.01	21.49
G7-083	141.74	11.19	39.94	0.02	18.97	bdl	0.04	4.98	0.16	3.30	bdl	22.00
G7-084	142.15	11.44	45.46	0.02	17.58	bdl	0.04	4.42	0.14	2.52	0.01	19.62
G7-085	142.71	13.21	46.17	0.02	15.32	bdl	0.05	5.24	0.14	2.24	0.01	18.07
G7-086	143.19	15.62	40.88	0.02	17.72	bdl	0.04	5.01	0.19	2.38	bdl	20.13
G7-087	143.63	15.58	42.47	0.02	14.51	bdl	0.06	6.40	0.30	2.98	0.01	17.80
G7-088	144.05	16.25	37.85	0.02	16.79	bdl	0.04	6.30	0.33	3.75	0.03	20.33
G7-089	144.53	15.27	41.58	0.02	13.54	bdl	0.04	7.00	0.18	3.96	0.02	19.33
G7-090	145.15	24.36	35.61	0.02	8.15	bdl	0.05	8.92	0.16	5.75	0.02	16.36
G7-091	145.56	26.05	24.53	0.02	7.48	bdl	0.05	13.86	0.19	7.64	0.02	19.95
G7-092	146.06	29.55	22.62	0.02	7.84	bdl	0.07	9.56	0.18	7.95	0.04	22.62
G7-093	146.48	26.86	24.51	0.02	4.10	bdl	0.04	15.04	0.21	9.02	0.03	20.92
G7-094	146.96	31.07	26.57	0.02	4.26	bdl	0.06	11.26	0.18	6.44	0.03	21.62
G7-095	147.44	41.95	18.25	0.02	3.08	bdl	0.05	14.76	0.11	7.83	0.03	15.79
G7-096	148.02	34.30	10.85	0.01	1.98	bdl	0.03	27.10	0.18	13.08	0.04	11.98
G7-097	148.47	41.42	14.87	0.02	2.18	bdl	0.07	19.00	0.21	9.22	0.03	14.10
G7-098	148.96	48.39	13.47	0.02	2.17	bdl	0.05	16.03	0.27	7.87	0.03	13.18
G7-099	149.39	47.75	11.99	0.02	2.66	bdl	0.09	17.54	0.19	8.51	0.02	12.22
G7-100	149.90	48.40	11.63	0.02	3.97	bdl	0.10	15.80	0.29	7.70	0.03	12.98
G7-101	150.40	42.12	8.63	0.01	8.59	bdl	0.02	14.02	0.07	8.14	0.03	17.60
G7-102	150.89	52.24	5.27	0.01	2.86	bdl	0.06	25.81	0.27	3.73	0.02	8.74
G7-103	151.50	58.69	2.69	0.01	4.80	bdl	0.06	22.64	0.09	2.82	0.03	8.04

MP-56 – BIF

Sample	Depth	Fe_2O_3	MnO_2	TiO_2	CaO	K_2O	P_2O_5	SiO_2	Al_2O_3	MgO	Na_2O	LOI
	(m)	(wt%)										
MP-BIF-01	396.45	15.5	1.57	0.00	10.50	0.01	0.10	61.24	0.04	0.46	0.02	10.20
MP-BIF-02	396.67	41.8	1.00	0.00	7.95	0.01	0.13	39.89	0.03	1.36	0.00	8.49
MP-BIF-03	397.19	42.5	1.35	0.00	6.34	0.02	0.07	38.97	0.05	2.80	0.00	8.78
MP-BIF-04	397.85	40.2	1.16	0.00	5.96	0.03	0.08	41.49	0.08	2.83	0.00	8.18
MP-BIF-05	398.48	44.8	0.90	0.00	4.53	0.02	0.13	40.96	0.05	1.93	0.07	5.77
MP-BIF-06	398.74	41.8	1.23	0.00	6.04	0.02	0.05	39.97	0.13	2.29	0.00	8.50
MP-BIF-07	399.22	43.5	0.78	0.00	3.28	0.03	0.11	46.38	0.04	1.89	0.00	4.51
MP-BIF-08	399.72	47.9	0.81	0.00	3.76	0.01	0.10	40.17	0.02	1.56	0.00	4.58
MP-BIF-09	400.21	49.2	0.57	0.00	1.83	0.03	0.18	42.20	0.01	3.38	0.00	2.56
MP-BIF-10	400.67	45.1	1.25	0.00	6.53	0.02	0.11	36.48	0.01	2.22	0.00	8.04
MP-BIF-11	401.24	47.3	1.39	0.00	8.61	0.02	0.10	30.39	0.02	1.90	0.00	9.93
MP-BIF-12	401.68	44.1	0.78	0.00	3.49	0.03	0.19	42.46	0.00	3.50	0.00	4.55
MP-BIF-13	402.04	48.8	0.62	0.00	2.35	0.03	0.18	42.83	0.03	2.37	0.00	2.67
MP-BIF-14	402.56	53.4	0.50	0.00	2.05	0.02	0.16	40.29	0.02	1.40	0.00	1.69
MP-BIF-15	403.06	46.1	0.71	0.00	3.08	0.03	0.28	42.54	0.01	2.76	0.00	3.67
MP-BIF-16	403.55	43.0	0.73	0.01	1.33	0.01	0.06	44.55	0.38	2.26	0.00	7.77
MP-BIF-17	404.04	47.9	0.78	0.00	2.50	0.03	0.18	41.75	0.01	3.23	0.00	3.68
MP-BIF-18	404.55	44.5	1.05	0.00	4.91	0.03	0.11	40.44	0.02	2.96	0.00	6.42
MP-BIF-19	405	43.0	1.42	0.00	4.71	0.03	0.10	39.87	0.03	2.91	0.00	7.50
MP-BIF-20	405.48	61.2	0.73	0.00	2.06	0.02	0.31	31.92	0.00	1.59	0.00	2.17
MP-BIF-21	405.92	50.2	1.00	0.00	3.03	0.02	0.21	39.14	0.03	2.10	0.00	4.37
MP-BIF-22	406.37	54.6	1.08	0.00	3.21	0.01	0.23	33.90	0.00	1.64	0.00	4.49
MP-BIF-23	406.79	51.9	0.64	0.00	1.38	0.03	0.30	40.20	0.02	3.53	0.00	2.24
MP-BIF-24	407.28	53.7	1.27	0.00	3.06	0.01	0.18	33.74	0.25	2.82	0.00	5.31
MP-BIF-25	407.80	55.6	0.86	0.00	2.44	0.01	0.42	35.64	0.01	1.52	0.00	3.51
MP-BIF-26	408.32	48.5	1.15	0.00	3.27	0.06	0.17	37.98	0.03	2.39	0.44	5.35
MP-BIF-27	408.70	49.9	0.50	0.00	0.76	0.04	0.22	43.10	0.04	3.87	0.00	1.88
MP-BIF-28	409.22	47.3	1.11	0.00	3.03	0.03	0.09	37.58	0.02	2.41	0.00	8.69
MP-BIF-29	409.73	43.2	1.18	0.00	3.29	0.03	0.09	43.02	0.08	2.66	0.00	5.92
MP-BIF-30	410.21	43.4	1.47	0.00	4.84	0.02	0.02	39.21	0.07	2.94	0.00	8.40
MP-BIF-31	410.55	37.4	2.05	0.00	6.88	0.02	0.03	39.11	0.09	3.36	0.00	11.65
MP-BIF-32	411.02	45.4	0.91	0.00	1.98	0.03	0.04	42.74	0.09	3.12	0.00	5.95
MP-BIF-33	411.45	48.1	0.60	0.00	1.10	0.03	0.18	44.12	0.08	2.41	0.00	2.52
MP-BIF-34	411.96	43.9	1.11	0.00	2.93	0.04	0.10	42.88	0.10	3.19	0.00	6.29
MP-BIF-35	412.47	45.9	1.69	0.00	5.38	0.01	0.05	35.03	0.07	2.59	0.00	9.81
MP-BIF-36	412.99	43.4	1.15	0.00	3.55	0.03	0.05	41.99	0.08	2.66	0.00	6.53
MP-BIF-37	413.49	44.4	1.07	0.00	6.84	0.03	0.15	39.07	0.03	3.52	0.00	4.90
MP-BIF-38	413.98	48.8	1.03	0.00	3.29	0.01	0.10	38.92	0.06	1.89	0.00	5.92
MP-BIF-39	414.53	45.1	0.69	0.00	1.72	0.03	0.29	45.92	0.11	2.54	0.00	3.67
MP-BIF-40	414.93	42.9	1.03	0.00	2.87	0.02	0.10	43.92	0.21	2.11	0.00	6.38
MP-BIF-41	415.51	47.4	0.79	0.00	2.97	0.01	0.15	41.58	0.11	2.02	0.00	4.92
MP-BIF-42	415.87	38.5	1.02	0.00	3.38	0.01	0.13	47.69	0.21	2.33	0.00	6.79
MP-BIF-43	416.30	38.2	1.35	0.00	6.11	0.01	0.05	41.23	0.25	2.57	0.00	9.68
MP-BIF-44	416.82	38.6	2.03	0.01	6.07	0.02	0.16	35.08	0.64	4.30	0.00	13.90
MP-BIF-45	417.29	37.8	1.08	0.00	3.60	0.02	0.07	47.76	0.25	2.53	0.00	7.00
MP-BIF-46	417.86	53.3	1.69	0.00	5.94	0.01	0.21	31.80	0.04	2.49	0.00	4.78
MP-BIF-47	418.43	52.2	0.76	0.00	1.93	0.01	0.06	37.53	0.23	1.97	0.00	4.38
MP-BIF-48	418.90	35.0	0.92	0.00	0.49	0.01	0.01	53.77	0.29	2.70	0.00	7.23
MP-BIF-49	419.41	48.8	1.15	0.00	3.96	0.01	0.21	39.56	0.05	1.92	0.00	4.58
MP-BIF-50	419.85	39.1	0.99	0.00	1.62	0.01	0.12	50.14	0.24	2.76	0.00	4.43
MP-BIF-51	420.30	40.9	0.56	0.00	0.27	0.01	0.01	53.96	0.27	2.38	0.00	2.11
MP-BIF-52	420.41	46.5	0.68	0.01	6.04	0.01	0.11	37.30	0.35	3.02	0.00	5.48
MP-BIF-53	420.92	64.8	1.19	0.00	3.64	0.00	0.46	22.51	0.10	2.92	0.00	3.79

MP-56 – Manganese ore

Sample	Depth	Fe_2O_3	MnO_2	TiO_2	CaO	K_2O	P_2O_5	SiO_2	Al_2O_3	MgO	Na_2O	LOI
	(m)	(wt%)										
MP-100	421.46	44.1	11.16	0.02	14.60	bdl	0.04	3.63	bdl	4.83	0.02	21.92
MP-101	421.70	30.1	10.43	0.01	15.51	bdl	0.06	9.93	0.13	8.93	0.03	24.87
MP-102	422.10	14.0	18.94	0.01	17.39	bdl	0.04	8.20	0.10	11.37	0.01	29.47
MP-103	422.75	12.4	18.58	0.01	17.83	bdl	0.04	8.62	0.10	11.87	0.03	29.82
MP-104	423.15	7.9	21.92	0.01	24.70	bdl	0.03	5.88	0.13	6.88	0.01	31.59
MP-105	423.74	7.7	26.91	0.01	27.93	bdl	0.03	4.87	0.08	3.92	bdl	27.60
MP-106	424.28	8.8	26.81	0.02	25.91	bdl	0.03	6.55	0.17	5.54	0.01	25.38
MP-107	424.49	8.7	31.90	0.02	25.98	bdl	0.03	4.53	0.13	3.06	0.01	24.68
MP-108	425.10	10.2	29.92	0.02	24.13	bdl	0.04	5.60	0.40	3.91	0.02	24.82
MP-109	425.70	8.9	27.75	0.01	28.96	bdl	0.04	3.95	0.26	2.93	bdl	26.54
MP-110	426.30	10.0	37.49	0.02	22.04	bdl	0.03	4.58	0.12	2.77	0.02	22.68
MP-111	426.85	30.9	33.04	0.03	12.32	bdl	0.06	5.11	0.21	3.00	0.03	15.58
MP-112	427.32	12.6	43.55	0.02	15.57	bdl	0.04	5.65	0.17	3.40	0.02	19.08
MP-113	427.93	25.8	38.31	0.02	10.76	bdl	0.06	5.82	0.19	3.09	0.03	15.14
MP-114	428.30	21.2	42.30	0.03	10.79	bdl	0.05	5.81	0.19	3.63	0.02	15.00
MP-115	428.65	21.0	43.83	0.02	10.30	bdl	0.05	5.75	0.29	3.30	0.02	14.62
MP-116	429.25	13.4	45.55	0.02	14.54	bdl	0.04	5.89	0.09	3.03	0.01	18.01
MP-117	429.50	12.8	29.20	0.02	25.93	bdl	0.05	4.58	0.43	2.61	0.01	23.99
MP-118	430.08	7.5	36.74	0.02	23.70	bdl	0.04	5.03	0.22	2.64	0.01	23.14
MP-119	430.48	6.9	28.83	0.01	29.87	bdl	0.03	3.98	0.16	2.63	0.01	26.68
MP-120	430.94	8.4	33.15	0.02	26.91	bdl	0.03	4.31	0.37	2.05	0.03	23.80
MP-121	431.39	6.2	35.48	0.02	26.29	bdl	0.03	4.77	0.16	2.05	0.00	24.06
MP-122	431.92	8.8	48.78	0.02	15.71	bdl	0.03	5.52	0.23	2.15	0.02	18.43
MP-123	432.31	7.9	48.01	0.02	16.66	bdl	0.03	5.06	0.20	2.03	0.01	19.25
MP-124	432.70	17.9	47.98	0.02	10.83	bdl	0.04	6.80	0.27	1.77	0.01	13.38
MP-125	433.10	6.8	46.24	0.02	18.10	bdl	0.03	4.58	0.12	3.33	0.03	21.22
MP-126	433.51	7.4	46.88	0.02	18.67	bdl	0.03	5.07	0.18	1.96	0.02	20.47
MP-127	433.85	10.4	37.10	0.02	22.03	bdl	0.05	4.29	0.26	2.47	0.01	23.11
MP-128	434.35	7.8	21.63	0.02	33.80	bdl	0.03	2.89	0.47	2.43	0.00	30.25
MP-129	434.95	6.8	47.17	0.02	16.54	bdl	0.03	4.74	0.08	3.53	0.01	22.15
MP-130	435.45	8.3	43.64	0.02	19.76	bdl	0.03	5.59	0.28	3.58	0.01	19.11
MP-131	435.90	9.2	49.92	0.02	14.34	bdl	0.02	5.43	0.13	3.14	0.01	17.93
MP-132	436.40	5.3	43.69	0.02	19.92	bdl	0.03	4.56	0.15	3.74	0.01	22.33
MP-133	436.80	6.1	44.94	0.02	20.98	bdl	0.04	2.42	0.08	3.05	0.01	21.59
MP-134	437.44	6.9	52.69	0.02	15.87	bdl	0.04	3.62	0.08	2.61	0.02	19.18
MP-135	437.95	8.3	31.13	0.01	28.31	bdl	0.04	2.77	0.17	2.28	bdl	26.56
MP-136	438.44	6.4	38.76	0.02	23.65	bdl	0.03	3.34	0.18	2.91	0.02	24.42
MP-137	438.95	5.9	56.68	0.02	16.10	bdl	0.03	3.71	0.04	1.58	0.02	17.08
MP-138	439.45	6.2	50.43	0.02	16.73	bdl	0.03	5.92	0.10	2.45	0.01	18.99
MP-139	439.80	6.6	58.84	0.02	11.05	bdl	0.03	7.22	0.13	2.70	0.01	15.06
MP-140	440.30	5.8	65.91	0.02	12.12	bdl	0.03	2.30	0.05	1.57	0.03	12.63
MP-141	440.75	8.5	58.35	0.03	9.42	bdl	0.03	6.88	0.12	3.15	0.03	14.47
MP-142	441.20	8.3	59.90	0.02	12.29	bdl	0.03	4.52	0.00	2.05	0.02	14.80
MP-143	441.80	9.7	54.65	0.02	14.40	bdl	0.03	3.89	0.03	2.42	0.02	16.69
MP-144	442.33	9.8	51.71	0.02	13.25	bdl	0.03	5.87	0.09	3.12	0.02	17.26
MP-145	442.90	11.3	46.84	0.02	16.12	bdl	0.04	5.28	0.12	2.49	0.02	19.41
MP-146	443.40	11.7	39.87	0.02	20.11	bdl	0.04	4.45	0.10	2.23	0.01	21.92
MP-147	443.85	15.9	35.24	0.02	19.08	bdl	0.05	5.60	0.23	3.16	0.02	22.65
MP-148	444.60	15.5	39.81	0.02	16.61	bdl	0.05	5.88	0.17	3.03	0.02	20.81
MP-149	445.30	19.0	37.29	0.02	11.93	bdl	0.05	7.61	0.16	4.24	0.02	18.87
MP-150	445.60	18.7	36.98	0.02	12.90	bdl	0.05	7.46	0.44	4.14	0.03	18.41
MP-151	446.30	27.0	21.35	0.02	10.92	bdl	0.06	8.82	0.09	8.00	0.04	23.69
MP-152	446.70	23.4	36.05	0.02	7.54	bdl	0.06	8.96	0.12	6.04	0.02	16.85
MP-153	447.22	40.4	17.91	0.02	3.86	bdl	0.06	14.31	0.09	7.97	0.03	16.92
MP-154	447.75	29.7	18.28	0.01	5.30	bdl	0.06	18.51	0.08	10.27	0.03	18.24
MP-155	448.15	29.0	18.61	0.02	3.43	bdl	0.05	20.69	0.12	10.99	0.03	17.54
MP-156	448.65	34.7	20.60	0.02	3.38	bdl	0.06	15.75	0.17	8.47	0.02	18.34
MP-157	449.25	41.1	14.10	0.01	2.39	bdl	0.05	19.71	0.10	9.84	0.03	13.65
MP-158	449.65	40.2	14.31	0.01	2.27	bdl	0.05	20.12	0.12	9.76	0.03	14.04
MP-159	450.05	37.5	18.78	0.02	2.66	bdl	0.09	16.93	0.20	8.32	0.03	16.75
MP-160	450.55	42.6	12.00	0.03	3.23	bdl	0.10	19.39	0.34	9.44	0.05	13.33
MP-161	451.15	26.9	10.43	0.02	2.50	bdl	0.08	42.04	0.27	5.17	0.04	11.60
MP-162	451.65	50.3	6.57	0.03	3.87	bdl	0.07	26.95	0.49	2.10	0.02	9.68
MP-163	452.20	46.0	4.68	0.02	2.87	0.01	0.05	36.62	0.37	1.87	bdl	7.42

MP-56 – Hematite lutite

Sample	Depth	Fe_2O_3	MnO_2	TiO_2	CaO	K_2O	P_2O_5	SiO_2	Al_2O_3	MgO	Na_2O	LOI
	(m)	(wt%)										
MP-164	452.70	21.8	3.01	0.01	2.02	0.01	0.03	67.98	0.16	0.64	0.03	3.84
MP-165	453.20	50.4	4.92	0.01	4.20	0.01	0.06	30.81	0.20	1.32	0.02	7.37
MP-166	453.60	65.7	3.54	0.02	4.47	0.01	0.08	19.08	0.26	1.71	0.01	6.27
MP-167	454.00	65.2	3.00	0.01	5.30	0.01	0.10	18.31	0.28	1.81	bdl	6.93
MP-168	454.50	54.3	3.38	0.02	5.44	0.03	0.08	27.09	0.26	2.09	0.01	7.71
MP-169	455.05	59.4	4.25	0.02	7.37	0.01	0.11	16.29	0.26	2.23	bdl	10.23
MP-170	455.55	48.1	5.53	0.01	6.37	bdl	0.11	28.32	0.24	1.35	0.02	9.61
MP-171	456.06	69.3	4.89	0.02	3.54	bdl	0.10	14.16	0.08	1.57	0.02	6.12
MP-172	456.68	56.4	3.82	0.02	5.02	0.01	0.07	27.13	0.29	1.45	0.01	6.68
MP-173	457.06	62.5	2.68	0.02	2.38	bdl	0.11	27.76	0.34	1.52	0.01	2.96
MP-174	457.36	55.1	4.38	0.01	0.80	0.01	0.06	33.01	0.30	3.24	0.01	3.79
MP-175	458	53.7	6.42	0.02	0.92	bdl	0.12	31.16	0.22	2.61	0.02	4.75
MP-176	458.55	52.0	3.21	0.02	1.01	0.01	0.08	40.91	0.33	1.08	bdl	2.31

A2. Transition metals raw data

G774 – BIF

Sample	Depth	Sc	V	Cr	Co	Ni	Cu	Pb	Mo
	(m)	(ppm)							
G7BF-01	90.81	2.09	7.2	29.2	24.52	18.8	4.4	0.9	0.2
G7BF-02	91.28	2.48	7.4	30.6	8.89	15.0	8.4	0.8	0.2
G7BF-03	91.65	2.02	7.2	34.0	3.48	39.7	10.9	1.2	0.2
G7BF-04	92.10	1.53	8.4	28.3	22.63	21.7	3.7	1.2	0.1
G7BF-05	92.48	2.52	8.3	29.1	6.98	23.1	7.2	1.1	0.2
G7BF-06	92.94	2.22	8.2	26.1	11.55	19.3	4.3	0.7	0.2
G7BF-07	93.34	2.26	6.8	26.2	8.56	12.4	3.7	1.2	0.2
G7BF-08	93.88	2.08	7.3	29.7	15.02	11.4	4.4	1.3	0.2
G7BF-09	94.35	2.55	10.7	30.2	33.95	28.6	6.6	0.9	0.4
G7BF-10	94.73	3.69	11.6	35.3	3.22	14.2	5.2	2.3	0.5
G7BF-11	95.11	3.13	9.9	27.5	9.9	16.0	5.9	0.8	0.2
G7BF-12	95.73	4.26	13.2	34.2	10.62	22.5	4.6	5.9	0.5
G7BF-13	96.23	4.24	12.6	35.1	11.78	42.3	4.0	1.8	0.6
G7BF-14	96.73	5.89	19.7	42.2	4.79	29.1	7.1	2.6	1.5
G7BF-15	97.15	3.18	11.1	26.1	0.01	18.8	7.7	1.4	0.5
G7BF-16	97.54	3.62	14.6	45.1	6.35	21.0	8.0	1.2	0.7
G7BF-17	98.02	4.10	12.8	33.2	9.91	22.6	4.5	1.8	1.8
G7BF-18	98.60	5.60	15.3	38.8	12.61	20.5	7.7	2.1	1.1
G7BF-19	99.02	6.20	21.6	46.2	3.02	20.4	6.9	1.5	1.4
G7BF-20	99.42	3.89	11.8	38.8	4.38	20.3	6.1	1.2	0.8
G7BF-21	100.18	6.84	21.6	50.5	13.62	36.2	16.8	4.8	1.7
G7BF-22	100.56	3.11	16.4	28.5	5.98	18.7	4.6	2.8	0.6
G7BF-23	101	3.20	13.3	56.8	5.98	29.1	7.4	1.5	0.8
G7BF-24	101.64	1.82	10.2	44.4	2.83	20.8	9.9	1.1	0.4

G774 – Hematite lutite

Sample	Depth	Sc	V	Cr	Co	Ni	Cu	Pb	Mo
	(m)	(ppm)							
G7-104	151.75	1.54	28.34	26.2	9.11	9.17	15.4	3.32	1.53
G7-105	152.05	1.77	27.12	22.1	35.7	10.02	34.1	2.68	1.56
G7-106	152.39	1.67	26.88	25.61	33.19	13.4	15.83	3.13	2.29
G7-107	152.85	1.68	26.87	28.3	27.96	11.4	17.7	2.92	2.11
G7-108	153.36	1.23	30.72	35.2	43.7	13	13.82	2.95	2.17
G7-109	153.80	1.39	29.82	32	18.99	11.2	22.88	3.10	2.35
G7-110	154.26	1.28	31.38	29.5	19.22	11	16.05	4.97	1.85
G7-111	154.73	1.49	29.97	26.6	30.18	10.65	14.12	4.31	1.98
G7-112	155.21	1.47	30.16	24.3	18.18	10.08	15.59	2.02	2.11
G7-113	155.69	1.92	28.85	24.2	33.64	12.6	13.78	4.64	2.81
G7-114	156.25	1.71	31.3	27.8	16.73	11.2	21.07	5.37	1.99
G7-115	156.74	1.54	30.94	25.6	12.53	11.04	16.75	10.20	1.95
G7-116	157.17	1.58	27.31	25.4	6.61	8.65	15.13	7.32	2.01
G7-117	157.62	1.81	27.24	24.99	9.04	9.78	24.9	48.10	1.95
G7-118	158.13	1.62	29.77	30.5	6.34	12.42	9.67	1.06	2.04
G7-119	158.58	1.49	37.26	55.5	8.7	17.9	21.46	1.22	3.60
G7-120	159.03	1.75	25.58	30.3	4.83	11.4	16.67	1.09	3.57
G7-121	159.63	1.09	19.64	14.4	23.05	7.74	8.37	1.18	2.37
G7-122	160.00	1.11	20.13	15.13	32.33	9.74	11.97	1.70	2.49
G7-123	160.53	1.04	21.45	16.13	50.15	8.75	12.1	1.79	2.30
G7-124	160.95	1.27	22.68	16.4	47.14	7.89	13.29	2.96	2.54
G7-125	161.44	0.93	21.17	13.3	30.7	6.12	8.98	2.24	1.61
G7-126	161.92	1.73	34.66	19.3	135.5	18.5	8.19	3.13	2.07
G7-127	162.50	0.93	13.31	12.14	11.89	5.36	5.84	0.74	2.82
G7-128	163.10	1.14	24.12	18.7	91.8	12.6	10.08	3.64	1.93
G7-129	163.49	1.22	18.82	18.26	27.53	8.79	12.98	1.84	3.35
G7-130	163.84	0.96	18.96	17.87	53.26	11.8	7.27	2.20	3.03
G7-131	164.40	0.84	20.2	14.94	60.9	10.2	7.91	4.83	2.39
G7-132	165.08	0.95	16.36	15.4	34.51	8.24	6.43	1.75	3.19
G7-133	165.64	0.9	20.56	17.25	16.61	7.39	10.65	1.94	2.70
G7-134	166.04	1.07	21.38	14.1	32.56	7.49	8.53	3.08	1.63
G7-135	166.63	1.09	33.6	43.4	12.72	15.1	21.58	1.96	3.11
G7-136	167.07	1.2	26.53	19.6	1.7	8.63	9.4	1.72	2.52

G774 – Manganese -ore

Sample	Depth	Sc	V	Cr	Co	Ni	Cu	Pb	Mo
	(m)	(ppm)							
G7-001	101.94	0.88	20.56	18.3	23.88	14.4	15.97	0.87	1.58
G7-002	102.29	0.89	22.88	15.1	24.02	10.17	15.73	0.48	1.33
G7-003	102.83	1.28	14.45	22.7	38.7	15.6	31	1.01	2.33
G7-004	103.27	0.62	11.49	15.8	27.55	8.54	11.78	1.23	1.89
G7-005	103.82	0.98	16.85	31.2	29.55	13.9	20.9	1.12	2.89
G7-006	104.30	1.03	12.46	18.5	30.28	10.31	11.66	0.84	2.16
G7-007	104.88	0.91	12.71	16.3	29.81	10.18	10.82	0.91	2.48
G7-008	105.32	1.12	13.73	19.5	34.74	11.18	13.24	1.08	2.80
G7-009	105.85	1.18	13.72	18	35.1	11	12.16	0.99	2.91
G7-010	106.27	0.89	13.99	17.2	36.7	11.5	14.14	1.07	3.51
G7-011	106.76	0.86	13.47	18.35	33.38	9.84	8.94	1.35	2.61
G7-012	107.25	1.33	14.5	17.4	34.42	13.4	15.4	0.87	2.93
G7-013	107.76	1.26	14.78	20.7	35	13.21	10.81	1.15	2.81
G7-014	108.16	0.71	14.72	16.9	35.93	11.09	21.2	0.85	3.40
G7-015	108.64	0.65	15.05	19.5	32.37	11.67	10.85	1.15	2.68
G7-016	109.03	0.97	13.12	17.95	27.64	11.4	11.16	0.91	2.77
G7-017	109.45	0.96	13.45	17.2	28.13	10.93	22.9	4.77	3.17
G7-018	109.97	1	12.47	15.2	37.28	9.02	13.63	0.58	3.09
G7-019	110.54	0.7	15.32	23.1	29.7	12.9	23.7	1.69	2.96
G7-020	110.95	0.92	12.85	18.2	32.15	10.71	14.27	0.77	3.24
G7-021	111.55	0.86	14.1	18.2	40.35	11.59	11.34	0.87	3.22
G7-022	111.89	0.82	13.26	16.55	33.74	11.48	11.65	0.98	3.06
G7-023	112.40	0.72	12.75	18.5	32.54	12.58	9.09	1.06	2.71
G7-024	112.85	0.8	12.03	16.9	26.16	10.24	11.1	1.02	2.85
G7-025	113.38	0.84	12.7	17.4	30.51	10.05	11.15	0.83	2.87
G7-026	113.86	0.76	13.05	18.72	28.79	10.82	8.67	0.94	2.53
G7-027	114.36	1	14.13	20.3	24.95	11.1	12.97	1.00	2.56
G7-028	114.82	0.77	11.74	16.9	20.18	10.09	12.66	0.78	2.84
G7-029	115.10	0.92	13.67	19	25.08	10.95	15.06	0.68	2.99
G7-030	115.53	0.79	12.68	16.44	23.09	10.4	15.66	0.67	3.06
G7-031	116.08	1.02	11.99	17	21.28	11.13	22.1	0.71	2.40
G7-032	116.62	0.97	12.1	16.5	19.28	9.84	8.69	0.72	2.63
G7-033	117.15	1.05	12.24	19.8	22.11	11.24	11.59	0.85	2.70
G7-034	117.49	0.82	12.6	16.7	22.75	9.68	7.49	0.53	2.51
G7-035	118.01	1	15.05	23.1	21.59	12.3	13.82	0.68	2.71
G7-036	118.50	0.86	13.73	18.2	25.72	11.35	11.15	0.52	2.57
G7-037	119.07	0.99	13.9	18.12	25.39	13.3	10.18	0.87	3.04
G7-038	119.49	1.18	13.53	22	24.03	13.3	10	1.01	3.01
G7-039	119.94	0.77	12.85	16.33	32.11	11.7	6.58	0.68	3.40
G7-040	120.38	1.17	12.3	19.9	29.83	12.4	10.18	0.50	3.32
G7-041	120.93	0.53	13.76	14.1	51	10.23	9.27	0.49	5.86
G7-042	121.35	1.08	14.39	21.5	32.98	13.9	12.69	1.13	3.91
G7-043	121.63	0.77	13.26	17.6	26.27	12.9	11.78	0.01	3.35
G7-044	122.05	0.84	13.48	19.6	27.76	13.97	6.29	0.86	3.31
G7-045	122.52	1.01	12.11	18.66	25.67	12.87	11.16	0.82	2.88
G7-046	123.04	0.96	12.27	18.4	26.89	13.2	9.74	0.57	2.39
G7-047	123.52	1.07	13.49	19.6	28.87	13.7	10.4	0.70	2.52
G7-048	123.95	1.03	13.17	18.8	24.59	13.28	9.42	0.93	2.64
G7-049	124.46	0.7	10.71	16.02	18.5	10.04	8.54	1.15	2.10
G7-050	124.98	0.59	13.51	17.8	26.44	12	26.4	1.11	2.74
G7-051	125.44	1.69	14.33	20	32.41	15.4	15.32	0.63	2.80

G774 – Manganese ore (Continued)

Sample	Depth	Sc	V	Cr	Co	Ni	Cu	Pb	Mo
	(m)	(ppm)							
G7-052	125.93	0.75	15.29	15.99	17.48	10.05	57.2	0.81	2.82
G7-053	126.41	1.55	20.23	26.3	29.49	15.7	11.46	1.27	2.89
G7-054	126.87	1.59	17.22	23	29.77	15.73	10.89	1.34	2.92
G7-055	127.40	0.77	18.02	17.88	28.93	11.79	11.07	1.62	4.23
G7-056	127.86	0.87	15.96	14.09	23.93	11.42	19.8	1.03	3.42
G7-057	128.37	0.68	16.68	14.5	25.74	11.75	11.3	1.13	4.02
G7-058	128.84	1	15.75	18.46	28.52	15	12.79	1.02	3.54
G7-059	129.33	1.01	16.54	15.12	34	12.09	7.98	0.98	4.21
G7-060	129.79	1.07	18.1	19.81	32.04	14.16	15.93	1.19	4.59
G7-061	130.25	0.76	18.58	19.54	39.1	13.58	9.72	1.80	4.71
G7-062	130.70	0.69	20.12	23	34.51	15.6	11.3	1.14	6.33
G7-063	131.24	0.67	18.36	16	37.6	12.17	11.7	1.08	5.17
G7-064	131.70	0.68	19.06	21.14	35.23	13.22	12.17	1.58	5.55
G7-065	132.23	0.78	18.8	16.4	38.32	15.5	15.02	1.37	4.94
G7-066	132.66	0.66	18.24	17.44	31.35	13.45	13.76	1.26	5.58
G7-067	133.09	0.7	17.93	15.2	31	12.98	9.65	1.71	5.10
G7-068	133.51	0.66	17.25	16.25	27.71	12.57	17.49	1.62	4.57
G7-069	134.02	0.51	17.68	15.62	29.19	10.68	10.02	1.42	4.57
G7-070	135.45	0.708	17.19	15.3	24.98	10.1	8.9	1.56	4.13
G7-071	135.97	0.65	16.25	21.6	37.1	13.17	8.78	1.73	4.39
G7-072	136.55	0.75	15.49	16.09	20.07	10.22	12.64	1.21	3.61
G7-073	137.14	0.59	13.86	11.52	20.62	9	10.33	0.96	3.25
G7-074	137.54	1.16	19.9	19.52	34.35	17.8	8.78	1.26	4.55
G7-075	138.03	0.61	17.99	15.13	26.57	11.28	9.97	0.78	3.88
G7-076	138.47	0.75	19.57	17.5	31.19	13.44	8.9	0.80	5.23
G7-077	138.94	0.78	17.26	17.6	28.91	14.2	11.04	0.62	4.45
G7-078	139.29	0.62	17.02	15.8	27.4	11.28	13.04	0.66	4.45
G7-079	139.80	0.76	19.1	18.1	29.25	13.23	27.8	0.74	4.49
G7-080	140.28	0.71	17.67	17.3	31.14	12.34	10.39	0.60	5.06
G7-081	140.79	0.69	19.94	17.9	32.03	11.81	11.56	0.54	4.93
G7-082	141.26	0.799	16.46	18.47	24.49	10.51	8.12	0.42	3.83
G7-083	141.74	1.07	18.18	20.6	25.65	13.1	10.93	0.92	3.63
G7-084	142.15	0.86	19.55	19	33.32	12.98	9.37	0.86	4.08
G7-085	142.71	1.11	18.96	18.8	36.17	15.1	15.3	1.12	4.50
G7-086	143.19	0.91	18.29	17.41	28.8	12.63	7.73	1.20	4.20
G7-087	143.63	1.39	20.27	21.9	35.28	14.1	7.84	1.94	4.46
G7-088	144.05	1.22	19.49	20.5	34.15	13.87	8.34	1.27	3.66
G7-089	144.53	0.98	21.32	19.8	36.16	12.17	12.66	1.63	4.27
G7-090	145.15	1.23	35.23	18.9	60.2	13.6	6.79	1.67	4.02
G7-091	145.56	1.25	23.59	21.5	56.69	13.59	7.6	0.78	3.64
G7-092	146.06	1.34	22.2	19.9	56.02	13.4	7.31	1.69	3.43
G7-093	146.48	1.43	22.72	20.2	65.22	14.9	11.12	1.65	4.02
G7-094	146.96	1.36	22.23	19.74	43.62	10.45	7.07	1.38	4.23
G7-095	147.44	1.51	22.55	22.4	48.16	13.45	8.98	2.20	2.96
G7-096	148.02	1.57	27.45	22.4	71.6	16.89	8.7	3.38	2.31
G7-097	148.47	1.39	25.11	24.78	55.6	13.5	10.46	4.09	2.95
G7-098	148.96	1.43	26	24.1	39.29	11.04	19.58	3.79	2.52
G7-099	149.39	1.76	26.32	20.8	40.01	10.5	10.69	1.92	2.32
G7-100	149.90	1.86	26.41	23.3	33.51	10.25	24.68	1.83	2.34
G7-101	150.40	1.35	21.65	17.8	33.62	7.38	17.02	2.42	1.94
G7-102	150.89	1.63	28.59	26.5	23.66	12.5	12.5	2.98	2.31
G7-103	151.50	1.4	27.33	26.59	7.56	10.46	13.96	2.23	1.90

MP-56 – BIF

Sample name	Depth	Sc	V	Cr	Co	Ni	Cu	Zn	Pb	Mo
	(m)	(ppm)								
MP-BIF-01	396.45	1.4	6.8	25.3	22.24	35.6	5.2	17.3	0.9	0.3
MP-BIF-02	396.67	1.7	6.9	25.7	4.47	12.9	7.0	75.1	1.5	0.2
MP-BIF-03	397.19	1.8	6.6	26.8	0.01	11.5	8.3	27.3	2.1	0.1
MP-BIF-04	397.85	2.6	7.8	27.7	3.55	7.7	4.7	26.2	1.7	0.2
MP-BIF-05	398.48	2.6	8.8	31.6	3.72	33.0	5.5	26.5	2.2	0.4
MP-BIF-06	398.74	2.5	8.9	25.1	7.01	16.8	8.7	34.9	2.0	0.4
MP-BIF-07	399.22	1.8	7.8	29.4	4.48	21.4	7.1	22.8	2.3	0.2
MP-BIF-08	399.72	2.3	8.1	29.5	3.55	17.8	5.6	21.4	1.6	0.3
MP-BIF-09	400.21	1.9	7.4	24.0	0.35	16.5	5.0	28.2	1.0	0.2
MP-BIF-10	400.67	2.2	7.1	23.2	0.01	8.2	4.7	25.8	1.0	0.1
MP-BIF-11	401.24	2.3	6.4	24.0	1.96	9.3	5.9	21.6	1.0	0.2
MP-BIF-12	401.68	2.0	7.8	31.0	3.15	18.9	5.8	28.5	1.2	0.1
MP-BIF-13	402.04	1.8	6.8	28.2	0.01	13.5	4.9	21.1	0.9	0.2
MP-BIF-14	402.56	2.1	7.1	28.0	1.81	14.9	4.4	17.7	2.0	0.2
MP-BIF-15	403.06	2.3	8.4	26.1	2.49	23.4	5.2	26.0	1.0	0.2
MP-BIF-16	403.55	4.0	16.0	39.5	4.06	22.2	5.2	23.4	2.9	0.9
MP-BIF-17	404.04	1.8	7.4	24.9	0.01	11.3	3.4	26.7	0.8	0.2
MP-BIF-18	404.55	2.2	7.2	44.3	2.53	32.6	6.3	24.7	43.0	0.1
MP-BIF-19	405	1.8	8.3	28.4	0.01	20.6	4.3	22.3	0.5	0.2
MP-BIF-20	405.48	2.0	7.9	29.5	1.88	18.0	8.1	25.0	0.8	0.1
MP-BIF-21	405.92	2.4	8.3	24.4	2.69	18.4	9.9	28.4	0.7	0.2
MP-BIF-22	406.37	1.8	9.0	28.4	5.76	19.1	5.1	21.6	1.0	0.2
MP-BIF-23	406.79	3.2	10.3	29.8	0.88	12.2	8.6	18.2	2.6	0.5
MP-BIF-24	407.28	3.2	14.6	34.4	13.29	16.6	3.9	19.3	2.1	0.9
MP-BIF-25	407.80	1.7	9.8	25.0	1.96	18.0	5.2	23.7	1.0	0.2
MP-BIF-26	408.32	2.3	7.5	27.3	1.50	16.0	4.7	25.3	0.9	0.2
MP-BIF-27	408.70	1.8	6.8	26.7	0.07	14.6	8.8	27.5	0.6	0.2
MP-BIF-28	409.22	2.1	7.5	28.0	0.01	9.4	5.9	24.3	1.0	0.2
MP-BIF-29	409.73	2.5	9.6	26.2	5.96	13.9	5.3	22.1	0.9	0.3
MP-BIF-30	410.21	2.3	8.7	24.8	0.01	24.8	5.7	24.6	1.3	0.3
MP-BIF-31	410.55	3.0	7.3	24.1	7.16	13.2	6.8	29.1	1.8	0.4
MP-BIF-32	411.02	2.9	6.8	22.8	0.01	21.5	6.4	27.8	1.5	0.4
MP-BIF-33	411.45	2.0	9.0	27.9	6.30	23.2	5.7	24.0	1.0	0.3
MP-BIF-34	411.96	3.1	7.2	24.0	10.74	12.1	6.1	33.2	0.9	0.2
MP-BIF-35	412.47	3.3	9.8	24.4	0.01	21.4	15.6	19.9	2.9	0.3
MP-BIF-36	412.99	2.8	9.5	30.6	24.66	29.8	13.8	28.5	1.2	0.4
MP-BIF-37	413.49	2.2	5.5	26.1	1.02	11.3	5.3	32.9	0.9	0.1
MP-BIF-38	413.98	2.7	10.0	29.8	2.13	19.0	16.8	19.6	1.4	0.3
MP-BIF-39	414.53	3.0	8.8	30.9	2.30	18.0	5.1	23.2	0.8	0.3
MP-BIF-40	414.93	2.8	12.7	32.8	3.76	30.2	4.0	26.7	1.2	0.5
MP-BIF-41	415.51	2.8	10.1	25.7	28.96	13.5	72.4	22.2	1.3	0.4
MP-BIF-42	415.87	3.3	10.3	31.2	28.95	22.9	63.5	23.0	1.7	0.4
MP-BIF-43	416.30	3.5	12.8	29.0	0.90	16.8	7.2	22.4	1.8	0.7
MP-BIF-44	416.82	5.3	15.5	34.1	0.01	16.4	5.6	25.2	2.2	1.1
MP-BIF-45	417.29	1.8	7.5	28.0	4.42	15.4	4.8	25.3	1.2	0.2
MP-BIF-46	417.86	2.2	8.5	30.7	0.01	31.7	5.2	21.1	1.2	0.3
MP-BIF-47	418.43	3.4	15.5	39.4	5.56	23.4	11.8	23.6	2.8	0.7
MP-BIF-48	418.90	3.9	11.1	31.1	15.66	13.4	6.7	26.1	1.8	0.6
MP-BIF-49	419.41	2.6	9.0	29.6	7.39	11.5	4.2	25.5	1.1	0.3
MP-BIF-50	419.85	2.7	11.1	31.5	4.09	21.7	5.4	16.9	1.3	0.5
MP-BIF-51	420.30	3.4	12.3	33.9	3.13	16.9	9.2	20.9	3.9	0.7
MP-BIF-52	420.41	4.3	14.8	38.9	7.93	24.2	7.3	20.9	0.0	0.6
MP-BIF-53	420.92	2.2	13.1	36.3	13.01	23.7	17.5	20.0	2.0	0.5

MP-56 – Manganese ore

Sample name	Depth	Sc	V	Cr	Co	Ni	Cu	Zn	Pb	Mo
	(m)	(ppm)								
MP-100	421.5	0.48	12.74	9.87	6.8	4.86	5.71	4.66	0.63	1.13
MP-101	421.7	0.92	15.79	12.87	49.2	10.43	11.94	16.9	1.00	1.46
MP-102	422.1	0.76	13.39	10.88	33.8	10.32	7.92	20.1	0.73	2.00
MP-103	422.8	0.72	13.74	12.29	34.8	10.66	8.89	16.6	0.69	1.86
MP-104	423.2	0.6	11.95	11.16	26.1	6.67	8.01	37.1	0.39	1.73
MP-105	423.7	0.567	12.05	9.69	19.0	6.6	6.5	45.8	0.01	2.10
MP-106	424.3	1.36	9.45	15.24	31.6	11.7	14.3	59	0.63	1.77
MP-107	424.5	0.91	7.12	11.98	30.0	8.88	9.24	45.9	1.24	1.74
MP-108	425.1	1.35	8.63	17.48	32.4	12.1	15.43	42.6	1.28	1.69
MP-109	425.7	0.86	6.09	10.53	21.4	8.78	21.32	29.2	1.11	1.53
MP-110	426.3	0.75	7.25	12.03	24.0	9.81	26.51	29.3	0.95	2.10
MP-111	426.9	1.2	8.7	14.81	27.9	11.6	13.93	15.1	1.36	2.07
MP-112	427.3	0.93	7.93	12.55	28.6	10.51	11.17	20	1.76	2.59
MP-113	427.9	1.19	8.37	14.46	32.3	13.7	10.56	21	1.90	2.25
MP-114	428.3	1.24	9.32	14.56	46.4	14	11.74	102	2.07	2.37
MP-115	428.7	0.94	9.06	14.62	47.9	13.1	18.24	82.2	8.63	2.45
MP-116	429.3	0.75	8.36	12.52	31.4	11.49	16.5	36	2.19	2.41
MP-117	429.5	1.36	8.45	20.26	25.5	14.1	18.6	73	2.14	1.97
MP-118	430.1	1.41	7.49	15.45	27.2	13.8	11.75	37.3	2.56	2.23
MP-119	430.5	1.04	6.22	12.92	20.6	11.8	9.58	18.7	2.25	1.96
MP-120	430.9	1.17	6.85	13.62	22.9	13.5	19.3	143	1.92	1.59
MP-121	431.4	0.89	7.82	14.27	25.1	15.2	17	213	1.23	2.11
MP-122	431.9	1.15	8.47	15.48	35.0	17	14.1	60.3	0.81	2.57
MP-123	432.3	0.97	8.58	18.06	29.9	12.4	15	61.7	0.57	2.58
MP-124	432.7	1.16	11.04	20.93	27.7	15.9	24.6	83	1.80	3.34
MP-125	433.1	0.99	7.46	13.97	24.9	12.1	14.4	92	0.69	2.34
MP-126	433.5	1.05	8.14	14.25	31.4	16.6	21.39	52	0.71	2.06
MP-127	433.9	1.03	6.52	14.66	26.7	16.1	14.3	52	0.68	1.89
MP-128	434.4	0.75	5.11	11.55	15.2	14.4	7.74	5.7	0.66	1.38
MP-129	435.0	0.86	6.4	13.02	22.7	12.5	9.92	17	0.60	1.82
MP-130	435.5	1.34	9.3	15.05	39.4	13.8	12.64	93.6	0.89	2.61
MP-131	435.9	0.94	8.1	15.27	14.8	9.5	13.07	64.9	0.69	2.60
MP-132	436.4	0.71	6.81	12.97	29.5	11.2	12.91	43.1	0.65	1.85
MP-133	436.8	0.68	5.66	10.79	22.9	9.3	8.3	69.8	0.48	1.64
MP-134	437.4	0.7	6.93	11.59	23.4	10.3	9.9	50.9	0.71	2.57
MP-135	438.0	0.95	5.22	9.83	13.1	7.26	6.63	19.7	0.36	1.49
MP-136	438.4	0.94	5.86	11.44	16.3	11	10.8	29.6	0.43	1.73
MP-137	439.0	0.82	9.24	14.02	25.0	11.7	10.48	88.8	1.24	2.23
MP-138	439.5	0.7	7.72	14.28	21.9	11.7	10.1	27.4	1.64	2.75
MP-139	439.8	0.87	10.43	18.81	30.3	14.7	15.4	47.9	0.99	3.46
MP-140	440.3	0.56	8.58	10.05	24.1	9.1	8.55	103	0.53	2.12
MP-141	440.8	0.85	13.27	28.3	30.4	17.4	19.7	72	1.04	3.97
MP-142	441.2	0.82	7.46	12.86	29.8	11.01	9.92	35.3	0.94	2.53
MP-143	441.8	0.71	8.11	10.74	26.0	9.15	7.69	57.3	1.01	1.98
MP-144	442.3	0.84	8.5	13.48	34.5	12.7	8.2	40.6	0.72	2.64
MP-145	442.9	1.08	9.1	15.74	30.5	10.4	11.55	51.7	1.23	2.45
MP-146	443.4	0.87	7.58	12.98	25.3	11.6	15.08	46.4	0.36	1.80
MP-147	443.9	1.11	10.3	21.79	24.7	13.6	18.21	24.8	0.77	2.87
MP-148	444.6	1.11	9.12	16.26	26.3	12.2	12.56	20.4	1.48	2.27
MP-149	445.3	0.92	10.07	16.43	34.7	12.6	9.57	15.4	0.91	2.75
MP-150	445.6	1.36	10.91	22.11	46.3	18.7	13.3	23.7	1.32	2.24
MP-151	446.3	1.33	10.07	14.34	57.1	14.8	9.43	13.8	1.03	1.82
MP-152	446.7	1.35	11.87	17.56	40.4	14.4	10.09	34	1.97	2.81
MP-153	447.2	1.6	12.2	17.83	45.9	11.6	10.4	29.7	2.03	2.18
MP-154	447.8	1.49	10.86	15.83	61.0	13	8.66	32.2	2.19	2.19
MP-155	448.2	1.39	12.22	17.14	63.4	14.2	7.32	29.9	2.82	2.20
MP-156	448.7	1.71	13.73	18.01	34.5	10.5	7.32	24.5	2.06	1.93
MP-157	449.3	1.37	10.8	15.32	39.6	9.9	8.16	27.7	2.19	1.91
MP-158	449.7	1.56	13.67	17	39.0	12.4	7.76	31.1	3.30	1.87
MP-159	450.1	1.63	12.68	17.39	34.3	16.1	6.3	27.9	2.47	1.68
MP-160	450.6	1.79	13.58	25.6	38.0	16.5	8.5	36.1	2.34	1.93
MP-161	451.2	1.85	17.14	34	39.7	15.1	12.81	27.6	1.59	2.62
MP-162	451.7	1.79	16.98	33.5	19.6	15.2	12.11	13.1	1.38	2.34
MP-163	452.2	1.84	20.35	40.3	9.7	17.5	13.87	16.4	1.16	3.56

MP-56 – Hematite lutite

Sample name	Depth	Sc	V	Cr	Co	Ni	Cu	Zn	Pb	Mo
	(m)	(ppm)								
MP-164	452.7	1.82	42.7	113.9	10.9	36.2	40.1	13.1	0.69	5.59
MP-165	453.2	1.5	18.2	32.4	9.0	16.4	12.88	19.1	1.59	2.48
MP-166	453.6	1.59	16.95	29.1	34.2	13.3	11.09	13.8	1.53	2.17
MP-167	454.0	1.27	15.41	23.5	4.4	11.3	10.45	14.6	1.27	1.94
MP-168	454.5	1.79	16.94	27.6	6.8	12	11.91	22.3	1.56	1.98
MP-169	455.1	1.59	17.97	26.8	9.8	11.2	16.1	16.3	1.02	1.73
MP-170	455.6	2.07	17.69	29	40.5	11.6	17.3	7	1.17	2.33
MP-171	456.1	1.41	15.22	21.18	14.6	12	10.3	14.1	1.07	1.90
MP-172	456.7	1.92	18.68	29.1	6.3	13.3	18.18	16.9	1.29	1.90
MP-173	457.1	2.1	20.7	33.5	5.3	13.4	14.6	14.1	1.86	1.89
MP-174	457.4	2.58	17.45	25.7	8.0	13.2	9.62	19.3	3.65	2.18
MP-175	458.0	2.52	20.85	36	10.4	14.9	12.45	19.5	2.34	1.78
MP-176	458.6	2.56	23.11	48	8.5	18.3	18.2	12.2	15.29	3.11

A3. Alkali-earth metals raw data

G774 – BIF

Sample	Depth	Rb	Ba	Sr	Cs
	(m)	(ppm)			
G7BF-01	90.81	0.6	18.2	46.6	0.2
G7BF-02	91.28	3.2	8.9	44.9	0.7
G7BF-03	91.65	3.6	9.1	62.2	1.5
G7BF-04	92.10	6.5	8.8	48.1	0.9
G7BF-05	92.48	5.2	10.7	34.5	0.8
G7BF-06	92.94	4.2	11.0	39.4	0.8
G7BF-07	93.34	2.8	22.2	178.5	0.5
G7BF-08	93.88	1.4	21.2	84.6	0.3
G7BF-09	94.35	1.2	17.5	103.4	0.4
G7BF-10	94.73	1.1	9.8	14.1	0.5
G7BF-11	95.11	2.1	17.3	121.4	0.5
G7BF-12	95.73	3.6	9.9	32.4	1.3
G7BF-13	96.23	2.7	10.4	25.0	0.9
G7BF-14	96.73	2.2	13.8	41.2	1.1
G7BF-15	97.15	2.9	9.4	17.5	0.9
G7BF-16	97.54	2.7	12.1	18.0	1.0
G7BF-17	98.02	2.4	16.8	14.1	1.0
G7BF-18	98.60	2.3	14.6	31.1	0.9
G7BF-19	99.02	1.4	14.6	35.1	1.0
G7BF-20	99.42	3.8	14.4	86.2	1.4
G7BF-21	100.18	2.3	53.0	301.9	1.2
G7BF-22	100.56	0.8	10.3	16.5	0.6
G7BF-23	101	0.6	29.0	112.4	0.3
G7BF-24	101.64	0.3	97.0	676.1	0.2

G774 – Hematite lutite

Sample	Depth	Rb	Ba	Sr	Cs
	(m)	(ppm)			
G7-104	151.75	2.73	25	17.22	0.50
G7-105	152.05	0.73	47	18.92	0.20
G7-106	152.39	1.09	44.5	20.04	0.27
G7-107	152.85	5.51	110.9	20.34	0.93
G7-108	153.36	1.55	51.5	14.86	0.37
G7-109	153.80	3.35	74.6	17.39	0.60
G7-110	154.26	2.97	53.7	14.69	0.61
G7-111	154.73	2.67	77.1	11.99	Below LOD
G7-112	155.21	0.39	29.1	13.34	Below LOD
G7-113	155.69	1.41	43.9	13.42	0.52
G7-114	156.25	2.38	32	9.62	0.53
G7-115	156.74	2.48	26.5	9.32	0.44
G7-116	157.17	1.64	21.5	6.81	0.32
G7-117	157.62	0.74	21.2	6.82	0.23
G7-118	158.13	0.92	35.6	5.28	0.28
G7-119	158.58	0.49	49.4	7.93	0.26
G7-120	159.03	0.319	28.1	8.46	Below LOD
G7-121	159.63	0.399	32.7	8.55	0.19
G7-122	160.00	0.425	34.4	8.35	0.15
G7-123	160.53	0.452	44.7	7.8	Below LOD
G7-124	160.95	0.45	6352	34.17	0.12
G7-125	161.44	0.49	149.7	7.49	0.19
G7-126	161.92	0.59	33.5	6.75	0.22
G7-127	162.50	0.412	306.8	7.19	0.37
G7-128	163.10	0.286	34.3	6.89	0.14
G7-129	163.49	0.98	20.2	7.65	0.81
G7-130	163.84	0.52	579	9.28	0.30
G7-131	164.40	0.475	73.8	6.71	0.25
G7-132	165.08	0.327	16.61	5.99	0.17
G7-133	165.64	0.75	63.1	9.83	0.43
G7-134	166.04	0.46	49.1	8.1	0.31
G7-135	166.63	0.59	4048	25.62	0.27
G7-136	167.07	2.75	79.3	21.52	0.77

G774 – Manganese ore

Sample	Depth	Rb	Ba	Sr	Cs
	(m)	(ppm)			
G7-001	101.94	0.188	421	633	Below LOD
G7-002	102.29	0.105	142.5	522	0.14
G7-003	102.83	0.24	233.8	854	0.17
G7-004	103.27	Below LOD	174.1	634	0.12
G7-005	103.82	0.15	158.2	525	0.13
G7-006	104.30	Below LOD	156.8	541.7	Below LOD
G7-007	104.88	0.121	126.7	452.3	Below LOD
G7-008	105.32	Below LOD	80	159.9	Below LOD
G7-009	105.85	Below LOD	79.3	130.7	Below LOD
G7-010	106.27	0.25	77.6	148.8	Below LOD
G7-011	106.76	Below LOD	74.9	150.3	Below LOD
G7-012	107.25	0.121	75.4	137	0.13
G7-013	107.76	Below LOD	77.1	115	0.09
G7-014	108.16	0.165	139.7	150.1	Below LOD
G7-015	108.64	0.138	67.7	203.4	Below LOD
G7-016	109.03	Below LOD	54.3	190.6	Below LOD
G7-017	109.45	Below LOD	66.2	135.3	Below LOD
G7-018	109.97	0.166	1034	165.9	Below LOD
G7-019	110.54	0.181	122.3	128.9	Below LOD
G7-020	110.95	Below LOD	242	125.5	Below LOD
G7-021	111.55	0.146	358.3	134.6	Below LOD
G7-022	111.89	0.122	236.1	192.3	Below LOD
G7-023	112.40	0.113	135	232.1	Below LOD
G7-024	112.85	Below LOD	117.5	138	Below LOD
G7-025	113.38	0.116	413.2	154.8	Below LOD
G7-026	113.86	0.119	222.4	198.6	Below LOD
G7-027	114.36	Below LOD	73.2	260.1	Below LOD
G7-028	114.82	Below LOD	73	258.9	Below LOD
G7-029	115.10	0.116	524	244.2	0.09
G7-030	115.53	0.09	168.9	249.5	Below LOD
G7-031	116.08	Below LOD	90.1	245.9	0.07
G7-032	116.62	Below LOD	137.4	288.4	Below LOD
G7-033	117.15	Below LOD	121.6	237.5	Below LOD
G7-034	117.49	Below LOD	273.7	304.3	0.09
G7-035	118.01	Below LOD	78	285.9	Below LOD
G7-036	118.50	Below LOD	73.8	243.6	Below LOD
G7-037	119.07	Below LOD	59.8	272.5	Below LOD
G7-038	119.49	Below LOD	58.7	177	0.09
G7-039	119.94	Below LOD	239.2	105.9	Below LOD
G7-040	120.38	Below LOD	54.4	120	Below LOD
G7-041	120.93	Below LOD	4980	217.9	Below LOD
G7-042	121.35	Below LOD	67.5	107.8	Below LOD
G7-043	121.63	Below LOD	50.7	134.8	Below LOD
G7-044	122.05	Below LOD	52.2	126.3	Below LOD
G7-045	122.52	Below LOD	51.1	148.6	Below LOD
G7-046	123.04	Below LOD	81.3	250.7	Below LOD
G7-047	123.52	Below LOD	112.4	314.5	Below LOD
G7-048	123.95	0.175	105.3	282.2	Below LOD
G7-049	124.46	Below LOD	113	330.9	Below LOD
G7-050	124.98	0.132	167.1	484.6	Below LOD
G7-051	125.44	Below LOD	123.5	338.8	Below LOD

G774 – Manganese ore (Continued)

Sample	Depth	Rb	Ba	Sr	Cs
	(m)		(ppm)		
G7-052	125.93	Below LOD	96.8	284.8	Below LOD
G7-053	126.41	Below LOD	80.6	227.9	Below LOD
G7-054	126.87	0.132	79.1	247.8	Below LOD
G7-055	127.40	0.11	125.6	387.9	Below LOD
G7-056	127.86	Below LOD	57.8	183.1	Below LOD
G7-057	128.37	0.106	52.6	146.7	Below LOD
G7-058	128.84	Below LOD	50.1	125.4	Below LOD
G7-059	129.33	Below LOD	63.9	122.6	Below LOD
G7-060	129.79	Below LOD	55.6	115.5	Below LOD
G7-061	130.25	Below LOD	44.9	95.3	Below LOD
G7-062	130.70	Below LOD	48.1	109.8	Below LOD
G7-063	131.24	Below LOD	41.9	135.4	Below LOD
G7-064	131.70	Below LOD	34.8	115.4	Below LOD
G7-065	132.23	Below LOD	34.7	99.9	Below LOD
G7-066	132.66	Below LOD	36.1	68.3	Below LOD
G7-067	133.09	Below LOD	46.6	92.5	Below LOD
G7-068	133.51	Below LOD	116.3	93.2	Below LOD
G7-069	134.02	Below LOD	81.6	83.9	Below LOD
G7-070	135.45	Below LOD	44.8	95.1	Below LOD
G7-071	135.97	0.134	39.3	103.1	Below LOD
G7-072	136.55	Below LOD	41.9	204.7	Below LOD
G7-073	137.14	Below LOD	299.5	202	Below LOD
G7-074	137.54	0.128	309.7	154.4	Below LOD
G7-075	138.03	Below LOD	378.2	233.8	Below LOD
G7-076	138.47	Below LOD	241.9	131	Below LOD
G7-077	138.94	0.297	1441	182	Below LOD
G7-078	139.29	Below LOD	378.6	129.3	Below LOD
G7-079	139.80	0.114	441	163	Below LOD
G7-080	140.28	Below LOD	478.2	119.8	Below LOD
G7-081	140.79	Below LOD	885	137.6	Below LOD
G7-082	141.26	Below LOD	253	184.8	Below LOD
G7-083	141.74	Below LOD	133.5	219.8	Below LOD
G7-084	142.15	Below LOD	120.3	160.5	Below LOD
G7-085	142.71	Below LOD	153.2	156.7	Below LOD
G7-086	143.19	Below LOD	275.3	176.8	Below LOD
G7-087	143.63	Below LOD	121.3	141.5	Below LOD
G7-088	144.05	Below LOD	80.2	181.7	Below LOD
G7-089	144.53	Below LOD	113.3	124.4	Below LOD
G7-090	145.15	Below LOD	82.7	120.5	Below LOD
G7-091	145.56	Below LOD	1376	53.2	Below LOD
G7-092	146.06	0.88	318.2	38.37	0.64
G7-093	146.48	1.66	95.6	25.78	1.54
G7-094	146.96	0.72	577.9	23.21	0.68
G7-095	147.44	0.82	97.3	17.88	0.61
G7-096	148.02	1.42	74.5	14.35	1.00
G7-097	148.47	1.27	65.8	14.25	0.71
G7-098	148.96	1.52	65.4	14.04	1.02
G7-099	149.39	1.32	55	14.65	1.05
G7-100	149.90	0.99	54	18.65	0.74
G7-101	150.40	0.38	2235	50.08	0.11
G7-102	150.89	0.95	36.4	13.76	0.22
G7-103	151.50	1.14	30.6	13.57	0.24

MP-56 – BIF

Sample	Depth	Rb	Sr	Ba	Cs
	(m)		(ppm)		
MP-BIF-01	396.45	1.25	67.38	121.57	0.20
MP-BIF-02	396.67	0.66	81.92	10.59	0.24
MP-BIF-03	397.19	1.35	31.02	10.37	0.47
MP-BIF-04	397.85	2.22	38.64	7.72	0.73
MP-BIF-05	398.48	1.25	29.09	8.49	0.38
MP-BIF-06	398.74	1.71	33.84	12.04	0.49
MP-BIF-07	399.22	1.99	24.37	8.27	0.48
MP-BIF-08	399.72	1.17	24.82	7.13	0.33
MP-BIF-09	400.21	3.30	22.92	13.46	0.98
MP-BIF-10	400.67	1.96	69.89	9.08	0.54
MP-BIF-11	401.24	1.66	102.85	10.53	0.48
MP-BIF-12	401.68	3.37	51.01	9.20	1.05
MP-BIF-13	402.04	2.82	35.38	7.88	0.71
MP-BIF-14	402.56	2.21	30.88	7.26	0.54
MP-BIF-15	403.06	2.79	46.78	7.92	0.82
MP-BIF-16	403.55	1.18	9.74	7.84	0.79
MP-BIF-17	404.04	3.43	38.27	8.89	0.85
MP-BIF-18	404.55	2.95	51.58	8.83	0.78
MP-BIF-19	405	2.43	34.67	8.07	0.65
MP-BIF-20	405.48	1.65	27.40	7.49	0.41
MP-BIF-21	405.92	2.04	22.92	7.04	0.55
MP-BIF-22	406.37	1.22	22.92	7.81	0.32
MP-BIF-23	406.79	1.31	15.54	7.68	0.44
MP-BIF-24	407.28	1.00	15.11	9.70	0.57
MP-BIF-25	407.80	1.39	27.80	7.45	0.36
MP-BIF-26	408.32	1.87	19.61	9.57	0.54
MP-BIF-27	408.70	3.42	12.86	7.00	1.35
MP-BIF-28	409.22	2.27	17.68	7.21	0.60
MP-BIF-29	409.73	2.13	14.88	7.46	0.58
MP-BIF-30	410.21	1.99	16.63	7.14	0.65
MP-BIF-31	410.55	1.67	22.29	7.57	0.89
MP-BIF-32	411.02	0.01	11.96	7.90	0.73
MP-BIF-33	411.45	1.98	11.16	7.22	0.52
MP-BIF-34	411.96	2.42	14.34	7.46	0.75
MP-BIF-35	412.47	1.25	20.38	7.76	0.34
MP-BIF-36	412.99	1.74	14.62	6.70	1.81
MP-BIF-37	413.49	3.90	85.09	12.16	1.09
MP-BIF-38	413.98	0.87	18.74	7.49	0.27
MP-BIF-39	414.53	1.58	19.57	8.28	0.51
MP-BIF-40	414.93	1.09	17.79	9.63	0.32
MP-BIF-41	415.51	0.92	17.86	6.83	0.34
MP-BIF-42	415.87	0.90	17.61	8.23	0.38
MP-BIF-43	416.30	0.68	21.88	6.57	0.35
MP-BIF-44	416.82	3.94	29.30	7.46	1.18
MP-BIF-45	417.29	3.28	22.12	8.94	0.89
MP-BIF-46	417.86	1.41	30.55	9.83	0.39
MP-BIF-47	418.43	0.94	17.58	7.99	0.70
MP-BIF-48	418.90	1.31	6.13	9.46	0.81
MP-BIF-49	419.41	1.03	20.61	7.70	0.29
MP-BIF-50	419.85	1.05	9.97	7.60	0.65
MP-BIF-51	420.30	1.34	4.57	10.38	2.41
MP-BIF-52	420.41	1.53	52.18	14.50	0.79
MP-BIF-53	420.92	0.47	24.68	11.76	0.24

MP-56 – Manganese ore

Sample	Depth	Rb	Sr	Ba	Cs
	(m)		(ppm)		
MP-100	421.5	0.062	12.75	12.19	Below LOD
MP-101	421.7	0.252	42.8	17.3	0.12
MP-102	422.1	0.512	79.7	24.7	0.30
MP-103	422.8	0.44	75.9	23.6	0.30
MP-104	423.2	0.09	163.8	417	Below LOD
MP-105	423.7	Below LOD	191.7	239.3	Below LOD
MP-106	424.3	0.143	296.4	219.8	0.09
MP-107	424.5	Below LOD	262.8	48.8	Below LOD
MP-108	425.1	0.094	230.3	51.9	Below LOD
MP-109	425.7	Below LOD	212.6	48.1	Below LOD
MP-110	426.3	Below LOD	143.3	44.3	Below LOD
MP-111	426.9	0.061	55.2	32.9	Below LOD
MP-112	427.3	Below LOD	68	34.9	Below LOD
MP-113	427.9	0.104	41.54	33.1	0.07
MP-114	428.3	0.119	39.37	31.6	0.05
MP-115	428.7	Below LOD	37.12	39.2	Below LOD
MP-116	429.3	Below LOD	61.6	37.8	Below LOD
MP-117	429.5	Below LOD	143.6	43.6	Below LOD
MP-118	430.1	0.081	135.4	41.9	Below LOD
MP-119	430.5	Below LOD	149.4	57.4	Below LOD
MP-120	430.9	Below LOD	125.5	50.5	Below LOD
MP-121	431.4	0.085	129.9	50.3	0.07
MP-122	431.9	0.074	60.5	40.4	Below LOD
MP-123	432.3	Below LOD	67.7	38.7	Below LOD
MP-124	432.7	Below LOD	48	33	Below LOD
MP-125	433.1	0.068	74.5	34.3	Below LOD
MP-126	433.5	Below LOD	61.44	35.7	Below LOD
MP-127	433.9	0.106	85.7	41.2	0.05
MP-128	434.4	0.064	128.6	43.4	Below LOD
MP-129	435.0	0.046	64	31.4	Below LOD
MP-130	435.5	Below LOD	127.2	77.9	Below LOD
MP-131	435.9	Below LOD	64.2	54	Below LOD
MP-132	436.4	Below LOD	74	100.4	Below LOD
MP-133	436.8	Below LOD	97.9	402.3	Below LOD
MP-134	437.4	Below LOD	67.3	649.4	Below LOD
MP-135	438.0	Below LOD	77	93.9	0.04
MP-136	438.4	Below LOD	84.8	394	Below LOD
MP-137	439.0	Below LOD	62.4	33.2	Below LOD
MP-138	439.5	Below LOD	57.67	43.5	Below LOD
MP-139	439.8	Below LOD	58.9	665	Below LOD
MP-140	440.3	Below LOD	57.2	47.9	Below LOD
MP-141	440.8	0.202	89.4	3362	Below LOD
MP-142	441.2	0.124	32.48	152	0.06
MP-143	441.8	Below LOD	30.08	45.3	Below LOD
MP-144	442.3	0.093	47.19	316.9	0.05
MP-145	442.9	Below LOD	53.5	67.1	0.05
MP-146	443.4	Below LOD	73.6	428.6	Below LOD
MP-147	443.9	Below LOD	69.8	67.3	Below LOD
MP-148	444.6	Below LOD	66.63	50	Below LOD
MP-149	445.3	Below LOD	47.32	74.6	Below LOD
MP-150	445.6	0.22	60.6	82.7	0.12
MP-151	446.3	0.906	58.6	65.9	0.66
MP-152	446.7	Below LOD	35.56	101	Below LOD
MP-153	447.2	0.66	13.12	24.3	0.40
MP-154	447.8	0.658	17.34	26	0.55
MP-155	448.2	0.491	12.25	23.4	0.34
MP-156	448.7	0.405	13.06	23.7	0.14
MP-157	449.3	0.69	12.51	20.3	0.46
MP-158	449.7	0.78	12.85	20.5	0.41
MP-159	450.1	0.85	13.84	20.7	0.36
MP-160	450.6	0.8	15.78	20.9	0.31
MP-161	451.2	0.67	43.63	6335	0.21
MP-162	451.7	0.77	10.96	28.1	0.10
MP-163	452.2	0.69	9.91	24.8	0.26

MP-56 – Hematite lutite

Sample	Depth	Rb	Sr	Ba	Cs
	(m)	(ppm)			
MP-164	452.7	0.43	7.78	56.6	0.21
MP-165	453.2	0.79	12.33	16.9	0.12
MP-166	453.6	1.05	9.65	19.7	0.21
MP-167	454.0	1.11	10.73	19.1	0.30
MP-168	454.5	1.8	9.88	17.3	0.49
MP-169	455.1	0.73	14	20.2	0.12
MP-170	455.6	0.334	14.42	57.2	Below LOD
MP-171	456.1	0.63	8.16	19.9	0.22
MP-172	456.7	0.63	8.98	18.1	0.18
MP-173	457.1	0.5	7.98	16.2	0.12
MP-174	457.4	0.94	6.48	13.13	0.11
MP-175	458.0	0.93	6.35	14.2	0.11
MP-176	458.6	0.54	6.24	17	0.11

A.4 High Field Strength Element raw data

G774 – BIF

Sample	Depth	Zr	Hf	Y	Nb	U	Th	Ta
	(m)	(ppm)						
G7BF-01	90.81	2.68	0.01	6.67	0.21	1.74	0	0.79
G7BF-02	91.28	4.95	0.08	9.83	0.55	0.09	0	2.78
G7BF-03	91.65	3.93	0.31	12.12	0.32	0.07	1.66	2.57
G7BF-04	92.10	3.61	0.78	6.44	0.26	0.08	0.00	0.80
G7BF-05	92.48	3.70	0.13	6.21	0.26	0.08	0.51	3.03
G7BF-06	92.94	8.60	0.33	8.45	0.31	0.14	1.44	0.88
G7BF-07	93.34	3.80	0.65	11.28	0.45	0.30	0.73	2.65
G7BF-08	93.88	4.53	0.22	8.71	0.38	0.08	0.00	3.30
G7BF-09	94.35	5.17	0.07	12.64	0.37	0.12	4.04	0.94
G7BF-10	94.73	10.89	0.48	18.28	0.73	4.97	4.30	2.07
G7BF-11	95.11	5.09	0.18	8.87	0.36	0.11	1.03	0.79
G7BF-12	95.73	7.88	0.37	7.81	0.68	0.18	1.05	2.79
G7BF-13	96.23	8.83	0.10	8.57	0.52	0.20	0.00	3.69
G7BF-14	96.73	22.19	0.37	12.80	1.21	0.99	2.07	0.83
G7BF-15	97.15	6.67	0.07	7.26	0.58	0.23	0	2.61
G7BF-16	97.54	8.01	0.78	12.17	0.81	0.32	1.78	0.71
G7BF-17	98.02	16.15	1.00	8.75	1.44	0.40	12.47	3.31
G7BF-18	98.60	14.09	0.00	9.30	0.96	0.35	2.21	2.34
G7BF-19	99.02	14.34	0.72	14.08	1.41	0.46	4.78	0.88
G7BF-20	99.42	7.30	0.03	15.05	0.71	0.42	2.31	2.67
G7BF-21	100.18	15.72	0.08	13.22	1.38	2.12	8.76	2.96
G7BF-22	100.56	5.44	0.67	8.61	0.62	0.23	0.78	0.67
G7BF-23	101	7.88	0.40	12.30	0.79	0.29	1.58	2.43
G7BF-24	101.64	5.53	9.37	9.08	0.68	0.20	11.04	0.62

G774 – Hematite lutite

Sample	Depth	Zr	Hf	Y	Nb	U	Th	Ta
	(m)	(ppm)						
G7-104	151.75	4.15	0.05	6.30	0.32	0.07	0.17	0.01
G7-105	152.05	6.17	0.06	9.13	0.41	0.11	0.36	0.04
G7-106	152.39	6.24	0.11	8.32	0.49	0.09	0.41	0.02
G7-107	152.85	6.00	0.11	9.27	0.51	0.12	0.41	0.03
G7-108	153.36	4.90	0.05	7.95	0.35	0.08	0.28	0.01
G7-109	153.80	6.17	0.11	8.85	0.63	0.10	0.37	0.03
G7-110	154.26	5.55	0.07	9.53	0.48	0.11	0.38	0.03
G7-111	154.73	6.54	0.10	8.58	0.50	0.13	0.46	0.02
G7-112	155.21	5.71	0.06	10.41	0.41	0.13	0.28	0.02
G7-113	155.69	5.91	0.08	8.92	0.40	0.13	0.35	0.02
G7-114	156.25	5.73	0.10	8.77	0.47	0.11	0.35	0.05
G7-115	156.74	5.52	0.10	9.29	0.38	0.12	0.30	0.02
G7-116	157.17	3.73	0.07	7.96	0.20	0.08	0.17	0.01
G7-117	157.62	6.26	0.08	9.00	0.49	0.13	0.50	0.03
G7-118	158.13	8.77	0.12	5.62	0.45	0.09	0.43	0.02
G7-119	158.58	6.53	0.11	8.48	0.42	0.07	0.28	Below LOD
G7-120	159.03	6.61	0.10	2.25	0.39	0.05	0.28	0.01
G7-121	159.63	4.90	0.09	6.92	0.32	0.07	0.30	0.02
G7-122	160.00	4.86	0.07	4.48	0.33	0.07	0.28	0.02
G7-123	160.53	4.46	0.08	8.33	0.26	0.05	0.23	0.01
G7-124	160.95	3.34	0.04	6.53	0.20	0.03	0.11	Below LOD
G7-125	161.44	4.38	0.06	5.69	0.14	0.04	0.11	Below LOD
G7-126	161.92	7.10	0.06	3.98	0.38	0.09	0.29	0.01
G7-127	162.50	3.21	0.05	5.80	0.20	0.06	0.21	0.02
G7-128	163.10	3.86	0.07	6.54	0.24	0.05	0.13	Below LOD
G7-129	163.49	4.52	0.07	7.06	0.31	0.07	0.27	0.01
G7-130	163.84	5.79	0.11	5.40	0.32	0.08	0.28	0.01
G7-131	164.40	5.86	0.06	5.41	0.23	0.06	0.19	Below LOD
G7-132	165.08	3.99	0.05	4.19	0.24	0.03	0.17	0.02
G7-133	165.64	4.06	0.06	6.09	0.34	0.06	0.30	0.02
G7-134	166.04	3.74	0.05	6.43	0.20	0.05	0.14	Below LOD
G7-135	166.63	24.34	0.45	5.56	0.25	0.06	0.16	0.00
G7-136	167.07	5.18	0.13	7.27	0.30	0.07	0.22	0.01

G774 – Manganese ore

Sample	Depth	Zr	Hf	Y	Nb	U	Th	Ta
	(m)	(ppm)						
G7-001	101.94	12.68	0.20	5.15	0.26	0.16	0.22	0.01
G7-002	102.29	5.28	0.11	5.48	0.20	0.12	0.25	0.01
G7-003	102.83	29.70	0.70	18.47	0.28	0.29	0.33	Below LOD
G7-004	103.27	3.38	0.09	4.63	0.32	0.06	0.32	0.02
G7-005	103.82	5.84	0.14	5.14	0.40	0.08	0.50	0.03
G7-006	104.30	4.32	0.12	5.01	0.28	0.08	0.40	0.02
G7-007	104.88	2.50	0.02	3.65	0.20	0.09	0.18	Below LOD
G7-008	105.32	3.56	0.05	4.72	0.36	0.08	0.33	0.02
G7-009	105.85	3.67	0.04	4.77	0.29	0.09	0.37	0.02
G7-010	106.27	2.93	0.04	4.02	0.27	0.10	0.25	0.03
G7-011	106.76	3.59	0.03	4.63	0.28	0.08	0.35	0.01
G7-012	107.25	4.50	0.07	5.24	0.37	0.07	0.45	0.02
G7-013	107.76	4.43	0.05	5.48	0.35	0.08	0.35	0.02
G7-014	108.16	3.15	0.05	3.89	0.20	0.10	0.25	0.00
G7-015	108.64	3.63	0.10	4.30	0.29	0.09	0.39	0.03
G7-016	109.03	3.74	0.08	4.53	0.27	0.09	0.33	0.02
G7-017	109.45	4.05	0.12	4.63	0.31	0.12	0.37	0.04
G7-018	109.97	2.93	0.04	3.81	0.25	0.10	0.20	0.01
G7-019	110.54	7.03	0.17	3.99	0.26	0.09	0.29	0.01
G7-020	110.95	3.66	0.05	4.93	0.31	0.13	0.27	0.02
G7-021	111.55	4.43	0.09	4.52	0.32	0.11	0.34	0.02
G7-022	111.89	4.96	0.14	4.34	0.24	0.10	0.30	0.00
G7-023	112.40	3.44	0.09	5.18	0.24	0.11	0.25	0.01
G7-024	112.85	3.26	0.06	4.84	0.28	0.12	0.30	0.02
G7-025	113.38	4.76	0.12	4.83	0.29	0.10	0.30	0.01
G7-026	113.86	16.69	0.35	5.43	0.34	0.10	0.41	0.02
G7-027	114.36	4.29	0.10	5.38	0.45	0.13	0.42	0.04
G7-028	114.82	8.16	0.15	4.39	0.26	0.11	0.29	0.01
G7-029	115.10	4.85	0.10	4.88	0.33	0.15	0.35	0.04
G7-030	115.53	3.04	0.08	5.01	0.33	0.12	0.32	0.03
G7-031	116.08	3.26	0.07	5.59	0.31	0.10	0.35	0.03
G7-032	116.62	3.80	0.08	4.42	0.27	0.08	0.37	0.02
G7-033	117.15	3.89	0.07	5.79	0.42	0.09	0.43	0.04
G7-034	117.49	3.26	0.04	4.78	0.29	0.10	0.34	0.01
G7-035	118.01	4.58	0.12	5.27	0.33	0.13	0.40	0.04
G7-036	118.50	3.64	0.10	5.58	0.34	0.17	0.41	0.02
G7-037	119.07	3.68	0.10	5.98	0.45	0.13	0.44	0.03
G7-038	119.49	4.43	0.05	7.29	0.47	0.12	0.57	0.03
G7-039	119.94	3.86	0.08	3.63	0.27	0.10	0.23	0.01
G7-040	120.38	3.71	0.08	4.28	0.31	0.10	0.41	0.02
G7-041	120.93	2.08	0.04	2.11	0.16	0.07	0.18	0.02
G7-042	121.35	3.11	0.04	4.05	0.24	0.09	0.29	0.02
G7-043	121.63	3.96	0.07	5.04	0.32	0.10	0.33	0.02
G7-044	122.05	3.82	0.08	5.61	0.36	0.11	0.50	0.03
G7-045	122.52	3.69	0.06	4.87	0.30	0.09	0.33	Below LOD
G7-046	123.04	4.04	0.11	6.68	0.35	0.14	0.51	0.03
G7-047	123.52	4.63	0.12	6.42	0.42	0.13	0.52	0.05
G7-048	123.95	5.44	0.14	6.76	0.36	0.13	0.45	0.03
G7-049	124.46	3.05	0.06	5.18	0.22	0.08	0.27	0.01
G7-050	124.98	2.98	0.06	5.70	0.27	0.11	0.28	0.01
G7-051	125.44	11.18	0.25	9.54	0.46	0.14	0.63	0.02

G774 – Manganese ore (Continued)

Sample	Depth	Zr	Hf	Y	Nb	U	Th	Ta
	(m)	(ppm)						
G7-052	125.93	8.18	0.18	5.44	0.41	0.10	0.29	0.02
G7-053	126.41	6.70	0.14	8.07	0.55	0.11	0.70	0.03
G7-054	126.87	6.85	0.17	10.13	0.53	0.16	0.80	0.04
G7-055	127.40	8.21	0.17	5.43	0.24	0.13	0.30	0.02
G7-056	127.86	2.98	0.06	4.60	0.21	0.09	0.22	0.01
G7-057	128.37	2.97	0.05	4.64	0.25	0.11	0.21	Below LOD
G7-058	128.84	4.15	0.09	5.80	0.45	0.09	0.41	0.04
G7-059	129.33	2.83	0.08	4.62	0.25	0.09	0.26	0.01
G7-060	129.79	3.50	0.07	4.83	0.40	0.10	0.41	0.03
G7-061	130.25	4.50	0.08	3.75	0.24	0.07	0.23	0.02
G7-062	130.70	3.42	0.05	4.17	0.27	0.10	0.23	0.02
G7-063	131.24	2.97	0.05	3.84	0.23	0.12	0.21	0.01
G7-064	131.70	3.68	0.05	4.32	0.30	0.11	0.24	0.02
G7-065	132.23	3.25	0.06	4.33	0.29	0.09	0.27	0.02
G7-066	132.66	3.80	0.07	4.20	0.27	0.11	0.29	0.04
G7-067	133.09	2.90	0.04	3.58	0.21	0.09	0.26	0.02
G7-068	133.51	3.30	0.08	4.10	0.29	0.09	0.24	0.01
G7-069	134.02	2.48	0.04	3.53	0.20	0.07	0.18	0.02
G7-070	135.45	3.00	0.06	3.88	0.22	0.09	0.19	0.01
G7-071	135.97	2.52	0.04	3.81	0.21	0.10	0.21	0.01
G7-072	136.55	7.56	0.15	3.62	0.26	0.06	0.26	0.01
G7-073	137.14	4.57	0.10	3.52	0.22	0.08	0.21	0.01
G7-074	137.54	46.30	1.07	6.69	0.54	0.14	0.50	0.03
G7-075	138.03	3.49	0.07	4.22	0.29	0.07	0.28	0.02
G7-076	138.47	15.70	0.36	3.33	0.22	0.14	0.26	0.01
G7-077	138.94	14.43	0.32	3.75	0.28	0.07	0.26	0.01
G7-078	139.29	3.48	0.07	3.24	0.25	0.07	0.19	0.00
G7-079	139.80	5.49	0.11	4.36	0.33	0.07	0.32	0.02
G7-080	140.28	2.98	0.04	3.67	0.28	0.10	0.27	0.02
G7-081	140.79	4.92	0.09	3.44	0.29	0.11	0.25	0.02
G7-082	141.26	4.05	0.10	4.23	0.38	0.06	0.31	0.02
G7-083	141.74	4.57	0.09	5.20	0.35	0.09	0.34	0.03
G7-084	142.15	4.34	0.11	4.21	0.30	0.10	0.34	0.02
G7-085	142.71	6.93	0.16	5.19	0.43	0.09	0.48	0.03
G7-086	143.19	5.05	0.10	4.99	0.35	0.11	0.41	0.03
G7-087	143.63	6.94	0.16	6.27	0.54	0.15	0.62	0.03
G7-088	144.05	5.63	0.15	5.17	0.47	0.15	0.51	0.05
G7-089	144.53	4.72	0.08	4.89	0.44	0.12	0.38	0.03
G7-090	145.15	5.02	0.08	6.05	0.41	0.15	0.36	0.02
G7-091	145.56	5.25	0.11	7.22	0.56	0.10	0.47	0.03
G7-092	146.06	5.86	0.07	7.15	0.49	0.10	0.41	0.03
G7-093	146.48	5.03	0.07	7.26	0.43	0.12	0.39	Below LOD
G7-094	146.96	4.91	0.10	7.25	0.33	0.10	0.38	0.03
G7-095	147.44	5.23	0.07	8.25	0.46	0.13	0.34	0.02
G7-096	148.02	5.20	0.08	6.33	0.37	0.10	0.33	0.02
G7-097	148.47	10.84	0.25	8.29	0.41	0.12	0.39	0.01
G7-098	148.96	6.55	0.07	7.66	0.52	0.22	0.52	0.04
G7-099	149.39	5.76	0.06	8.85	0.51	0.28	0.46	0.12
G7-100	149.90	7.20	0.08	9.86	0.55	0.17	0.58	0.04
G7-101	150.40	2.74	0.04	15.70	0.28	0.09	0.19	0.01
G7-102	150.89	5.57	0.07	7.61	0.44	0.22	0.58	0.03
G7-103	151.50	4.25	0.05	8.83	0.36	0.10	0.24	Below LOD

MP-56 – BIF

Sample name	Depth	Zr	Hf	Y	Nb	U	Th	Ta
	(m)	(ppm)						
MP-BIF-01	396.45	2.2	0.53	9.4	0.4	0.6	4.28	0.75
MP-BIF-02	396.67	3.5	0.14	10.1	0.4	0.1	1.96	2.75
MP-BIF-03	397.19	3.1	0.03	9.7	0.3	0.0	4.67	2.35
MP-BIF-04	397.85	3.1	0.08	12.7	0.4	0.1	5.50	2.93
MP-BIF-05	398.48	4.4	0.29	10.0	0.2	2.1	0.71	0.87
MP-BIF-06	398.74	5.2	0.04	9.9	0.5	0.9	2.96	2.83
MP-BIF-07	399.22	6.2	0.04	8.2	0.4	0.1	2.10	2.37
MP-BIF-08	399.72	4.0	0.48	8.8	0.3	0.1	2.99	0.81
MP-BIF-09	400.21	2.8	0.26	7.3	0.3	0.0	4.93	3.31
MP-BIF-10	400.67	3.4	0.36	14.2	0.3	0.0	1.93	2.64
MP-BIF-11	401.24	4.0	0.51	16.5	0.3	0.0	4.34	2.67
MP-BIF-12	401.68	3.6	0.34	10.6	0.4	0.0	1.68	0.87
MP-BIF-13	402.04	3.3	0.06	8.6	0.3	0.0	0.11	2.49
MP-BIF-14	402.56	5.8	0.00	8.1	0.4	0.1	0.64	3.12
MP-BIF-15	403.06	4.3	0.00	11.6	0.4	0.1	0.00	0.82
MP-BIF-16	403.55	12.2	0.11	8.2	0.9	0.3	0.00	2.50
MP-BIF-17	404.04	3.9	0.01	10.1	0.3	0.0	0	2.80
MP-BIF-18	404.55	3.4	0.00	12.8	0.4	0.1	1.46	2.35
MP-BIF-19	405	4.4	0.04	13.9	0.5	0.2	3.07	0.86
MP-BIF-20	405.48	4.3	0.45	12.8	0.5	0.1	1.10	2.78
MP-BIF-21	405.92	4.1	0.48	12.4	0.3	0.0	0.05	2.81
MP-BIF-22	406.37	4.2	0.81	15.6	0.5	0.1	5.36	0.88
MP-BIF-23	406.79	7.2	0.27	10.5	0.7	0.2	0.76	2.84
MP-BIF-24	407.28	9.1	0.07	18.1	0.9	1.6	0.00	3.08
MP-BIF-25	407.80	4.7	0.34	15.9	0.4	0.1	5.03	2.48
MP-BIF-26	408.32	4.4	0.19	13.9	0.4	0.0	0.00	0.90
MP-BIF-27	408.70	4.1	0.25	9.4	0.4	0.1	0.82	3.13
MP-BIF-28	409.22	4.3	0.02	14.1	0.4	0.1	2.83	2.57
MP-BIF-29	409.73	5.0	0.19	13.7	0.3	0.1	0.00	0.88
MP-BIF-30	410.21	5.6	0.03	17.0	0.5	0.1	4.31	2.58
MP-BIF-31	410.55	5.3	0.48	24.0	0.4	0.1	0.00	2.21
MP-BIF-32	411.02	5.7	0.03	9.1	0.5	0.0	1.02	2.94
MP-BIF-33	411.45	4.8	0.19	8.5	0.5	0.1	0.67	0.88
MP-BIF-34	411.96	4.6	0.26	13.7	0.4	0.1	0.01	2.67
MP-BIF-35	412.47	6.7	0.04	20.1	0.5	0.3	4.19	2.99
MP-BIF-36	412.99	5.0	0.19	12.7	0.5	0.1	2.41	0.90
MP-BIF-37	413.49	3.2	0.03	14.0	0.3	0.1	0.00	3.23
MP-BIF-38	413.98	6.3	0.55	13.1	0.5	0.1	5.66	3.92
MP-BIF-39	414.53	4.7	0.12	11.8	0.3	0.1	5.43	2.63
MP-BIF-40	414.93	7.4	0.17	12.1	0.6	0.4	3.36	0.76
MP-BIF-41	415.51	5.4	0.78	10.6	0.4	0.0	4.92	2.39
MP-BIF-42	415.87	5.1	0.04	11.7	0.5	1.1	3.72	2.71
MP-BIF-43	416.30	8.0	0.05	12.0	0.8	0.1	4.04	0.75
MP-BIF-44	416.82	11.9	0.04	12.3	1.0	0.5	1.76	2.59
MP-BIF-45	417.29	4.3	0.00	12.2	0.5	0.2	0.00	3.49
MP-BIF-46	417.86	6.3	0.07	26.6	0.5	0.1	5.69	2.86
MP-BIF-47	418.43	8.4	0.00	11.0	0.6	0.4	6.62	1.41
MP-BIF-48	418.90	8.2	0.03	5.9	0.7	0.2	7.29	2.59
MP-BIF-49	419.41	6.7	0.01	18.1	0.6	0.1	3.74	2.84
MP-BIF-50	419.85	6.4	0.03	13.7	0.7	0.2	1.06	0.77
MP-BIF-51	420.30	8.3	0.07	5.5	0.7	0.5	0.09	2.33
MP-BIF-52	420.41	11.0	0.16	15.8	0.8	0.2	2.43	2.89
MP-BIF-53	420.92	7.0	1.40	35.1	0.6	0.1	7.08	0.79

MP-56 – Manganese ore

Sample name	Depth	Zr	Hf	Y	Nb	U	Th	Ta
	(m)	(ppm)						
MP-100	421.5	3.82	0.08	4.00	0.12	0.03	0.11	0.00
MP-101	421.70	3.94	0.05	4.97	0.21	0.08	0.19	Below LOD
MP-102	422.10	2.99	0.03	4.43	0.24	0.08	0.21	0.01
MP-103	422.75	3.31	0.08	5.32	0.17	0.09	0.21	0.01
MP-104	423.15	6.85	0.15	4.22	0.21	0.09	0.20	0.02
MP-105	423.74	2.15	0.03	3.57	0.19	0.07	0.18	0.01
MP-106	424.28	3.94	0.08	5.74	0.40	0.15	0.35	0.02
MP-107	424.49	2.78	0.04	4.43	0.19	0.11	0.26	0.02
MP-108	425.10	6.93	0.16	5.66	0.36	0.12	0.40	0.02
MP-109	425.70	2.49	0.05	4.10	0.22	0.06	0.24	0.01
MP-110	426.30	2.80	0.04	3.93	0.22	0.07	0.23	0.01
MP-111	426.85	4.12	0.06	5.71	0.31	0.08	0.34	0.04
MP-112	427.32	4.67	0.11	4.43	0.28	0.10	0.28	0.03
MP-113	427.9	3.98	0.05	5.84	0.32	0.10	0.33	0.01
MP-114	428.3	4.02	0.06	5.71	0.33	0.09	0.34	0.01
MP-115	428.7	4.34	0.07	4.84	0.27	0.08	0.34	0.02
MP-116	429.3	3.74	0.07	4.86	0.21	0.11	0.21	0.02
MP-117	429.5	5.68	0.11	6.89	0.57	0.07	0.54	0.04
MP-118	430.1	5.69	0.11	5.39	0.45	0.10	0.43	0.04
MP-119	430.5	3.95	0.11	5.44	0.28	0.07	0.37	0.02
MP-120	430.9	5.16	0.14	6.46	0.52	0.09	0.45	0.04
MP-121	431.4	7.96	0.16	5.32	0.54	0.12	0.42	0.03
MP-122	431.9	4.09	0.08	5.11	0.40	0.14	0.42	0.03
MP-123	432.3	3.59	0.07	4.32	0.30	0.10	0.31	0.02
MP-124	432.7	4.15	0.08	5.46	0.51	0.15	0.28	0.02
MP-125	433.1	5.95	0.16	3.99	0.29	0.09	0.30	0.02
MP-126	433.5	3.34	0.15	4.08	0.40	0.10	0.31	0.02
MP-127	433.9	4.42	0.09	6.02	0.47	0.10	0.49	0.04
MP-128	434.4	2.44	0.07	5.18	0.29	0.07	0.34	0.02
MP-129	435.0	2.61	0.06	3.98	0.23	0.10	0.23	0.01
MP-130	435.5	3.83	0.05	5.87	0.34	0.16	0.36	0.02
MP-131	435.9	2.99	0.06	4.60	0.28	0.09	0.22	0.01
MP-132	436.4	2.44	0.05	3.78	0.26	0.07	0.24	0.02
MP-133	436.8	2.49	0.04	4.22	0.23	0.04	0.21	0.01
MP-134	437.4	2.38	0.06	3.89	0.20	0.09	0.18	0.02
MP-135	438.0	2.85	0.04	3.85	0.26	0.06	0.29	0.02
MP-136	438.4	2.80	0.05	5.24	0.25	0.08	0.23	0.02
MP-137	439.0	2.04	0.04	2.91	0.24	0.08	0.18	0.02
MP-138	439.5	2.68	0.04	3.81	0.26	0.07	0.25	0.02
MP-139	439.8	2.78	0.06	3.98	0.30	0.14	0.23	0.00
MP-140	440.3	1.66	0.03	2.19	0.15	0.04	0.15	0.01
MP-141	440.8	3.54	0.07	3.46	0.38	0.11	0.29	0.03
MP-142	441.2	2.48	0.05	2.94	0.23	0.08	0.22	0.01
MP-143	441.8	2.77	0.06	2.80	0.21	0.06	0.21	0.01
MP-144	442.3	2.89	0.06	3.54	0.23	0.07	0.22	0.01
MP-145	442.9	4.83	0.11	3.30	0.26	0.07	0.30	0.01
MP-146	443.4	3.28	0.06	3.41	0.29	0.08	0.27	0.02
MP-147	443.9	4.85	0.10	4.55	0.42	0.10	0.42	0.04
MP-148	444.6	3.82	0.08	4.27	0.32	0.11	0.37	0.02
MP-149	445.3	4.95	0.08	4.66	0.28	0.10	0.35	0.02
MP-150	445.6	5.57	0.16	5.32	0.44	0.13	0.50	0.03
MP-151	446.3	4.25	0.08	7.07	0.32	0.08	0.32	0.02
MP-152	446.7	4.83	0.08	5.18	0.32	0.09	0.32	0.01
MP-153	447.2	5.16	0.08	7.08	0.35	0.08	0.35	0.01
MP-154	447.8	4.07	0.05	7.16	0.25	0.08	0.28	0.02
MP-155	448.2	5.94	0.08	5.96	0.39	0.08	0.29	0.01
MP-156	448.7	5.41	0.07	6.67	0.39	0.09	0.38	0.02
MP-157	449.3	6.75	0.12	6.33	0.31	0.08	0.30	0.03
MP-158	449.7	5.65	0.09	7.01	0.37	0.09	0.34	0.02
MP-159	450.1	5.66	0.09	10.36	0.43	0.13	0.40	0.04
MP-160	450.6	7.55	0.11	9.67	0.71	0.17	0.77	0.05
MP-161	451.2	5.56	0.06	6.67	0.53	0.09	0.44	0.02
MP-162	451.7	6.73	0.09	7.84	0.61	0.24	0.75	0.04
MP-163	452.2	5.03	0.11	8.65	0.56	0.18	0.48	0.04

MP-56 – Hematite lutite

Sample name	Depth	Zr	Hf	Y	Nb	U	Th	Ta
	(m)	(ppm)						
MP-164	452.7	4.46	0.10	3.09	0.62	0.06	0.22	Below LOD
MP-165	453.2	4.38	0.05	8.06	0.42	0.06	0.18	0.02
MP-166	453.6	5.35	0.09	7.40	0.50	0.10	0.33	0.02
MP-167	454.0	6.04	0.07	9.39	0.45	0.09	0.28	0.02
MP-168	454.5	5.47	0.07	8.17	0.45	0.08	0.32	0.01
MP-169	455.1	6.39	0.08	11.44	0.57	0.11	0.42	0.02
MP-170	455.6	5.91	0.10	11.01	0.40	0.08	0.34	0.02
MP-171	456.1	5.58	0.10	6.75	0.37	0.07	0.36	0.03
MP-172	456.7	5.90	0.08	7.24	0.40	0.08	0.36	0.03
MP-173	457.1	7.38	0.08	8.23	0.55	0.16	0.48	0.02
MP-174	457.4	6.15	0.06	8.39	0.56	0.12	0.36	0.01
MP-175	458.0	8.18	0.12	7.54	0.69	0.14	0.60	0.05
MP-176	458.6	6.32	0.13	5.07	0.60	0.13	0.47	0.02

A5. $\delta^{13}C$ raw data

G774 - BIF

Sample	Depth (m)	$\delta^{13}C$ (‰)
G7BF - 01	90.81	-11.4
G7BF - 02	91.28	-11.9
G7BF - 03	91.65	-12.9
G7BF - 04	92.10	-12.6
G7BF - 05	92.48	-12.9
G7BF - 06	92.94	-12.5
G7BF - 07	93.34	-12.2
G7BF - 08	93.88	-12.6
G7BF - 09	94.35	-12.4
G7BF - 10	94.73	-12.7
G7BF - 11	95.11	-11.7
G7BF - 12	95.73	-14.3
G7BF - 13	96.23	-15.4
G7BF - 14	96.73	-18.0
G7BF - 15	97.15	-18.3
G7BF - 16	97.54	-18.0
G7BF - 17	98.02	-18.4
G7BF - 18	98.60	-17.8
G7BF - 19	99.02	-17.5
G7BF - 20	99.42	-15.0
G7BF - 21	100.18	-14.8
G7BF - 22	100.56	-15.7
G7BF - 23	101	-12.1
G7BF - 24	101.64	-12.8

G774 - Hematite lutite

Sample	Depth (m)	$\delta^{13}C$ (‰)
G7-104	151.75	-14.5
G7-105	152.05	-15.6
G7-106	152.39	-13.4
G7-107	152.85	-13.3
G7-108	153.36	-14.2
G7-109	153.80	-13.1
G7-110	154.26	-13.6
G7-111	154.73	-14.9
G7-112	155.21	-15.2
G7-113	155.69	-13.6
G7-114	156.25	-15.6
G7-115	156.74	-16.6
G7-116	157.17	-16.8
G7-117	157.62	-18.1
G7-118	158.13	-17.2
G7-119	158.58	-15.7
G7-120	159.03	-18.6
G7-121	159.63	-16.9
G7-122	160.00	-17.5
G7-123	160.53	-16.8
G7-124	160.95	-17.9
G7-125	161.44	-18.5
G7-126	161.92	-21.2
G7-127	162.50	-19.7
G7-128	163.10	-21.2
G7-129	163.49	-20.5
G7-130	163.84	-20.2
G7-131	164.40	-20.0
G7-132	165.08	-18.1
G7-133	165.64	-18.3
G7-134	166.04	-18.4
G7-135	166.63	-17.5
G7-136	167.07	-14.7

G774 - Manganese - ore

Sample	Depth (m)	$\delta^{13}C$ (‰)
G7-001	101.94	-8.7
G7-002	102.29	-8.1
G7-003	102.83	-6.9
G7-004	103.27	-6.3
G7-005	103.82	-7.2
G7-006	104.30	-6.8
G7-007	104.88	-7.9
G7-008	105.32	-9.3
G7-009	105.85	-9.6
G7-010	106.27	-9.2
G7-011	106.76	-9.6
G7-012	107.25	-9.7
G7-013	107.76	-10.3
G7-014	108.16	-10.3
G7-015	108.64	-10.0
G7-016	109.03	-9.1
G7-017	109.45	-8.8
G7-018	109.97	-9.1
G7-019	110.54	-9.2
G7-020	110.95	-8.8
G7-021	111.55	-8.6
G7-022	111.89	-8.6
G7-023	112.40	-7.9
G7-024	112.85	-7.9
G7-025	113.38	-7.8
G7-026	113.86	-7.7
G7-027	114.36	-7.9
G7-028	114.82	-7.0
G7-029	115.10	-7.5
G7-030	115.53	-6.7
G7-031	116.08	-7.2
G7-032	116.62	-7.5
G7-033	117.15	-7.3
G7-034	117.49	-7.4
G7-035	118.01	-7.5
G7-036	118.50	-7.8
G7-037	119.07	-7.9
G7-038	119.49	-8.1
G7-039	119.94	-8.5
G7-040	120.38	-9.0
G7-041	120.93	-9.5
G7-042	121.35	-9.8
G7-043	121.63	-9.6
G7-044	122.05	-9.8
G7-045	122.52	-9.5
G7-046	123.04	-8.1
G7-047	123.52	-7.5
G7-048	123.95	-7.4
G7-049	124.46	-7.9
G7-050	124.98	-7.5
G7-051	125.44	-8.0

G774 - Manganese - ore (Continued)

Sample	Depth (m)	$\delta^{13}C$ (‰)
G7-052	125.93	-7.2
G7-053	126.41	-7.0
G7-054	126.87	-7.2
G7-055	127.40	-7.5
G7-056	127.86	-9.2
G7-057	128.37	-9.8
G7-058	128.84	-10.2
G7-059	129.33	-10.5
G7-060	129.79	-10.4
G7-061	130.25	-10.8
G7-062	130.70	-11.6
G7-063	131.24	-11.1
G7-064	131.70	-11.3
G7-065	132.23	-11.1
G7-066	132.66	-11.3
G7-067	133.09	-11.5
G7-068	133.51	-10.9
G7-069	134.02	-10.8
G7-070	135.45	-10.7
G7-071	135.97	-10.8
G7-072	136.55	-10.8
G7-073	137.14	-10.3
G7-074	137.54	-11.1
G7-075	138.03	-11.2
G7-076	138.47	-11.2
G7-077	138.94	-11.4
G7-078	139.29	-11.4
G7-079	139.80	-11.5
G7-080	140.28	-11.6
G7-081	140.79	-11.4
G7-082	141.26	-11.3
G7-083	141.74	-11.4
G7-084	142.15	-11.1
G7-085	142.71	-10.7
G7-086	143.19	-10.3
G7-087	143.63	-9.6
G7-088	144.05	-10.5
G7-089	144.53	-11.7
G7-090	145.15	-11.6
G7-091	145.56	-11.4
G7-092	146.06	-13.0
G7-093	146.48	-10.7
G7-094	146.96	-13.3
G7-095	147.44	-14.9
G7-096	148.02	-14.2
G7-097	148.47	-14.5
G7-098	148.96	-13.3
G7-099	149.39	-13.7
G7-100	149.90	-13.4
G7-101	150.40	-14.7
G7-102	150.89	-14.5
G7-103	151.50	-14.5

MP-56 - BIF

Sample	Depth (m)	$\delta^{13}C$ (‰)
MP-BIF-01	396.45	-14.2
MP-BIF-02	396.67	-13.7
MP-BIF-03	397.19	-14.6
MP-BIF-04	397.85	-14.6
MP-BIF-05	398.48	-15.2
MP-BIF-06	398.74	-15.3
MP-BIF-07	399.22	-15.6
MP-BIF-08	399.72	-16.0
MP-BIF-09	400.21	-16.4
MP-BIF-10	400.67	-16.6
MP-BIF-11	401.24	-16.7
MP-BIF-12	401.68	-16.9
MP-BIF-13	402.04	-17.2
MP-BIF-14	402.56	-17.3
MP-BIF-15	403.06	-17.4
MP-BIF-16	403.55	-17.4
MP-BIF-17	404.04	-17.5
MP-BIF-18	404.55	-17.6
MP-BIF-19	405	-17.8
MP-BIF-20	405.48	-17.9
MP-BIF-21	405.92	-17.7
MP-BIF-22	406.37	-17.9
MP-BIF-23	406.79	-17.1
MP-BIF-24	407.28	-17.8
MP-BIF-25	407.80	-17.8
MP-BIF-26	408.32	-17.3
MP-BIF-27	408.70	-17.9
MP-BIF-28	409.22	-17.8
MP-BIF-29	409.73	-17.6
MP-BIF-30	410.21	-17.7
MP-BIF-31	410.55	-17.7
MP-BIF-32	411.02	-17.2
MP-BIF-33	411.45	-18.1
MP-BIF-34	411.96	-17.8
MP-BIF-35	412.47	-17.7
MP-BIF-36	412.99	-18.5
MP-BIF-37	413.49	-17.8
MP-BIF-38	413.98	-17.5
MP-BIF-39	414.53	-17.7
MP-BIF-40	414.93	-17.6
MP-BIF-41	415.51	-17.0
MP-BIF-42	415.87	-16.9
MP-BIF-43	416.30	-17.5
MP-BIF-44	416.82	-17.3
MP-BIF-45	417.29	-17.1
MP-BIF-46	417.86	-17.7
MP-BIF-47	418.43	-17.6
MP-BIF-48	418.90	-19.2
MP-BIF-49	419.41	-20.7
MP-BIF-50	419.85	-19.0
MP-BIF-51	420.30	-19.4
MP-BIF-52	420.41	-17.8
MP-BIF-53	420.92	-18.4

MP-56 - Manganese ore

Sample	Depth (m)	$\delta^{13}C$ (‰)
MP-100	421.46	-16.0
MP-101	421.70	-14.0
MP-102	422.10	-9.4
MP-103	422.75	-9.3
MP-104	423.15	-6.9
MP-105	423.74	-6.4
MP-106	424.28	-6.5
MP-107	424.49	-6.2
MP-108	425.10	-6.6
MP-109	425.70	-6.2
MP-110	426.30	-7.9
MP-111	426.85	-9.4
MP-112	427.32	-9.5
MP-113	427.93	-9.8
MP-114	428.30	-10.0
MP-115	428.65	-9.9
MP-116	429.25	-9.9
MP-117	429.50	-9.4
MP-118	430.08	-8.5
MP-119	430.48	-8.7
MP-120	430.94	-8.5
MP-121	431.39	-8.4
MP-122	431.92	-9.5
MP-123	432.31	-9.4
MP-124	432.70	-9.6
MP-125	433.10	-9.5
MP-126	433.51	-9.5
MP-127	433.85	-9.0
MP-128	434.35	-8.6
MP-129	434.95	-9.1
MP-130	435.45	-9.5
MP-131	435.90	-9.8
MP-132	436.40	-9.5
MP-133	436.80	-9.7
MP-134	437.44	-9.5
MP-135	437.95	-9.9
MP-136	438.44	-9.4
MP-137	438.95	-10.2
MP-138	439.45	-10.4
MP-139	439.80	-10.4
MP-140	440.30	-10.7
MP-141	440.75	-11.0
MP-142	441.20	-11.3
MP-143	441.80	-11.1
MP-144	442.33	-11.1
MP-145	442.90	-11.4
MP-146	443.40	-11.7
MP-147	443.85	-11.2
MP-148	444.60	-11.7
MP-149	445.30	-12.2
MP-150	445.60	-11.2
MP-151	446.30	-13.4
MP-152	446.70	-12.9
MP-153	447.22	-16.8
MP-154	447.75	-16.0
MP-155	448.15	-16.2
MP-156	448.65	-15.4
MP-157	449.25	-15.3
MP-158	449.65	-14.5
MP-159	450.05	-13.2
MP-160	450.55	-13.6
MP-161	451.15	-15.2
MP-162	451.65	-13.8
MP-163	452.20	-13.8

MP-56 - Hematite lutite

Sample	Depth (m)	$\delta^{13}C$ (‰)
MP-164	452.70	-14.5
MP-165	453.20	-13.3
MP-166	453.60	-13.5
MP-167	454.00	-12.3
MP-168	454.50	-12.9
MP-169	455.05	-12.0
MP-170	455.55	-13.3
MP-171	456.06	-13.8
MP-172	456.68	-14.6
MP-173	457.06	-15.9
MP-174	457.36	-17.6
MP-175	458	-17.6
MP-176	458.55	-18.4

A6. REE raw data

G774 - BIF

Sample	Depth	La	Ce	Pr	Nd	Sm	Eu	Gd	Tb	Dy	Y	Ho	Er	Tm	Yb	Lu
	(m)	(ppm)														
G7BF-01	90.81	0.13	0.10	0.09	0.08	0.12	0.10	0.10	0.08	0.08	0.25	0.11	0.15		0.17	0.12
G7BF-02	91.28	0.11	0.05	0.07	0.07	0.09	0.16	0.22	0.14	0.15	0.36	0.14	0.17		0.28	0.25
G7BF-03	91.65	0.12	0.07	0.08	0.08	0.09	0.15	0.15	0.14	0.18	0.45	0.23	0.18		0.25	0.36
G7BF-04	92.10	0.05	0.02	0.02	0.04	0.04	0.09	0.06	0.07	0.06	0.24	0.12	0.12		0.15	0.15
G7BF-05	92.48	0.06	0.03	0.03	0.04	0.04	0.11	0.19	0.07	0.11	0.23	0.12	0.12		0.15	0.19
G7BF-06	92.94	0.08	0.04	0.05	0.05	0.04	0.12	0.13	0.09	0.13	0.31	0.13	0.16		0.17	0.29
G7BF-07	93.34	0.13	0.07	0.08	0.08	0.06	0.15	0.21	0.16	0.11	0.42	0.18	0.22		0.26	0.31
G7BF-08	93.88	0.11	0.06	0.06	0.08	0.09	0.13	0.17	0.16	0.19	0.32	0.15	0.27		0.20	0.28
G7BF-09	94.35	0.15	0.10	0.10	0.11	0.13	0.16	0.23	0.15	0.21	0.47	0.27	0.25		0.26	0.37
G7BF-10	94.73	0.27	0.21	0.20	0.22	0.22	0.28	0.30	0.33	0.36	0.68	0.47	0.51		0.73	0.72
G7BF-11	95.11	0.14	0.10	0.10	0.11	0.10	0.15	0.16	0.13	0.19	0.33	0.17	0.20		0.24	0.23
G7BF-12	95.73	0.17	0.12	0.12	0.12	0.18	0.18	0.18	0.13	0.16	0.29	0.19	0.24		0.22	0.30
G7BF-13	96.23	0.14	0.10	0.11	0.14	0.14	0.15	0.18	0.19	0.24	0.32	0.27	0.21		0.30	0.29
G7BF-14	96.73	0.19	0.16	0.17	0.20	0.26	0.20	0.31	0.24	0.33	0.47	0.38	0.42		0.33	0.44
G7BF-15	97.15	0.09	0.07	0.08	0.09	0.12	0.15	0.13	0.16	0.19	0.27	0.20	0.25		0.23	0.28
G7BF-16	97.54	0.11	0.10	0.11	0.12	0.17	0.20	0.25	0.23	0.25	0.45	0.29	0.32		0.32	0.46
G7BF-17	98.02	0.07	0.05	0.06	0.06	0.10	0.11	0.19	0.17	0.23	0.32	0.22	0.29		0.48	0.51
G7BF-18	98.60	0.09	0.08	0.09	0.10	0.13	0.20	0.20	0.18	0.25	0.34	0.26	0.33		0.38	0.45
G7BF-19	99.02	0.26	0.22	0.24	0.26	0.33	0.35	0.41	0.36	0.39	0.52	0.44	0.36		0.44	0.54
G7BF-20	99.42	0.25	0.21	0.22	0.24	0.29	0.31	0.47	0.28	0.32	0.56	0.38	0.49		0.31	0.41
G7BF-21	100.18	0.24	0.19	0.20	0.22	0.24	0.30	0.33	0.31	0.32	0.49	0.33	0.49		0.36	0.46
G7BF-22	100.56	0.10	0.09	0.10	0.11	0.15	0.20	0.21	0.20	0.21	0.32	0.23	0.23		0.22	0.26
G7BF-23	101	0.13	0.09	0.11	0.12	0.13	0.20	0.26	0.25	0.30	0.46	0.30	0.37		0.48	0.52
G7BF-24	101.64	0.12	0.08	0.08	0.09	0.13	0.19	0.14	0.15	0.19	0.34	0.20	0.21		0.18	0.23

G774 – Hematite lutite

Sample	Depth	La	Ce	Pr	Nd	Sm	Eu	Gd	Tb	Dy	Y	Ho	Er	Tm	Yb	Lu
	(m)	(ppm)														
G7-104	151.75	3.06	3.79	0.47	2.16	0.38	0.08	0.53	0.07	0.52	7.61	0.16	0.54	0.08	0.60	0.08
G7-105	152.05	3.05	3.15	0.40	1.74	0.26	0.10	0.40	0.09	0.55	8.83	0.16	0.55	0.07	0.57	0.10
G7-106	152.39	2.98	3.59	0.47	2.11	0.37	0.09	0.45	0.08	0.61	9.13	0.18	0.65	0.07	0.58	0.11
G7-107	152.85	2.85	3.38	0.43	1.75	0.37	0.08	0.55	0.07	0.59	8.32	0.15	0.44	0.08	0.50	0.09
G7-108	153.36	3.14	3.57	0.43	1.82	0.29	0.09	0.53	0.10	0.65	9.27	0.17	0.59	0.07	0.66	0.12
G7-109	153.80	2.71	3.44	0.44	2.04	0.34	0.10	0.40	0.08	0.56	7.95	0.16	0.45	0.06	0.47	0.09
G7-110	154.26	3.03	3.58	0.49	1.86	0.42	0.09	0.55	0.07	0.70	8.85	0.17	0.59	0.09	0.68	0.09
G7-111	154.73	3.30	3.94	0.51	1.96	0.34	0.15	0.59	0.09	0.65	9.53	0.20	0.60	0.12	0.71	0.11
G7-112	155.21	3.06	3.71	0.46	1.73	0.41	0.12	0.52	0.09	0.73	8.58	0.18	0.57	0.09	0.52	0.11
G7-113	155.69	3.81	4.53	0.56	2.37	0.44	0.14	0.85	0.09	0.86	10.41	0.20	0.69	0.11	0.78	0.11
G7-114	156.25	2.96	3.34	0.43	2.03	0.38	0.11	0.57	0.08	0.65	8.92	0.15	0.64	0.08	0.62	0.11
G7-115	156.74	2.97	3.61	0.42	1.95	0.29	0.13	0.62	0.10	0.67	8.77	0.16	0.51	0.10	0.67	0.12
G7-116	157.17	3.07	3.50	0.44	2.13	0.43	0.13	0.61	0.09	0.70	9.29	0.20	0.67	0.11	0.62	0.11
G7-117	157.62	2.37	3.01	0.39	1.55	0.22	0.09	0.55	0.08	0.60	7.96	0.16	0.58	0.10	0.62	0.13
G7-118	158.13	3.79	4.91	0.61	2.68	0.48	0.14	0.63	0.11	0.85	9.00	0.19	0.73	0.10	0.75	0.13
G7-119	158.58	2.19	3.56	0.39	1.82	0.31	0.06	0.52	0.09	0.51	5.62	0.15	0.48	0.05	0.58	0.07
G7-120	159.03	3.13	4.38	0.53	2.16	0.38	0.14	0.60	0.11	0.75	8.48	0.19	0.60	0.09	0.60	0.09
G7-121	159.63	0.87	1.11	0.14	0.55	0.12	0.01	0.18	0.02	0.20	2.25	0.06	0.16	0.02	0.19	0.06
G7-122	160.00	2.36	2.78	0.38	1.51	0.31	0.09	0.38	0.07	0.49	6.92	0.15	0.54	0.08	0.56	0.12
G7-123	160.53	1.75	1.99	0.24	1.08	0.22	0.06	0.41	0.05	0.41	4.48	0.11	0.37	0.07	0.37	0.07
G7-124	160.95	2.50	2.78	0.38	1.58	0.36	0.07	0.40	0.08	0.63	8.33	0.14	0.56	0.09	0.54	0.10
G7-125	161.44	1.61	1.52	0.20	0.88	0.14	0.12	0.30	0.05	0.38	6.53	0.12	0.40	0.06	0.48	0.07
G7-126	161.92	1.49	1.45	0.15	0.94	0.16	0.06	0.28	0.04	0.33	5.69	0.11	0.37	0.06	0.44	0.06
G7-127	162.50	1.62	1.89	0.27	1.03	0.22	0.06	0.33	0.05	0.31	3.98	0.09	0.34	0.05	0.37	0.07
G7-128	163.10	2.05	2.31	0.30	1.35	0.32	0.06	0.45	0.06	0.42	5.80	0.11	0.37	0.05	0.40	0.06
G7-129	163.49	2.78	2.87	0.35	1.35	0.29	0.13	0.35	0.05	0.48	6.54	0.10	0.40	0.06	0.48	0.07
G7-130	163.84	2.29	2.90	0.36	1.51	0.33	0.07	0.51	0.07	0.53	7.06	0.15	0.47	0.06	0.48	0.07
G7-131	164.40	2.17	2.44	0.32	1.44	0.34	0.08	0.42	0.07	0.49	5.40	0.11	0.35	0.06	0.44	0.07
G7-132	165.08	2.43	2.50	0.28	1.17	0.31	0.10	0.38	0.06	0.50	5.41	0.10	0.38	0.05	0.43	0.06
G7-133	165.64	1.45	1.66	0.21	0.90	0.10	0.05	0.31	0.04	0.28	4.19	0.09	0.28	0.05	0.29	0.04
G7-134	166.04	2.66	3.40	0.46	1.79	0.34	0.08	0.41	0.06	0.52	6.09	0.11	0.45	0.06	0.42	0.06
G7-135	166.63	2.08	2.50	0.31	1.33	0.22	0.07	0.35	0.06	0.51	6.43	0.14	0.44	0.07	0.55	0.09
G7-136	167.07	1.70	1.97	0.25	0.81	0.16	0.11	0.29	0.04	0.33	5.56	0.11	0.37	0.05	0.41	0.07

G774 – Manganese ore

Sample	Depth	La	Ce	Pr	Nd	Sm	Eu	Gd	Tb	Dy	Y	Ho	Er	Tm	Yb	Lu
	(m)	(ppm)														
G7-001	101.94	2.09	1.94	0.33	1.49	0.42	0.08	0.42	0.06	0.46	5.15	0.10	0.37	0.04	0.38	0.06
G7-002	102.29	2.36	2.10	0.37	1.58	0.31	0.07	0.36	0.07	0.44	5.48	0.12	0.39	0.04	0.44	0.07
G7-003	102.83	3.69	16.60	0.81	4.42	0.85	0.39	1.76	0.21	1.44	18.47	0.30	0.81	0.07	0.49	0.08
G7-004	103.27	3.29	2.93	0.51	1.93	0.38	0.10	0.44	0.06	0.42	4.63	0.10	0.33	0.05	0.31	0.05
G7-005	103.82	3.51	3.72	0.52	2.33	0.45	0.09	0.45	0.06	0.44	5.14	0.12	0.38	0.04	0.30	0.07
G7-006	104.30	3.12	3.44	0.50	2.10	0.34	0.08	0.49	0.07	0.52	5.01	0.13	0.34	0.05	0.29	0.04
G7-007	104.88	2.34	2.15	0.33	1.41	0.17	0.06	0.35	0.05	0.38	3.65	0.09	0.22	0.04	0.28	0.03
G7-008	105.32	2.51	2.77	0.33	1.64	0.30	0.07	0.35	0.06	0.43	4.72	0.09	0.28	0.04	0.35	0.08
G7-009	105.85	2.44	2.85	0.35	1.50	0.31	0.06	0.45	0.07	0.46	4.77	0.11	0.37	0.06	0.43	0.06
G7-010	106.27	2.42	2.45	0.38	1.51	0.28	0.09	0.25	0.05	0.38	4.02	0.11	0.30	0.05	0.25	0.06
G7-011	106.76	2.61	2.91	0.35	1.62	0.34	0.08	0.33	0.07	0.40	4.63	0.14	0.32	0.05	0.36	0.05
G7-012	107.25	2.70	3.44	0.40	1.61	0.35	0.08	0.45	0.05	0.47	5.24	0.11	0.39	0.05	0.38	0.08
G7-013	107.76	2.73	3.46	0.35	1.69	0.35	0.08	0.46	0.07	0.52	5.48	0.13	0.47	0.07	0.44	0.05
G7-014	108.16	2.53	2.35	0.39	1.53	0.31	0.07	0.49	0.05	0.35	3.89	0.10	0.31	0.04	0.27	0.05
G7-015	108.64	2.96	2.78	0.44	1.65	0.36	0.07	0.49	0.05	0.41	4.30	0.09	0.30	0.04	0.32	0.07
G7-016	109.03	3.15	2.89	0.51	2.06	0.37	0.10	0.44	0.07	0.46	4.53	0.10	0.34	0.04	0.35	0.05
G7-017	109.45	2.79	3.20	0.45	1.90	0.36	0.10	0.44	0.07	0.49	4.63	0.11	0.38	0.06	0.30	0.04
G7-018	109.97	2.12	2.21	0.36	1.64	0.27	0.07	0.29	0.05	0.40	3.81	0.09	0.31	0.04	0.27	0.03
G7-019	110.54	2.55	2.57	0.45	1.79	0.35	0.09	0.37	0.06	0.35	3.99	0.09	0.28	0.05	0.26	0.06
G7-020	110.95	3.05	3.02	0.51	2.11	0.37	0.10	0.48	0.08	0.51	4.93	0.13	0.33	0.03	0.33	0.05
G7-021	111.55	2.80	3.06	0.49	2.20	0.46	0.11	0.47	0.07	0.52	4.52	0.10	0.34	0.04	0.37	0.05
G7-022	111.89	2.33	2.53	0.40	1.56	0.36	0.07	0.48	0.06	0.39	4.34	0.09	0.35	0.05	0.34	0.04
G7-023	112.40	2.89	3.51	0.48	2.01	0.36	0.11	0.46	0.09	0.55	5.18	0.12	0.30	0.04	0.28	0.04
G7-024	112.85	2.85	2.98	0.49	2.33	0.38	0.09	0.47	0.08	0.39	4.84	0.08	0.32	0.04	0.35	0.05
G7-025	113.38	2.94	3.08	0.49	2.11	0.34	0.11	0.55	0.06	0.52	4.83	0.10	0.35	0.04	0.30	0.05
G7-026	113.86	3.28	3.31	0.53	2.39	0.42	0.12	0.48	0.08	0.58	5.43	0.12	0.44	0.06	0.28	0.07
G7-027	114.36	3.53	3.56	0.56	2.28	0.39	0.15	0.58	0.08	0.55	5.38	0.13	0.30	0.06	0.32	0.07
G7-028	114.82	3.17	2.72	0.49	2.00	0.48	0.07	0.33	0.06	0.50	4.39	0.09	0.27	0.04	0.29	0.05
G7-029	115.10	3.55	3.29	0.55	2.30	0.32	0.11	0.51	0.08	0.51	4.88	0.11	0.33	0.05	0.31	0.04
G7-030	115.53	3.60	3.33	0.58	2.50	0.35	0.14	0.44	0.08	0.58	5.01	0.11	0.38	0.05	0.32	0.04
G7-031	116.08	3.68	3.28	0.59	2.41	0.50	0.11	0.57	0.06	0.60	5.59	0.12	0.37	0.04	0.31	0.04
G7-032	116.62	3.17	2.77	0.51	1.98	0.44	0.10	0.42	0.08	0.45	4.42	0.11	0.26	0.04	0.27	0.04
G7-033	117.15	3.82	3.89	0.64	2.82	0.50	0.11	0.46	0.10	0.59	5.79	0.14	0.45	0.06	0.31	0.06
G7-034	117.49	3.34	3.21	0.53	2.25	0.45	0.12	0.59	0.07	0.53	4.78	0.11	0.30	0.04	0.32	0.06
G7-035	118.01	4.02	3.47	0.61	2.65	0.51	0.13	0.68	0.10	0.59	5.27	0.11	0.36	0.06	0.31	0.07
G7-036	118.50	4.31	4.13	0.71	3.06	0.56	0.12	0.71	0.08	0.50	5.58	0.14	0.44	0.05	0.29	0.06
G7-037	119.07	3.99	4.08	0.70	2.86	0.55	0.15	0.57	0.08	0.65	5.98	0.14	0.44	0.06	0.41	0.06
G7-038	119.49	3.98	4.54	0.62	2.91	0.67	0.16	0.75	0.08	0.79	7.29	0.19	0.52	0.08	0.55	0.08
G7-039	119.94	2.02	2.31	0.38	1.69	0.38	0.06	0.37	0.05	0.36	3.63	0.09	0.23	0.03	0.27	0.04
G7-040	120.38	2.11	2.90	0.37	1.39	0.35	0.10	0.41	0.06	0.38	4.28	0.12	0.34	0.04	0.43	0.05
G7-041	120.93	1.48	1.34	0.20	0.85	0.14	0.09	0.20	0.03	0.24	2.11	0.06	0.18	0.03	0.18	0.02
G7-042	121.35	2.91	2.60	0.39	1.56	0.30	0.09	0.38	0.06	0.42	4.05	0.09	0.31	0.03	0.29	0.05
G7-043	121.63	3.48	3.32	0.50	2.28	0.32	0.11	0.55	0.08	0.49	5.04	0.12	0.34	0.05	0.38	0.03
G7-044	122.05	3.74	3.91	0.55	2.24	0.40	0.11	0.48	0.08	0.51	5.61	0.11	0.34	0.04	0.32	0.05
G7-045	122.52	3.75	3.27	0.52	2.13	0.34	0.07	0.40	0.08	0.50	4.87	0.13	0.28	0.04	0.35	0.05
G7-046	123.04	3.96	4.16	0.67	2.80	0.59	0.16	0.61	0.09	0.58	6.68	0.14	0.48	0.07	0.42	0.07
G7-047	123.52	4.25	4.31	0.72	3.11	0.47	0.15	0.68	0.08	0.64	6.42	0.16	0.48	0.05	0.45	0.08
G7-048	123.95	3.90	3.94	0.61	2.52	0.54	0.09	0.69	0.09	0.57	6.76	0.14	0.47	0.06	0.48	0.07
G7-049	124.46	2.81	2.67	0.38	1.70	0.42	0.09	0.47	0.07	0.40	5.18	0.12	0.37	0.03	0.31	0.05
G7-050	124.98	3.57	2.92	0.51	2.09	0.38	0.09	0.56	0.06	0.42	5.70	0.12	0.45	0.05	0.41	0.06
G7-051	125.44	4.45	4.89	0.72	3.38	0.61	0.18	0.90	0.11	0.85	9.54	0.19	0.53	0.11	0.60	0.09

G774 – Manganese ore (Continued)

Sample	Depth	La	Ce	Pr	Nd	Sm	Eu	Gd	Tb	Dy	Y	Ho	Er	Tm	Yb	Lu
	(m)	(ppm)														
G7-052	125.93	3.64	3.23	0.61	2.49	0.33	0.09	0.44	0.06	0.48	5.44	0.12	0.38	0.05	0.31	0.05
G7-053	126.41	4.82	5.72	0.91	3.86	0.62	0.17	1.05	0.12	0.75	8.07	0.19	0.53	0.08	0.50	0.07
G7-054	126.87	5.11	6.64	1.02	4.26	0.88	0.20	0.92	0.15	0.98	10.13	0.24	0.81	0.10	0.61	0.12
G7-055	127.40	4.03	3.16	0.61	2.43	0.34	0.10	0.54	0.08	0.49	5.43	0.10	0.33	0.04	0.30	0.04
G7-056	127.86	3.05	2.49	0.40	1.81	0.25	0.07	0.33	0.05	0.48	4.60	0.10	0.31	0.05	0.26	0.05
G7-057	128.37	3.13	2.60	0.42	2.01	0.29	0.08	0.46	0.05	0.48	4.64	0.11	0.31	0.06	0.32	0.06
G7-058	128.84	3.18	3.45	0.49	2.18	0.47	0.08	0.53	0.07	0.58	5.80	0.13	0.43	0.07	0.33	0.07
G7-059	129.33	2.97	2.77	0.45	1.83	0.39	0.10	0.37	0.07	0.44	4.62	0.10	0.33	0.04	0.32	0.04
G7-060	129.79	3.38	3.72	0.50	2.20	0.43	0.12	0.52	0.09	0.49	4.83	0.10	0.34	0.05	0.23	0.05
G7-061	130.25	2.05	1.91	0.30	1.22	0.23	0.05	0.28	0.04	0.30	3.75	0.09	0.25	0.04	0.31	0.05
G7-062	130.70	2.41	2.33	0.40	1.55	0.37	0.07	0.36	0.06	0.33	4.17	0.09	0.26	0.05	0.30	0.04
G7-063	131.24	1.97	1.69	0.31	1.19	0.14	0.07	0.36	0.05	0.38	3.84	0.11	0.37	0.04	0.31	0.04
G7-064	131.70	1.97	2.18	0.32	1.27	0.24	0.06	0.41	0.06	0.46	4.32	0.11	0.37	0.04	0.34	0.04
G7-065	132.23	2.22	2.44	0.38	1.45	0.30	0.06	0.44	0.08	0.37	4.33	0.11	0.32	0.05	0.38	0.04
G7-066	132.66	2.43	2.60	0.40	1.73	0.29	0.08	0.47	0.06	0.42	4.20	0.11	0.33	0.05	0.23	0.05
G7-067	133.09	2.38	2.25	0.36	1.56	0.28	0.05	0.39	0.05	0.37	3.58	0.08	0.24	0.04	0.30	0.03
G7-068	133.51	2.33	2.25	0.38	1.57	0.26	0.09	0.46	0.05	0.39	4.10	0.10	0.33	0.04	0.34	0.05
G7-069	134.02	1.96	1.75	0.30	1.22	0.18	0.05	0.32	0.05	0.34	3.53	0.07	0.29	0.04	0.21	0.04
G7-070	135.45	2.08	1.82	0.32	1.33	0.28	0.09	0.36	0.06	0.45	3.88	0.11	0.33	0.04	0.25	0.04
G7-071	135.97	2.03	1.93	0.40	1.49	0.28	0.08	0.34	0.06	0.31	3.81	0.07	0.29	0.03	0.24	0.03
G7-072	136.55	2.44	2.53	0.42	1.79	0.31	0.08	0.42	0.05	0.44	4.17	0.10	0.35	0.04	0.29	0.04
G7-073	137.14	2.00	2.11	0.34	1.33	0.21	0.06	0.39	0.04	0.32	3.56	0.09	0.25	0.03	0.22	0.04
G7-074	137.54	2.01	2.36	0.35	1.45	0.24	0.06	0.39	0.05	0.34	3.62	0.09	0.26	0.04	0.28	0.05
G7-075	138.03	1.79	1.93	0.32	1.30	0.24	0.08	0.32	0.05	0.36	3.52	0.08	0.26	0.04	0.21	0.03
G7-076	138.47	3.08	4.04	0.50	2.28	0.48	0.11	0.63	0.10	0.73	6.69	0.15	0.49	0.06	0.50	0.08
G7-077	138.94	2.06	2.49	0.33	1.52	0.24	0.08	0.38	0.06	0.43	4.22	0.10	0.31	0.04	0.30	0.06
G7-078	139.29	2.16	2.13	0.41	1.59	0.29	0.06	0.34	0.05	0.29	3.33	0.07	0.25	0.03	0.27	0.03
G7-079	139.80	1.92	2.25	0.33	1.29	0.27	0.09	0.38	0.04	0.36	3.75	0.09	0.29	0.03	0.25	0.04
G7-080	140.28	1.69	2.00	0.29	1.15	0.23	0.05	0.27	0.04	0.33	3.24	0.08	0.20	0.03	0.26	0.04
G7-081	140.79	2.10	2.71	0.38	1.61	0.34	0.10	0.34	0.07	0.39	4.36	0.09	0.34	0.04	0.30	0.04
G7-082	141.26	1.93	2.26	0.30	1.49	0.24	0.08	0.38	0.04	0.34	3.67	0.08	0.26	0.03	0.20	0.04
G7-083	141.74	2.20	2.37	0.34	1.54	0.26	0.06	0.44	0.04	0.42	3.44	0.09	0.24	0.04	0.22	0.03
G7-084	142.15	1.71	2.46	0.27	1.08	0.21	0.07	0.31	0.05	0.38	4.23	0.10	0.28	0.03	0.27	0.04
G7-085	142.71	2.09	2.91	0.38	1.32	0.29	0.09	0.46	0.06	0.43	5.20	0.12	0.35	0.06	0.33	0.07
G7-086	143.19	2.21	2.83	0.34	1.40	0.31	0.07	0.38	0.05	0.33	4.21	0.08	0.29	0.04	0.30	0.06
G7-087	143.63	2.77	3.75	0.42	1.90	0.35	0.09	0.55	0.09	0.58	5.19	0.13	0.43	0.06	0.39	0.05
G7-088	144.05	2.68	3.66	0.45	1.99	0.36	0.08	0.48	0.06	0.49	4.99	0.13	0.33	0.05	0.36	0.06
G7-089	144.53	3.67	4.78	0.62	2.67	0.49	0.12	0.53	0.09	0.62	6.27	0.16	0.45	0.06	0.52	0.07
G7-090	145.15	3.08	4.10	0.48	2.16	0.37	0.09	0.59	0.07	0.51	5.17	0.11	0.42	0.06	0.42	0.05
G7-091	145.56	2.88	3.37	0.47	1.83	0.32	0.10	0.46	0.07	0.51	4.89	0.11	0.35	0.05	0.32	0.07
G7-092	146.06	3.41	4.00	0.48	2.00	0.42	0.10	0.53	0.07	0.62	6.05	0.12	0.41	0.08	0.40	0.07
G7-093	146.48	3.82	4.03	0.53	2.21	0.41	0.11	0.57	0.08	0.52	7.22	0.16	0.46	0.07	0.52	0.08
G7-094	146.96	2.50	3.78	0.43	1.97	0.37	0.09	0.53	0.07	0.61	7.15	0.15	0.58	0.07	0.58	0.09
G7-095	147.44	3.96	4.37	0.64	2.70	0.39	0.14	0.52	0.10	0.57	7.26	0.14	0.55	0.07	0.49	0.09
G7-096	148.02	3.02	3.54	0.48	1.81	0.38	0.09	0.50	0.07	0.56	7.25	0.15	0.50	0.07	0.42	0.08
G7-097	148.47	3.32	4.15	0.52	2.26	0.34	0.10	0.56	0.09	0.70	8.25	0.18	0.52	0.08	0.60	0.11
G7-098	148.96	2.39	2.79	0.39	1.45	0.29	0.09	0.44	0.07	0.55	6.33	0.15	0.44	0.08	0.46	0.10
G7-099	149.39	3.36	3.94	0.49	1.90	0.40	0.12	0.58	0.08	0.68	8.29	0.18	0.54	0.07	0.60	0.09
G7-100	149.90	3.20	3.93	0.50	1.95	0.29	0.08	0.63	0.08	0.56	7.66	0.17	0.45	0.08	0.52	0.09
G7-101	150.40	3.72	4.68	0.60	2.40	0.48	0.13	0.64	0.10	0.72	8.85	0.19	0.60	0.07	0.61	0.11
G7-102	150.89	4.19	4.96	0.65	2.66	0.51	0.12	0.65	0.12	0.81	9.86	0.22	0.66	0.10	0.76	0.11
G7-103	151.50	5.54	5.52	0.66	2.66	0.53	0.16	0.65	0.10	1.06	15.70	0.27	0.84	0.12	0.80	0.16

MP-56 – BIF

Sample	Depth	La	Ce	Pr	Nd	Sm	Eu	Gd	Tb	Dy	Y	Ho	Er	Tm	Yb	Lu
	(m)	(ppm)														
MP-BIF-01	396.45	0.20	0.16	0.13	0.11	0.19	0.17	0.18	0.14	0.17	0.35	0.12	0.14		0.10	0.21
MP-BIF-02	396.67	0.15	0.10	0.10	0.09	0.09	0.16	0.16	0.15	0.17	0.37	0.15	0.21		0.39	0.21
MP-BIF-03	397.19	0.08	0.06	0.06	0.06	0.09	0.11	0.16	0.09	0.12	0.36	0.16	0.14		0.21	0.20
MP-BIF-04	397.85	0.11	0.07	0.07	0.07	0.10	0.10	0.16	0.13	0.19	0.47	0.21	0.26		0.23	0.33
MP-BIF-05	398.48	0.09	0.06	0.07	0.07	0.06	0.11	0.13	0.15	0.12	0.37	0.20	0.16		0.21	0.19
MP-BIF-06	398.74	0.08	0.05	0.05	0.05	0.03	0.17	0.13	0.11	0.15	0.37	0.16	0.20		0.19	0.31
MP-BIF-07	399.22	0.08	0.05	0.05	0.05	0.06	0.10	0.12	0.07	0.08	0.30	0.17	0.15		0.22	0.23
MP-BIF-08	399.72	0.07	0.04	0.04	0.05	0.04	0.09	0.13	0.13	0.10	0.33	0.16	0.18		0.19	0.21
MP-BIF-09	400.21	0.06	0.04	0.04	0.04	0.05	0.06	0.07	0.08	0.09	0.27	0.10	0.15		0.14	0.16
MP-BIF-10	400.67	0.09	0.05	0.05	0.06	0.07	0.09	0.10	0.10	0.14	0.53	0.24	0.25		0.32	0.52
MP-BIF-11	401.24	0.10	0.06	0.06	0.06	0.06	0.11	0.12	0.14	0.20	0.61	0.24	0.27		0.31	0.54
MP-BIF-12	401.68	0.08	0.04	0.05	0.06	0.08	0.10	0.10	0.11	0.17	0.39	0.17	0.23		0.28	0.30
MP-BIF-13	402.04	0.07	0.04	0.04	0.05	0.05	0.10	0.13	0.09	0.12	0.32	0.15	0.18		0.14	0.18
MP-BIF-14	402.56	0.07	0.04	0.04	0.05	0.07	0.11	0.19	0.07	0.10	0.30	0.14	0.16		0.14	0.18
MP-BIF-15	403.06	0.09	0.06	0.07	0.08	0.06	0.16	0.22	0.17	0.15	0.43	0.19	0.21		0.18	0.32
MP-BIF-16	403.55	0.18	0.13	0.13	0.14	0.17	0.13	0.19	0.22	0.19	0.30	0.23	0.21		0.27	0.30
MP-BIF-17	404.04	0.09	0.05	0.06	0.07	0.07	0.10	0.09	0.11	0.13	0.37	0.16	0.19		0.17	0.19
MP-BIF-18	404.55	0.08	0.04	0.05	0.05	0.06	0.08	0.12	0.17	0.13	0.47	0.20	0.24		0.34	0.43
MP-BIF-19	405	0.07	0.04	0.05	0.05	0.06	0.11	0.12	0.14	0.16	0.52	0.25	0.31		0.35	0.46
MP-BIF-20	405.48	0.11	0.07	0.08	0.09	0.06	0.17	0.17	0.15	0.20	0.47	0.30	0.21		0.21	0.21
MP-BIF-21	405.92	0.08	0.05	0.06	0.07	0.07	0.16	0.16	0.13	0.19	0.46	0.19	0.22		0.24	0.37
MP-BIF-22	406.37	0.10	0.06	0.07	0.08	0.11	0.14	0.16	0.16	0.19	0.58	0.23	0.31		0.50	0.44
MP-BIF-23	406.79	0.10	0.08	0.09	0.11	0.17	0.17	0.22	0.20	0.21	0.39	0.25	0.35		0.30	0.43
MP-BIF-24	407.28	0.24	0.20	0.21	0.22	0.27	0.29	0.40	0.35	0.48	0.67	0.52	0.56		0.48	0.61
MP-BIF-25	407.80	0.14	0.09	0.09	0.12	0.13	0.22	0.26	0.17	0.23	0.59	0.27	0.31		0.26	0.37
MP-BIF-26	408.32	0.09	0.06	0.06	0.08	0.09	0.13	0.16	0.14	0.18	0.51	0.27	0.24		0.33	0.42
MP-BIF-27	408.70	0.13	0.12	0.06	0.09	0.07	0.18	0.20	0.13	0.15	0.35	0.17	0.17		0.14	0.19
MP-BIF-28	409.22	0.08	0.05	0.05	0.06	0.07	0.14	0.15	0.18	0.19	0.52	0.24	0.30		0.32	0.47
MP-BIF-29	409.73	0.08	0.05	0.06	0.07	0.08	0.19	0.13	0.14	0.19	0.51	0.21	0.26		0.32	0.41
MP-BIF-30	410.21	0.07	0.04	0.05	0.06	0.08	0.12	0.15	0.15	0.29	0.63	0.29	0.46		0.60	0.64
MP-BIF-31	410.55	0.11	0.05	0.08	0.09	0.08	0.20	0.21	0.28	0.29	0.89	0.43	0.55		0.69	0.84
MP-BIF-32	411.02	0.12	0.07	0.06	0.07	0.10	0.13	0.15	0.11	0.15	0.34	0.20	0.22		0.27	0.41
MP-BIF-33	411.45	0.09	0.06	0.07	0.08	0.10	0.10	0.11	0.16	0.13	0.31	0.19	0.16		0.15	0.24
MP-BIF-34	411.96	0.10	0.07	0.07	0.07	0.09	0.13	0.17	0.16	0.24	0.51	0.28	0.29		0.31	0.49
MP-BIF-35	412.47	0.12	0.08	0.08	0.10	0.08	0.15	0.21	0.18	0.31	0.74	0.47	0.49		0.59	0.74
MP-BIF-36	412.99	0.09	0.06	0.06	0.06	0.10	0.12	0.14	0.18	0.17	0.47	0.24	0.31		0.45	0.54
MP-BIF-37	413.49	0.11	0.06	0.06	0.07	0.07	0.11	0.15	0.13	0.16	0.52	0.22	0.24		0.24	0.33
MP-BIF-38	413.98	0.12	0.08	0.09	0.11	0.09	0.18	0.24	0.19	0.19	0.49	0.27	0.29		0.27	0.53
MP-BIF-39	414.53	0.17	0.11	0.11	0.13	0.16	0.18	0.23	0.23	0.23	0.44	0.22	0.23		0.21	0.27
MP-BIF-40	414.93	0.10	0.07	0.08	0.09	0.10	0.18	0.13	0.15	0.22	0.45	0.22	0.28		0.32	0.40
MP-BIF-41	415.51	0.14	0.10	0.10	0.11	0.13	0.16	0.20	0.17	0.17	0.39	0.21	0.21		0.26	0.27
MP-BIF-42	415.87	0.11	0.09	0.12	0.12	0.16	0.18	0.20	0.16	0.22	0.43	0.27	0.30		0.28	0.31
MP-BIF-43	416.30	0.19	0.13	0.12	0.13	0.16	0.20	0.21	0.18	0.25	0.44	0.28	0.23		0.36	0.40
MP-BIF-44	416.82	0.17	0.14	0.15	0.18	0.20	0.31	0.26	0.24	0.29	0.46	0.29	0.32		0.24	0.52
MP-BIF-45	417.29	0.11	0.07	0.08	0.08	0.13	0.22	0.24	0.15	0.19	0.45	0.23	0.23		0.20	0.24
MP-BIF-46	417.86	0.14	0.09	0.08	0.13	0.15	0.35	0.22	0.26	0.43	0.99	0.51	0.58		0.78	0.93
MP-BIF-47	418.43	0.19	0.14	0.12	0.14	0.17	0.15	0.22	0.17	0.29	0.41	0.28	0.35		0.36	0.52
MP-BIF-48	418.90	0.03	0.02	0.03	0.03	0.06	0.08	0.09	0.11	0.14	0.22	0.16	0.18		0.26	0.30
MP-BIF-49	419.41	0.14	0.09	0.10	0.12	0.14	0.19	0.21	0.22	0.33	0.67	0.39	0.44		0.41	0.58
MP-BIF-50	419.85	0.13	0.10	0.12	0.15	0.20	0.26	0.30	0.28	0.40	0.51	0.41	0.49		0.47	0.45
MP-BIF-51	420.30	0.03	0.02	0.03	0.04	0.05	0.07	0.07	0.11	0.14	0.20	0.18	0.18		0.31	0.31
MP-BIF-52	420.41	0.19	0.14	0.14	0.16	0.15	0.24	0.22	0.27	0.27	0.59	0.32	0.39		0.32	0.50
MP-BIF-53	420.92	0.36	0.28	0.32	0.36	0.43	0.54	0.73	0.66	0.86	1.30	0.95	1.16		1.11	1.15

MP-56 – Manganese-ore

Sample	Depth	La	Ce	Pr	Nd	Sm	Eu	Gd	Tb	Dy	Y	Ho	Er	Tm	Yb	Lu
	(m)	(ppm)														
MP-100	421.46	1.69	1.55	0.21	0.83	0.12	0.07	0.28	0.05	0.33	4.00	0.08	0.26	0.04	0.31	0.05
MP-101	421.70	2.29	2.41	0.37	1.47	0.27	0.09	0.41	0.05	0.42	4.97	0.11	0.37	0.06	0.36	0.07
MP-102	422.10	2.16	1.71	0.30	1.21	0.20	0.06	0.38	0.05	0.34	4.43	0.09	0.30	0.05	0.32	0.06
MP-103	422.75	2.29	2.08	0.35	1.59	0.25	0.07	0.42	0.06	0.47	5.32	0.14	0.35	0.05	0.38	0.05
MP-104	423.15	2.54	2.24	0.38	1.57	0.29	0.06	0.29	0.05	0.37	4.22	0.10	0.27	0.04	0.25	0.05
MP-105	423.74	2.32	1.99	0.32	1.48	0.26	0.06	0.36	0.04	0.40	3.57	0.08	0.25	0.03	0.20	0.02
MP-106	424.28	3.55	3.31	0.60	2.45	0.35	0.12	0.43	0.08	0.47	5.74	0.14	0.40	0.06	0.37	0.06
MP-107	424.49	3.02	2.76	0.45	1.98	0.41	0.10	0.40	0.06	0.41	4.43	0.09	0.33	0.05	0.26	0.05
MP-108	425.10	3.50	3.62	0.58	2.52	0.44	0.08	0.55	0.06	0.53	5.66	0.13	0.37	0.05	0.38	0.05
MP-109	425.70	2.31	2.34	0.34	1.63	0.29	0.04	0.40	0.05	0.41	4.10	0.09	0.28	0.04	0.22	0.04
MP-110	426.30	2.15	2.22	0.31	1.38	0.25	0.07	0.31	0.05	0.33	3.93	0.08	0.27	0.03	0.24	0.04
MP-111	426.85	2.52	2.94	0.36	1.53	0.29	0.07	0.41	0.06	0.52	5.71	0.12	0.49	0.06	0.42	0.08
MP-112	427.32	2.54	2.67	0.36	1.63	0.32	0.07	0.33	0.05	0.41	4.43	0.10	0.29	0.05	0.32	0.06
MP-113	427.93	2.61	3.07	0.41	1.77	0.39	0.08	0.45	0.07	0.57	5.84	0.15	0.39	0.07	0.42	0.06
MP-114	428.30	2.67	3.38	0.46	1.91	0.36	0.12	0.46	0.08	0.63	5.71	0.13	0.40	0.06	0.50	0.06
MP-115	428.65	2.36	3.01	0.44	1.58	0.32	0.08	0.49	0.06	0.44	4.84	0.12	0.42	0.07	0.38	0.07
MP-116	429.25	2.53	2.19	0.37	1.31	0.23	0.05	0.46	0.06	0.45	4.86	0.11	0.38	0.05	0.28	0.05
MP-117	429.50	3.49	4.72	0.67	2.67	0.56	0.14	0.66	0.11	0.70	6.89	0.16	0.49	0.08	0.52	0.08
MP-118	430.08	3.20	3.44	0.55	2.22	0.49	0.10	0.58	0.07	0.59	5.39	0.13	0.38	0.06	0.35	0.06
MP-119	430.48	2.86	3.23	0.48	1.92	0.44	0.11	0.45	0.09	0.50	5.44	0.14	0.39	0.05	0.38	0.06
MP-120	430.94	3.45	4.37	0.59	2.68	0.50	0.13	0.73	0.09	0.73	6.46	0.17	0.51	0.07	0.42	0.07
MP-121	431.39	3.58	3.58	0.64	2.77	0.47	0.12	0.46	0.08	0.54	5.32	0.12	0.34	0.06	0.34	0.06
MP-122	431.92	2.96	3.45	0.47	2.05	0.38	0.08	0.49	0.07	0.56	5.11	0.13	0.41	0.06	0.42	0.06
MP-123	432.31	2.56	2.98	0.39	1.65	0.28	0.09	0.50	0.07	0.43	4.32	0.11	0.30	0.05	0.31	0.05
MP-124	432.70	2.51	2.83	0.46	2.00	0.37	0.10	0.42	0.06	0.57	5.46	0.12	0.44	0.06	0.36	0.07
MP-125	433.10	1.96	2.74	0.39	1.62	0.25	0.08	0.37	0.05	0.42	3.99	0.10	0.33	0.05	0.32	0.06
MP-126	433.51	2.75	2.55	0.43	1.78	0.35	0.08	0.33	0.05	0.43	4.08	0.09	0.28	0.04	0.25	0.05
MP-127	433.85	3.76	4.22	0.64	2.84	0.49	0.12	0.72	0.09	0.59	6.02	0.17	0.43	0.05	0.39	0.07
MP-128	434.35	2.46	2.86	0.48	2.16	0.33	0.10	0.59	0.08	0.48	5.18	0.11	0.33	0.05	0.32	0.06
MP-129	434.95	2.56	2.31	0.39	1.48	0.25	0.06	0.35	0.05	0.36	3.98	0.07	0.29	0.05	0.29	0.04
MP-130	435.45	2.32	3.51	0.42	1.79	0.43	0.11	0.47	0.07	0.56	5.87	0.13	0.38	0.05	0.32	0.06
MP-131	435.90	1.57	2.11	0.33	1.28	0.26	0.05	0.35	0.06	0.41	4.60	0.11	0.31	0.05	0.33	0.06
MP-132	436.40	1.88	1.98	0.34	1.42	0.25	0.06	0.36	0.05	0.38	3.78	0.07	0.28	0.03	0.27	0.04
MP-133	436.80	1.25	2.35	0.20	1.00	0.23	0.06	0.33	0.05	0.34	4.22	0.09	0.28	0.03	0.29	0.04
MP-134	437.44	1.67	2.44	0.32	1.50	0.44	0.13	0.59	0.06	0.33	3.89	0.08	0.26	0.04	0.22	0.04
MP-135	437.95	1.64	2.65	0.33	1.53	0.33	0.10	0.40	0.05	0.43	3.85	0.09	0.27	0.04	0.29	0.04
MP-136	438.44	1.75	2.42	0.25	1.00	0.22	0.07	0.34	0.08	0.59	5.24	0.15	0.59	0.09	0.60	0.09
MP-137	438.95	1.67	1.66	0.23	0.96	0.22	0.05	0.24	0.04	0.31	2.91	0.07	0.26	0.03	0.21	0.03
MP-138	439.45	1.92	2.46	0.34	1.49	0.32	0.10	0.41	0.04	0.42	3.81	0.08	0.28	0.04	0.19	0.05
MP-139	439.80	2.21	2.26	0.36	1.49	0.22	0.08	0.32	0.04	0.33	3.98	0.08	0.30	0.04	0.23	0.04
MP-140	440.30	0.92	1.31	0.12	0.38	0.18	0.03	0.16	0.04	0.18	2.19	0.05	0.15	0.02	0.17	0.03
MP-141	440.75	2.06	2.34	0.34	1.46	0.30	0.10	0.32	0.04	0.33	3.46	0.07	0.26	0.04	0.22	0.03
MP-142	441.20	1.84	2.05	0.31	1.25	0.14	0.05	0.24	0.04	0.24	2.94	0.08	0.19	0.03	0.23	0.03
MP-143	441.80	1.48	1.83	0.21	0.76	0.19	0.04	0.27	0.03	0.29	2.80	0.06	0.20	0.03	0.21	0.03
MP-144	442.33	2.09	2.40	0.35	1.46	0.22	0.06	0.24	0.04	0.27	3.54	0.07	0.25	0.04	0.20	0.03
MP-145	442.90	2.11	2.57	0.36	1.46	0.22	0.06	0.32	0.04	0.30	3.30	0.08	0.27	0.03	0.27	0.04
MP-146	443.40	2.05	2.50	0.34	1.44	0.20	0.07	0.30	0.05	0.37	3.41	0.07	0.28	0.04	0.22	0.04
MP-147	443.85	2.58	3.75	0.47	1.91	0.40	0.08	0.48	0.06	0.50	4.55	0.10	0.31	0.05	0.40	0.06
MP-148	444.60	2.57	3.36	0.41	1.80	0.34	0.09	0.41	0.05	0.37	4.27	0.11	0.25	0.04	0.28	0.05
MP-149	445.30	3.27	3.53	0.46	2.09	0.32	0.10	0.38	0.06	0.43	4.66	0.12	0.32	0.04	0.36	0.07
MP-150	445.60	3.05	4.85	0.58	2.37	0.48	0.10	0.55	0.08	0.52	5.32	0.13	0.38	0.05	0.43	0.07
MP-151	446.30	2.83	3.95	0.49	2.02	0.40	0.14	0.65	0.08	0.57	7.07	0.16	0.47	0.05	0.52	0.06
MP-152	446.70	2.83	3.95	0.49	2.02	0.40	0.14	0.65	0.08	0.57	7.07	0.16	0.47	0.05	0.52	0.06
MP-153	447.22	3.69	3.13	0.47	1.78	0.36	0.09	0.31	0.08	0.49	5.18	0.13	0.38	0.05	0.29	0.07
MP-154	447.75	2.76	3.78	0.48	1.94	0.28	0.11	0.61	0.09	0.59	7.08	0.15	0.47	0.08	0.48	0.10
MP-155	448.15	2.81	3.32	0.44	1.73	0.34	0.09	0.40	0.05	0.58	7.16	0.15	0.45	0.07	0.38	0.06
MP-156	448.65	2.14	2.55	0.32	1.33	0.25	0.06	0.40	0.06	0.49	5.96	0.12	0.45	0.07	0.42	0.06
MP-157	449.25	2.41	3.03	0.38	1.63	0.30	0.09	0.33	0.05	0.54	6.67	0.13	0.52	0.08	0.55	0.09
MP-158	449.65	2.66	3.04	0.38	1.56	0.32	0.09	0.49	0.07	0.52	6.33	0.13	0.45	0.06	0.45	0.08
MP-159	450.05	2.59	3.08	0.41	1.67	0.42	0.08	0.52	0.08	0.58	7.01	0.14	0.50	0.08	0.58	0.08
MP-160	450.55	3.76	4.54	0.61	2.42	0.53	0.11	0.71	0.09	0.87	10.36	0.21	0.67	0.09	0.69	0.11
MP-161	451.15	4.35	5.41	0.66	3.03	0.62	0.14	0.69	0.09	0.71	9.67	0.19	0.63	0.10	0.80	0.12
MP-162	451.65	2.86	3.86	0.49	1.93	0.44	0.15	0.52	0.07	0.54	6.67	0.12	0.42	0.07	0.48	0.10
MP-163	452.20	3.81	4.71	0.61	2.54	0.49	0.11	0.54	0.09	0.63	7.84	0.18	0.57	0.08	0.59	0.11

MP-56 – Hematite lutite

Sample	Depth	La	Ce	Pr	Nd	Sm	Eu	Gd	Tb	Dy	Y	Ho	Er	Tm	Yb	Lu
	(m)	(ppm)														
MP-164	452.70	1.38	1.91	0.19	0.93	0.14	0.06	0.24	0.02	0.20	3.09	0.06	0.21	0.04	0.30	0.06
MP-165	453.20	2.95	3.50	0.51	1.85	0.24	0.09	0.50	0.09	0.61	8.06	0.16	0.55	0.06	0.55	0.08
MP-166	453.60	2.94	3.87	0.45	1.89	0.44	0.10	0.47	0.08	0.52	7.40	0.13	0.41	0.06	0.50	0.09
MP-167	454.00	4.26	5.66	0.71	2.41	0.54	0.14	0.49	0.11	0.73	9.39	0.19	0.60	0.10	0.56	0.09
MP-168	454.50	4.02	5.40	0.64	2.47	0.41	0.14	0.64	0.10	0.66	8.17	0.17	0.50	0.08	0.50	0.09
MP-169	455.05	6.38	8.22	0.91	3.59	0.66	0.18	0.79	0.11	0.87	11.44	0.25	0.71	0.11	0.73	0.16
MP-170	455.55	6.35	8.90	1.02	4.22	0.78	0.22	1.03	0.12	0.89	11.01	0.25	0.71	0.11	0.60	0.11
MP-171	456.06	2.86	3.46	0.46	1.88	0.38	0.08	0.43	0.07	0.51	6.75	0.16	0.51	0.07	0.52	0.07
MP-172	456.68	3.15	3.57	0.45	1.75	0.28	0.11	0.43	0.08	0.54	7.24	0.16	0.58	0.09	0.70	0.12
MP-173	457.06	3.82	5.25	0.68	2.91	0.50	0.12	0.75	0.11	0.84	8.23	0.19	0.62	0.08	0.53	0.11
MP-174	457.36	4.38	6.07	0.71	2.77	0.59	0.16	0.77	0.09	0.73	8.39	0.19	0.56	0.10	0.68	0.12
MP-175	458	4.45	6.16	0.76	2.91	0.61	0.10	0.66	0.10	0.65	7.54	0.17	0.50	0.08	0.61	0.11
MP-176	458.55	2.43	3.98	0.52	2.39	0.22	0.08	0.76	0.08	0.50	5.07	0.14	0.48	0.07	0.48	0.09

A7. Cobalt's correction

Thibon et al (2019) Co data

Sample	Depth (m)	Lithology	Co (ppm)
MP9c	398.00	BIF	0.65
MP10	401.00	BIF	0.75
MP11	403.20	BIF	0.58
MP12	404.90	BIF	0.80
MP13	407.90	BIF	0.55
MP14	410.90	BIF	0.53
MP17	417.70	BIF	1.55

Difference between MP-56 BIF Co data and Thibon et al (2019)'s Co data

Sample	Depth (m)	Lithology	Co (ppm)	Difference	
MP-BIF-05	398.40	BIF	23	22.35	***(23 - 0.65)***
MP-BIF-11	401.24	BIF	21.24	20.49	***(21.24 - 0.75)***
MP-BIF-15	403.06	BIF	21.77	21.19	***(21.77 - 0.58)***
MP-BIF-19	405.00	BIF	16.32	15.52	***(16.32 - 0.80)***
MP-BIF-25	407.80	BIF	21.24	20.69	***(21.24 - 0.55)***
MP-BIF-32	411.20	BIF	18.12	17.59	***(18.12 - 0.53)***
MP-BIF-46	417.86	BIF	18.71	17.16	***(18.71 - 1.55)***
			Average	**19.28**	

Equation: ((Original Co)) - (Average of the difference (19.28)))

MP-56

Sample code	Depth (m)	Original Co (ppm)	Corrected Co (ppm)
MP-BIF-01	396.45	41.52	22.24
MP-BIF-02	396.67	23.75	4.47
MP-BIF-03	397.19	16.03	0
MP-BIF-04	397.85	22.83	3.55
MP-BIF-05	398.48	23	3.72
MP-BIF-06	398.74	26.29	7.01
MP-BIF-07	399.22	23.76	4.48
MP-BIF-08	399.72	22.83	3.55
MP-BIF-09	400.21	19.63	0.35
MP-BIF-10	400.67	17.76	0
MP-BIF-11	401.24	21.24	1.96
MP-BIF-12	401.68	22.43	3.15
MP-BIF-13	402.04	18.67	0
MP-BIF-14	402.56	21.09	1.81
MP-BIF-15	403.06	21.77	2.49
MP-BIF-16	403.55	23.34	4.06
MP-BIF-17	404.04	18.88	0
MP-BIF-18	404.55	21.81	2.53
MP-BIF-19	405	16.38	0
MP-BIF-20	405.48	21.16	1.88
MP-BIF-21	405.92	21.97	2.69
MP-BIF-22	406.37	25.04	5.76
MP-BIF-23	406.79	20.16	0.88
MP-BIF-24	407.28	32.57	13.29
MP-BIF-25	407.80	21.24	1.96
MP-BIF-26	408.32	20.78	1.50
MP-BIF-27	408.70	19.35	0.07
MP-BIF-28	409.22	19.22	0
MP-BIF-29	409.73	25.24	5.96
MP-BIF-30	410.21	17.13	0
MP-BIF-31	410.55	26.44	7.16
MP-BIF-32	411.02	18.12	0
MP-BIF-33	411.45	25.58	6.30
MP-BIF-34	411.96	30.02	10.74
MP-BIF-35	412.47	18.29	0
MP-BIF-36	412.99	43.94	24.66
MP-BIF-37	413.49	20.3	1.02
MP-BIF-38	413.98	21.41	2.13
MP-BIF-39	414.53	21.58	2.30
MP-BIF-40	414.93	23.04	3.76
MP-BIF-41	415.51	48.24	28.96
MP-BIF-42	415.87	48.23	28.95
MP-BIF-43	416.30	20.18	0.90
MP-BIF-44	416.82	17.01	0
MP-BIF-45	417.29	23.7	4.42
MP-BIF-46	417.86	18.71	0
MP-BIF-47	418.43	24.84	5.56
MP-BIF-48	418.90	34.94	15.66
MP-BIF-49	419.41	26.67	7.39
MP-BIF-50	419.85	23.37	4.09
MP-BIF-51	420.30	22.41	3.13
MP-BIF-52	420.41	27.21	7.93
MP-BIF-53	420.92	32.29	13.01

G774

Sample Code	Depth (m)	Original Co (ppm)	Corrected Co (ppm)
G7BF-01	90.81	43.9	24.62
G7BF-02	91.28	28.27	8.89
G7BF-03	91.65	22.86	3.48
G7BF-04	92.10	42.02	22.63
G7BF-05	92.48	26.36	6.98
G7BF-06	92.94	30.93	11.55
G7BF-07	93.34	27.94	8.56
G7BF-08	93.88	34.4	15.02
G7BF-09	94.35	53.33	33.95
G7BF-10	94.73	22.6	3.22
G7BF-11	95.11	29.28	9.9
G7BF-12	95.73	30	10.62
G7BF-13	96.23	31.16	11.78
G7BF-14	96.73	24.17	4.79
G7BF-15	97.15	17.58	0
G7BF-16	97.54	25.73	6.35
G7BF-17	98.02	29.29	9.91
G7BF-18	98.60	31.99	12.61
G7BF-19	99.02	22.4	3.02
G7BF-20	99.42	23.76	4.38
G7BF-21	100.18	33	13.62
G7BF-22	100.56	25.36	5.98
G7BF-23	101	25.36	5.98
G7BF-24	101.64	22.21	2.83